Magnetotransport, structural and optical characterization of p-type modulation doped heterostructures with high Ge content $Si_{1-x}Ge_x$ channel grown by SS-MBE on $Si_{1-y}Ge_y$/Si(001) virtual substrates

BY

MAKSYM MYRONOV

Thesis submitted in partial fulfilment of the requirements for the degree of Doctor of Philosophy in Physics

Department of Physics, University of Warwick, UK

April 2001

TABLE OF CONTENTS

LIST OF FIGURES AND TABLES

page

FIGURES

TABLES

ACKNOWLEDGEMENTS

I would like to thank my supervisors Professor E.H.C. Parker and Professor T.E. Whall for their valuable guidance throughout my PhD course. I am very grateful to Dr. O.A. Mironov for his everyday supervision, fruitful discussions and his technical expertise throughout the magnetotransport characterization phase of my research. My thanks to Dr. C.P. Parry and Dr. P.J. Phillips for SS-MBE growth of samples that have been studied in my research and useful discussions. To all my other colleagues from Advanced Semiconductors Research group (Department of Physics, University of Warwick, Coventry, UK), both past and present. I would like to thank Dr. S.G. Lyapin and Dr. P.C. Klipstein from Clarendon Laboratory (Department of Physics, University of Oxford, Oxford, UK) for 3 years of our collaboration, which consisted of Raman spectroscopy and Photoluminescence measurements of SiGe heterostructures, and very useful discussions. I would like to thank Dr. U. Konig and members of his group from Daimler Chrysler AG Research and Technology (Ulm, Germany) for our collaboration. In particular to Dr. T. Hackbarth for SS-MBE growth of SiGe heterostructures and Dr. G. Hoeck for supply of samples and useful discussions. The great thanks to those people with whom were discussed the experimental results obtained during this research, their teaching and advising. Especially to Professor R.A. Stradling and Dr. J.J. Harris (Imperial College of Science, Technology and Medicine, London, UK), Professor E.B. Yakimov (Institute of Microelectronics Technology, Russian Academy of Sciences, Chernogolovka, Russia), Professor V.G. Kantser (International Laboratory of SSE, Academy of Sciences, Kishinev, Moldova), Professor A.G. Cullis (University of Sheffield, Sheffield, UK) and Professor M.G. Dowsett (University of Warwick, Coventry, UK).

Maksym Myronov

DECLARATION

This thesis is the result of research carried out by the author in Department of Physics, University of Warwick, UK between December 1997 and December 2000 and is submitted as partial fulfilment of the requirements for the award of the degree of Doctor of Philosophy in Physics. The work described here is all my own, except where acknowledged as otherwise in the text.

A large amount of the performed work during this research has been published in scientific journals and presented at the international scientific conferences.

Publications in journals during this research

1. **M. Myronov**, C.P. Parry, T.E. Whall and E.H.C. Parker "Annealing effect on transport and structural properties of $Si_{1-x}Ge_x/Si_{1-y}Ge_y/Si(001)$ p-type modulation doped heterostructures" submitted to Applied Physics Letters

2. **M. Myronov**, C.P. Parry, O.A. Mironov, T.E. Whall and E.H.C. Parker "Very high hole mobility in $Si_{0.2}Ge_{0.8}/Si_{0.65}Ge_{0.35}/Si(001)$ p-type MOD metamorphic heterostructures" submitted to Applied Physics Letters

3. S. Kiatgamolchai, O.A. Mironov, V.G. Kantser, **M. Myronov**, E.H.C. Parker, T.E. Whall, Z. Dziuba "Maximum Entropy Mobility Spectrum Analysis for Electron Transport in Layered Semiconductor Structures" submitted to Physical Review B.

4. Yu.F. Komnik, V.V. Andrievskii, I.B. Berkutov, S.S. Kryachko, **M. Myronov** and T.E. Whall "Quantum effects in the hole-type Si/SiGe heterojunctions". Low Temperature Physics, Vol.26, N8, pp.609-614, 2000.

Publications in conference proceedings during this research

1. O.A. Mironov, **M. Myronov**, E.H.C. Parker, T.E. Whall "High Ge content SiGe MODFET heterostructures on virtual substrates for device applications: HOLE MOBILITIES higher than electrons in the room temperature range of operation". Abstract book: "SiGe (C) 2001 Workshop", 21-23 January 2001, Tohoku University, Sendai, Japan, p.V-02.

2. **M. Myronov**, O.A. Mironov, E.H.C. Parker, T.E. Whall, V.V. Andrievskii, Yu.F. Komnik, I.B. Berkutov "Transport properties of charge carriers in p-type modulation doped heterostructures with $Si_{1-x}Ge_x$ channel". Abstracts book: "CMMP 2000" (Condensed Matter and Materials Physics), 19-21 December 2000, University of Bristol, Bristol, UK, p.154.

3. **M. Myronov**, C.P. Parry, O.A. Mironov, E.H.C. Parker, O.A. Soltanovich and E.B. Yakimov "Growth and annealing induced defects analysis in $Si_{1-x}Ge_x/Si_{1-y}Ge_y/Si(001)$ heterostructures with high Ge content". Abstract book: "International Conference on Solid State Crystals 2000: Materials Science and Applications", 2-13 October 2000, Zakopane, Poland, p.69.

4. **M. Myronov**, S. Kiatgamolchai, O.A. Mironov, T.E. Whall, E.M. Sheregii, G. Tomaka, T. Kakol, J. Klamut "Mobility spectrum analysis of high Ge content SiGe/Si heterostructures". Abstract book: "International Conference on Solid State Crystals 2000: Materials Science and Applications", 2-13 October 2000, Zakopane, Poland, p.140.

5. **M. Myronov**, E.H.C. Parker, T.E. Whall, S.G. Lyapin, P.C. Klipstein "Thermal annealing effect on properties of $Si_{0.2}Ge_{0.8}/Si_{0.7}Ge_{0.3}/Si(001)$ p-type modulation doped heterostructures". Abstract book: "10th European Heterostructure Technology Workshop", 18-19 September 2000, University of Ulm, International Institute Schloss Reisensburg, Gunzburg, Germany, p.31.

6. **M. Myronov**, C.P. Parry, O.A. Mironov, E.H.C. Parker, T.E. Whall, E. Hoeflinger, G. Bauer "Post-growth annealing effect on magnetotransport and structural properties of $Si_{0.2}Ge_{0.8}/Si_{0.65}Ge_{0.35}/Si(001)$ modulation doped heterostructure". Abstract book: "10th European Heterostructure Technology Workshop", 18-19 September 2000, University of Ulm, International Institute Schloss Reisensburg, Gunzburg, Germany, p.57.

7. G. Hoeck, T. Hackbarth, **M. Myronov**, O.A. Mironov, E.H.C. Parker, E. Kohn "Magnetotransport properties of $Si_{1-x}Ge_x/Si_{1-y}Ge_y/Si(001)$ p-type modulation doped heterostructures with high Ge content channel". Abstract book: "10th European Heterostructure Technology Workshop", 18-19 September 2000, University of Ulm, International Institute Schloss Reisensburg, Gunzburg, Germany, p.35.

8. S. Kiatgamolchai, **M. Myronov**, O.A. Mironov, E.H.C. Parker, T.E. Whall "A Novel Mobility Spectrum Maximum Entropy Approach for Magnetotransport Analysis of SiGe/Si heterostructures". Abstract book: "10th European Heterostructure Technology Workshop", 18-19 September 2000, University of Ulm, International Institute Schloss Reisensburg, Gunzburg, Germany, p.65.

9. **M. Myronov**, S.G. Lyapin, C. Parry, E.H.C. Parker, T.E. Whall, P.C. Klipstein, J.M. Bonar "Post-growth annealing effect on properties of p-type modulation doped $Si_{0.2}Ge_{0.8}/Si_{0.65}Ge_{0.35}/Si(001)$ heterostructure studied by XTEM and Raman spectroscopy". Abstracts book: "CMMP'99", 19-22 December 1999, University of Leicester, Leicester, UK, SEMd.P1.21.

10. S. Kiatgamolchai, **M. Myronov**, E.H.C. Parker, T.E. Whall, J.C. Yeoh, T.K. Fobelets, T.J. Thornton "Mobility Spectrum of 2DHG and 2DEG in SiGe-Si Heterostructures". Abstracts book: "11th General Conference of the European Physical Society (EPS-11): Trends in Physics", 6-10 September 1999, Church House Conference Centre, London, UK, p.53.

11. M.A. Sadeghzadeh, **M. Myronov**, E.H.C. Parker, T.E. Whall "Magnetotransport Study of Two-Dimensional Hole Gases in Si/SiGe/Si Inverted Modulation Doped Structures Grown by MBE". Abstracts book: "CMMP'98", 21-23 December 1998, Manchester, UK, p.135.

ABSTRACT

This thesis is a report on experimental investigations of magnetotransport, structural and optical properties of p-type modulation doped (MOD) heterostructures with $Si_{1-x}Ge_x$ channel of high Ge content ($0.6<x<1$) grown on $Si_{1-y}Ge_y$/Si(001) virtual substrate (VS). The active layers of MOD heterostructures were grown by solid source molecular beam epitaxy (SS-MBE). The VSs were grown either by SS-MBE or low-pressure chemical vapour deposition (LP-CVD).

The influence of thermal annealing on magnetotransport, structural and optical properties of $Si_{1-x}Ge_x/Si_{1-y}Ge_y$ heterostructures was studied by performing the post growth furnace thermal annealing (FTA) treatments in the temperature range of 600-900C for 30min and rapid thermal annealing (RTA) treatments at temperature 750C for 30sec.

Structural and optical analysis of p-type MOD $Si_{1-x}Ge_x/Si_{1-y}Ge_y$ heterostructures involved the techniques of cross-sectional transmission electron microscopy, ultra low energy secondary ion mass spectrometry, photoluminescence spectroscopy, micro-Raman spectroscopy and scanning white-light interferometry. From the combinations of experimental results obtained by these techniques the Ge composition in the SiGe heteroepilayers, their thicknesses, state of strain in the heteroepilayers and dislocations microstructure in VSs were obtained.

After post growth thermal annealing treatments were observed broadening of the $Si_{1-x}Ge_x$ channel accompanied with the reduction of Ge content in the channel and smearing of $Si_{1-x}Ge_x/Si_{1-y}Ge_y$ interfaces.

The $Si_{0.7}Ge_{0.3}$ on low-temperature Si buffer VSs with very good structural properties were designed and grown by SS-MBE. These include: relatively thin 850nm total thickness of VS, 4-6nm Peak-to-Valley values of surface roughness, less than $10^5 cm^{-2}$ threading dislocations density and more than 95% degree of relaxation in the top layers of VS.

The Hall mobility and sheet carrier density of as-grown and annealed p-type MOD $Si_{1-x}Ge_x/Si_{1-y}Ge_y$ heterostructures were obtained by a combination of resistivity and Hall effect measurements in the temperature range of 9-300K. The FTA at 600C for 30min was seen to have a negligible effect on the Hall mobility and sheet carrier density. Increasing the annealing temperature resulted in pronounced successive increases of Hall mobility accompanied by the opposite behaviour of sheet carrier density. Each sample had the optimum FTA temperature corresponded to the maximum Hall mobility. After RTA at 750C for 30sec the increase of Hall mobility for researched samples was observed as well. The highest mobility (at sheet carrier density) of 2DHG measured at 9K was observed for sample containing Ge channel grown on thick $Si_{0.4}Ge_{0.6}$ linearly graded VS and corresponds to $14855 cm^2 \cdot V^{-1} \cdot s^{-1}$ ($2.87 \cdot 10^{12} cm^{-2}$). The highest Hall mobility (at sheet carrier density) measured at 293K was observed for $Si_{0.2}Ge_{0.8}/Si_{0.65}Ge_{0.35}$ heterostructure after FTA at 750C for 30min and corresponds to $1776 cm^2 \cdot V^{-1} \cdot s^{-1}$ ($2.37 \cdot 10^{13} cm^{-2}$).

To extract the drift mobility and sheet carrier density of 2DHG at temperatures up to 300K, magnetotransport measurements in magnetic fields up to 11T were performed on several heterostructures. The data were analyzed by technique of Maximum-Entropy Mobility Spectrum Analysis. The highest drift mobility (at sheet carrier density) of 2DHG at 290K was obtained for the $Si_{0.2}Ge_{0.8}/Si_{0.65}Ge_{0.35}$ heterostructure after FTA at 750C and corresponds to $3607 cm^2 \cdot V^{-1} \cdot s^{-1}$ ($4.94 \cdot 10^{12} cm^{-2}$).

Low temperature magnetotransport measurements down to 350 mK and at magnetic fields up to 11T were carried out on several heterostructures. From the temperature dependence of the Shubnikov-de Haas oscillations observed at temperatures below 20K were extracted followed parameters of 2DHG, — effective mass, sheet carrier density, transport and quantum scattering times, and related parameters. For the $Si_{0.05}Ge_{0.95}/Si_{0.37}Ge_{0.63}$ heterostructure was obtained the lowest hole effective mass $m^* = 0.15 \cdot m_0$ and the highest transport to quantum scattering times ratio $\alpha = 2.18$.

List of abbreviations

2DCG	Two dimensional carrier gas
2DEG	Two dimensional electron gas
2DHG	Two dimensional hole gas
CMOS	Complementary metal oxide semiconductor
CVD	Chemical vapour deposition
DOS	Density of states
FET	Field effect transistor
HH	Heavy-hole
I-QMSA	Improved quantitative mobility spectrum analysis
LH	Light-hole
LP-CVD	Low pressure chemical vapour deposition
LT-Si	Low-temperature Si
MBE	Molecular beam epitaxy
MEMSA	Maximum-entropy mobility spectrum analysis
MOD	Modulation-doping
MODQW	Modulation doped quantum well
MOSFET	Metal oxide semiconductor field effect transistor
MSA	Mobility spectrum analysis
QMSA	Quantitative mobility spectrum analysis
SdH	Shubnikov-de Haas
SO	Spin-orbit-split hole
SOI	Si-on-insulator
SS-MBE	Solid source molecular beam epitaxy
UHV	Ultra high vacuum
UHV-CVD	Ultra high vacuum chemical vapour deposition
VLSI	Very large-scale integration
VS	Virtual substrate

1. Introduction

1.1 Impact of SiGe on Si microelectronics

While the first transistor was fabricated using germanium in 1947 [1] and III-V semiconductor materials have consistently demonstrated superior high-speed performance, it is silicon that completely dominates the present semiconductor market. At present, the vast majority of all semiconductor devices produced on production lines are used the Si-based technologies. One may put forward many subtle and non-subtle reasons for this position but there is one that dominates all, — cost. It is clear that the silicon complementary metal oxide semiconductor (CMOS) field effect transistors (FETs) have an advantageous position compared to III-V-based transistors with costs in 1999 being over 200 times cheaper than GaAs per square millimeter. The low cost of CMOS may be traced to the ability to fabricate billions of transistors all with near identical properties across slices of silicon of ever-increasing diameter. The fabrication processes and the device performance rely heavily on a number of natural properties of silicon, but the most important reason for the unrivaled success of Si devices lies in the combination of an easily available semiconductor and an excellent natural oxide, namely SiO_2, which serves as an insulator and as a protecting passivation layer. SiO_2 have allowed Si to dominate over faster materials such as GaAs because for these alternative and more expensive fabrication schemes must be used, which cannot reach the phenomenal yields achievable on a CMOS line. The increase in density and performance of CMOS has been produced by down-scaling the transistors and circuits over the years. The gate-lengths of the transistors in circuits have followed an exponential scaling law since the first metal oxide semiconductor FET (MOSFET) was produced in the early 1960s [2]. The exponential decrease in size has been termed Moore's law after Gordon Moore, who first analyzed the effect. While this decrease in size has allowed an increase in density and a decrease in cost per transistor, the cost of fabrication plants has also been scaling upwards at an exponential rate [3]. At some

point, however, this scaling must finish, whether fundamental or economic, will eventually appear to prevent smaller transistors or circuits being fabricated. With the amount of capital and knowledge presently tied up in both Si production and research, the impetus to design and produce devices in Si is enormous. With present production plants costing in excess of $100 billion, it is almost impossible to persuade companies to change to completely new, untried technologies. CMOS is so cheap and dominant that one must find applications where it cannot be used, such as optoelectronics, analogue or high-speed markets, if a new technology is to appear on the market place. One compromise is to use a new material system that is CMOS compatible, such as SiGe, to allow bandgap-engineered devices with higher performance or new functionality [4]. One may suggest that this is going back to the roots of the original Ge transistor by adding Ge to the system, but the SiGe is strained, which completely changes the material and electronic properties along with the physics. Increased integration levels reduce the number of chips in final products and hence should lower costs and increase yields. SiGe has the advantage that it may be used to modify conventional transistors to give higher speed and lower power. The Semiconductor Industry Association roadmap [5] predicts that conventional, CMOS transistors cannot operate below gate lengths of order of 70 nm while the use of SiGe in conventional FET devices has been predicted to allow smaller dimensions. Coupled to this the ability to produce quantum devices on the same chip gives SiGe substantial potential for future circuits.

The $Si_{1-x}Ge_x$/Si is a very good suited heterosystem, which can be considered as a kind of natural choice: the two group-IV elements Si and Ge crystallize in the same diamond lattice, and form random $Si_{1-x}Ge_x$ alloys of arbitrary composition. By means of these alloys the bandstructure can be tuned within the relatively wide margins given by the two elemental semiconductors. In addition, the structural and chemical properties are very similar, which simplify epitaxial growth and the application of standard Si technologies,

but they differ to a large enough extent to allow selective structuring procedures. These obvious advantages of a Si-based all-group-IV heterosystem were recognized at an early stage of heterostructure research, with the first report on a $Si_{1-x}Ge_x/Si$ superlattices appearing already back in 1975 [6].

One of the main problems in growing $Si_{1-x}Ge_x$ alloy on a Si(001) substrate is the lattice mismatch, which increases from 0 to 4.2% as x is varied from 0 to 1. The larger x becomes, the thinner the $Si_{1-x}Ge_x$ channel has to be grown in order to prevent misfit dislocations from relaxing the strain. Hence if Ge is grown on Si then only 4 atomic monolayers may be grown before the energy from the strain in the system creates dislocations. There is therefore a critical thickness, above which defects in the form of dislocations are produced if a strained layer is grown too thick. One of the possibilities to obtain Ge compositions $x>0.5$, while retaining strain in the $Si_{1-x}Ge_x$ layer, is to use relaxed $Si_{1-y}Ge_y$ substrate with the bulk lattice constant of the $Si_{1-y}Ge_y$. This allows strained Si, Ge or $Si_{1-x}Ge_x$ to be grown on an underlying Si wafer. Such substrates are termed virtual substrates (VSs).

Nevertheless, progress in material growth and basic understanding of the band alignment lagged initially behind similar investigations made in the much more popular, lattice-matched GaAs/AlGaAs heterosystem. With growth techniques, such as molecular beam epitaxy (MBE), then still in their infancy, a main reason can be seen in the quite significant lattice mismatch between Si and Ge, but also in severe doping problems caused by the strong segregation of most dopants then available. Over the years, most of the growth and doping problems have been solved, and the understanding of the strain effects induced by the lattice mismatch has reached a state that allows their exploitation as a further parameter in the field of man-made bandstructures.

An example for the high level reached in the last years is the $Si_{1-x}Ge_x/Si$ heterobipolar transistor [7] (HBT), with demonstrated cut-off frequencies and maximum

oscillation frequencies well beyond 100 GHz [8,9]. This is roughly a factor-of-two improvement as compared to the best existing Si bipolar junction transistors (BJTs), but, what is more important, the $Si_{1-x}Ge_x$/Si HBT boosts Si-based technologies into an area that has so far been a exclusive domain of III–V devices.

At present, the HBT is the most advanced device type in the $Si_{1-x}Ge_x$/Si heterosystem, with products having already been announced, or being expected to be available commercially in the very near future [10]. In addition, a variety of other potential applications are pursued by the ever-increasing number of research groups working in the field of Si-based heterostructures. As an example, optoelectronic functions including infrared detectors and waveguides, and even light emitters, are investigated intensely [11].

Since the aforementioned Si-MOSFETs are the most widespread of all electronic devices, a successful introduction of the $Si_{1-x}Ge_x$/Si heterostructure into that mainstream area is expected to have an enormous impact. Referring to the experiences gained with III–V MODFETs, the advantages a hetero-MOSFET can offer are obvious: at room temperature the carrier mobility can be increased by a factor of two to three by employing the band offset at the $Si_{1-x}Ge_x$/Si heterojunction to spatially separate the mobile carriers from the ionized dopants on the one side, and from the interface with the SiO_2 insulator on the other side. This will provide the hetero-MOSFET with higher operation frequencies without sacrificing its intrinsic very large-scale integration (VLSI) ability. Enhanced electron and hole mobilities are not only important for future device applications; they can also provide new insights in the transport properties of low-dimensional carrier gases. The low-temperature electron mobility in the Si channel of a modulation-doped quantum well structure (MODQW) has recently been driven to a value beyond 500,000 $cm^2 \cdot V^{-1} \cdot s^{-1}$ [12], which is an improvement of more than a factor of ten as compared to the best MOSFETs reported. Such high mobilities, which approach the best values, reached in III–V heterostructures to within an order of magnitude, correspond to mean free paths of several

μm. This is large enough to conduct experiments on quantum point contacts and in the mesoscopic range, which so far were mainly restricted to high-mobility III–V heterostructures. Enhanced hole mobilities are another topic, which will become even more exciting, because the recently demonstrated realization of high Ge content $Si_{1-x}Ge_x$ channels allows unprecedented high hole mobilities.

References:

1. Bardeen J., W. H. Brattain, *Phys. Rev. 1948, 71, 230.*
2. Kahng D., *in Semiconductor Devices: Pioneering Papers (Ed: S. M. Sze), World Scientific, Singapore 1991, p. 583.*
3. *The National Technology Roadmap for Semiconductors, Semiconductor Industry Association, San Jose, CA 1997.*
4. People R., *IEEE J. Quantum Electron. 1986, QE-22, 1696.*
5. *The National Technology Roadmap for Semiconductors, Semiconductor Industry Association, San Jose, CA 1997.*
6. Kasper E., H.J. Herzog and H. Kibbel *1975 Appl. Phys. 8 199*
7. Gruhle A. 1994 *Silicon-Based Millimeter-Wave Devices (Springer Series in Electronics and Photonics 32)* ed J-F Luy and P Russer (Berlin:Springer) ch 4
8. Crabbe E. *et al* 1993 *Tech. Digest 51st Device Research Conf.* (New York: IEEE)
9. Schuppen A., A. Gruhle, H. Kibbel, U. Erben and U. Konig 1994 *IEDM Tech. Digest 1994* (New York: IEEE) p 377
10. Kerrmarec C., T. Tewksburry, G. Dawe, R. Bains, B.S. Meyerson, D. Harame and M. Gilbert 1994 *Microwave J.* **37** 22
11. Presting H., H. Kibbel, M. Jaros, R.M. Turton, U. Menczigar, G. Abstreiter and H.G. Grimmeiss 1992 *Semicond. Sci. Technol.* **7** 1127
12. Ismail K., M. Arafa, K.L. Saenger, J.O. Chu and B.S. Meyerson 1995 *Appl. Phys. Lett.* **66** 1077

2. Theoretical concepts and review of previous works

2.1 Structural and electronic properties of bulk Si and Ge

2.1.1 Energy band structure

Silicon and germanium are the only group-IV elements that are completely miscible, i.e. they form a continuous series of solid substitutional solutions with gradually varying properties over the entire composition range. The elements and the random $Si_{1-x}Ge_x$ alloys crystallize in the cubic diamond lattice with a lattice parameter that increases almost linearly [1] with x. The maximum mismatch amounts to 4.2% between pure Si and pure Ge. The fundamental band gap in both Si and Ge is indirect (Table 2.1), and remains so for all compositions in the $Si_{1-x}Ge_x$ alloys. The conduction band minima are six-fold degenerate in Si, where they are located along the [100] directions near the X point (usually referred to as Δ minima), and eightfold degenerate in Ge, where they are located at the Brillouin-zone boundary in the [111] directions (L minima) (Figure 2.1). The crossover between these two types of band structure occurs at x=0.85 in unstrained (i.e. cubic) $Si_{1-x}Ge_x$ alloys. The indirect bandgap at 300K (4.2K) decreases monotonically from 1.11eV (1.17eV) to 0.66eV (0.74eV) as the Ge content x increases from 0 to 1. A distinct kink occurs at the crossover point (top curve in Figure 2.2). The most important structural parameters [2] are listed in Table 2.1.

Table 2.1 Selected structural parameters of unstrained bulk silicon and germanium at room temperature [2].

	Silicon (Si)	Germanium (Ge)
Lattice type	Diamond	Diamond
Lattice constant, a (Å)	5.431	5.657
Direct bandgap, E_g^d (eV)	3.40	0.80
Indirect bandgap, E_g^i (eV)	1.11(Δ)	0.664(L)
Dielectric constant, ε	11.9	16.2

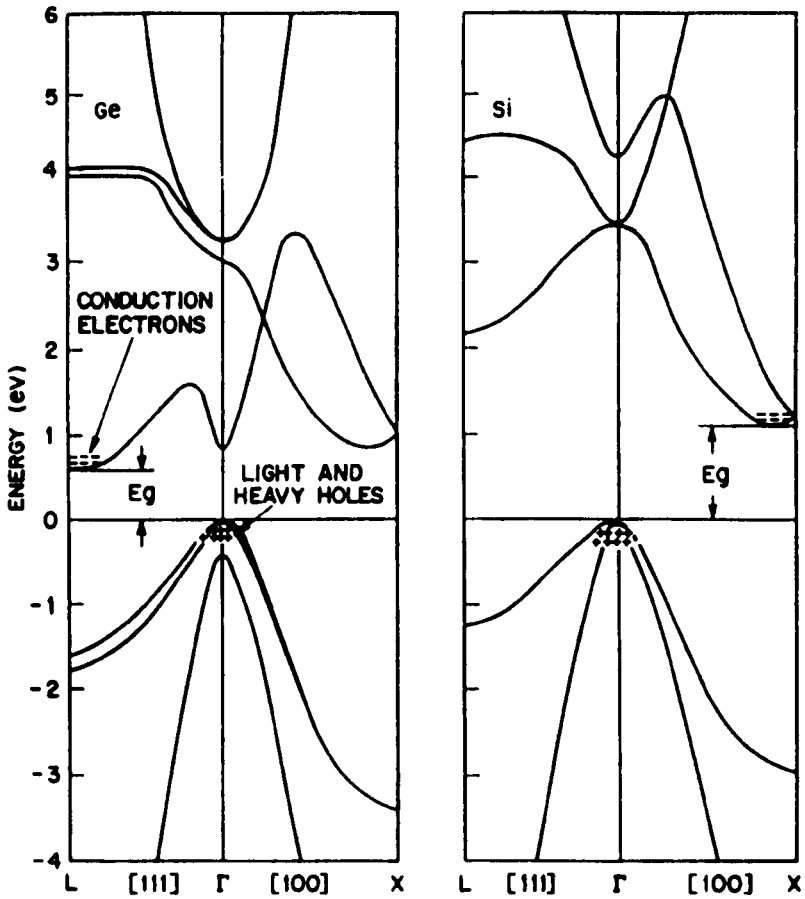

Figure 2.1 Energy band structures of Ge and Si, where E_g is the indirect energy bandgap. Plus (+) signs indicate holes in the valence bands and minus (−) signs indicate electrons in the conduction bands [3].

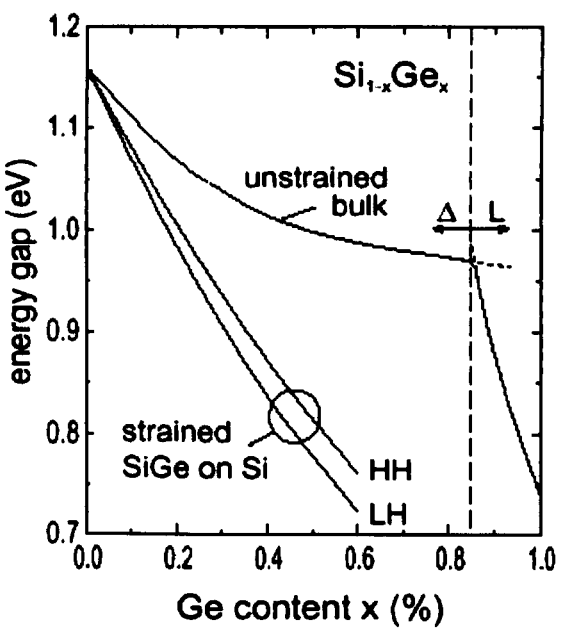

Figure 2.2 Band gap variation of $Si_{1-x}Ge_x$ alloys against Ge content x. The top curve gives the band gap energy for unstrained (cubic) alloys, which show a crossover from the Si-like (conduction band minima at Δ) to the Ge-like bandstructure (conduction band minima at the L point) at x=0.85. The two other curves are for pseudomorphic $Si_{1-x}Ge_x$ layers on a cubic Si substrate, which leads to a splitting of the valence band [4].

The bandgap variation is strongly affected by strain in the $Si_{1-x}Ge_x$ crystal, a situation that occurs in most of the thin-film applications. To illustrate the span of energy gaps accessible, the lower two curves in Figure 2.2 show the bandgap variations of $Si_{1-x}Ge_x$ alloys grown pseudomorphically on an Si(100) substrate. Under these conditions the in-plane lattice constant of the substrate is conserved throughout the alloy layer, which leads to a tetragonal distortion of the film according to the elastic properties of the lattice. Two curves exist because of the strain-induced heavy-hole/light-hole splitting of the valence band maximum [4]. Evidently, the main effects of the compressive in-plane strain are a significant and monotonic reduction of the indirect bandgap with increasing x, and a suppression of the aforementioned crossover from the Si-like to a Ge-like band structure. Experimental bandgap data are so far only available for unstrained bulk alloys and for pseudomorphic $Si_{1-x}Ge_x$ films on Si substrates. For the latter case, which is technologically important (e.g. for the Si/SiGe HBT) the data points agree well with the calculated bandgap variations. The more general case of fully strained $Si_{1-x}Ge_x$ layers on a relaxed $Si_{1-y}Ge_y$ substrate has been treated theoretically by several authors; however, their results differ quite substantially, due to the different methods used in the calculations [5].

2.1.2 Carriers effective mass

A direct consequence of the band structure is the effective transport mass both of electrons and holes. Since the areas of constant energy in the conduction band minima consist of six (Δ) and eight (L) ellipsoids of revolution for Si and Ge, respectively, the electrons in both materials are completely described by two mass parameters: m_l is the longitudinal mass along the symmetry axis of the ellipsoid ([100] directions in Si, [111] directions in Ge) and m_t is the transversal mass within the plane normal to the symmetry axis (Table 2.2).

Table 2.2 Experimental band parameters of unstrained, undoped bulk Si and Ge at room temperature. m_0 is the free electron mass. Note that the effective masses are band-edge masses, which apply only for low-doped structures at low electric fields. (Data from [2]).

		Silicon	Germanium
Electron mass (m_0)	m_t	0.19	0.08
	m_l	0.91	1.59
Valence band parameters	A	-4.26	-13.27
	B	-0.63	-8.63
	|C|	4.93	12.4
Band-edge masses of hole (m_0)	m_{hh}	0.53	0.28
	m_{lh}	0.15	0.04
	m_{so}	0.23	0.09

In both materials the longitudinal mass is significantly larger than the transversal mass. Measured electron masses in bulk Si and Ge showed that the conduction band minima behave to good approximation parabolic, i.e. the mass parameters are only weakly affected by band-filling effects via temperature or doping [6]. No experimental data on the electron masses in unstrained $Si_{1-x}Ge_x$ alloys are available. However, theoretical investigations suggest that Δ (Si-like) and L (Ge-like) mass parameters remain almost unaffected over the entire range of compositions, and that they are also rather insensitive to strain [7]. Thus, the main effect of (uniaxial) strain on the conduction band minima is the experimentally verified lifting of the respective degeneracy.

The situation at the valence band edge is even in the elemental semiconductors more complex, because the Γ-point valence band maximum is made up of three strongly interacting bands. In unstrained Si and Ge the heavy-hole (HH) and light-hole (LH) bands (Γ_8^+ symmetry) are degenerate at the Γ point, whereas the spin-orbit-split hole (SO) band (Γ_7^+ symmetry) is separated by Δ_{Si}=44 meV in Si and Δ_{Ge}=290 meV in Ge [2]. The Γ_8^+ bands are warped, i.e. the effective masses depend on the crystal direction. In a first approximation the band dispersion is frequently described by the three band parameters A, B, and C according to

$$E_{HH,LH} = E_v - \frac{\hbar^2 \cdot k^2}{2 \cdot m_0} \cdot \left(A \pm \sqrt{B^2 + \frac{C^2}{k^4} \cdot (k_x^2 \cdot k_y^2 + k_x^2 \cdot k_z^2 + k_y^2 \cdot k_z^2)} \right) \qquad (2.1)$$

$$E_{SO} = E_v - \Delta - \frac{\hbar^2}{2 \cdot m_0} A \cdot k^2 \qquad (2.2)$$

where E_v is the Γ-point energy, m_0 is the free electron mass, Δ is the spin-orbit splitting, and $\hbar$ is Planck's constant. The + and – signs describe the LH and HH bands, which split for $k \neq 0$. The parabolic approximation in (2.1) is only valid next to the Γ point. The close proximity of the bands leads also to a significant non-parabolicity, especially of the HH band, even for minor changes of the hole energy. As a result, the effective hole masses depend sensitively on external electric fields as well as on doping concentration and temperature. Hence the experimental values of the three hole masses for Si and Ge given in Table 2.2 apply only to small hole densities and are averaged values over all crystal directions.

Experimental and theoretical works concerning the valence bands in $Si_{1-x}Ge_x$ alloys have been performed by several groups. It was found that a linear interpolation of the SO splitting between the values of Si and Ge agrees reasonably well with experimental results conducted on $Si_{1-x}Ge_x$ bulk alloys [8]. On the other hand, the variation of the band parameters with x, and thus of the effective hole masses, is the subject of much more controversial discussions. Most of the calculations or interpolation schemes employing the band parameters A, B, and C, or other sets of band parameters derived from the different matrix representations of the valence band, failed to reproduce all experimental data available. At least qualitative agreement of the x dependence has been achieved by the non-linear interpolation scheme proposed by Lawaetz [9].

Application of strain lifts the degeneracy of the HH and LH bands at the Γ point [10]. In the important case of a pseudomorphic $Si_{1-x}Ge_x$ layer on an Si substrate, or, more generally, on an unstrained $Si_{1-y}Ge_y$ substrate with x>y, the HH band is shifted upward. In addition, the effective in-plane mass of the HH hole band becomes lighter and warping is reduced [11]. High enough strain can even lead to a mass inversion, i.e. the topmost HH

band can have a lower mass than the lower-lying LH band. This class of layer sequences corresponds to biaxial compressive strain in the (100) plane concomitant with uniaxial tensile strain perpendicular to this plane. The strain components are reversed, if a pseudomorphic $Si_{1-x}Ge_x$ layer is grown on cubic $Si_{1-y}Ge_y$ with $x<y$. Accordingly, the LH is shifted up while simultaneously its effective mass becomes heavy-hole-like.

2.1.3 Carriers mobility

The most important transport parameter of a semiconductor material and device is the carrier mobility. The mobility depends very much on the manner in which it is measured and it is important to understand the mobility determined by a particular characterization method and method's limitations. The carrier mobility, influences the device behavior through its frequency response or time response in two ways. First, the carrier velocity is proportional to the mobility for low electric fields. Hence higher mobility material is likely to have a higher frequency response, because carriers take less time to travel through device. Second, the device current depends on the mobility, and higher mobility materials have higher current. Higher currents charge capacitances more rapidly, resulting in a higher frequency response. There are several mobilities in use [12]:

- *Microscopic mobility* is the fundamental mobility calculated from basic concepts. It describes the mobility of the carriers in their respective band.

$$\mu = \frac{e}{m^*} \cdot \tau \tag{2.3}$$

where e is the electron charge, τ is transport scattering time and m^* is the effective mass of the respective carrier. Within the limits of the wave-vector-independent relaxation time approximation τ^{-1} is the sum of all reciprocal scattering times associated with the various scattering mechanisms (Mathiessen's rule). Thus the mobility is limited by the mechanism with the smallest scattering time.

- *Hall mobility* is determined from the combination of conductivity and Hall effect measurements.

$$\mu_H = R_H \cdot \sigma \tag{2.4}$$

where R_H is Hall coefficient for low magnetic fields and σ is conductivity.

- *Drift mobility* is the mobility measured when minority carriers drift in an electric field. It is device-oriented mobility and therefore very useful. But it is not as easy to measure as the Hall mobility, and is not used as extensively for that reason.

$$\mu_d = \frac{\upsilon}{E} \tag{2.5}$$

where υ is carrier velocity for low electric fields E (and in the absence of external magnetic fields).

The geometry has a major influence on the mobility in some devices. Surface scattering has a major influence in reducing the mobility in MOS field effect transistors. The resulting mobility, determined from the device current-voltage characteristic, is termed the *effective mobility*. In addition there are considerations that cause further division between *majority carrier mobility* and *minority carrier mobility*. Momentum considerations show that electron-electron or hole-hole scattering has no first-order effect on the mobility. However, electron-hole scattering does reduce the mobility, since electrons and holes have opposite average drift velocities. Hence minority carriers experience ionized impurity and electron-hole scattering, while majority carriers experience ionized impurity scattering.

The Hall mobility (μ_H) and drift mobility (μ_d) are differ by Hall scattering factor (r_H) and related by [13]

$$\mu_H = r_H \cdot \mu_d = (\mathrm{K} \cdot \mathrm{M}) \cdot \mu_d \tag{2.6}$$

r_H usually deviates from unity which can be expressed as the product of factors K and M. K is concerned with the energy dependence of the relaxation time in a non-degenerate gas which is

$$\mathrm{K} = \frac{\langle \tau^2 \rangle}{\langle \tau \rangle^2} \tag{2.7}$$

Any quantity A (τ^2 or τ for this case) can be averaged according to their energy dependence as [14]

$$\langle A(E) \rangle = \frac{\int_0^\infty E \cdot N(E) \cdot \exp\left(-\frac{E}{k_B \cdot T}\right) \cdot A(E) dE}{\int_0^\infty E \cdot N(E) \cdot \exp\left(-\frac{E}{k_B \cdot T}\right) dE} \tag{2.8}$$

where $N(E)$ is the density of states which has the form [15]

$$N(E) = \begin{cases} \frac{\sqrt{2} \cdot m^{*3/2}}{\pi^2 \cdot \hbar^3} \cdot E^{1/2} & \text{for 3D system} \\ \frac{m^*}{\pi \cdot \hbar^2} \cdot E^0 & \text{for 2D system} \\ \frac{\sqrt{2} \cdot m^{*1/2}}{\pi \cdot \hbar} \cdot E^{-1/2} & \text{for 1D system} \end{cases} \tag{2.9}$$

Because $\langle \tau^2 \rangle$ is always greater than $\langle \tau \rangle^2$, K is therefore greater than unity. For example, for acoustic phonon scattering mechanism K=1.18, while for the ionized impurity scattering mechanism K=1.93.

M is concerned with the anisotropy of the constant-energy surface (or contour for 2D system) and the non-parabolic nature of the energy dispersion $E(k)$. For the valence band, the constant energy surface is too complex to yield a simple form of M and it is possible only give the conclusion that M for the valence band is less than unity [13].

The main scattering mechanisms in the elemental (non-polar) semiconductors are scattering at acoustic and optical phonons (lattice scattering), and scattering at ionized and neutral impurities. In $Si_{1-x}Ge_x$ crystals random alloy scattering contributes as a fourth independent mechanism. Strain will affect all scattering mechanisms, because the strain-

induced changes in the valence and conduction band structure affect the relative importance of intra- and inter-valley scattering events [16].

Ample experimental and theoretical data exist for bulk Si, and, to some extent, for bulk Ge. The available models work best for unstrained n-type bulk material at temperatures above 100K and for rather small doping concentrations below some $10^{17}cm^{-3}$. Under these conditions intra- and inter-valley lattice scattering is dominating. With the freezing out of phonons at cryogenic temperatures ionized impurity scattering becomes the limiting mechanism whereas the influence of neutral impurity scattering remains moderate. For higher doping concentrations and/or for lower temperatures phenomenological expressions have been derived, which are based on a combination of physical models and fits to experimental data. This is especially true for holes, which are, due to the aforementioned complexity of the valence band structure, hard to describe by physical models for larger variations of doping concentration or temperature. A concise phenomenological model description was recently published by Klaassen, who treated both electrons and holes in unstrained bulk Si over very wide ranges of doping concentrations and temperatures [17].

The experimental room-temperature electron and hole mobilities of undoped, unstrained bulk Si and Ge are listed in Table 2.3. These values are of special interest, since they represent the limiting case of lattice scattering alone, as neither neutral nor ionized impurities are present. Hence these are the maximum values achievable at room temperature as long as the effective mass of the system is not affected.

Table 2.3 Room-temperature bulk mobilities of electrons and holes in unstrained, undoped Si and Ge (from [2]).

		Silicon	Germanium
Bulk mobility ($cm^2 \cdot V^{-1} \cdot s^{-1}$)	Electrons	1450	3900
	Holes	505	1800

The values in Table 2.3 reveal that both electron and hole mobilities are significantly larger in Ge, which is of course related to the smaller effective masses. Especially the hole mobility of Ge is worth mentioning, since it is higher than in any of the III–V compounds, and, what will turn out to be an interesting feature of the SiGe material system, matches the electron mobility of Si to within 20%.

While experimental data for the carrier mobilities in Si and Ge are available, and satisfactory models exist, the experimental and theoretical situation concerning the $Si_{1-x}Ge_x$ alloys is quite rudimentary. It is clear from the above discussion that not only alloy scattering has to be added as an additional mechanism but that also the other mechanisms are modified by the variations of the band structure and of the phonon spectra. The most prominent, and experimentally confirmed example is the transition from the Si-like to the Ge-like conduction band in unstrained alloys at x=0.85, which leads to a kink in the electron mobility–x curve that follows the behaviour of the effective mass [18].

Of major interest for the following chapters are the hole mobilities in $Si_{1-x}Ge_x$ alloys. In unstrained bulk alloys early experiments (on crystals of certainly debatable quality) found a U-shaped behaviour of the mobility, i.e. the lowest values were found at intermediate Ge contents [8]. This trend was qualitatively confirmed by recent calculations [19], which, on the other hand, predict a strong influence of strain in pseudomorphic $Si_{1-x}Ge_x$ layers on Si substrates.

2.2 The strained $Si_{1-x}Ge_x/Si_{1-y}Ge_y$ heterostructures

2.2.1 Energy band alignment in heterostructures

It came as a surprise to the scientific community when in 1985 Jorke and Herzog provided experimental evidence for a staggered (type-II) band alignment at the interface of a Si/SiGe heterostructure with tetragonal strain distortion in both layers [20]. In analogy to the situation in the GaAs/AlGaAs heterostructure, until then a type-I alignment was

assumed, which means that the band gap of the narrow-gap material lies entirely within the gap of the wide-gap semiconductor. Aided by additional strain measurements on the samples of Jorke and Herzog, Abstreiter and coworkers were the first to introduce the concept of a strain-induced type-II ordering in the Si/SiGe heterosystem [21]. In this eminent publication the splitting of the six-fold degenerate conduction band in a tensilely strained Si layer was correctly identified and quantified as a key element of the band alignment.

Strain effects are only one part of a general solution to the problem of band alignment at a strained layer heterointerface. The other contribution results from the chemical difference between the two heteromaterials being brought into contact. Since the long-range nature of the Coulomb interaction prevents the definition of an unambiguous, global energy scale for an infinite bulk crystal, the "chemical" band alignment cannot be derived accurately from band structure calculations of the individual materials. Instead, a "super cell" is required, that contains both materials and accounts for the changes in the bonding configuration and a concomitant dipole layer at the interface. Several such theoretical treatments have been performed for lattice-matched combinations of III–V compound semiconductors.

By calculating the band offsets at the Si/Ge interface, Van de Walle and Martin [22], [23] were the first to explicitly consider both the "chemical" band alignment and strain effects. They performed for the interface between pure Si and pure Ge on an unstrained (cubic) substrate self-consistent local-density-functional calculations employing *ab initio* pseudopotentials. Since for well-defined offsets the in-plane lattice constant $a_{||}$ has to be conserved throughout the layer sequence (pseudomorphic boundary condition), the strain conditions within the active heterolayers are determined by the lattice constant of the substrate. This leads to tetragonal distortions of the unit cells with the associated strain components in layer i parallel and perpendicular to the interface:

$$\varepsilon_{i\parallel} = \left(\frac{a_{i\parallel}}{a_i} - 1 \right) \tag{2.10}$$

$$\varepsilon_{i\perp} = \left(\frac{a_{i\perp}}{a_i} - 1 \right) \tag{2.11}$$

where a_i denotes the cubic (unstrained) lattice constant of layer i, and

$$a_{i\perp} = a_i \left[1 - D^i \cdot \left(\frac{a_{i\parallel}}{a_i} - 1 \right) \right] \tag{2.12}$$

is the lattice constant perpendicular to the interface. The elastic properties of the crystal link $a_{i\perp}$ and $a_{\parallel}$ according to equation (2.12). In the following only the (001) interface will be considered, since it is the only one compatible with MOS technologies. In this case the constant D^i depends only on the elastic constants ${c_{11}}^i$ and ${c_{12}}^i$ of the respective material:

$$D^i_{(001)} = 2 \cdot \left(\frac{c_{12}}{c_{11}} \right) \tag{2.13}$$

With these relations for the strain distribution Van de Walle and Martin calculated in a first step the valence band offsets of the Si/Ge heterojunction for substrate compositions of y=0, y=1, and y=0.4. An essential result of their computation was that the discontinuity ΔE_v of the weighted average valence band position at Γ_{25} depends only weakly (and in a linear fashion) on strain and is largely unaffected (to within ±40 meV) by the crystallographic orientation of the interface. Thus ΔE_v was proposed as a parameter that is characteristic of the intrinsic Si/Ge heterointerface, a finding that was subsequently confirmed both theoretically [24] and experimentally [25], [26] by other groups.

The significant computational effort required for a general set of valence band offsets and the unique properties of ΔE_v led Van de Walle and Martin to suggest a linear interpolation scheme for the average valence band offset, both with respect to strain and composition. This linear variation of the valence band offset was subsequently confirmed by the experiments of Morar *et al*, who employed electron-energy-loss spectroscopy on a

large quantity of samples with systematically varying Ge content [27]. Rieger and Vogl [7] adapted this concept, and, employing the slightly lower ΔE_v values of [24] that appear to be somewhat closer to experimental values [25], derived the following interpolation formula for ΔE_v at the heterointerface between a strained $Si_{1-x}Ge_x$ layer and an unstrained substrate:

$$\Delta E_v(x,y) = (0.47 - 0.06 \cdot y) \cdot (x - y) \tag{2.14}$$

Knowing ΔE_v(x,y) for arbitrary values of x and y, and exploiting its properties of being additive and transitive [23], allows a complete description of the band alignment problem in the SiGe heterosystem. This requires a determination of the relative positions of the respective band edges in either heterolayer by utilizing the values for the band gaps, the spin–orbit splittings and the deformation potentials for the respective band. This procedure was described in [23].

Figure 2.3 shows a complete set of contour plots for the offsets between the topmost valence bands (E_v^{max}(x)-E_v^{max}(y)) and the lowest conduction bands (E_c^{min}(x)-E_c^{min}(y)) of a strained $Si_{1-x}Ge_x$ layer on an unstrained $Si_{1-y}Ge_y$ substrate based on empirical pseudopotential calculations of the valence and conduction bands [7].

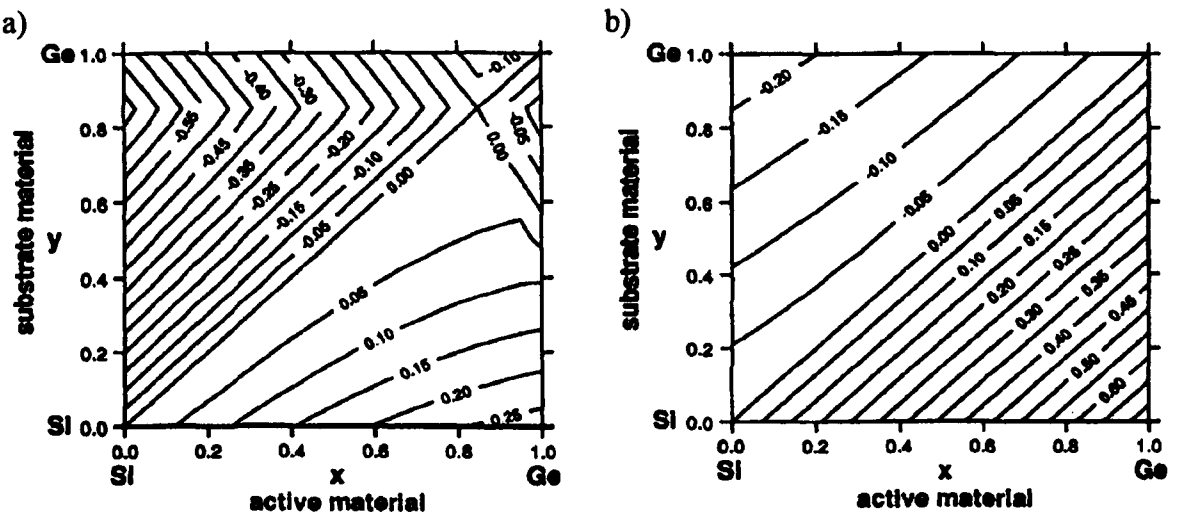

Figure 2.3 (a) Conduction-band offsets E_c^{min}(x)-E_c^{min}(y) and (b) valence-band offsets E_v^{max}(x)-E_v^{max}(y) in eV at interface of a lattice matched (001) strained $Si_{1-x}Ge_x$ alloy and an unstrained (cubic) $Si_{1-y}Ge_y$ bulk substrate (after [7]).

The values were calculated using the deformation potentials for the elements, as listed in Table 2.4, and linear interpolations for the alloys. Because of the approximations and interpolations involved, this approach is estimated to leave an uncertainty of the band offsets of about 100 meV. Only a limited number of experimental results conducted under well-defined strain conditions are available, mainly for Si/Ge, $Si/Si_{1-x}Ge_x$ and $Si_{1-x}Ge_x/Si$ heterostructures [5]. These basically confirm the respective theoretical offsets within the error margins mentioned.

Table 2.4 Deformation potentials [7], spin–orbit splittings Δ_0 and elastic constants c_{11} and c_{12} for Si and Ge [2].

	Si	Ge
$(\Xi_d+(1/3)\cdot\Xi_u)^{\Delta}-a$ (Δ minimum)	0.29	-1.90
$(\Xi_d+(1/3)\cdot\Xi_u)^{L}-a$ (L minimum)	-3.65	-5.17
a (eV)	-10.2	-12.4
b (eV)	2.33	2.08
Ξ_u^{Δ} (Δ minimum)	9.29	10.20
Δ_0 (meV)	44	296
c_{11} (10^6 N·cm^{-2})	16.75	13.15
c_{12} (10^6 N·cm^{-2})	6.5	4.94

There are four general features in Figure 2.3 worth mentioning. (i) The valence band maximum occurs always in the layer with the higher Ge content, independently of the strain condition. (ii) For $x<y$ the conduction band minimum lies in the (tensilely) strained $Si_{1-x}Ge_x$ layer, i.e. the band alignment in this regime is of type II. (iii) In an area defined by $x>y$ and $y<0.6$ the conduction band offset is smaller than ±20 meV, which means a basically flat conduction band alignment within the accuracy of the calculations. (iv) For Ge-rich strained layers ($x>0.8$) on Ge-rich substrates ($y>0.6$) a type-I alignment is predicted, i.e. the valence band maximum and the conduction band minimum are both located in the strained $Si_{1-x}Ge_x$ layer. This prediction has yet to be confirmed experimentally. Therefore Figure 2.3 allows predictions for arbitrary SiGe heterojunctions with respect to band offsets.

2.2.2 Strain adjustment in heterostructures

It has been shown in the preceding section that the valence and conduction band offsets in an Si/SiGe heterojunction depend strongly on the strain distribution throughout the layers, making strain as essential a parameter as the layer compositions. As has been detailed above, well-defined interface conditions require a conservation of the in-plane lattice constant, i.e. pseudomorphic (or coherent) growth of the active layers on a substrate whose lattice parameter has been properly adjusted. Hence, in order to exploit "strain engineering" for the tailoring of the band structure both the strain-defining substrate and the pseudomorphic heterolayers have to be realized. Bulk $Si_{1-x}Ge_x$ can be ruled out as substrates, both because of the inherent problems of pulling homogeneous $Si_{1-x}Ge_x$ crystals, and because such substrates would jeopardize the main advantage of the Si/SiGe heterosystem, namely its compatibility with existing silicon technologies. It is therefore mandatory to employ Si substrates and provide strain adjustment by means of a relaxed, intermediate $Si_{1-y}Ge_y$ buffer layer with the bulk lattice constant of the $Si_{1-y}Ge_y$. Occasionally, this combination is referred to as a *virtual substrate* (VS).

For relaxed buffers as well as for pseudomorphic layers the most relevant material parameter is the critical thickness t_c, an equilibrium parameter which is defined as the film thickness at which strain relaxation by the generation of misfit dislocations commences [28],[29]. Films thinner than t_c cannot relax, because the elastic energy stored in such a homogeneously strained layer is lower than the elastic energy associated with the local distortion around a misfit dislocation. Above t_c misfit dislocations become energetically favourable, and provide partial strain relaxation of the film, the degree of which increases with increasing layer thickness. Under non-equilibrium conditions a metastable thickness range between t_c and an apparent critical thickness t_c^* exists, in which the nucleation and propagation of misfit dislocations is kinetically suppressed [30], [31]. t_c^* depends strongly on the growth temperature, but also on the nucleation sites and mechanisms available in

the actual growth environment. Low-temperature epitaxy techniques, such as molecular beam epitaxy (MBE) or the different variants of low-temperature chemical vapour deposition (CVD) can in this way significantly extend the range of useful layer thicknesses. This is shown in Figure 2.4, where for $Si_{1-x}Ge_x$ on Si substrate the equilibrium critical thickness t_c and experimental values of films grown by MBE at 550C are plotted as a function of x. Although reasonable film thicknesses appear feasible even at a higher lattice mismatch, one has to keep in mind that metastable layers may partly relax upon subsequent heat treatments.

The three phases labeled "stable", "metastable" and "relaxed" in Figure 2.4 mark the limitations of strain engineering in the SiGe material system: strain within an active layer is always associated with a maximum (critical) thickness of this layer. This usually requires compromises concerning the maximum exploitable strain in such a layer, since highly strained layers have necessarily to be so thin that quantum size effects finally limit the achievable band offsets. On the other hand, relaxed buffer layers for strain adjustment become relatively thick, since a high degree of relaxation and low defect densities are required, which both rule out buffers deep in the metastable range.

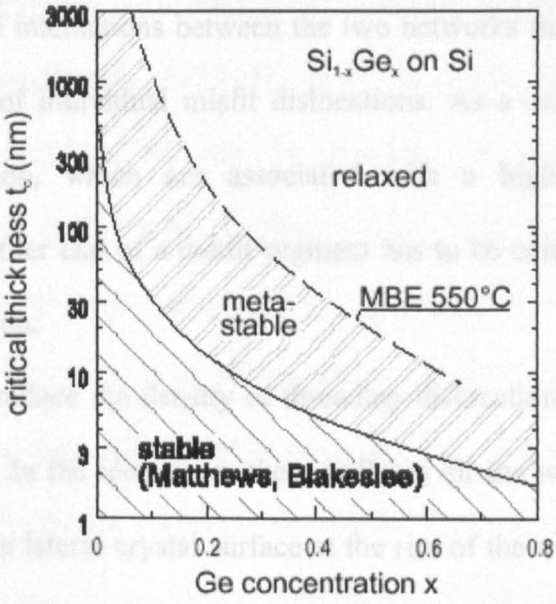

Figure 2.4 Critical thickness versus composition for $Si_{1-x}Ge_x$ on Si. The lowest curve gives the theoretical limit in thermal equilibrium [29], whereas the experimental curve is for a metastable layer grown at 550C by MBE.

Because of their importance for strain engineering, and the problems encountered in the initial attempts to realize such buffers, the next section will treat state-of-the-art buffer layer growth in some details.

2.2.3 Strain relaxed $Si_{1-y}Ge_y$/Si(001) buffer layers

The simplest way of implementing a strain-adjusting buffer layer is the growth of a constant-composition SiGe layer with a thickness exceeding t_c* by a large enough margin to allow a reasonably high degree of strain relaxation [31]. However, it was soon recognized that such buffer layers are associated with 10^9 to 10^{11} threading dislocations per cm^2 penetrating through the buffer, and ending at the respective growth front [32], [33]. A major reason for these unacceptably high densities lies in the step-like strain variation at the interface between the substrate and a constant composition buffer, which leads to an efficient confinement of the misfit dislocations to the (001) interface plane. For this orientation two equivalent networks of strain-relaxing misfit dislocations exist, which are defined by intersect of the [111] glide planes with the (001) interface plane, resulting in line vectors along the [110] and $[1\bar{1}0]$ directions. Misfit accumulation in the interface plane causes substantial interactions between the two networks that can impede and even arrest the propagation of individual misfit dislocations. As a consequence, rather short misfit segments develop, which are associated with a high density of threading dislocations, because either end of a misfit segment has to be connected to a free surface via a threading dislocation.

The only way to reduce the density of threading dislocations is an extension of the misfit segment lengths. In the ideal case, these will run all the way across the substrate, until they finally reach a lateral crystal surface at the rim of the wafer, where they can no longer affect the active layers to be grown on top of the buffer. In order to approach such a situation, three conditions have to be fulfilled. (i) The growth (or annealing) temperatures

have to be sufficiently high to allow a fast enough misfit dislocation propagation in relation to the growth rate. (ii) The density of pinning centers or arresting misfit interactions has to be low enough to promote long misfit segments. (iii) Nucleation and multiplication mechanisms for dislocations are required, but the associated activation energies should be higher than the activation energy associated with propagation in order to prevent the introduction of many short misfit segments.

Since at Ge contents beyond about 10% none of these conditions can be fulfilled in a constant-composition buffer, alternative ways have been proposed to overcome the problems associated with misfit pinning by dislocation interaction [34]. The most successful approach at present employs a linear Ge gradient throughout an initial buffer layer B1, followed by a second layer B2, throughout which the final composition of B1 is kept constant [35], [36], [37]. The advantages of this concept are obvious: the misfit dislocations are distributed over the thickness of B1 rather than being crowded into the interface plane. This strongly reduces dislocation interactions, allowing most of the dislocations to propagate unaffected with a velocity determined by the growth temperature.

In the last few years a significant amount of effort has been dedicated to an understanding and optimization of graded buffers both with respect to relaxation [37], [38], [39], [40] and surface morphology [41], [42]. These two parameters are not independent of each other, because both are affected by grading rate, growth temperature, and composition, albeit in a different fashion: while high growth temperatures are advantageous for dislocation propagation, they also support strain-driven 3D growth, which leads to a rough surface morphology that may affect lithographic steps during subsequent device processing. However, in contrast to constant-composition buffers, the grading rate offers an additional degree of freedom for controlling the strain at the growth front: shallow gradients were found both theoretically [43] and experimentally [44], [45] to lead to reduced amounts of surface strain, thus allowing higher growth temperatures

without sacrificing layer-by-layer growth. Consequently, the best buffers grown by MBE employed growth temperatures between 750 and 900C and compositional grading on the order of 10%μm^{-1} or less. Under these conditions threading densities in the 10^5 to 10^6 cm^{-2} ranges were observed on buffers with final Ge concentrations of about 30% [37], [46].

Characteristically, the surface morphology of these buffers is dominated by a rather regular cross-hatch pattern oriented along the [110] directions, which basically results from a local accumulation of the double-atomic surface steps introduced by every misfit dislocation [45], [41]. The pile-up of these steps is caused by multiplication mechanisms, which release on the order of 10 to 30 dislocations half-loops with identical Burgers vector into the same [111] plane [38], [40]. Additional growth phenomena can lead to a strain- and temperature-dependent enhancement of the dislocation-mediated corrugation height [42], but the exact mechanisms behind these observations are still the subject of intense research.

With increasing Ge content the surface mobility of the arriving atoms increases at a given substrate temperature, which shifts the onset of strain-driven 3D growth to lower temperatures. This trend has to be counteracted by a further reduction of the surface strain, or by reducing the growth temperature. Considering the relatively thick buffer layers resulting already at conventional grading of around 10%μm^{-1}, a kinetic suppression of 3D growth via lower growth temperature is usually preferred [47].

While meanwhile most of the successful MBE buffers follow the basic concept outlined above, CVD techniques are more severely restricted in the choice of growth parameters, because growth rates and temperatures can hardly be selected independently. Nevertheless, step-graded buffers were very successfully fabricated by UHV–CVD at growth temperatures of just 550C and often with steeper gradients than were found useful in high-temperature MBE growth [36]. It is not entirely clear why the significant differences in growth conditions lead to quite similar results. A likely reason accounting

for some of the differences lies in the hydrogen termination of the surface during UHV–CVD growth, which is known to act as a surfactant that can, to some extent, suppress 3D growth. Also, the kinetics of dislocation nucleation and multiplication appear to be different in MBE- and UHV–CVD-grown layers [37], again possibly because of the presence of the surfactant hydrogen.

Further improvements of the relaxed buffer layers aiming toward device applications are to be expected: very promising results were recently reported of step-graded buffers grown by atmospheric pressure (AP) CVD with intermediate *in situ* annealing steps at high temperatures [48], which create equilibrium dislocation densities in each successive composition step. Threading dislocations density as low as $100cm^{-2}$ was found, which basically means that most of the misfit segments actually extended all across the wafer. Although the surface morphology of these first layers, which were annealed at temperatures well above the melting point of pure Ge, has certainly to be improved, the defect densities are already close to device grade specifications.

Although misfit dislocation lengths approaching the wafer dimensions have successfully been demonstrated, it would be much easier if misfit segment lengths of several 10μm rather than centimeters could satisfy the demands of device-quality substrate material. Given the fact that devices in integrated circuits eventually require lateral separation, dislocation lengths defined by prepatterning of the substrate via trenches or local oxides appears to be a straightforward approach [49]. Strained-layer epi-growth on both types of patterned substrates [50], [51], [52], and also on porous Si [53] have been performed. Especially selective epitaxy on oxide patterned substrates has turned out to be promising, as the oxide strips separating the templates for epitaxial growth act both as nucleation sources and as sinks for the misfit dislocations that are to be launched into the epilayers. With linear spacings between adjacent SiO_2 walls on the order of several tens of μm, misfit segments have just to travel that length in order to find a Si/SiO_2 interface

where they can end. This way, it is relatively easy to keep the epi-patches free of threading dislocations, most of which are swept out into the oxide strips. The main challenge of such a patterning technique lies therefore in the layout of the oxide pattern, which has to be compatible with the final device arrangement. Also, the growth parameters for selective growth have to be properly adjusted, and especially the boundaries between the epi-patches and the amorphous SiO_2 ridges will have to be characterized more thoroughly with respect to long-term stability and spurious parallel conductivity.

Another interesting idea employs full-size Si-on-insulator (SOI) substrates, which might lead to entirely threading-free buffer layers [54]. Consider a very thin (<10nm) back-etched Si layer on a wafer-bonded or oxygen implanted SOI substrate, with the chemical bonds at the Si/SiO_2 interface being weak enough so that the Si layer can be considered as quasi-free-standing. Under these conditions it will be energetically favourable if the silicon substrate relaxes upon deposition of a thick enough constant-composition SiGe layer, rather than the SiGe layer itself [55], [56]. If this happens, dislocation nucleation and glide are confined to the compliant substrate, which means that the threading ends are terminated at the weakly bonded Si/SiO_2 interface that acts as an inner surface in this respect. After a first successful demonstration of the soundness of this approach [54] suitable techniques remain still to be developed for homogeneously implementing the extremely demanding SOI layers with a thickness on the order of 10nm on substrates of technically relevant diameters.

Recently, it was reported that a compositionally uniform $Si_{1-y}Ge_y$ layer with a rather low threading dislocation density ($10^4 cm^{-2}$) can be grown epitaxially on Si (001) substrate by introducing a low-temperature (LT) Si buffer layer [57], [58], [59]. Relaxed $Si_{1-y}Ge_y$ epilayers grown on LT-Si buffer have been found having lower threading dislocation density (10^4-$10^5 cm^{-2}$), smaller layer thickness (<1μm), and smoother surface in comparison with the comparable compositionally graded SiGe buffer layers. Therefore, it

may be used as the buffer for the growth of high carrier mobility SiGe heterostructures. However, the mechanism of strain relaxation of these structures is still not clear, and is under investigation. An appropriate approach should be able to explain the results of reduction of threading dislocation density, the inhomogeneous relaxation, and the relative small corrugation at the surface. Of course the LT-Si layer played an important role: not only provides low energy sites for dislocation nucleation, or point defects for trapping of propagating dislocations, but also involves in strain adjustment.

2.2.4 Layers sequence in modulation doped $Si_{1-x}Ge_x/Si_{1-y}Ge_y$ heterostructures

The first modulation-doped Si/SiGe heterostructures were realized by People, Bean and coworkers employing pseudomorphic $Si_{1-x}Ge_x$ quantum wells clad between the Si substrate and an unstrained Si cap layer [60]. As has been shown in section 2.2 in this situation the bandgap difference is almost exclusively adapted by the valence band offset. Consequently, mobility enhancement was found when the Si cladding layers were selectively p-type doped, which is consistent with the formation of a 2DHG in the $Si_{1-x}Ge_x$ channel. Based on present understanding of the band alignment, it is no longer surprising that a second experiment of People, Bean and coworkers where n-type doping was employed in an otherwise identical layer sequence, failed to show any indications of a 2D electron channel [61]. As mentioned before, Si channels with tensile in-plane strain are required for the realization of a useful conduction band offset. These were first implemented by Jorke and Herzog [20] employing a strain-symmetrizing virtual $Si_{1-y}Ge_y$ substrate. Relaxed SiGe buffers were subsequently also utilized for p-type modulation-doped structures with Ge-rich or even pure Ge channels, which cannot be deposited coherently on a Si substrate because of the large lattice mismatch involved.

In all three cases the active layers of a modulation-doped structure are similar and consist of an undoped channel for the mobile carriers, an undoped spacer layer that separates the ionized dopants from the channel, and a doping layer. The heterointerface is located between the channel and the spacer and separates the two regions energetically. Often, the doping concentration is reduced toward the surface to avoid Schottky barrier lowering, and a thin undoped Si cap layer may be added, to protect against in-depth oxidation and to allow for a well-defined Schottky gate. The layer sequences and typical thicknesses for the three types of modulation-doped structure are schematically plotted in Figure 2.5.

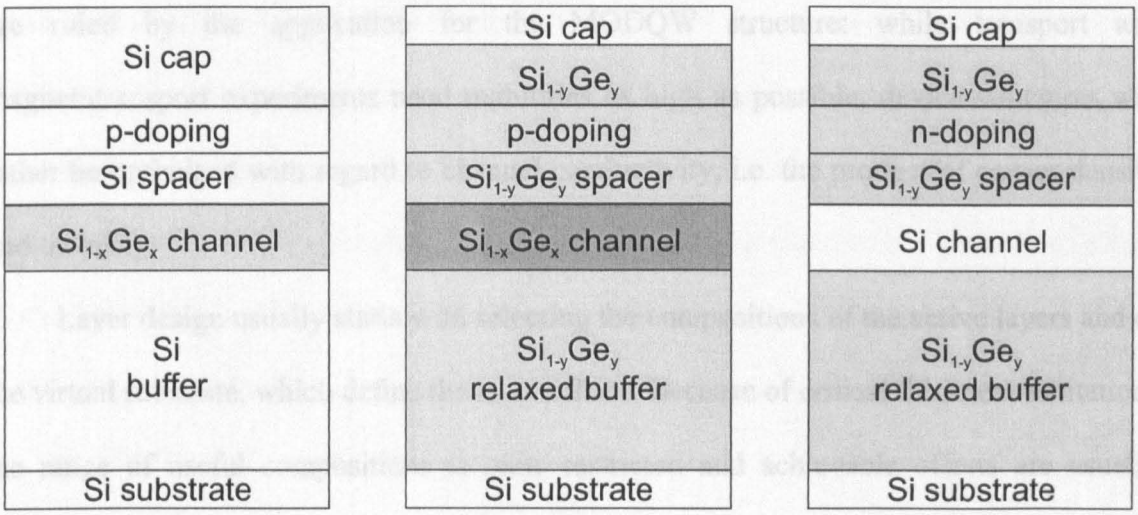

Figure 2.5 Layer sequences typically employed for (a) pseudomorphic p-type MODQWs with $Si_{1-x}Ge_x$ channel, (b) p-MODQWs with Ge-rich $Si_{1-x}Ge_x$ (or pure Ge) channel on relaxed $Si_{1-y}Ge_y$ buffer layer, and (c) n-MODQWs with Si channel on relaxed $Si_{1-y}Ge_y$ buffer layer.

A proper design of a MODQW structure requires a careful adjustment of the layer thicknesses, the compositions and strain states, and of the doping levels of the three active layers. In addition, the surface potential (often defined by a Schottky gate) and the thickness of the Si cap layer affect the electronic properties of the layers. Several interrelations between the layer parameters and also boundary conditions have to be met. The most basic design rule requires that under operational conditions all dopant atoms should be ionized, whereas all free carriers should be restricted to the channel region. This

condition defines the integral doping concentration for a given layer sequence and a defined surface potential, but still leaves ample design freedom for optimizing an MODQW structure for different purposes. High mobilities, for example, require thick spacer layers to reduce Coulomb scattering at the ionized impurities of the doping layer. Because of the linear potential drop across the (undoped) spacer, charge transfer from the supply layer into the channel becomes less and less efficient as the spacer is increased. The carrier transfer depends also to some extent on the volume concentration in the doping layer, which should be as high as possible for maximum efficiency.

The interrelation between carrier density and mobility requires compromises, which are ruled by the application for the MODQW structure: while transport and magnetotransport experiments need mobilities as high as possible, device structures will rather be optimized with regard to channel conductivity, i.e. the product of carrier density and mobility.

Layer design usually starts with selecting the compositions of the active layers and of the virtual substrate, which define the band offsets. Because of critical thickness limitations the range of useful compositions is quite restricted and achievable offsets are usually $\leq$350meV (see also section 2.2.1). The next input parameters are the surface potential and the desired density of free carriers in the channel. The required spacer width and the integral doping concentration are then obtained to good approximation by employing Boltzmann statistics and solving the Poisson equation for the layer sequence with built-in band offsets. This approach does not account correctly for quantum confinement in the channel, which requires a self-consistent solution of the Poisson and Schrodinger equations. Nevertheless, at higher temperatures, when several subbands are occupied in the well, the result of the simple Boltzmann approach agrees quite well with the self-consistent solution.

Technical reasons or growth-related restrictions can lead to modifications of the standard layer sequence discussed so far. Prominent examples are an inverted of the layer arrangement with doping on the substrate side and the channel on top, or a symmetric configuration with spacer and doping layers on either side of the channel. The inverse succession can be advantageous if the quality of the heterointerface depends on the order of deposition. This phenomenon occurs in most heterostructures and results either from segregation of one component (Ge in this case), or is related to the fact that growth morphologies are frozen in at the interface. Since strained SiGe and Ge layers tend to 3D growth (or even island growth in extreme cases, such as Ge on Si), a Si to SiGe interface is usually much more abrupt and laterally smoother than the inverse sequence. The main disadvantage of a sequence reversal is the increased background doping level in the channel, which is caused by dopants segregation or diffusion from the low-lying doping layer. Invert-doped heterostructures are not well suited for field-effect transistors either because of the increased distance between gate and doping layer, and also because of the higher demands concerning doping uniformity.

The implementation of symmetric layer geometry can have two reasons. For one, the density of carriers in the channel can be doubled, which is useful for device applications that require low channel resistances rather than extremely high mobilities. A second reason is the implementation of a symmetric wave-function in an almost rectangular potential well, which minimizes wave-function penetration into the heterobarrier. For this purpose, the influence of a surface depletion layer has to be ruled out either by employing a thick cap layer, or by proper adjustment of the respective doping concentration in the two supply layers.

2.3 Transport properties of 2DHG formed in the $Si_{1-x}Ge_x$ channel of p–type modulation doped heterostructures

2.3.1 Relaxation time approximation theory of carriers transport

Essentially all theoretical treatments of electron and hole transport in semiconductors are based upon a one-electron transport equation, which usually is the Boltzman transport equation. As with most transport equation, this equation determines the distribution function under the balanced application of the driving and dissipative forces. In the case of low electric fields, the transport is linear; that is, the current is a linear function of the electric field, with a constant conductivity independent of the field. The Fermi energy for concentration $10^{12}cm^{-2}$ is about 10meV and the thermal energy at room temperature is 25meV, nearly all carriers are in the HH subband at room temperature and below. Therefore, we deal with essentially one subband transport. Linear transport theory assumes the energy band is parabolic and isotropic

$$E = \frac{\hbar^2 \cdot k^2}{2 \cdot m^*} \tag{2.15}$$

where k is the wave vector and m* is the HH effective mass.

The solution of the Boltzmann equation for an elastic scattering leads to the following expression for the inverse transport relaxation time [62]:

$$\frac{1}{\tau} = -\frac{2 \cdot \pi}{\hbar \cdot k} \cdot \int \frac{\left|M_q\right|^2 \cdot q \cdot \cos(\phi)}{\varepsilon(0,q)^2} \cdot \delta(E_{k+q} - E_k) \frac{d^2 q}{(2 \cdot \pi)^2} \tag{2.16}$$

Here E_k is the energy of a carrier with wave vector k, q is the wave vector transferred in a scattering event, M_q is a scattering matrix element, and ϕ is the angle between k and q. The static dielectric function $\varepsilon(0,q)$ in the integrand in equation (2.16) results from the screening of the scattering potential by two-dimensional (2D) gas. The calculation of $\varepsilon(0,q)$ is reduced to the solution of electrostatic equations in the quantum well and substrate. The

result is expressed in terms of dimensionless polarization operator $\Pi(0,q)$ and the scattering matrix element $H(q)$ [63]

$$\varepsilon(0,q) = 1 + \frac{q_s}{q} \cdot H(q) \cdot \Pi(0,q) \tag{2.17}$$

Here $q_s=(m^* \cdot e^2)/(2 \cdot \pi \cdot \varepsilon \cdot \varepsilon_0 \cdot \hbar^2)$ is the screening parameter, e is the electron charge, and ε is dielectric constant. The polarization operator describes the response of 2D gas on an external perturbation [63], and the screening matrix element is a form factor depending on the wave functions and electric-field distribution. For a square infinite quantum well it has the form

$$H(q) = \frac{2}{q \cdot L} + \frac{q \cdot L}{(q \cdot L)^2 + 4 \cdot \pi^2} - \frac{32 \cdot \pi^4}{(q \cdot L)^2 \cdot [(q \cdot L)^2 + 4 \cdot \pi^2]^2} \cdot (1 - e^{q \cdot L}) \tag{2.18}$$

The dimensionless polarization operator for zero transferred energy (i.e. omitting all dynamic effects) [63] can be reduced to

$$\Pi(0,q) = \int_0^1 \frac{dx}{\exp\left(\frac{E_q}{4 \cdot k_B \cdot T} \cdot (1 - x^2) - \frac{\zeta}{k_B \cdot T}\right) + 1} \tag{2.19}$$

Here the chemical potential ζ is connected with the concentration p_s and Fermi energy $E_F \equiv \zeta \big|_{T=0} = \pi \cdot \hbar^2 \cdot p_s \cdot (m^*)^{-1}$ by the relation

$$\exp\left(\frac{E_F}{k_B \cdot T}\right) = 1 + \exp\left(\frac{\zeta}{k_B \cdot T}\right) \tag{2.20}$$

Both E_F and ζ refer to hole energies. Equation (2.19) can be simplified in the case of low and high temperatures,

$$\Pi(0,q) = 1, \qquad k_B \cdot T \ll E_F \tag{2.21}$$

$$\Pi(0,q) = \frac{E_F}{k_B \cdot T} \cdot \int_0^1 \frac{dx}{\exp\left(\frac{E_q}{4 \cdot k_B \cdot T} \cdot (1 - x^2)\right)}, \qquad k_B \cdot T \gg E_F \tag{2.22}$$

The integration with respect to ϕ in equation (2.16) reduces it to a simpler form [64], [65]

$$\frac{1}{\tau}=\frac{m^*}{\pi\cdot\hbar^3\cdot k^2}\cdot\int_0^{2\cdot k}\frac{\left|M_q\right|^2}{\left(1+\frac{q_s}{q}\cdot H(q)\cdot\Pi(0,q)\right)^2}\cdot\frac{q^2\cdot dq}{\sqrt{4\cdot k^2-q^2}} \tag{2.23}$$

It is worth noting that equation (2.23) is simplified at sufficiently high temperatures, when $(q_s \cdot E_F)/(k_B \cdot T) \ll q$, the screening can be neglected.

The relaxation time τ, which determines the mobility of holes, is a combination of relaxation times from various physical scattering mechanisms taking place. The relaxation times from *i* scattering mechanisms are combined using Mathiessen's rule,

$$\frac{1}{\tau}=\sum_i\frac{1}{\tau_i} \tag{2.24}$$

which assumes that all the individual scattering mechanisms occur independently. τ is then used in subsequent mobility calculations.

The mobility is expressed as

$$\mu=\frac{e}{4\cdot\pi\cdot\hbar^2\cdot p_s\cdot k_B\cdot T}\cdot\int_0^{\infty}\frac{E\cdot\tau(E)dE}{\cosh\left(\frac{E-\zeta}{2\cdot k_B\cdot T}\right)} \tag{2.25}$$

In the case of low and high temperature equation (2.25) can be reduced to

$$\mu=\frac{e\cdot\tau(E_F)}{m^*},\qquad k_B\cdot T\ll E_F \tag{2.26}$$

$$\mu=\frac{e}{m^*\cdot(k_B\cdot T)^2}\cdot\int_0^{\infty}\frac{E\cdot\tau(E)dE}{\exp\left(\frac{E}{k_B\cdot T}\right)},\qquad k_B\cdot T\gg E_F \tag{2.27}$$

2.3.2 Carriers scattering mechanisms

Scattering does not occur in a perfectly periodic lattice where there are no forms of resistance. A carriers scattering happens as the result of a collision that abruptly changes the carriers motion after a particle has been, on average, traveling for a time τ. Each scattering mechanism has a certain dependence on the temperature. Below the major

scattering mechanisms, which limit the carrier transport properties in the SiGe heterosystem, are presented.

2.3.2.1 Background impurity scattering

Typically a semiconductor contains defects such as impurities and dislocations. The presence of ionized impurities in quantum well causes deviations in lattice periodicity. Such impurities provide and excess or deficit of local charges donating more electrons or holes for conduction effect where more carriers are scattered.

For uniform background ionized impurity scattering the matrix element is [62]

$$\left|M_q\right|^2 = \left(\frac{e^2}{2\cdot\varepsilon_{SiGe}\cdot\varepsilon_0\cdot q}\right)^2 \cdot N_B \cdot L \cdot F_B(q,L) \tag{2.28}$$

where N_B is the concentration of background impurities in the quantum well, L is the quantum well width and

$$F_B(q,L) = \frac{4}{(q\cdot L)^2} + \frac{2\cdot(q\cdot L)^2}{((q\cdot L)^2+4\cdot\pi^2)^2} - \frac{96\cdot\pi^4}{(q\cdot L)^3\cdot((q\cdot L)^2+4\cdot\pi^2)^2}\cdot(1-e^{-q\cdot L}) - \\ -\frac{128\cdot\pi^4}{(q\cdot L)\cdot((q\cdot L)^2+4\cdot\pi^2)^3}\cdot(1-e^{-q\cdot L}) + \frac{32\cdot\pi^4}{(q\cdot L)^2\cdot((q\cdot L)^2+4\cdot\pi^2)^2}\cdot e^{-q\cdot L} \tag{2.29}$$

The background impurity scattering limited mobility is

$$\mu_{BI} \propto \frac{1}{N_B\cdot L} \tag{2.30}$$

2.3.2.2 Remote impurity scattering

A distinct advantage that may be realised using modulation-doped heterostructures is the reduction in the magnitude of ionised impurity scattering. This reduction is due to the spatial separation of the confined carrier gas from the ionised dopant impurity atoms. The charge associated with ionised impurity atoms result in local fluctuations of the periodic lattice potential, which is reducing carrier motion.

For remote impurity scattering the matrix element is [66]

$$|M_q|^2 = \left(\frac{e^2}{2 \cdot \varepsilon_{SiGe} \cdot \varepsilon_0 \cdot q}\right)^2 \cdot N_A \cdot F_R(q, L_s)^2 \tag{2.31}$$

where, N_A is the concentration of impurities and form factor due to the distance L_s between the impurity layer and the carrier gas is

$$F_R(q, L_s) = \exp(-q \cdot L_s) \tag{2.32}$$

The remote impurity scattering limited mobility is

$$\mu_{RI} \propto \frac{p_s^{3/2}}{N_A} \cdot L_s^3 \tag{2.33}$$

2.3.2.3 Interface-roughness scattering

The interface roughness in quantum well is usually considered as a random modulation of the width of the quantum well, which changes the position of the subband levels [64]. The roughness is characterized by two parameters, the average height Δ in the growth direction and the correlation length Λ in the plane. Such an approach is justified only if Δ is much smaller than the width of the well while Λ is much larger than the width. The scattering matrix element is [62]

$$|M_q|^2 = \frac{\pi^5 \cdot \hbar^4 \cdot \Delta^2 \cdot \Lambda^2}{m_z^2 \cdot L^6} \cdot e^{-\frac{q^2 \cdot \Lambda^2}{4}} \tag{2.34}$$

where m_z is the effective mass of HH1 subband in the z direction.

In the case of large correlation length $\Lambda >> L$, the main contribution to the integral in equation (2.23) comes from a region of q so small that the relaxation rate due to the interface-roughness scattering can be reduced to a simpler form. In this case $H(q)=1$, $\Pi(0,q)=1-\exp(-E_F/k_B \cdot T)$ and further simplification is possible for low temperatures when q in the integrand can be neglected compared to q_s which is typically about k_F

$$\frac{1}{\tau_{IR}} = \frac{6 \cdot \pi^{3/2} \cdot \hbar \cdot \Delta^2 \cdot m^*}{m_z^2 \cdot L^6 \cdot q_s^2 \cdot \Lambda^3 \cdot k^3}, \qquad k_B \cdot T \ll E_F \tag{2.35}$$

The physical reason for the resulting dependence of the scattering rate on Λ and k is understandable. With the increase of the product $\Lambda \cdot k$ carriers "see" a smoother interface and scattering drops.

Making use of equations (2.35) and (2.26) we can get a simple expression for the interface-roughness limited mobility at low temperatures

$$\mu_{IR} = \frac{\sqrt{2} \cdot e \cdot m_z^2 \cdot L^6 \cdot q_s^2 \cdot \Lambda^3 \cdot p_s^{3/2}}{3 \cdot \pi^3 \cdot \hbar \cdot \Delta^2 \cdot m^{*2}}, \qquad k_B \cdot T \ll E_F \tag{2.36}$$

Another simple expression for μ_{IR} can be obtained in the case of high temperatures such that $\Lambda \cdot q_s \cdot E_F (k_B \cdot T)^{-1} << 1$ and the screening can be neglected. Then

$$\frac{1}{\tau_{IR}} = \frac{\pi^{3/2} \cdot \hbar \cdot \Delta^2 \cdot m^*}{m_z^2 \cdot L^6 \cdot \Lambda^3 \cdot k^3}, \qquad k_B \cdot T \gg E_F \tag{2.37}$$

and equation (2.27) gives

$$\mu_{IR} = \frac{15 \cdot e \cdot m_z^2 \cdot L^6 \cdot \Lambda^3 \cdot (k_B \cdot T)^{3/2}}{2^{3/2} \cdot \pi^4 \cdot \hbar^4 \cdot \Delta^2 \cdot \sqrt{m^*}}, \qquad k_B \cdot T \gg E_F \tag{2.38}$$

2.3.2.4 Alloy scattering

Alloy scattering results from local fluctuations in the coulomb potential from alloying Ge atoms that dope the Si lattice. It is assumed that the Ge atoms are substituted randomly on the Si lattice sites. The fluctuations are temperature independent and thus the relaxation time is also temperature independent.

For alloy scattering in a $Si_{1-x}Ge_x$ alloy the matrix element is [62]

$$\left|M_q\right|^2 = \frac{3 \cdot E_{al}^2 \cdot a_{SiGe}^3 \cdot x \cdot (1-x)}{4 \cdot L} \tag{2.39}$$

where E_{al} is the energy associated with an alloy atom, a_{SiGe} is the lattice constant and x is the Ge composition in the $Si_{1-x}Ge_x$ alloy. The alloy scattering limited mobility is [63]

$$\mu_{AL} \propto \frac{L}{m^{*2} \cdot u_{al}^2 \cdot a_{SiGe}^3 \cdot x \cdot (1-x)} \tag{2.40}$$

Scattering from alloying effect becomes more pronounced as x increases, reaching a maximum at x=0.5 in $Si_{1-x}Ge_x$.

2.3.2.5 Acoustic-phonon scattering

Scattering from lattice vibrations (phonons) induced by thermal effects, which limit the hole mobility at high temperatures, occurs in two forms — acoustic and optical phonons. For acoustic-phonon scattering the matrix element is [62]

$$\left|M_q\right|^2 = \frac{3 \cdot a^2 \cdot k_B \cdot T}{2 \cdot \rho \cdot \hbar^3 \cdot u_l^2 \cdot L} \tag{2.41}$$

where a is hydrostatic deformation potential, ρ is the density, u_l is the velocity of the longitudinal sound.

At high temperature, $k_B \cdot T \gg E_F$, where screening can be neglected the integration in equation (2.23) can be carried out analytically and for the acoustic-phonon relaxation rate we get

$$\frac{1}{\tau_{AP}} = \frac{3 \cdot m^* \cdot a^2 \cdot k_B \cdot T}{2 \cdot \rho \cdot \hbar^3 \cdot u_l^2 \cdot L} \tag{2.42}$$

Equation (2.42) gives the following expression for the acoustic-phonon limited mobility

$$\mu_{AP} = \frac{2 \cdot e \cdot \rho \cdot \hbar^3 \cdot u_l^2 \cdot L}{3 \cdot m^{*2} \cdot a^2 \cdot k_B \cdot T} \tag{2.43}$$

The mobility rapidly decreases with increasing temperature. The acoustic-phonon scattering dominates other scattering processes at room temperature and above.

2.3.2.6 Optical-phonon scattering

For optical-phonon scattering the relaxation time is [62]

$$\frac{1}{\tau_{OP}} = \frac{3 \cdot d_0^2 \cdot m^*}{\rho \cdot \hbar^2 \cdot \omega \cdot L \cdot a_{SiGe}} \cdot \frac{1 + H(E - \hbar \cdot \omega) e^{\hbar\omega / k_B \cdot T}}{e^{\hbar\omega / k_B \cdot T} - 1} \tag{2.44}$$

where d_0 is the optical deformation potential, $\hbar \cdot \omega$ is the optical-phonon energy and $H(E - \hbar \cdot \omega)$ is the Heavyside step function taking the form of

$$H(E - \hbar \cdot \omega) = \begin{cases} 1, & E_F > \hbar \cdot \omega \\ 0, & E_F < \hbar \cdot \omega \end{cases}$$

2.3.2.7 Threading dislocations scattering

D. Monroe and coworkers [67] considered the potential effect of additional scattering mechanisms. The most interesting ones are related to the relaxed buffer layer, which had obviously a dominant effect during the opening stages of Si/SiGe MODQW growth. The most evident detrimental influence of such a buffer is related to the density of threading dislocations, the reduction of which, as we know, was the major achievement of graded buffers. For a first estimate it was assumed that each threading dislocation contains a sufficiently high density of traps to pin the Fermi level at around midgap. This will result in a cylindrical depletion region in the 2D gas around each threading segment with a radius on the order of the 2D Debye length L_{2D}. Treating scattering at the penetrating threading elements as classical hard-core scattering on N_{TD} objects of diameter L_{2D}, the contribution of the threadings alone to the mobility was given as [67]

$$\mu_{TD} = \frac{e}{2 \cdot \hbar \cdot \sqrt{\pi \cdot p_s} \cdot N_{TD} \cdot L_{2D}} \tag{2.45}$$

Despite the relatively coarse assumptions the experimentally observed influence of the threading density is qualitatively well reproduced: for $N_{TD} \geq 10^9 cm^{-2}$, which is typically observed in constant-composition buffers, the mobility of 2DEG was found to be limited to

about $20 \cdot 10^6 cm^2 \cdot V^{-1} \cdot s^{-1}$ [67], whereas this mechanism is entirely negligible at threading densities of $10^6 cm^{-2}$, which can easily be achieved in well designed buffers.

The second effect results from the long-range strain fields associated with the misfit dislocation segments located in the graded part of the buffer, or at the interface to the Si substrate in the case of a constant-composition buffer. It was assumed that the misfit-free buffer thickness L_{B2}, which is basically identical to the width of the constant-composition part B2 of a graded buffer, filters out all short-range fluctuations smaller than L_{B2}. Under these conditions the influences of inhomogeneous strain fields were found irrelevant for L_{B2}=1μm, but, because of the strong influence of the cut-off scattering wave vector, a thickness reduction of the dislocation free layer underneath the channel by a factor of ten was expected to contribute to the mobility-limiting mechanisms.

2.3.3 Carriers transport in p-type modulation doped $Si_{1-x}Ge_x/Si_{1-y}Ge_y$ heterostructures

Since the band offset between a pseudomorphic $Si_{1-x}Ge_x$ layer and cubic Si (or $Si_{1-y}Ge_y$) is almost exclusively restricted to the valence band, a layer sequence utilizing a $Si_{1-x}Ge_x$ channel is the natural choice for the implementation of a p-type MODQW structure. Several groups have exploited this concept, most of them with the doping layer located above the channel to avoid background doping in the channel due to dopants segregation. Over the years a substantial number of data have been published, focusing on the electronic properties as a function of the layer parameters. The low-temperature hole mobilities showed a continuous increase, with the best values to date being close to $20000 cm^2 \cdot V^{-1} \cdot s^{-1}$ [68]. On first sight, this appears as an enhancement by a factor of six as compared to the very first such structures [60]. However, upon closer inspection it turns out that a significant part of this improvement is correlated with a recent trend toward a reduction of the Ge content to values below 15%, with the highest mobilities occurring at

around x=10%. Although these improved mobilities are certainly an important achievement with respect to a deeper understanding of the materials properties, it has to be mentioned that such layer sequences are not well suited for device applications, because the strongly reduced valence band offsets restrict the 2D carrier densities to the low $10^{11}cm^{-2}$ range.

The failure to fabricate pseudomorphic $Si_{1-x}Ge_x$ MODQWs with reasonable carrier densities and enhanced mobilities led several groups to the conclusion that pure Ge channels or at least Ge-rich channels with x>60% would be a more promising alternative. In either case, critical thickness considerations in connection with quantum confinement energies do not allow pseudomorphic growth on Si substrates. For an assessment of the ultimate performance some research groups employed Ge substrates [69], [70], but most of the investigations are based on virtual substrates with relaxed $Si_{1-y}Ge_y$ buffer layers, similar to the ones employed for the n-channel MODQWs.

In this respect, Ge-rich channels have a distinct advantage, since the final composition of the $Si_{1-y}Ge_y$ buffer layer can be kept in the same range as for the n-type Si-channel structures, i.e. at around 30% [71]. That means a common $Si_{1-y}Ge_y$ buffer can be used for both types of MODQW, which greatly simplifies the complementary MODFET layer sequence. A disadvantage of this concept is certainly the alloyed channel, but it can be expected that the strain-induced mass reduction outweighs alloy scattering at compositions beyond the minimum of the $(x\cdot(1-x))^{-1}$, i.e. for $x \geq 50\%$.

For pure Ge channels $Si_{1-y}Ge_y$ buffer layers with final compositions above 60% Ge are required. After the pioneering work of Murakami *et al* [69], who used constant-composition buffers on a Ge substrate, the well tried linearly graded buffers were adapted and, after some frustrating attempts with constant growth temperatures T_s throughout buffer deposition, down-ramping of T_s with increasing x was introduced, as has been mentioned in section 2.2.3. In a first approximation, the melting point of a $Si_{1-x}Ge_x$ alloy at

a given composition x is frequently used as a scaling parameter for temperature-driven phenomena. Starting at 750C with pure Si, a simple estimate suggests a temperature of around 450C for the final deposition of pure Ge. Even lower temperatures are required in the case of strained Ge channels, as can be judged from a publication of Xie *et al* [72], who found 3D growth of the Ge channels even though temperature ramping provided layer-by-layer growth of their relaxed SiGe buffers with final compositions between 60% and 70%. This result led the authors to an inverted MODQW design with remote doping located on the well-defined substrate side of the channel. Meanwhile, it has been demonstrated that 3D growth in the Ge layer can ultimately be preserved at growth temperatures T_s as low as 300C. But reduced crystal quality due to an enhanced nucleation of point defects may occur at such low growth temperatures.

Although the number of publications on Ge or Ge-rich p-type MODQWs is still quite limited, the superior mobility behaviour of this concept is beyond any doubt. Despite the fact that the Ge-channel MODQWs are not yet optimized with respect to material quality, strain level in the channel, and spacer width, low temperature mobilities of 2DHG as high as 55000$cm^2 \cdot V^{-1} \cdot s^{-1}$ have been achieved in Ge channel at 4.2K so far [72]. In the heterostructures with $Si_{0.2}Ge_{0.8}$ channel, the highest room temperature mobility equal to 1050 $cm^2 \cdot V^{-1} \cdot s^{-1}$was obtained by Ismail *et al* [71]. Also, room temperature mobility of 1300 $cm^2 \cdot V^{-1} \cdot s^{-1}$ in the heterostructure with Ge channel have been reported, which has to be taken as a lower limit, since no corrections for a parallel channel have been made [47]. But even this lower limit approaches the best mobilities of n-channel MODQWs to within a factor of two, and means an improvement of at least a factor of five as compared to the best pseudomorphic $Si_{1-x}Ge_x$ channel layer sequences on Si substrates.

Further improvements are to be expected once the problem of fabricating Ge-rich virtual substrates has been overcome. These were so far grown by MBE, the inherently low growth rates of which make the deposition of a 6–10 μm thick relaxed buffer layer tedious.

Hence, it will be essential to fabricate high-quality virtual substrates by a high-throughput technique, such as CVD. MBE or UHV-CVD might then provide the precision control for the active MODQW layers with regard to layer thickness, composition, and doping profile.

2.3.4 Carriers transport in magnetic field: Classical approach

Electron motion in magnetic field has been studying for many years. The theory of this motion can be divided into two main parts: classical and quantum approaches. This separation is not strict. Some quantum effects of electron transport in magnetic fields can be good described in frames of the classical model. And, by all means, any quantum model use general classical principles and general solutions of electron motion in magnetic field.

The development of modern electronic devices requires an accurate modelling and analysis of transport phenomena in semiconductor materials and low dimensional structures. The conventional and most general approach to the investigation and simulation of carrier transport in semiconductors used the semiclassical Boltzmann equation. On its basis usual transport characteristics of the materials can be calculated via continuum model of ensemble averaging or using the Monte Carlo method [73]. The last in particular can take into account explicitly both the band structure and the various scattering processes. This method permits to compute directly all the quantities relative to transport (such as distribution function, density of carriers, velocity, energy etc.), but at a cost of long computation times and stochastic noise in data. Therefore these approaches are complex and in their framework meaningful comparisons of experimental results with the theoretical predictions are difficult, especially for multicarrier systems (compound semiconductors, layered and device structures). In the last decades in order to circumvent the complexity of conventional approach new methods of transport characterization in semiconductor materials and structures was developed. The first approach in this area of investigations was the method of mobility spectrum analysis (MSA), which had been

proposed by Beck and Anderson [74], and was developed by Dziuba [75], Antoszewski [76], Vurgaftman [77] and Kiatgamolchai [78] as a useful technique for analyzing the galvanomagnetic phenomena. MSA is the transformation of the electrical conductivity tensor versus magnetic field into conductivity density versus mobility spectrum. This procedure is a new method of presentation and analyzing of carrier parameters instead of the commonly used parameters in the conventional transport approach: concentration, average mobility and Hall factor. It is worth to outline that MSA does not require any preliminary assumptions about the number of different types of carriers and this aspect is very important for transport phenomena analysis in semiconductor device structures.

2.3.4.1 Mobility spectrum approach

Mobility spectrum analysis is a multi-carrier characterization tool that employs the magnetic field dependent resistivity ($\rho_{xx}(B)$) and Hall coefficient ($R_H(B)$). It is capable of identification of various groups of carriers in multi-layer semiconductor structures according to their different average mobilities, and hence different responses to the magnetic field. Using a set of experimental data points (B, $\rho_{xx}(B)$, $R_H(B)$), the magnetoconductivity tensor components σ_{xx} and σ_{xy} can be obtained from relations:

$$\sigma_{xx}(B) = \frac{\rho_{xx}(B)}{|\rho_{xx}(B)|^2 + |B \cdot R_H(B)|^2} \tag{2.46}$$

$$\sigma_{xy}(B) = \frac{B \cdot R_H(B)}{|\rho_{xx}(B)|^2 + |B \cdot R_H(B)|^2} \tag{2.47}$$

These tensor components are related to the mobility dependent conductivity density $s(\mu)$ by the integral transforms:

$$\sigma_{xx}(B) = \int_{-\infty}^{\infty} \frac{s(\mu)}{1+(\mu \cdot B)^2} d\mu \tag{2.48}$$

$$\sigma_{xy}(B) = \int_{-\infty}^{\infty} \frac{s(\mu) \cdot \mu \cdot B}{1+(\mu \cdot B)^2} d\mu \tag{2.49}$$

which were derived from McClure's expression [79] by Beck and Anderson [74]. In their pioneering paper, mathematical procedures have been developed to solve equations (2.48) and (2.49), i.e. to obtain $s(\mu)$ for any given measured set of data points which are usually discrete in magnetic field. However, because the number of data points are finite, it is impossible to determine $s(\mu)$ uniquely. In fact, the proposed procedures can only provide an envelope of all possible conductivity density solutions. This envelope can be regarded as yielding the maximum conductivity at each mobility that the measured material might have. Nevertheless, the $s(\mu)$ peaks in this envelope have been shown to provide good approximations to the mobility and carrier concentration of each carriers groups.

This method of calculation has been applied to a number of different semiconductor materials both bulk and thin film, for example bulk-HgTe [80], thin film HgTe [81], HgCdTe [82], HgTe-CdTe superlattices [83], AlGaAs/GaAs heterostructures [84], Si-δ-doped GaAs [85], InGaAs/InP heterostructures [86], Si-δ-doped InSb [87], InP on a semi-insulating substrate [88], and SiGe/Si heterostructures [89].

Beck and Anderson argue that if $s(\mu)$ can be solved accurately, rather than merely obtaining the envelope, it will provide all the information that can be possibly be extracted from the magnetoconductivity, which can be summarized as follows.

- The conductivities of different carriers groups will be indicated by distinct peaks in $s(\mu)$.
- The broadening of each peak will indicate an energy dependence of the relaxation time and non-parabolic variation of energy with crystal momentum.
- If the constant energy "surfaces" is anisotropic (i.e. nonspherical), the $s(\mu)$ spectrum of a given group of carriers will contain several peaks which are harmonica of the mobility.
- Constant energy "surfaces" with both concave and convex segments will result in both hole-like and electron-like terms in equation (2.49).

Subsequent developments in the mobility spectrum approach over the last 10 years have involved mathematical techniques which have gone some way towards meeting the goal of obtaining accurate values of $s(\mu)$.

Dziuba and Gorska [75], [90] have transformed equations (2.48) and (2.49) into the discrete forms

$$\sigma_{xx}(B_j) = \sum_{i=1}^{N} \frac{s_i}{1+(\mu_i \cdot B_i)^2} \tag{2.50}$$

$$\sigma_{xy}(B_j) = \sum_{i=1}^{N} \frac{s_i \cdot \mu_i \cdot B_i}{1+(\mu_i \cdot B_i)^2} \tag{2.51}$$

where s_i is a partial conductivity corresponding to the mobility μ_i. N represents the number of mobilities which are arbitrarily defined to cover a wide range of likely mobilities of all carriers. It should be large enough so that a resultant set of partial conductivities s_i is virtually quasi-continuous, and is equivalent to the conductivity density $s(\mu)$. As a result, the term "mobility spectrum" usually refers to either a set of partial conductivities s_i and mobilities μ_i or a conductivity density $s(\mu)$. Taking all data points into account, equations (2.50) and (2.51) constitute two systems of equations that are linear in s_i. A set of partial conductivities s_i is deduced by a simple iterative technique [75]. The plot of s_i versus μ_i oscillates around zero partial conductivity with the biggest positive partial conductivity occurring at the mobility corresponding to the actual average mobility of majority group of carriers in the material. The oscillation means that some of the partial conductivity is negative which is unphysical. An additional "smoothing procedure" has been proposed to minimize this effect but it was found that the negative partial conductivity couldn't be entirely suppressed while maintaining an acceptable fit to data. In this iterative technique, a set of mobility points μ_i is arbitrarily chosen in the range B_{min}^{-1} to B_{max}^{-1} where B_{min} and B_{max} are the minimum and maximum measured magnetic fields. The number of mobility

points is then limited by the number of measured magnetic field points and the lowest mobility is set by the maximum magnetic field available.

Antoszewski *et al* have developed an extended version of the iterative technique, which is known as the Quantitative Mobility Spectrum Analysis (QMSA) [76]. In QMSA, the Gauss-Seidel successive over relaxation iteration method is employed to give faster convergence and the partial conductivities are constrained to be nonnegative at all iteration steps. The mobility range has been extended to values of μ less than B_{max}^{-1} by the extrapolation of experimental data to higher fields than the maximum measured magnetic field [91]. A higher number of mobility points are also obtained by spline interpolation between the experimental data points. Even though these procedures seem to overcome problems inherent in the iterative technique, the use of interpolation and (or) extrapolation of experimental data is questionable because there are several interpolation and extrapolation techniques available and the modification of original data prior to calculation is subject to investigator bias and error.

An improved QMSA (I-QMSA) [77] has removed the limitation in the number of mobility points by not confining these to values $\mu_i=B_i^{-1}$. The range of mobilities and the number of mobility points are then independent of the range and the number of points of measured magnetic field. I-QMSA differs from the iterative technique and QMSA in that it minimizes the least square deviation of both the conductivity tensor and its derivative with respect to magnetic field. In addition, empirical procedures (two/three-point swapping and point elimination) for manipulating the mobility spectrum are introduced and shown improve the fits while smoothing the spectrum and making it "more physically reasonable". Despite these refinements, it must be said that empirical procedures are likely to be case-specific and are dependent on individual bias.

2.3.4.2 Maximum-entropy mobility spectrum analysis

Recently Somchai Kiatgamolchai [78] has developed a totally new approach named Maximum-entropy mobility spectrum analysis (MEMSA). Unlike I-QMSA, it does not contain any empirical procedures and the mobility spectrum obtained by this new technique is smoother and more stable without the need for interpolation of experimental data. The strategy was to consider the mobility spectrum in a form of probability distribution of several events. The probability is proportional to the partial conductivity s_i and each event is associated with a mobility μ_i. From the information theory viewpoint, prior to the measurement, there are no measured data and the most probable distribution is justifiably an equal distribution among all events. As we start to obtain the first few data points, they allow us to adjust the probability distribution in such a way that the modified probability distribution produces a good fit to the measured data. However, at this early stage, there are not enough data points to produce a unique probability distribution because the number of data points is much less than the number of the events. Consequently, there are many feasible probability distributions that agree well with all the data points. Rationally, one would prefer to choose the probability distribution, which is maximally noncommittal with regard to unavailable (unmeasured) data. Examples of unavailable data are those between two adjacent measured data points on the magnetic field axis and data at higher magnetic fields than are available. Jaynes [92] had shown that the most likely probability distribution among feasible distributions could be found by assigning an "entropy" to each probability distribution and choosing the one with the highest entropy. Therefore, a new approach to mobility spectrum calculations is to continue a minimization of deviation of the fit from measured data with entropy maximization.

By analogy with the entropy defined in information theory, for first time, define the entropy (H) of the mobility spectrum as

$$H(s) = -\sum_{i=1}^{N} p_i \cdot \ln(p_i) \tag{2.52}$$

$$p_i = \frac{s_i}{\sigma_0} \tag{2.53}$$

where s is a set of partial conductivities s_i, p_i is a probability of s_i, and σ_0 is the conductivity at zero magnetic field. Within this formalism, holes and electrons have nonnegative partial conductivities and their mobilities are positive and negative, respectively. Assuming that the resistivity and Hall coefficient are measured at M different magnetic fields, the summations of equations (2.50) and (2.51) can be written in a matrix form as

$$K \cdot p = \sigma^{tot} \tag{2.54}$$

$$K_{ji} = \frac{1 + \mu_i \cdot B_j}{1 + (\mu_i \cdot B_j)^2} \tag{2.55}$$

$$\sigma_j^{tot} = \frac{\sigma_{xx}(B_j) + \sigma_{xy}(B_j)}{\sigma_0} \tag{2.56}$$

where p is a set of probabilities p_i, i=1...N and j=1...M. The probabilities of mobility spectrum having maximum entropy is obtained from the method of Lagrangian multipliers [92] which gives

$$p_i = \exp(-\lambda_0 - \sum_{j=1}^{M} \lambda_j \cdot K_{ji}) \tag{2.57}$$

where λ_j is a Lagrangian multiplier. Because $\sum_{i=1}^{N} p_i = 1$, λ_0 can be presented in terms of other λ_i as

$$\exp(\lambda_0) = \sum_{i=1}^{N} \exp(-\sum_{j=1}^{M} \lambda_j \cdot K_{ji}) \tag{2.58}$$

By substitution of equation (2.57) into (2.54) and using (2.58), one arrives at an implicit set of M nonlinear equations

$$\sum_{i=1}^{N}\left[(K_{ji}-\sigma_j^{tot})\cdot\exp\left(-\sum_{j=1}^{M}\lambda_j\cdot K_{ji}\right)\right]=0 \tag{2.59}$$

which have M unknown Lagrangian multipliers.

Agmon *et al* [93] showed that these nonlinear equations could be solved by recasting the problem of determining the Lagrangian multipliers as a variational problem. The set of Lagrangian multipliers which satisfies equation (2.59) can be obtained indirectly by finding a minimum of a concave function

$$F=\ln\left(\sum_{i=1}^{N}\exp\left(-\sum_{j=1}^{M}\lambda_j\cdot(K_{ji}-\sigma_j^{tot})\right)\right) \tag{2.60}$$

Using successive approximation [94], the maximum-entropy mobility spectrum is achieved by iteration of equation (2.57) and the following equation:

$$\lambda_j^{new}=\lambda_j^{old}-\alpha\cdot\left(\sigma_j^{tot}-\sum_{i=1}^{N}K_{ji}\cdot p_i\right) \tag{2.61}$$

where α is an adjustable parameter, until the set of probabilities p_i converges.

The advantages of using the maximum-entropy approach are as follows

- The partial conductivity is guaranteed to be nonnegative according to equations (2.53) and (2.57).
- The number of mobility points can be higher than the number of magnetic field points.
- A knowledge of the partial conductivity at mobility μ_i does not necessitate a measurement at a field of $B=\mu_i^{-1}$ and the range of mobilities can be extended to much higher or lower values than B_{min}^{-1} and B_{max}^{-1} respectively.

2.3.5 Carriers transport in magnetic field: Quantum approach

As in studies of 3D carriers, transport measurements under strong magnetic fields (in the so-called quantum regime, $\omega_c \cdot \tau >> 1$) provide a vast amount of information about the parameters of 2D carrier gas (2DCG).

2.3.5.1 2D carriers in magnetic field

In the strong vertical magnetic field B_z the carriers can make complete orbits around the magnetic flux lines. The time taken to complete one orbit is [95]

$$t = \frac{2 \cdot \pi \cdot m^*}{e \cdot B} \tag{2.62}$$

and the angular frequency of the motion is

$$\omega_c = \frac{2 \cdot \pi}{t} = \frac{e \cdot B}{m^*} \tag{2.63}$$

which is the cyclotron frequency.

Combining this with equation (2.26) then yields the important relation

$$\omega_c \cdot \tau = \mu \cdot B \tag{2.64}$$

If carriers are scattered in a time short compared with t it makes little sense to talk about cyclotron orbits and we adopt as a suitable criterion the condition that the electron sweeps out at least one radian before being scattered. From equations (2.62) and (2.63) this can be expressed as $\omega_c \cdot \tau \geq 1$ and, in practice, it is usual to define a high and low magnetic fields conditions according to whether

$$\omega_c \cdot \tau = \mu \cdot B \gg 1 \quad \text{(High magnetic field)} \tag{2.65}$$

$$\omega_c \cdot \tau = \mu \cdot B \ll 1 \quad \text{(Low magnetic field)} \tag{2.66}$$

In the high magnetic field limit, where carriers complete many orbits before being scattered, the circular motion can be represented as equivalent to two linear harmonic oscillators at right angles ($\pi/2$ out of phase with one another) both characterized by an

angular frequency ω_c. In high magnetic fields when $\hbar \cdot \omega_c > k_B \cdot T$ and $\omega_c \cdot \tau > 1$ the motion for this becomes quantized into discrete energy levels. These levels are called the Landau levels and given by

$$E_n = \hbar \cdot \omega_c \cdot \left(n + \frac{1}{2} \right) \qquad n = 0,1,2,... \tag{2.67}$$

Thus the size of the orbit is also quantized. In the lowest level equation (2.67) gives the radial velocity and this allows to find the Larmor radius, more commonly called the magnetic length l_B,

$$r_L = l_B = \sqrt{\frac{\hbar}{e \cdot B}} \tag{2.68}$$

This is the quantized radius of the harmonic oscillator and is the minimum radius, as the higher energy states involve a large energy, which converts to a larger radial velocity and then to a larger radius. As the magnetic field is raised, the radius of the harmonic oscillator orbit is reduced and the radial velocity is increased. In fact we can define the cyclotron radius at the Fermi surface as

$$r_c = k_F \cdot r_L^2 = \frac{\hbar \cdot k_F}{e \cdot B} = l_B \cdot \sqrt{2 \cdot n_{\max} + 1} \tag{2.69}$$

where n_{max} is the highest occupied Landau level (that in which the Fermi level resides).

For a 2DCG structure with magnetic field B_z normal to the interface, carriers are also constrained (electrostatically) in the vertical (z) direction and the Landau levels are, therefore, fully quantized into discrete levels (rather than magnetic sub-bands). Including spin splitting, the energies of these states are given by [95]

$$E_n = \hbar \cdot \omega_c \cdot \left(n + \frac{1}{2} \right) + s \cdot g \cdot \mu_B \cdot B = \frac{\hbar \cdot e \cdot B}{m^*} \cdot \left(n + \frac{1}{2} \right) \pm \frac{1}{2} \cdot g \cdot \mu_B \cdot B \tag{2.70}$$

where s is the spin, g is the Lande g-factor and μ_B is the Bohr magneton. The cyclotron and spin energy terms are comparable so the net result is a ladder of somewhat unequally

spaced states whose energies are proportional to B_z. The density of states associated with each level is

$$n_{2D} = \frac{1}{2 \cdot \pi \cdot r_L^2} = \frac{e \cdot B}{h} \tag{2.71}$$

From equation (2.71) is follows that the number of levels occupied by carriers is

$$\nu = \frac{p_s}{n_{2D}} = \frac{h \cdot p_s}{e \cdot B} \tag{2.72}$$

so, as B_z is increased, ν decreases and there is a series of values of B_z for which ν takes integral values and for which the conductivity, therefore, goes to zero.

2.3.5.2 Shubnikov-de Haas effect

The Shubnikov-de Haas effect is essentially quantum mechanical phenomenon, which occurs at high magnetic fields — i.e. when the valence (or conduction) band states are magnetically quantized. It is manifest as a large oscillation in longitudinal magnetoresistance, which is periodic in reciprocal magnetic field. Three conditions are necessary for its observation

- The hole (or electron) distribution be degenerate: $E_F - E_v \gg k_B \cdot T$
- The magnetic field B be large enough for Landau level quantization: $\mu \cdot B \gg 1$
- The temperature be low enough that thermally induced transitions between Landau levels are negligible: $\hbar \cdot \omega_c \gg k_B \cdot T$

These conditions clearly restrict the range of applications, which explains why it has not previously been developed as a routine characterization technique; however it is ideally suited to measurements on 2DCG samples at low temperatures and is now widely used for measuring the sheet carrier density and effective mass.

Theory model can fully describe the picture of SdH effect and allows to build dependences $\rho_{xx}(B)$ and $\rho_{xy}(B)$ is rather complicated. It was derived in [63] and [96]. The more exact expression is [96]

$$\rho_{xx} = \frac{1}{\sigma_0}\cdot\left(1+2\cdot\frac{\Delta g(T)}{g_0}\right)$$

$$\rho_{xy} = \frac{\omega_c\cdot\tau}{\sigma_0}\cdot\left(1-2\cdot\frac{1}{(\omega_c\cdot\tau)^2}\cdot\frac{\Delta g(T)}{g_0}\right)$$

$$\frac{\Delta g(T)}{g_0} = 2\cdot\sum_{s=1}^{\infty}\exp\left(-\frac{\pi\cdot s}{\omega_c\cdot\tau}\right)\cdot\frac{2\cdot\pi^2\cdot s\cdot k_B\cdot T}{\hbar\cdot\omega_c}\cdot\frac{1}{\sinh\left(\frac{2\cdot\pi^2\cdot s\cdot k_B\cdot T}{\hbar\cdot\omega_c}\right)}\cdot\cos\left(\frac{2\cdot\pi\cdot s\cdot E_F}{\hbar\cdot\omega_c}-\pi\cdot s\right) \tag{2.73}$$

where ρ_{xx} and ρ_{xy} are longitudinal and transverse resistivity respectively, σ_0 is the conductivity at zero magnetic field, g is DOS (density of states) and Δg is oscillatory part of DOS (depends on temperature), s is Fourier harmonic index. As can be seen from equations (2.73), the result is presented using the sum of Fourier harmonics. Increase the number of used harmonics leads to adjusting the shape of peaks what is important for low temperatures, where peak has Lorentzian-like shape instead of sin-like shape at high temperatures. The amplitude of SdH oscillations and their period are independent of the number of the used harmonics. Thus, most of authors used to use one harmonic approach [63], [97]

$$\sigma_{xx} = \sigma_0\cdot\frac{1}{1+(\omega_c\cdot\tau)^2}\cdot\left[\begin{array}{l}1-\frac{2\cdot(\omega_c\cdot\tau)^2}{1+(\omega_c\cdot\tau)^2}\cdot\frac{2\cdot\pi^2\cdot k_B\cdot T}{\hbar\cdot\omega_c}\cdot \\ \cdot\cosh\left(\frac{2\cdot\pi^2\cdot k_B\cdot T}{\hbar\cdot\omega_c}\right)\cdot\cos\left(\frac{2\cdot\pi\cdot E_F}{\hbar\cdot\omega_c}\right)\cdot\exp\left(-\frac{\pi}{\omega_c\cdot\tau}\right)\end{array}\right] \tag{2.74}$$

The SdH part of the longitudinal resistance can be modeled as a product of 3 units

$$\Delta\rho_{xx} \sim A_1(E_F,\omega_c)\cdot A_2(\omega_c,\tau)\cdot A_3(\omega_c,T)$$

$$A_1(E_F,\omega_c)=\cos\left(\frac{2\cdot\pi\cdot E_F}{\hbar\cdot\omega_c}\right),\qquad A_2(\omega_c,\tau)=\exp\left(-\frac{\pi\cdot s}{\omega_c\cdot\tau}\right), \tag{2.75}$$

$$A_3(\omega_c,T)=\frac{2\cdot\pi^2\cdot k_B\cdot T}{\hbar\cdot\omega_c}\cdot\frac{1}{\sinh\left(\frac{2\cdot\pi^2\cdot k_B\cdot T}{\hbar\cdot\omega_c}\right)}$$

The first term is written as cos in (2.75) gives the oscillations of ρ_{xx} with period proportional to $1/B$. 2DCG concentration comes directly from this period. The second term gives exponential growth of the oscillations amplitude with the increase of the magnetic field. This growth also depends on the effective mass and relaxation time. The third term in (2.75) is very interesting. The hyperbolic sinus has about the same power as exponent in the second term. Thus, the second term has big influence on the amplitude of the oscillations. The third term depends on three parameters: effective mass, magnetic field and temperature. Very important is its temperature dependence. This dependence allows to change the value of the third term (the amplitude of SdH oscillations) vary temperature only. Note that varying the temperature one does not change anything else (e.g. position of peaks). This phenomenon can be used to find the cyclotron effective mass using SdH measurements.

2.3.5.3 Quantum Hall Effect

The quantum Hall effect was first discovered in silicon metal oxide (MOS) semiconductor transistors. [98]. Klaus von Klitzing was awarded the Nobel Prize for this discovery. The effect leads to quantized resistance, which can be used to provide a much better measurement of fine structure constant used in quantum field theory. When an integral number of Landau levels (counting spin splitting levels separately) are filled, the Hall resistance ρ_{xy} is a plateau and its value is given accurately by

$$\rho_{xy} = \frac{h}{\nu \cdot e^2} = \frac{1}{\nu} \cdot 25813\Omega, \qquad \nu = 1,2,3,... \tag{2.76}$$
$$\rho_{xx} \to 0$$

This quantization is universal and independent of all microscopic details such as the type of semiconductor material, the purity of the sample, the precise value of the magnetic field, and etc. As a result, nowadays the effect is used to maintain the standard of electrical resistance by metrology laboratories around the world.

References:

1. Dismukes, J.P., L. Ekstrom, and R.J. Paff, J. Phys. Chem., 1964. **68**: p. 3021.
2. Madelung, O., ed. *Landolt-Bornstein numerical data and functional relationships in science and techology New series Group III.* Vol. 17. 1982, Springer: Berlin.
3. Sze, S.M., *Physics of semiconductor devices.* 2nd ed. 1981: New York; Chichester : Wiley.
4. Lang, D.V., et al., Applied Physics Letters, 1985. **47**(12): p. 1333-1335.
5. Kasper, E., ed. *Properties of Strained and Relaxed Silicon Germanium.* 1985, INSPEC: London.
6. Ousset, J.C., et al., J. Phys. C: Solid State Phys., 1976. **9**: p. 2803.
7. Rieger, M.M. and P. Vogl, Physical Review B-Condensed Matter, 1993. **48**(19): p. 14276-14287.
8. Braunstein, R., Phys. Rev, 1963. **130**: p. 869.
9. Lawaetz, P., Phys. Rev. B, 1971. **4**: p. 3460.
10. Pikus, G.E. and G.L. Bir, *Symmetry and Strain-Induced Effects in Semiconductors.* 1974: Wiley, New York.
11. Hasegawa, H., Phys. Rev., 1963. **129**: p. 1029.
12. Schroder, D.K., *Semiconductor material and device characterization.* Second ed. 1998: A Willey-Interscience Publication.
13. Bube, R.H., *Electronic Properties of Crystalline Solids.* 1974, New York: Academic Press.
14. Smith, R.A., *Semiconductors.* 2nd ed. 1978: Cambridge University Press.
15. Singh, J., *Physics of Semiconductors and Their Heterostructures.* 1993, Singapore: McGraw-Hill.
16. Kay, L.E. and T.W. Tang, Journal of Applied Physics, 1991. **70**(3): p. 1483-1488.
17. Klaassen, D.B.M., Solid-State Electronics, 1992. **35**(7): p. 953-959.
18. Krishnamurthy, S., A. Sher, and A.B. Chen, Applied Physics Letters, 1985. **47**(2): p. 160-162.
19. Manku, T. and A. Nathan, Ieee Electron Device Letters, 1991. **12**(12): p. 704-706.
20. Jorke, H. and H. H.J. in *1st Int. Symp. on Silicon MBE.* 1985.
21. Abstreiter, G., et al., Physical Review Letters, 1985. **54**(22): p. 2441-2444.
22. Vandewalle, C.G. and R.M. Martin, Journal of Vacuum Science & Technology B, 1986. **4**(4): p. 1055-1059.
23. Vandewalle, C.G. and R.M. Martin, Physical Review B-Condensed Matter, 1986. **34**(8): p. 5621-5634.

24. Colombo, L., R. Resta, and S. Baroni, Physical Review B-Condensed Matter, 1991. **44**(11): p. 5572-5579.
25. Schwartz, G.P., et al., Physical Review B-Condensed Matter, 1989. **39**(2): p. 1235-1241.
26. Yu, E.T., et al., Applied Physics Letters, 1990. **56**(6): p. 569-571.
27. Morar, J.F., P.E. Batson, and J. Tersoff, Physical Review B-Condensed Matter, 1993. **47**(7): p. 4107-4110.
28. Van der Merve, J.H., Surf. Sci., 1972. **31**: p. 198.
29. Matthews, J.W. and A.E. Blakeslee, J. Crystal Growth, 1974. **27**: p. 118.
30. Bean, J.C., et al., Journal of Vacuum Science & Technology a-Vacuum Surfaces and Films, 1984. **2**(2): p. 436-440.
31. Herzog, H.J., et al., Journal of the Electrochemical Society, 1989. **136**(10): p. 3026-3030.
32. Legoues, F.K., K. Eberl, and S.S. Iyer, Applied Physics Letters, 1992. **60**(23): p. 2862-2864.
33. Schaffler, F., et al., Semiconductor Science and Technology, 1992. **7**(2): p. 260-266.
34. Luryi, S., A. Kastalsky, and J.C. Bean, Ieee Transactions on Electron Devices, 1984. **31**(9): p. 1135-1139.
35. Fitzgerald, E.A., et al., Applied Physics Letters, 1991. **59**(7): p. 811-813.
36. Legoues, F.K., B.S. Meyerson, and J.F. Morar, Physical Review Letters, 1991. **66**(22): p. 2903-2906.
37. Hohnisch, M., H.J. Herzog, and F. Schaffler, Journal of Crystal Growth, 1995. **157**(1-4): p. 126-131.
38. Legoues, F.K., et al., Journal of Applied Physics, 1992. **71**(9): p. 4230-4243.
39. Legoues, F.K., P.M. Mooney, and J.O. Chu, Applied Physics Letters, 1993. **62**(2): p. 140-142.
40. Mooney, P.M., et al., Applied Physics Letters, 1995. **67**(16): p. 2373-2375.
41. Hsu, J.W.P., et al., Applied Physics Letters, 1992. **61**(11): p. 1293-1295.
42. Lutz, M.A., et al., Applied Physics Letters, 1995. **66**(6): p. 724-726.
43. Tersoff, J., Applied Physics Letters, 1993. **62**(7): p. 693-695.
44. Li, J.H., et al., Applied Physics Letters, 1995. **67**(2): p. 223-225.
45. Mooney, P.M., et al., Applied Physics Letters, 1995. **66**(26): p. 3642-3644.
46. Fitzgerald, E.A., et al., Journal of Vacuum Science & Technology B, 1992. **10**(4): p. 1807-1819.
47. Konig, U. and F. Schaffler, Ieee Electron Device Letters, 1993. **14**(4): p. 205-207.
48. Kissinger, G., et al., Applied Physics Letters, 1995. **66**(16): p. 2083-2085.
49. Luryi, S. and E. Suhir, Applied Physics Letters, 1986. **49**(3): p. 140-142.
50. Fitzgerald, E.A., et al., Journal of Applied Physics, 1989. **65**(6): p. 2220-2237.
51. Noble, D.B., et al., Applied Physics Letters, 1990. **56**(1): p. 51-53.
52. Hull, R., et al., Applied Physics Letters, 1992. **60**(12): p. 1468-1470.
53. Xie, Y.H. and J.C. Bean, Journal of Vacuum Science & Technology B, 1990. **8**(2): p. 227-231.
54. Powell, A.R., S.S. Iyer, and F.K. Legoues, Applied Physics Letters, 1994. **64**(14): p. 1856-1858.
55. Lo, Y.H., Applied Physics Letters, 1991. **59**(18): p. 2311-2313.
56. Freund, L.B. and W.D. Nix, Applied Physics Letters, 1996. **69**(2): p. 173-175.
57. Linder, K.K., et al., Applied Physics Letters, 1997. **70**(24): p. 3224-3226.
58. Li, J.H., et al., Applied Physics Letters, 1997. **71**(21): p. 3132-3134.
59. Li, D.Z., et al., Journal of Crystal Growth, 2000. **213**(3-4): p. 308-311.
60. People, R., et al., Applied Physics Letters, 1984. **45**(11): p. 1231-1233.

61. People, R., J.C. Bean, and D.V. Lang, Journal of Vacuum Science & Technology a-Vacuum Surfaces and Films, 1985. **3**(3): p. 846-850.
62. Laikhtman, B. and R.A. Kiehl, Physical Review B-Condensed Matter, 1993. **47**(16): p. 10515-10527.
63. Ando, T., A.B. Fowler, and F. Stern, Reviews of Modern Physics, 1982. **54**(2): p. 437-672.
64. Gold, A., Physical Review B-Condensed Matter, 1987. **35**(2): p. 723-733.
65. Gold, A. and V.T. Dolgopolov, Physical Review B-Condensed Matter, 1986. **33**(2): p. 1076-1084.
66. Gold, A., Physical Review B-Condensed Matter, 1988. **38**(15): p. 10798-10811.
67. Monroe, D., et al., Journal of Vacuum Science & Technology B, 1993. **11**(4): p. 1731-1737.
68. Paul, D.J., et al., Applied Physics Letters, 1996. **69**(18): p. 2704-2706.
69. Murakami, E., et al., Ieee Electron Device Letters, 1991. **12**(2): p. 71-73.
70. Nutzel, J.F., et al., Journal of Crystal Growth, 1995. **150**(1-4 Pt2): p. 1011-1014.
71. Ismail, K., J.O. Chu, and B.S. Meyerson, Applied Physics Letters, 1994. **64**(23): p. 3124-3126.
72. Xie, Y.H., et al., Applied Physics Letters, 1993. **63**(16): p. 2263-2264.
73. Look, D.C., *Electrical Characterization of GaAs Materials and Devices*. 1989, NewYork: Wiley.
74. Beck, W.A. and J.R. Anderson, Journal of Applied Physics, 1987. **62**(2): p. 541-544.
75. Dziuba, Z. and M. Gorska, Journal De Physique Iii, 1992. **2**(1): p. 99-110.
76. Antoszewski, J., et al., Journal of Electronic Materials, 1995. **24**(9): p. 1255-1262.
77. Vurgaftman, I., et al., Journal of Applied Physics, 1998. **84**(9): p. 4966-4973.
78. Kiatgamolchai, S., et al., submitted to Phys. Rev. B.
79. McClure, J.W., Phys. Rev., 1956. **101**: p. 1642.
80. Beck, W.A., et al., Journal of Vacuum Science & Technology a-Vacuum Surfaces and Films, 1988. **6**(4): p. 2772-2774.
81. Meyer, J.R., et al., Journal of Vacuum Science & Technology a-Vacuum Surfaces and Films, 1988. **6**(4): p. 2775-2778.
82. Meyer, J.R., et al., Semiconductor Science and Technology, 1993. **8**(6): p. 805-823.
83. Hwang, S., et al., Journal of Vacuum Science & Technology B, 1991. **9**(3): p. 1799-1804.
84. Colvard, C., et al., Journal of the Electrochemical Society, 1989. **136**(11): p. 3463-3466.
85. Panaev, I.A., et al., Semiconductor Science and Technology, 1993. **8**(10): p. 1822-1828.
86. Svensson, S.P., et al., Journal of Crystal Growth, 1991. **111**(1-4): p. 450-455.
87. Panaev, I.A., et al., Semiconductor Science and Technology, 1996. **11**(12): p. 1857-1862.
88. Achard, J., et al., Applied Surface Science, 1999. **142**(1-4): p. 455-459.
89. Hock, G., et al., Thin Solid Films, 1998. **336**(1-2): p. 141-144.
90. Dziuba, Z., Acta Physica Polonica A, 1991. **80**(6): p. 827-839.
91. Meyer, J.R., et al., Journal of Applied Physics, 1997. **81**(2): p. 709-713.
92. Jaynes, E.T., Phys. Rev., 1957. **106**: p. 620.
93. Agmon, N., Y. Alhassid, and R.D. Levine, J. Comput. Phys., 1979. **30**: p. 250.
94. Hollis, J.M., J.E. Dorband, and F. Yusefzadeh, Astrophysical Journal, 1992. **386**(1): p. 293-&.
95. Blood, P. and J.W. Orton, *The electrical characterization of semiconductors: majority carriers and electron states*. 1992: Academic Press.

96. Isihara, A. and L. Smrcka, Journal of Physics C-Solid State Physics, 1986. **19**(34): p. 6777-6789.
97. Weisbuch, C. and B. Vinter, *Quantum semiconductor stuctures*. 1991: Academic Press.
98. Klitzing, K.v., G. Dorda, and M. Pepper, Phys. Rev. Lett., 1980. **45**: p. 494-497.

3. Experimental methods

3.1 Solid source molecular beam epitaxy

Molecular beam epitaxy (MBE) provides a powerful tool for basic research into the physics and device potential of modern semiconductor materials. The control capability over the growth process particularly allows many considerations of both the material system and future devices to be fine tuned and investigated.

The growth of heterostructures for present research was performed using a VG Semicon V90S SS-MBE system at Warwick University (Coventry, UK) and "home-made" SS-MBE system at DaimlerChrysler AG Research and Technology (Ulm, Germany). Further, the author will describe the VG Semicon V90S system. The system and its components are manufactured from either grade 316 stainless steel or from refractory metals. Typically, base pressures of $1 \cdot 10^{-11}$mbar were achieved after a week long bake out at 200C. Background pressures of approximately $1 \cdot 10^{-8}$mbar were sustained during epitaxial growth and residual gas analysis was performed throughout growth using mass spectrometry techniques. The MBE system incorporated a load-lock wafer transfer chamber, allowing base pressures within the growth chamber to be maintained during wafer loading and unloading. Ultra high vacuum (UHV) pumping was achieved using a combination of turbo pumps, getter-ion pumps, titanium sublimation pumps and liquid nitrogen cryopanels.

The growth of p-type modulation doped heterostructures was performed on clean Si(001) substrates or $Si_{1-y}Ge_y$/Si(001) virtual substrates of 4 inch diameter. Prior to growth some of substrates were pre-cleaned using a modified RCA wet chemical clean. Such cleans leave a residual surface oxide layer, typically of thickness <1.5nm. The oxide results in a passivated Si surface and was evaporated within the growth chamber by briefly heating the wafer to 800-860C immediately prior to MBE growth, whereby the surface oxide desorbs, leaving a clean Si surface.

Substrates were loaded into the V90S system via the load-lock. During the growth, substrates were rotated at approximately 20-60rpm so as to ensure temperature and growth rate uniformity across the whole wafer. Radiative substrate heating was performed using a graphite-heating element and temperature measurements were performed using an optical pyrometer operating at an infrared wavelength of 1.1μm. In this manner substrate temperatures were determined to within a minimum absolute error of ±25C, with a reproducibility of ±5C. Optical pyrometric thermometry has the distinct advantage of being an ex-situ, non-contact method, however at substrate temperatures below approximately 500C the method is deemed unreliable due to the opacity of Si to infrared radiation at such temperatures. Growth temperatures below 500C were achieved by extrapolation of the heater power curve and resulted in an absolute substrate temperature error of approximately ±40C.

Si and Ge fluxes were established using separated electron beam evaporation sources (e-guns) from solid source Si and Ge charges. Heated tungsten filaments, biased at high voltages, were used to produce an electron beam (e-beam) via thermionic emission. The e-beam was deflected through 270°, using an electromagnetic coil, and directed onto the solid source charges. The incident e-beam flux resulted in the heating and subsequent evaporation of the Si and Ge charges. Both charges were water cooled and shielded from the copper hearths using Si crucibles. In this manner, any possible electron beam evaporation of copper contaminants was avoided. At the beginning of every growth series, calibration samples ($Si/Si_{1-x}Ge_x$ superlattices) were characterized, using double angle X-ray diffractometry to determine $Si_{1-x}Ge_x$ alloy compositions.

Boron doping was achieved by the co-evaporation of elemental Boron from a resistively heated graphite crucible. High purity graphite was used and crucible temperatures in excess of 2200C were obtainable. Using such a method, boron doping of $1x10^{20}cm^{-3}$ were readily attainable. Furthermore, carbon background contamination from

the crucible was below the detection limits of secondary ion mass spectrometry (SIMS) techniques (approximately $1x10^{17}cm^{-3}$). The Boron flux rate was maintained using a constant current source, calibrated against control samples, and allowed doping reproducibility of approximately 20%. In all cases, growth rates, epilayer compositions and doping interrupts were achieved using PC-computer controlled shutters.

For a more detailed description of SiGe MBE growth technique and procedure the reader is referred to the book of Robert Hull and John C. Bean [1].

3.2 Transmission electron microscopy

Transmission electron microscopy (TEM) is a technique of characterizing materials down to the atomic limits. Cross-sectional transmission electron microscopy (XTEM) was performed on numerous heterostructures to determine the structural integrity of the epilayers and their thicknesses. In particular, the technique was used to determine the dislocations microstructure of relaxed epilayers.

Firstly, cross sectional specimens were prepared from wafer samples by cleaving orthogonal <110> directions to an approximate sample area of $1x1cm^2$. Generally, two specimens of each wafer were cleaved and the adjacent epilayers glued together using Araldite at a temperature of 80C. The sample was then mounted between two Si support blocks (glued to the back of the original Si growth wafer), again using warm Araldite, and the sandwiched specimen clamped in a strong vice for approximately 24 hours so as to allow the glue to cure completely. The use of two adjacent epilayers increased the probability of successfully thinning the region of epilayer of interest. Also, great care was taken to ensure that all three glued interfaces were as thin as possible and that no particulates were sandwiched within the glue layers of the specimen.

The specimen was then mounted on a glass slide using melted wax and mechanically polished on one side using a successively finer grit size. A smooth, highly polished mirror

surface was achieved by polishing the ground sample, firstly using a 6μm diamond grit suspension followed by a light 1μm final polish.

3mm copper grids were then carefully glued onto the polished specimen so as to be central along region of interest. Again, the glue was allowed to cure for approximately 12-24 hours.

The specimen was then carefully removed from the glass slide by dissolving the wax in warm xylene. Using an identical method, the polished side of the sample, together with the mounted copper grids, was then mounted on a glass slide again using melted wax and mechanically thinned to a thickness of approximately 30-50μm. Again, a successively finer grit size was used so as to ensure a smooth surface was obtained. A smooth mirror finish was then obtained by polishing in a 6μm, followed by a 1μm, diamond suspension. The thinned specimen surrounding the copper disk was then carefully chipped away using a sharp scalpel.

Finally, the thinned specimen, together with the copper grids, was removed from the glass slide by dissolving the wax in xylene followed by a warm isopropanol clean.

In order to produce thinned samples, transparent to a high-energy electron beam, the specimens were then milled in an argon ion beam until just perforated. The ion milling was performed at a base pressure of approximately $1x10^{-6}$ mbar, rising to approximately $6x10^{-5}$ mbar with the introduction of the argon gas. An accelerating potential of 5keV and a beam current of 4mA were used during thinning. For XTEM specimens ion milling was performed simultaneously on both the front and backside of the specimen, with the incident ion beams at an angle of approximately 65° to the specimen normal. In addition, in order to achieve uniform thinning the samples were rotated at 1 r.p.m. during milling. Typically, ion beam thinning times varied from 2 hours to 24 hours, depending on the original specimen thickness.

Specimens were then characterised using a JEOL JEM-2000fx transmission electron microscope, operating at an accelerating voltage of 200keV.

For a more detailed description of Transmission Electron Microscopy the reader is referred to the book of David B. Williams and C. Barry Carter [2].

3.3 Secondary ion mass spectrometry

The Si and Ge profiles of the heterostructures epilayers, together with Boron remote impurity doping, were determined using Secondary Ion Mass Spectrometry (SIMS). The SIMS technique employs a primary ion beam with energies in the range of 500eV to 30KeV to bombard the sample surface under UHV. This causes sputtering of the particles from the sample surface as well as incorporation of the incident ions. Some of the sputtered particles are in the form of secondary ions, which are extracted into mass spectrometer and separated according to their mass to charge ratio. Primary ions raster the sample surface in a very controlled way causing a crater the size of which is generally in the range $5x5\mu m^2$ to $500x500\mu m^2$. The counts of one or more mass peaks as a function of bombardment time are monitored. In order to obtain a dopant concentration-depth profile, counts are converted into concentration by running standards (usually ion implanted material) and, erosion time is converted into depth after measuring the crater with a surface profilemeter by assuming a constant erosion rate.

SIMS measurements were done in the EVA 2000 machine at Warwick University. The investigations were carried out using primary beam of O_2^+ ions, accelerated to 500eV and 1000eV, and normal and 20° angels of incidence respectively. The base pressure of the samples chamber was typically $1 \cdot 10^{-9}$mbar.

For a full description of SIMS the reader is referred to the book of A. Beninghoven *et al* [3].

3.4 Photoluminescence spectroscopy

The photoluminescence (PL) is the technique in which, incident laser radiation, which is usually of significantly higher energy than fundamental bandgap E_g, is focused onto the sample, exciting carriers high up into the electronic bands. Due to the fact that thermalization processes, such as phonon or impurity scattering, occur on a much shorter timescale than recombination processes (typically 10^{-13}s compared with 10^{-10}s), these carriers rapidly relax to the band edges. At low temperatures, the Coulombic interaction between electrons and holes leads to the formation of excitons, and subsequent recombination leads to the emission of photons. These are collected and imaged onto the entrance slit of a spectrometer, and their spectral energy distribution measured.

Although PL provides information on the band structure of the sample, results are complicated by the short timescale of thermalization processes, which mean that carriers always recombine from the lowest point of the bands. Therefore the regions of lower carrier confinement produced by fluctuations in the layer widths, or other disorder-activated effects, dominate the recombination process, even though the density of these states may be small.

Photoluminescence spectroscopy measurements were carried out in Clarendon Laboratory, University of Oxford, UK. All samples were cooled down to 5.5K and 647.1nm line of a Kr^+ ion laser was used. The laser light power was 60mW.

It is necessary to note, the technique is non-destructive and the measurements were performed on the same samples (Hall-bars and Van der Pauw cross) used for magnetotransport characterization.

For a more detailed description of photoluminescence spectroscopy the reader is referred to the book of Peter Y. Yu and Manuel Cardona [4].

3.5 Raman spectroscopy

Inelastic light scattering by phonons has been used for several decades to obtain information about the electronic and vibrational states of semiconductors. The technique is performed in similar fashion to PL, with an intense laser source focused onto the sample and the scattered light collected and analysed. However, since Raman signals are generally very weak, perhaps as small as 20 detected events per second compared with 10^{14} incident photons, the optical system has to be highly efficient. Given that the Raman signal is usually within 500 wavenumbers (cm^{-1}) of the laser, this requires a spectrometer with very good stray light rejection, and very high efficiency.

Raman is an inelastic light scattering process. Incident photons either create (Stockes scattering) or annihilate (anti-Stokes) an elementary excitation of the crystal structure. These excitations are phonons, though anything capable of producing a fluctuation in the dielectric susceptibility of the material can theoretically produce scatter [4]. The process conserves both energy and momentum, and so for an incident photon of energy $\hbar \cdot \omega_L$ and wavevector k_L, a scattered photon of $\hbar \cdot \omega_S$ and k_S, and a phonon of $\hbar \cdot \Omega$ and q, we have

$$\hbar \cdot \omega_S = \hbar \cdot \omega_L \pm \hbar \cdot \Omega \tag{3.1}$$

$$k_S = k_L \pm q \tag{3.2}$$

where the – (+) refers to Stokes (anti-Stokes) scattering. Only Stokes scattering (phonon creation) is considered in this thesis. The energy of the created phonons can be determined through an accurate knowledge of the laser energy, and measurement of the scattered photon energy, whereas the phonon wavevector is fixed by the scattering geometry. In opaque semiconductors most experiments are performed in backscattering ($k_L \cong -k_S$), which results in a phonon wavevector given by

$$q = \frac{4 \cdot \pi \cdot \eta}{\lambda_L} \tag{3.3}$$

where η is the refractive index of the material and λ_L (~500nm) the incident laser wavelength.

Raman spectroscopy measurements were carried out in Clarendon Laboratory, University of Oxford, UK. The 457.9nm, 476.5nm, 488nm, 514.5nm and 528.7nm lines of an Ar^+ ion laser were used to obtain Raman spectra containing information about buried layers of heterostructures allocated at various depth from the surface. The laser light power was 300mW and the spectral resolution ~$0.3cm^{-1}$. The size of focused spot was varied from 3μm to 10μm, which depended from the quality of the sample surface. The Raman measurements were carried out at 293K and 12K in a backscattering configuration. Further the Raman spectra measured in optical phonon range were analyzed and information about state of strain in the $Si_{1-x}Ge_x$ and $Si_{1-y}Ge_y$ layers was estimated. Also, the Ge composition in the $Si_{1-y}Ge_y$ layers was obtained.

In particular, the technique is non-destructive and the measurements were performed on the same samples (Hall-bars and Van der Pauw cross) used for magnetotransport characterization.

For a more detailed description of Raman spectroscopy the reader is referred to the book of Peter Y. Yu and Manuel Cardona [4].

3.6 Scanning white-light interferometry

The white-light interferometers allow fast and noncontact semiconductor materials surface analysis and surface profiling with high accuracy. The scanning white-light interferometry is a traditional technique in which a pattern of bright and dark lines (fringes) result from an optical path difference between a reference and a sample beam. The mechanism is simple. Incoming light is split inside an interferometer, one beam going to an internal reference surface and the other to investigated sample. After reflection, the beams

recombine inside the interferometer, undergoing constructive and destructive interference and producing the light and dark fringe pattern.

The surface roughness measurements of $Si_{1-x}Ge_x$/ $Si_{1-y}Ge_y$ heterostructures were done using Zygo NewView 5000 scanning white-light interferometry system at Warwick University. The system's vertical resolution is 0.1nm and lateral resolution is from 0.62 to 11.8μm (objective dependent). In the NewView 5000, a precision vertical scanning transducer and camera together generate a three-dimensional interferogram of the surface, processed by the computer and transformed by frequency domain analysis resulting in a quantitative 3-D image.

For detailed description of scanning white-light interferometry the reader is referred to the work of L. Deck. and P. Degroot [5].

3.7 Devices fabrication for magnetotransport measurements

3.7.1 Van der Pauw device

The standard techniques for the resistivity and Hall coefficient measurements of semiconductor materials at different temperatures were proposed by Van der Pauw [6]. The recommended shape was a "clover-leaf" shape where the contact influences are minimal. The Greek-cross shape was used in the present work because it was much simpler to make and the error in measurements of V_{xx} and V_{xy} were small (<0.5%) for a sample width less than half of the length [7]. From the starting wafer, the sample is cleaved by diamond-pen into a small square ($0.5x0.5cm^2$). Nitrogen gas is used to remove any small particles on the both sides of the sample. Ohmic contacts to cleaved samples were prepared by the sputtering of Aluminium dots through a 1mm in diameter shadow mask, to a thickness of 500nm into an "ION TECH Microvac 350" magnetron sputterer, followed by a sinter in furnace at 420C for 10-30 minutes in a flow Nitrogen ambient. The time is varied due to the depth of the channel bellow the surface, to achieve ohmic contacts. Black

wax is subsequently painted onto the surface in the shape of a cross having an aluminium contact at each end. The wax was allowed to dry and the cross defined by etching the exposed region with a HNO_3:HF(50%):$C_2H_4O_2$ in the volume ratio 75:8:17 mixture. An etch depth of approximately 1-4μm (depending on the thickness of the heterostructure) was used so as to ensure no parasitic electrical measurements were obtained from the underlying dislocation network of the VS region. Finally, the black wax was then removed by xylene and the sample was rinsed thoroughly in deionised water.

In addition, the technique is particularly useful in that no lithographic stages are required.

3.7.2 Hall bar devices

The Hall-bar is more favorable than a Van der Pauw device for the magnetic-field dependence measurements because its geometry is much simpler to analyze and the latter requires the calculation of the *f* factor. The geometry of Hall bar have to be designed in such a way that current flow is uniform within the measuring region and there is minimal current passing through the Hall contacts. The design was done in accordance with the published ASTM standard [8].

The fabrication procedure is quite similar to that for the Van der Pauw device, except that the black wax is replaced by a standard photolithography procedure. This requires well-designed masks and a mask aligner.

In this research two types of Hall-bars fabricated at Warwick Universty (Coventry, UK) and at DaimlerChrysler AG Research and Technology (Ulm, Germany) were used. The first one was fabricated by wet chemical etching, and ohmic contacts were formed by sputtering of Al (500nm) followed by alloying at 420C in N_2 ambient for 10-30min. Typical sizes of Hall-bars were 1700 μm in channel length and 500 μm in width, with a 4400 μm separation between current-source probes. The second type of Hall-bars was

fabricated by dry etching in SF_6/O_2 plasma and ohmic contacts were formed by evaporation of Pt/Au (20nm/200nm) followed by alloying at 290C in N_2 ambient for 30s. Typical sizes of these Hall-bars were 315μm in channel length and 54μm in width, with a 535μm separation between current-source probes.

As soon as Hall-bars were fabricated they were glued into a chip package and sample contacts were connected to the gold pads of the chip package by ball-bonding of gold wires.

3.8 Cryostats equipment and operations

3.8.1 Closed-cycle cryostat system (9-300K)

The 9-300K temperature dependences of Hall mobility and sheet carrier density of p-type MOD $Si_{1-x}Ge_x/Si_{1-y}Ge_y$ heterostructures were obtained by using closed-cycle cryostat system. The closed-cycle cryostat was built by "Air Products". After the sample mounted, the pressure is reduced to 10^{-5} mbar to provide a good thermal shield. The temperature of the sample is reduced by means of the Helium compressor to a base temperature of 9K before starting the resistivity and Hall measurements. High-pressure helium, supplied by the compressor at ~310psi, entered the expander module where it was cooled to the refrigeration temperature. The work done by the high-pressure gas expansion, as it left the expander matrix as the much lower pressure of ~85psi, caused the gas temperature to drop and provided refrigeration. The refrigeration cycle was repeated sixty times per minute causing rapid cooling of the copper expander assembly. To increase the temperature, a metal film heater is used and the temperature monitored with a Si-diode. The temperature was maintained stable within ±0.5K at all temperatures between 9K and 300K by "Lake Shore" temperature controller. The data were obtained in the dark beginning at low temperature. The "EG&G Instruments, Model 5209" lock-in amplifier acts both as an A.C. voltage source and phase sensitive voltage detector. A signal frequency of 7Hz was used to

avoid the main power supply frequency of 50 Hz. The current to the sample was limited by a series resistor of 1-10MΩ and the typical current supplied is 0.1-1 μA. The higher supply current could heat up the sample while the lower one will reduce the Hall voltage, for a given magnetic field of 0.4-1.2T, to below the measurable level of the lock-in amplifier.

3.8.2 Cryomagnetic system (0.35-300K)

Measurements of the magnetic-field dependence of magnetoresistance and Hall resistance were carried out in an Oxford Instruments ^{3}He cryomagnetic system with a base temperature of 0.35 K. Magnetic fields up to 11T were generated by a superconducting solenoid submerged in liquid ^{4}He. The magnetic field is generated by passing a D.C. current through the superconducting coil, which can be swept, continuously to 11T by supplying a current of 91.96A. At higher currents, the coil will stop being a superconductor, consequently Joule heating happens, a process known as "quenching", and it will boil of all liquid ^{4}He.

Three lock-in amplifiers were used to measure the longitudinal voltage (V_{xx}), Hall voltage (V_{xy}), and current voltage simultaneously while the magnetic field is continuously swept. The signal from latter lock-in amplifier is used as a reference signal for another two lock-in amplifiers and also as the current supply to the sample. The current limited series resistance can be changed to provide the supply current between 10-3000nA. Because the magnetic field is changed continuously and the lock-in amplifier has a time delay, hysteresis of resistivity and Hall resistance can occur which can be removed by averaging the up and down sweeping signal.

0.35-1.6K temperatures operation

After the standard preparation of the cryostat and the overnight cooling, the liquid ^{4}He from the main bath is drawn into the 1K pot and pumped continuously to lower the

sample temperature down to around 1.3-1.6 K. During this pumping process, the temperature of the sorb is also controlled to be around 50-60K by means of resistive coil heating and liquid ^{4}He flow through the sorb heat exchanger pipe. Then the ^{3}He gas, which is kept in a dump vessel, is allowed into the sample space. Upon reaching the 1K pot region, ^{3}He gas starts to condense and its pressure drops. Then, the sorb temperature is gradually decreased manually. The sorb contains a charcoal, which acts as a pump when it is cooled down below 35 K. As the sorb temperature decreases below this temperature, the sorb starts to pump the liquid ^{3}He and this process lowers the temperature of the sample, which is now submerged under this liquid, to the lowest temperature of 0.35K. The higher temperatures can be achieved by increasing the sorb temperature that causes less pumping of liquid ^{3}He. The sample temperature was read from a Ge resistance thermometer ("Lake Shore Cryotronics"), calibrated in the range 0.3-9K, when in a stable condition and in the absence of a magnetic field. In Shubnikov-de Haas experiments temperature measurements were taken at the start and finish of the run to check the stability and were averaged.

10-300K temperatures operation

This cryostat was originally designed for the low-temperature (0.35-70K) measurements, which has a very poor heat sink due to the use of a fiber glass insert for the sample holder. This means that only the gas inside the sample space will act as a heat transfer medium, which is by far less stable than a standard metal medium. To achieve the high temperature measurement with sufficient temperature stability, the following work-around solutions were developed without modifying the cryostat. A heater wire and a "Lakeshore" capacitance sensor (CS-500) were installed onto the sample holder. This sensor has a very low magnetic-field dependence and high sensitivity especially at 77-300K. The "Lakeshore" temperature controller (CA-91CA) was used in conjunction with this sensor. To achieve a stable temperature below 30K, the 1K pot was pumped with an

only slightly opened pumping-valve together with the use of the sample heater. Temperature control is more difficult than that at higher temperature because the sensitivity of the capacitance sensor is comparatively lower. To obtain stable temperatures higher than 30K but less than 150K, only the sample heater is used. For higher temperatures, the sorb temperature is controlled to be around 50-60K so that the accumulating heat at the top of the insert can be drawn out effectively. The temperature is measured using a silicon diode thermometer (Institute of Cryogenic, Southampton University) calibrated in the range 1.5-300K with an uncertainty of ±30mK. The optimum operation was achieved with the temperature stability of ±0.5K for at least 1 hour at all temperatures (10-300K).

3.9 Resistivity and Hall measurements

As discussed earlier, carrier concentration (p_s) and carrier mobility (μ) are two key parameters, which govern the transport and electrical properties of semiconductor. Both parameters are usually determined by using resistivity and Hall effect measurements.

The Hall effect was discovered by Edwin H. Hall in 1879. When a magnetic field is applied at right angle to the direction of current flow, an electric field is set up in a direction perpendicular to both the direction of the current and the magnetic field.

Resistivity and Hall effect measurements consist of the measurements of the longitudinal (V_{xx}) and transverse (Hall) (V_{xy}) voltages as a function of applied current (I) and perpendicular magnetic field (B_z). The measurements and calculations of resistivity and Hall coefficient depend on the sample geometry. In this researched were used Hall-bars and Van der Pauw crosses.

3.9.1 Van der Pauw device

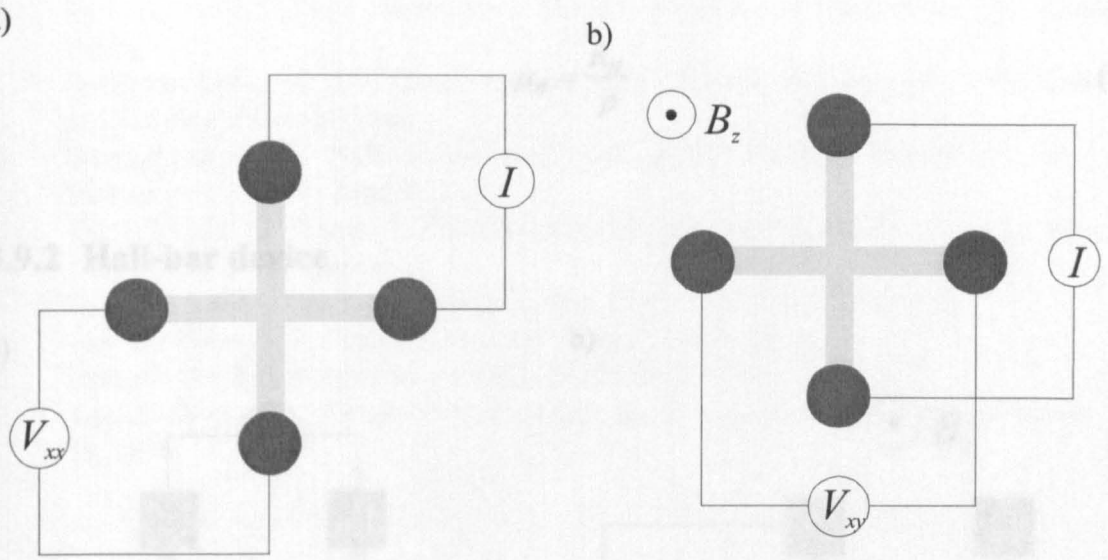

Figure 3.1 Van der Pauw cross sample: a) resistivity measurements b) Hall effect measurements.

For Van der Pauw cross sample geometry the longitudinal voltage was measured in four different configurations (Figure 3.1 a). The resistivity can be calculated from:

$$\rho = \frac{\pi \cdot d}{\ln 2} \cdot \frac{V_R}{I} \cdot f \tag{3.4}$$

where V_R is an average voltage of V_{xx}, I is the current, and d is the thickness of the measured sample. d is usually unknown but conventionally set to unity and the resistivity is therefore the sheet resistivity. The correction factor f is geometry-dependent that is found to be close to unity due to the symmetry in the cross sample. The Hall voltage was measured in four different configurations (Figure 3.1 b); two configurations for each magnetic field polarity. The Hall coefficient can then be calculated from:

$$R_H = \frac{d}{B} \cdot \frac{V_H}{I} \tag{3.5}$$

where V_H is an average Hall voltage of V_{xy} and B is the applied magnetic field. Using equations (3.4) and (3.5) the sheet carrier density (p_s) and Hall carrier mobility (μ_H) for one type of carriers can be obtained from:

$$p_s = \frac{1}{R_H \cdot e} \tag{3.6}$$

$$\mu_H = \frac{R_H}{\rho} \tag{3.7}$$

3.9.2 Hall-bar device

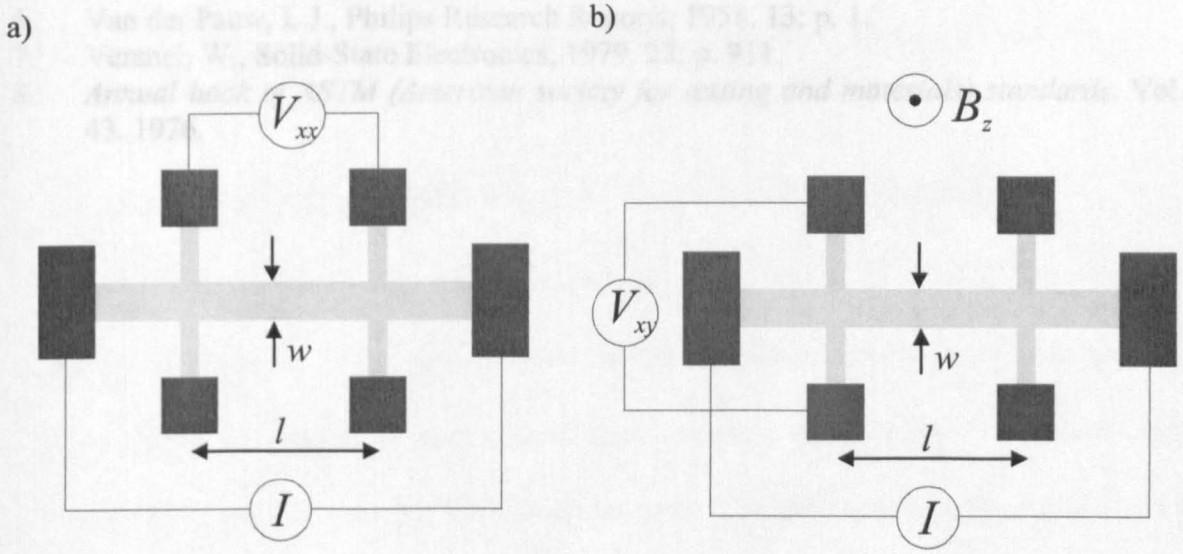

Figure 3.2 Hall-bar sample: a) resistivity measurements b) Hall effect measurements.

For Hall-bar sample geometry (Figure 3.2) the resistivity as a function of magnetic field can be calculated as

$$\rho = \frac{V_{xx}}{I} \cdot \frac{w}{l} \tag{3.8}$$

where *w/l* is the width to length ratio of the channel. The Hall coefficient is calculated according to equation.

$$R_H = \frac{1}{B} \cdot \frac{V_{xy}}{I} \tag{3.9}$$

Using equations (3.8) and (3.9) the sheet carrier density (p_s) and Hall carrier mobility (μ_H) at given temperature for one type of carriers can be obtained according to equations (3.6) and (3.7) respectively.

References:

1. Hull, R. and J.C. Bean, *Germanium Silicon: Physics and Materials*. 1999: Academic Press.
2. Williams, D.B. and C.B. Carte, *Transmission Electron Microscopy*. 1996, New York and London: Plenum Press.
3. Beninghoven, A., F.G. Rudenauer, and H.W. Warner, *Secondary Ion Mass Spectrometry*. 1987: John Willey.
4. Yu, P.Y. and M. Cardona, *Fundamentals of Semiconductors: Physics and Materials Properties*. 1996: Springer.
5. Deck, L. and P. Degroot, Applied Optics, 1994. **33**(31): p. 7334-7338.
6. Van der Pauw, L.J., Philips Research Reports, 1958. **13**: p. 1.
7. Versnel, W., Solid-State Electronics, 1979. **22**: p. 911.
8. *Annual book of ASTM (American society for testing and materials) standards*. Vol. 43. 1976.

4. Design, growth and annealing procedure of p-type MOD $Si_{1-x}Ge_x/Si_{1-y}Ge_y$ heterostructures

During the research p-type MOD $Si_{1-x}Ge_x/Si_{1-y}Ge_y$ heterostructures were designed and grown by SS-MBE on Si(001) substrates. To research the effect of thermal influence on magnetotransport, structural and optical properties of p-type MOD $Si_{1-x}Ge_x/Si_{1-y}Ge_y$ heterostructures the post growth thermal annealing treatments were performed.

4.1 Design of p-type MOD $Si_{1-x}Ge_x/Si_{1-y}Ge_y$ heterostructures

As was mentioned in chapter 2.2.4, the active layers of a MOD heterostructure consist of an undoped $Si_{1-x}Ge_x$ channel for the mobile carriers (in this case holes), an undoped $Si_{1-y}Ge_y$ spacer layer that separates the ionized dopants from the channel, and a doping layer (in this case B). The heterointerface is located between the channel and the spacer and separates the two regions energetically. Often, the doping concentration is reduced toward the surface to avoid Schottky barrier lowering, and a thin undoped Si cap layer may be added, to protect against in-depth oxidation and to allow for a well-defined Schottky gate.

A proper design of a MOD heterostructure requires a careful adjustment of the layer thicknesses, the compositions and strain states, and of the doping levels of the three active layers. In addition, the surface potential (often defined by a Schottky gate) and the thickness of the Si cap layer affect the electronic properties of the layers. Several interrelations between the layer parameters and also boundary conditions have to be met. The most basic design rule requires that under operational conditions all dopant atoms should be ionized, whereas all free carriers should be restricted to the channel region. This condition defines the integral doping concentration for a given layer sequence and a defined surface potential. Because of the linear potential drop across the undoped spacer,

charge transfer from the supply layer into the channel becomes less and less efficient as the spacer is increased (Figure 4.1). The carrier transfer depends also to some extent on the volume concentration in the doping layer, which should be as high as possible for maximum efficiency (Figure 4.1).

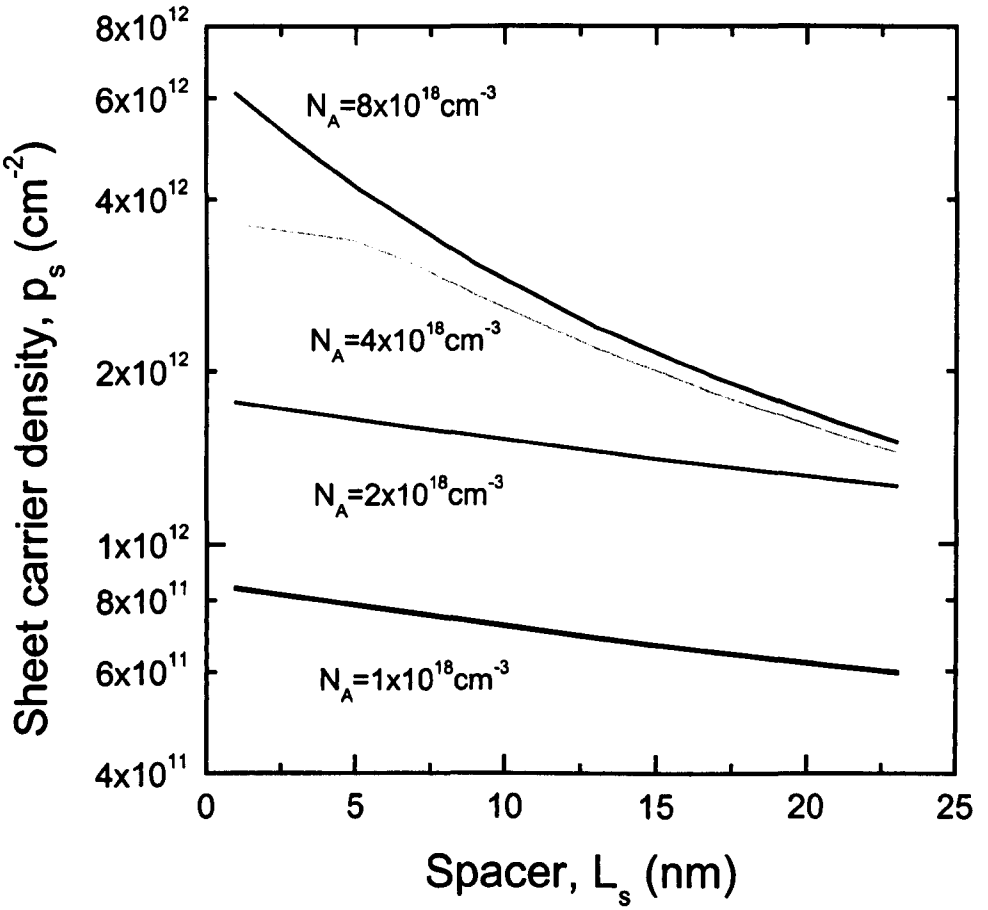

Figure 4.1 Variations of sheet carrier density versus spacer width at B doping $1{\cdot}10^{18}cm^{-3}$, $2{\cdot}10^{18}cm^{-3}$, $4{\cdot}10^{18}cm^{-3}$ and $8{\cdot}10^{18}cm^{-3}$ for p-type MOD $Si_{0.2}Ge_{0.8}/Si_{0.7}Ge_{0.3}$ heterostructure calculated using self-consistent solution of 1D Poisson-Schrodinger equations.

Layer design usually starts with selecting the compositions of the active layers and of the virtual substrate, which define the band offsets. Because of critical thickness limitations the range of useful compositions is quite restricted and achievable valence band offset is usually ≤350meV (see also section 2.2.1). By increasing the valence band offset the carrier

density of 2DHG is increase. The next input parameters are the surface potential and the desired density of free carriers in the channel. The required spacer width and the integral doping concentration are then obtained to good approximation by self-consistent solution of the Poisson and Schrodinger equations (Figure 4.1, Figure 4.2).

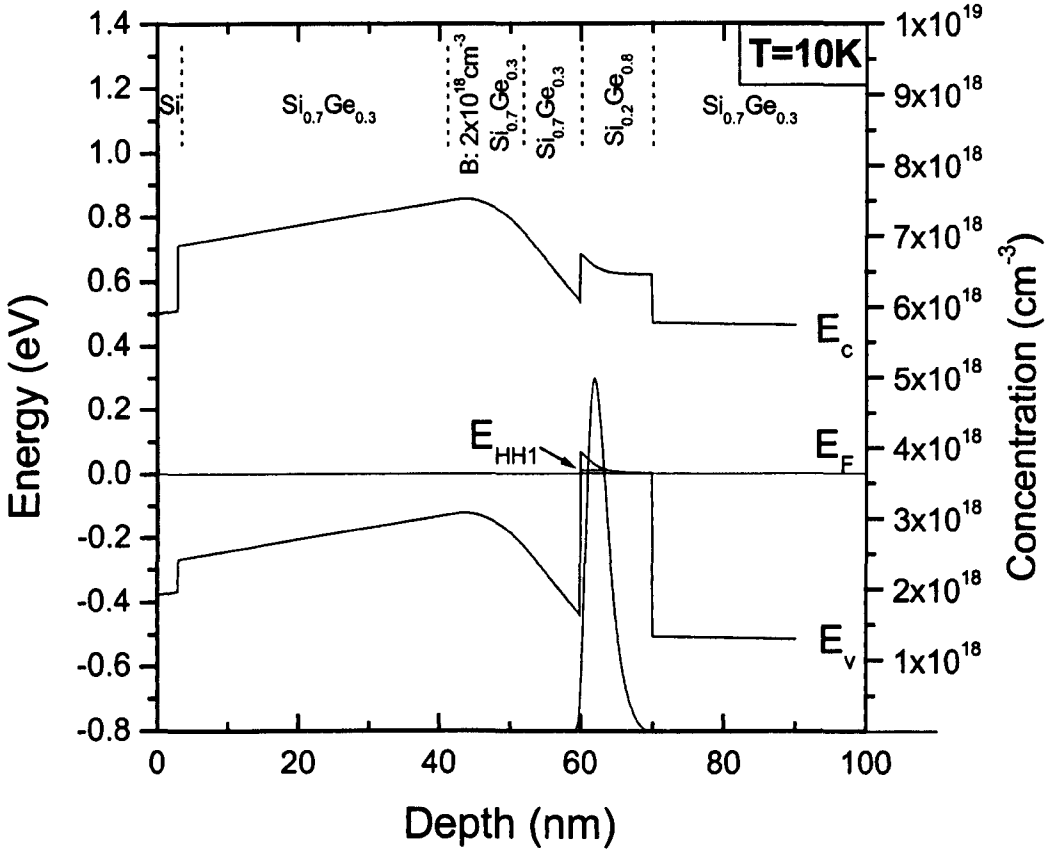

Figure 4.2 Energy band diagram and carriers distribution at 10K for p-type MOD $Si_{0.2}Ge_{0.8}/Si_{0.7}Ge_{0.3}$ heterostructure calculated using self-consistent solution of 1D Poisson-Schrodinger equations.

Further is necessary to take into account carriers scattering mechanisms, which limit the mobility of 2DHG (see also section 2.3.2). The complete optimisation is a complicated procedure due to the large number of scattering mechanisms, which limit hole mobility. Also these calculations contain the large number of adjustable parameters. The calculations of 2DHG mobility versus temperature (see chapters 2.3.1 and 2.3.2) performed for MOD $Si_{0.2}Ge_{0.8}/Si_{0.7}Ge_{0.3}$ heterostructure are showed that theoretical mobility of 2DHG formed

in the $Si_{0.2}Ge_{0.8}$ channel could be ~10000cm^2·V^{-1}·s^{-1} at 10K and more than 2000cm^2·V^{-1}·s^{-1} at 293K for a given set of parameters (Figure 4.3). For this case the low temperature mobility of 2DHG formed in the $Si_{0.2}Ge_{0.8}$ channel (L=10nm) at sheet carrier density p_s=1.8·10^{12}cm^{-2} and effective mass m^*=0.18·m_0 is limited by alloy scattering (E_{al}=0.3eV) followed by remote impurities scattering (L_s=7nm and N_A=2·10^{12}cm^{-2}), interface roughness scattering (Δ=1nm and Λ=5nm) and background impurities scattering (N_B=10^{16}cm^{-3}). The room temperature mobility is mainly limited by acoustic-phonon scattering (a=11.9eV) followed by optical-phonon scattering (d_0=37.8eV, $\hbar\cdot\omega$=42.5eV), alloy scattering, remote impurities scattering, interface roughness scattering and background impurities scattering.

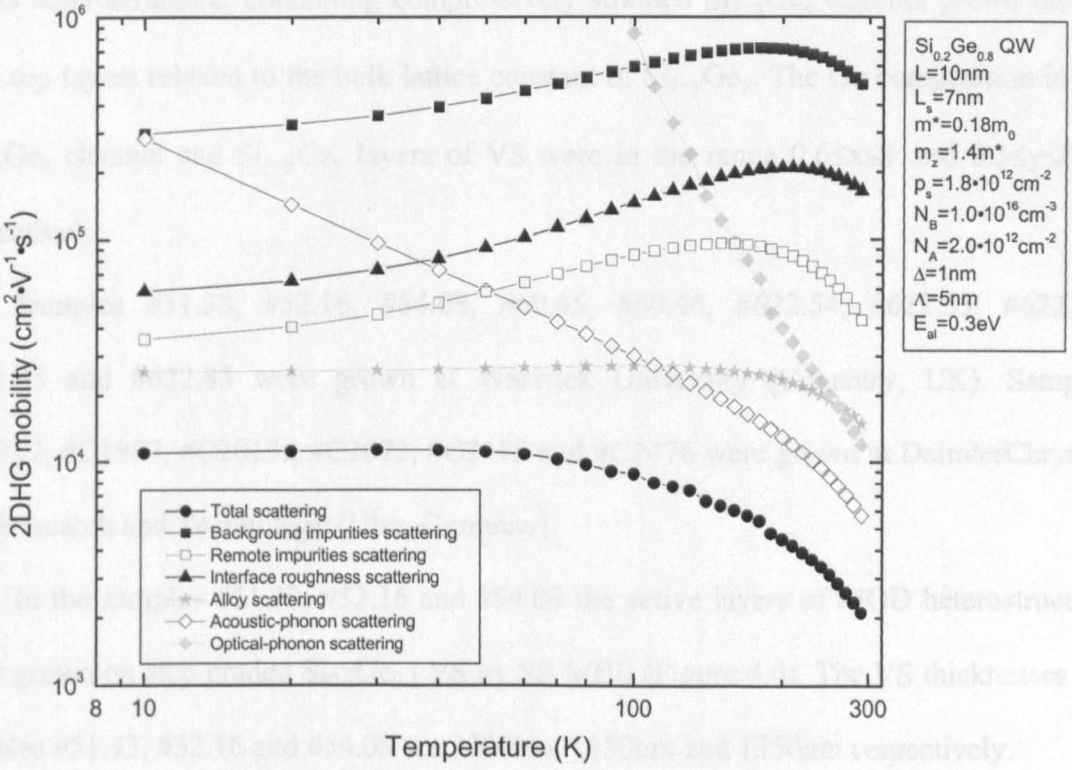

Figure 4.3 Temperature dependence of mobility of 2DHG formed in the $Si_{0.2}Ge_{0.8}$ channel of p-type MOD $Si_{0.2}Ge_{0.8}/Si_{0.7}Ge_{0.3}$ heterostructure calculated with relaxation time approximation theory of carriers' transport. Also shown the variation of mobility with temperature for each scattering mechanism taken in isolation.

Finally from the complex of performed calculations, assumptions and limitations is necessary to find optimum parameters for MOD heterostructure due to the purpose of research and application, because the interrelation between carrier density and mobility requires compromises. The investigated in this work p-type MOD $Si_{1-x}Ge_x/Si_{1-y}Ge_y$ heterostructures were designed to get high 2DHG mobility ($>500cm^2 \cdot V^{-1} \cdot s^{-1}$) at high sheet carrier density ($>10^{12}cm^{-2}$) at room temperature for further applications in FET devices.

4.2 The p-type MOD $Si_{1-x}Ge_x/Si_{1-y}Ge_y$ heterostructures investigated in current research

The samples investigated in current research were p-type MOD $Si_{1-x}Ge_x/Si_{1-y}Ge_y$ heterostructures grown on Si(001) substrates. The structures consist of active layers of MOD heterostructure, containing compressively strained $Si_{1-x}Ge_x$ channel grown on VS with top layers relaxed to the bulk lattice constant of $Si_{1-y}Ge_y$. The Ge composition in the $Si_{1-x}Ge_x$ channel and $Si_{1-y}Ge_y$ layers of VS were in the range $0.6 \leq x \leq 1$ and $0.3 \leq y \leq 0.63$ respectively.

Samples #51.33, #52.16, #54.08, #60.45, #60.46, #622.54, #622.55, #622.56, #622.83 and #622.83 were grown at Warwick University (Coventry, UK). Samples #C1957, #C1987, #C2015f, #C2072, #C2475 and #C2476 were grown at DaimlerChrysler AG Research and Technology (Ulm, Germany).

In the samples #51.33, #52.16 and #54.08 the active layers of MOD heterostructure were grown on step graded $Si_{0.7}Ge_{0.3}$ VS by SS-MBE (Figure 4.4). The VS thicknesses for samples #51.33, #52.16 and #54.08 are 2200nm, 1150nm and 1350nm respectively.

The active layers of MOD heterostructure in sample #51.33 consist of 10nm thickness B doped ($4 \cdot 10^{18}cm^{-3}$) $Si_{0.8}Ge_{0.2}$ layer followed by 5nm $Si_{0.7}Ge_{0.3}$ spacer, 5nm $Si_{0.22}Ge_{0.78}$ channel and 50nm $Si_{0.7}Ge_{0.3}$ cap (Figure 4.4). All layers were grown at 440C.

The active layers of MOD heterostructure in sample #52.16 consist of 5nm $Si_{0.24}Ge_{0.76}$ channel followed by 10nm $Si_{0.7}Ge_{0.3}$ spacer, 50nm B doped ($2.4 \cdot 10^{18} cm^{-3}$) $Si_{0.7}Ge_{0.3}$ layer and 3nm Si cap (Figure 4.4). All layers were grown at 450C.

The active layers of MOD heterostructure in sample #54.08 consist of 6nm $Si_{0.4}Ge_{0.6}$ channel followed by 15nm $Si_{0.7}Ge_{0.3}$ spacer, 50nm B doped ($2 \cdot 10^{18} cm^{-3}$) $Si_{0.7}Ge_{0.3}$ layer and 3nm Si cap (Figure 4.4). All layers were grown at 450C.

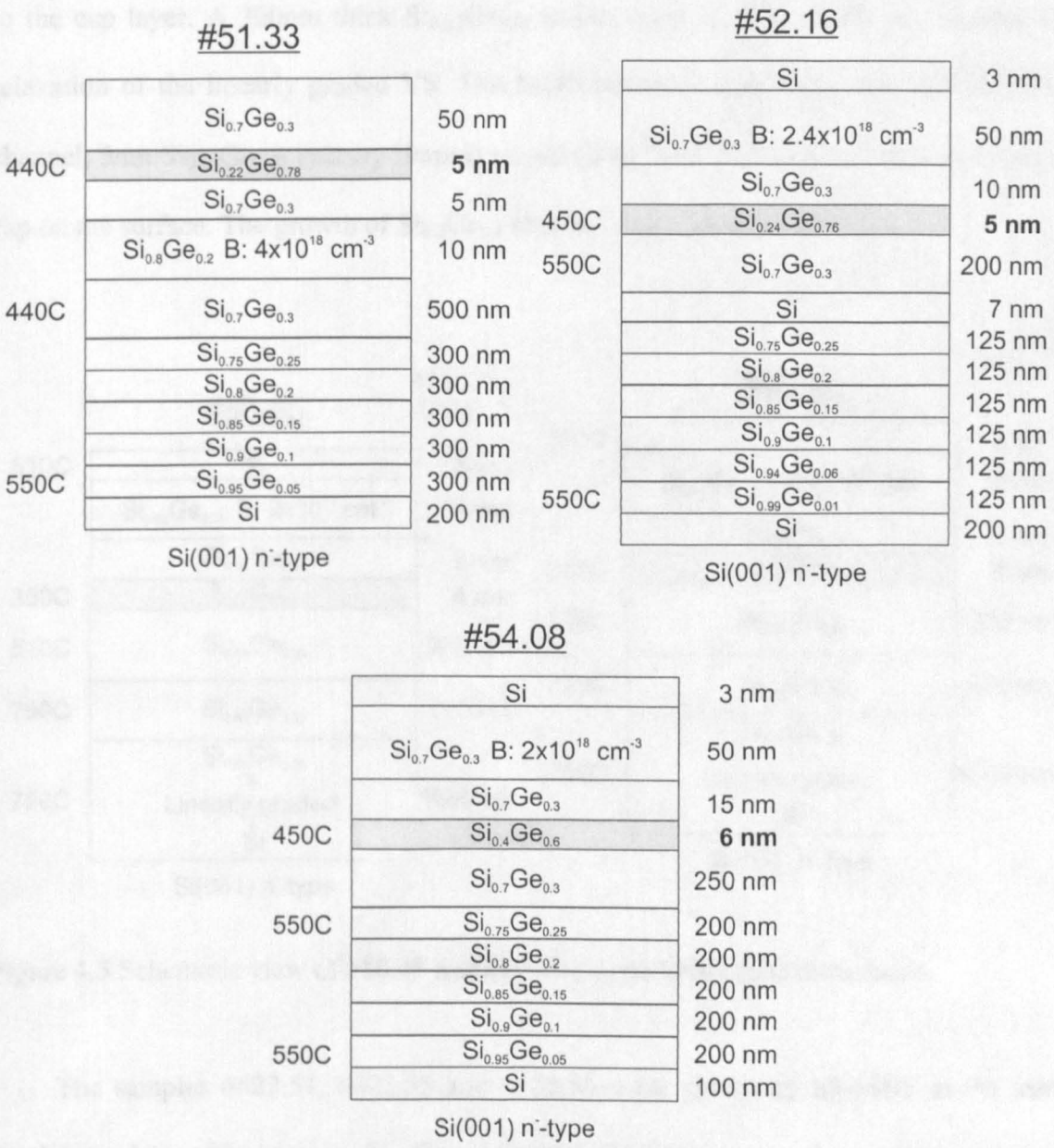

Figure 4.4 Schematic view of #51.33, #52.16 and #54.08 p-type MOD heterostructures.

The samples #60.45 and #60.46 were grown at the same conditions but in the sample #6045 after the growth of $Si_{0.65}Ge_{0.35}$ spacer was done interrupt for 30min accompanied with annealing of grown layers at 800C (Figure 4.5). In order to grow $Si_{0.2}Ge_{0.8}$ channel, an initial 1200nm thick linearly graded VS with a Ge content increasing linearly from 0.05 to 0.35 was grown, which was relaxed to the lattice constant of $Si_{0.65}Ge_{0.35}$. The VS was grown by LP CVD to reduce time consumption. After this the wafer was transferred to the SS-MBE chamber through air. Epilayers were then successively grown from buffer layer to the cap layer. A 300nm thick $Si_{0.65}Ge_{0.35}$ buffer layer is than grown to complete the relaxation of the linearly graded VS. The MOD structure consists of the 4nm $Si_{0.2}Ge_{0.8}$ channel, 5nm $Si_{0.65}Ge_{0.35}$ spacer, 10nm B doped ($2 \cdot 10^{18} cm^{-3}$) $Si_{0.65}Ge_{0.35}$ layer and 3nm Si cap on the surface. The growth of $Si_{0.2}Ge_{0.8}$ channel was performed at 350C.

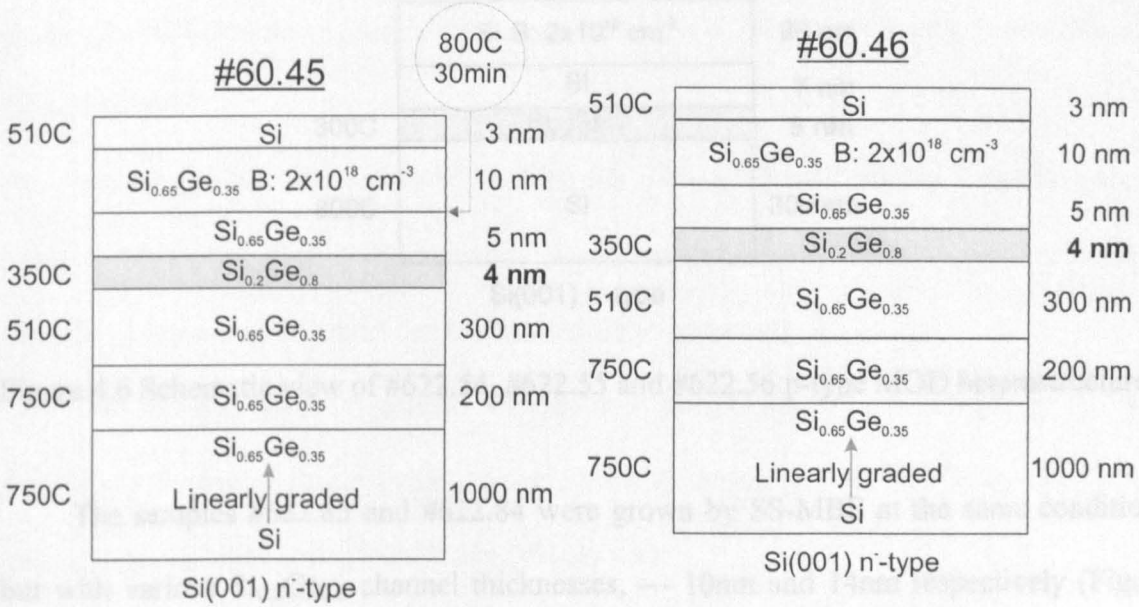

Figure 4.5 Schematic view of #60.45 and #60.46 p-type MOD heterostructures.

The samples #622.54, #622.55 and #622.56 were grown by SS-MBE at the same conditions but with various $Si_{0.2}Ge_{0.8}$ channel thicknesses, — 2nm, 4nm and 8nm respectively (Figure 4.6). Initially 300nm Si buffer was grown followed by $Si_{0.2}Ge_{0.8}$

channel, 7nm Si spacer, 20nm B doped ($2 \cdot 10^{18} cm^{-3}$) Si layer and 70nm Si cap. The $Si_{0.2}Ge_{0.8}$ channel was grown at 300C.

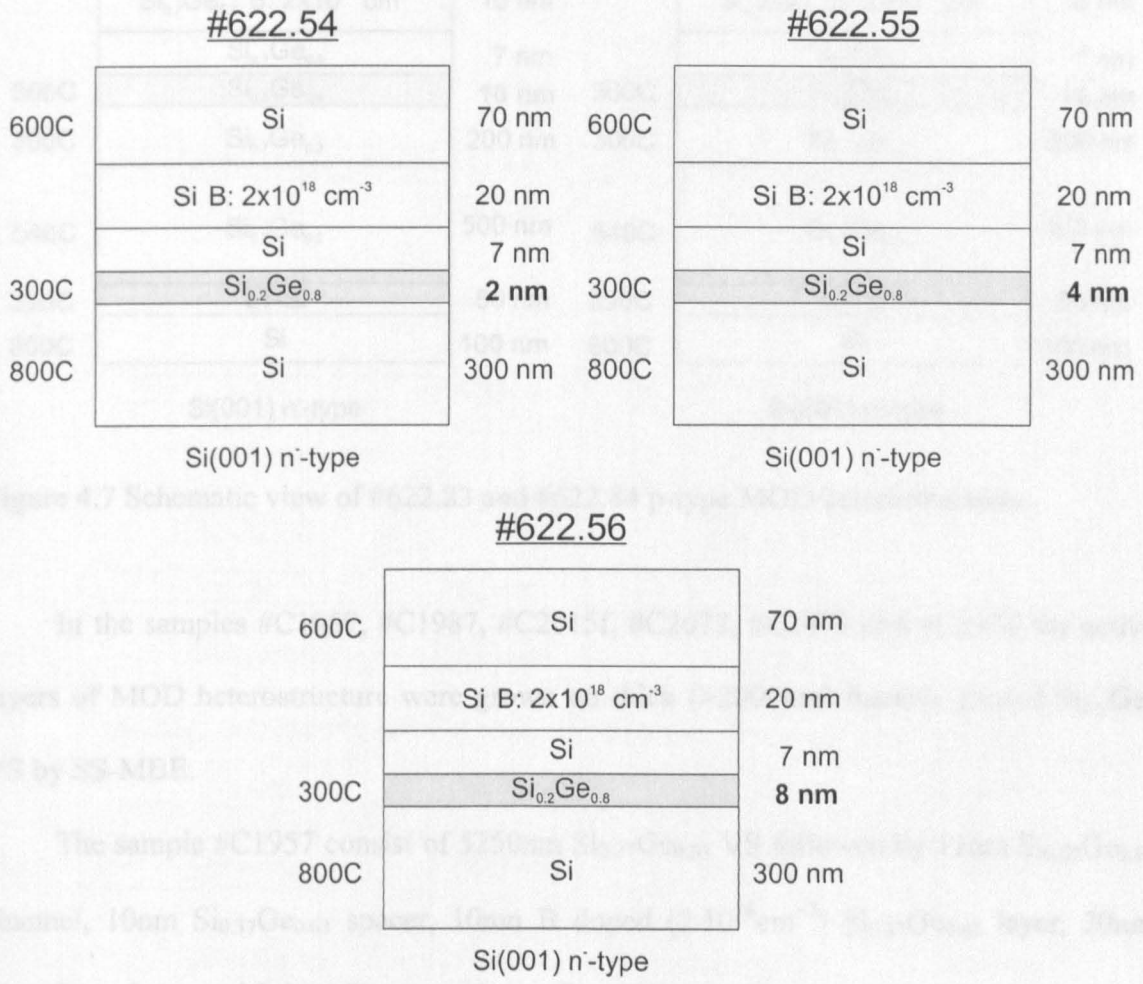

Figure 4.6 Schematic view of #622.54, #622.55 and #622.56 p-type MOD heterostructures.

The samples #622.83 and #622.84 were grown by SS-MBE at the same conditions but with various $Si_{0.2}Ge_{0.8}$ channel thicknesses, — 10nm and 14nm respectively (Figure 4.7). The VS consist of 100nm Si layer followed by 50nm LT-Si layer grown 390C and 700nm $Si_{0.7}Ge_{0.3}$ relaxed layer. The active layers of MOD heterostructure consist of $Si_{0.2}Ge_{0.8}$ channel followed by 7nm $Si_{0.7}Ge_{0.3}$ spacer 10nm B doped ($2 \cdot 10^{18} cm^{-3}$) $Si_{0.7}Ge_{0.3}$, 40nm $Si_{0.7}Ge_{0.3}$ layer and 5nm Si cap on the surface. The $Si_{0.2}Ge_{0.8}$ channel was grown at 300C.

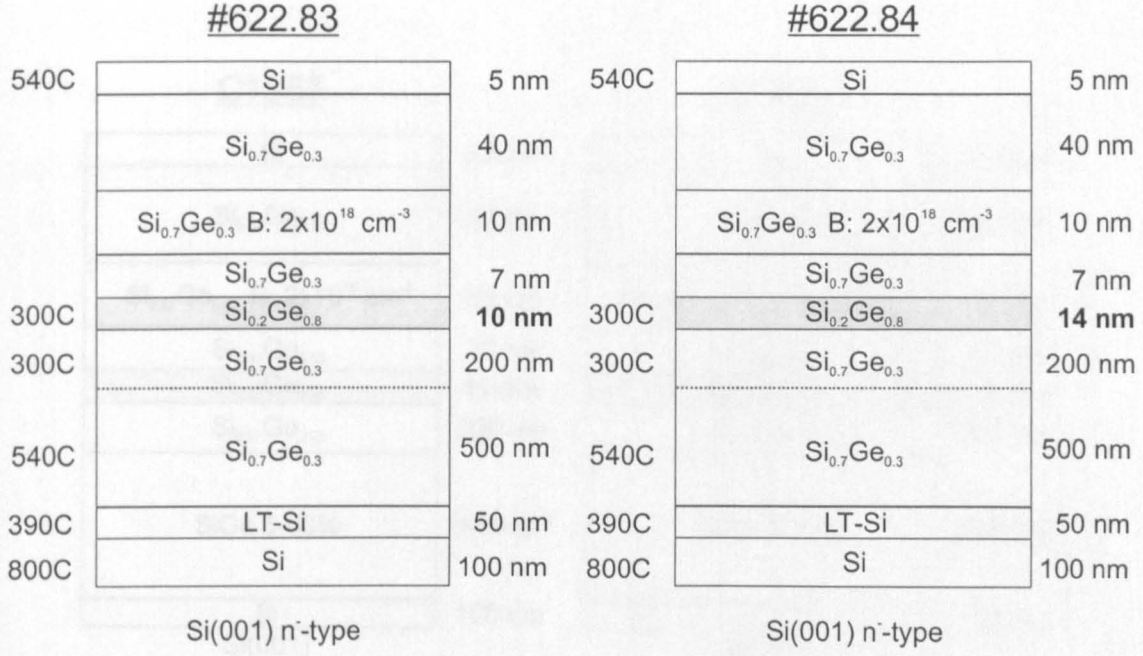

Figure 4.7 Schematic view of #622.83 and #622.84 p-type MOD heterostructures.

In the samples #C1957, #C1987, #C2015f, #C2072, #C2475 and #C2476 the active layers of MOD heterostructure were grown on thick (>2000nm) linearly graded $Si_{1-y}Ge_y$ VS by SS-MBE.

The sample #C1957 consist of 5250nm $Si_{0.37}Ge_{0.63}$ VS followed by 11nm $Si_{0.05}Ge_{0.95}$ channel, 10nm $Si_{0.37}Ge_{0.63}$ spacer, 10nm B doped ($2\cdot10^{18}cm^{-3}$) $Si_{0.37}Ge_{0.63}$ layer, 20nm $Si_{0.37}Ge_{0.63}$ layer and 3.5nm Si cap on the surface (Figure 4.8).

The sample #C1987 consist of 3600nm $Si_{0.65}Ge_{0.35}$ VS followed by 12.3nm $Si_{0.34}Ge_{0.66}$ channel, 10nm $Si_{0.7}Ge_{0.3}$ spacer, 10nm B doped ($2.4\cdot10^{18}cm^{-3}$) $Si_{0.7}Ge_{0.3}$ layer, 20nm $Si_{0.7}Ge_{0.3}$ layer and 3.5nm Si cap (Figure 4.8).

The sample #C2015f consist of 4350nm $Si_{0.5}Ge_{0.5}$ VS followed by 12nm $Si_{0.18}Ge_{0.82}$ channel, 10nm $Si_{0.5}Ge_{0.5}$ spacer, 6.5nm B doped ($2.4\cdot10^{18}cm^{-3}$) $Si_{0.5}Ge_{0.5}$ layer, 20nm $Si_{0.5}Ge_{0.5}$ layer and 3.5nm Si cap (Figure 4.8).

The sample #C2072 consist of 3100nm $Si_{0.47}Ge_{0.53}$ VS followed by 12nm $Si_{0.18}Ge_{0.82}$ channel, 10nm $Si_{0.47}Ge_{0.53}$ spacer, 10nm B doped ($2.4\cdot10^{18}cm^{-3}$) $Si_{0.47}Ge_{0.53}$ layer, 5nm $Si_{0.47}Ge_{0.53}$ layer and 4nm Si cap (Figure 4.8).

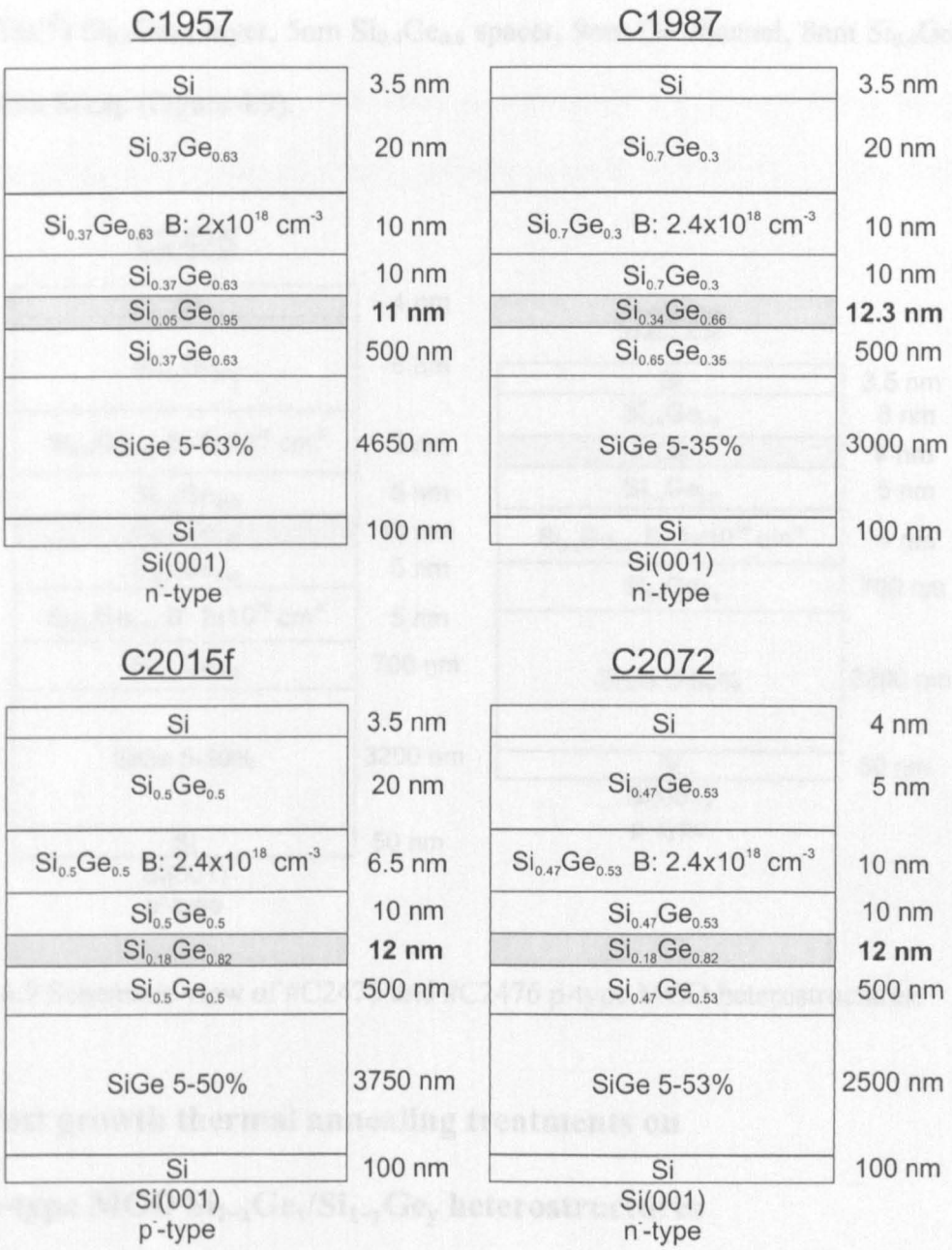

Figure 4.8 Schematic view of #C1957, #C1987, #C2015f and #C2072 p-type MOD heterostructures.

The sample #C2475 consist of 3950nm $Si_{0.41}Ge_{0.59}$ VS followed by 5nm B doped ($2{\cdot}10^{18}cm^{-3}$) $Si_{0.41}Ge_{0.59}$ layer, 5nm $Si_{0.41}Ge_{0.59}$ spacer, 10nm $Si_{0.02}Ge_{0.98}$ channel, 5nm $Si_{0.41}Ge_{0.59}$ spacer, 5nm B doped ($8{\cdot}10^{18}cm^{-3}$) $Si_{0.4}Ge_{0.59}$ layer, 6nm $Si_{0.41}Ge_{0.59}$ layer and 4nm Si cap (Figure 4.9).

The sample #C2476 consist of 3950nm $Si_{0.4}Ge_{0.6}$ VS followed by 4nm B doped ($1 \cdot 10^{19} cm^{-3}$) $Si_{0.4}Ge_{0.6}$ layer, 5nm $Si_{0.4}Ge_{0.6}$ spacer, 9nm Ge channel, 8nm $Si_{0.4}Ge_{0.6}$ layer and 3.5nm Si cap (Figure 4.9).

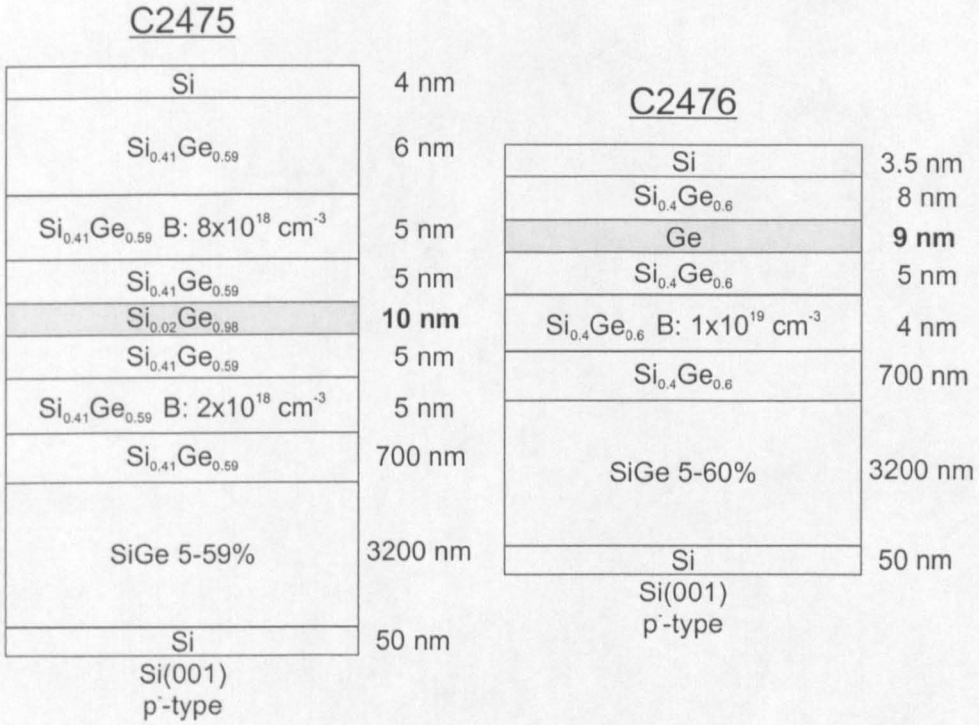

Figure 4.9 Schematic view of #C2475 and #C2476 p-type MOD heterostructures.

4.3 Post growth thermal annealing treatments on p-type MOD $Si_{1-x}Ge_x/Si_{1-y}Ge_y$ heterostructures

To research the effect of thermal influence on magnetotransport, structural and optical properties of p-type MOD $Si_{1-x}Ge_x/Si_{1-y}Ge_y$ heterostructures the post growth thermal annealing treatments were done. Post growth thermal annealing treatments were performed on investigated heterostructures after growth by two various methods, — furnace thermal annealing (FTA) and rapid thermal annealing (RTA).

Furnace thermal annealing treatments were performed in flow N_2 ambient at temperatures 600C, 700C, 750C, 800C and 900C for 30min. FTA treatments were applied

to samples #51.33, #52.16, #54.08, #60.45, #60.46, #622.54, #622.55, #622.56, #622.83 and #622.84.

Rapid thermal annealing treatments were performed in N_2 ambient at temperatures 750C for 30sec. RTA treatments were applied to samples #C1987, #C2015f and #C2072.

5. Results and discussions of structural and optical analysis of p-type MOD $Si_{1-x}Ge_x/Si_{1-y}Ge_y$ heterostructures

5.1 Introduction

In this chapter the results and discussions of structural and optical analysis of p-type MOD $Si_{1-x}Ge_x/Si_{1-y}Ge_y$ heterostructures are presented. The samples were analysed by cross-sectional transmission electron microscopy (XTEM), ultra-low energy secondary ion mass spectrometry (ULE-SIMS), photoluminescence spectroscopy (PL), micro-Raman spectroscopy and scanning white-light interferometry.

5.2 Transmission electron microscopy analysis of p-type MOD $Si_{1-x}Ge_x/Si_{1-y}Ge_y$ heterostructures

XTEM images of sample #60.46 (see chapter 4.2) are presented in Figure 5.1. The bottom image in Figure 5.1 shows the cross-section of the grown structure starting from the Si(001) substrate and finishing with thin Si cap on the surface. The linearly graded $Si_{0.65}Ge_{0.35}$ VS grown by CVD consists of 1μm region with graded Ge composition up to $Si_{0.65}Ge_{0.35}$ followed by ~200nm $Si_{0.65}Ge_{0.35}$ layer. The dislocations are clearly observable as dark lines in the VS. The massive dislocations network can be seen in the linearly graded part of VS. Also the dislocations are visible in the Si substrate. The top $Si_{0.65}Ge_{0.35}$ layer of VS is dislocation free as well as all epitaxial layers grown on top by SS-MBE. After VS growth by CVD the wafer was transferred to MBE chamber through the air and the growth was continued. Before the growth of active layers of MOD heterostructure the 300nm $Si_{0.65}Ge_{0.35}$ buffer layer was grown on top of VS (bottom of Figure 5.1). The thin dark line close to the surface corresponds to $Si_{0.2}Ge_{0.8}$ channel.

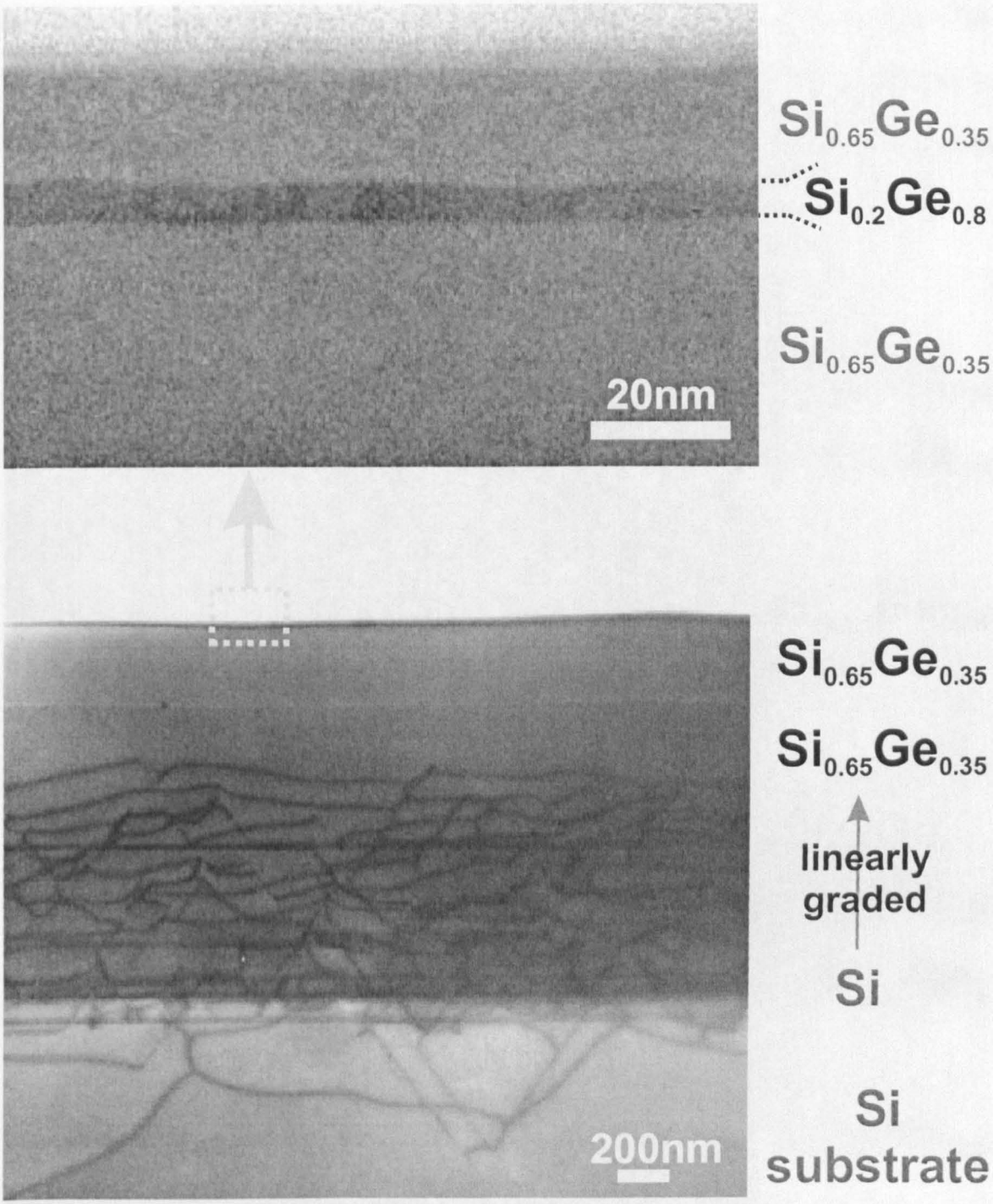

Figure 5.1 XTEM images of $Si_{0.2}Ge_{0.8}$ channel region (top) and all grown layers (bottom) of as-grown sample #60.46.

The XTEM image of $Si_{0.2}Ge_{0.8}$ channel region obtained with high magnification is presented in the top of Figure 5.1. The $Si_{0.2}Ge_{0.8}$ channel is clearly visible as a stripe of dark contrast between $Si_{0.65}Ge_{0.35}$ layers. This region is dislocation free. The bottom and top $Si_{0.2}Ge_{0.8}/Si_{0.65}Ge_{0.35}$ interfaces are abrupt. The average thickness of $Si_{0.2}Ge_{0.8}$ channel

is 4.2nm. It is clear to see roughness of the top interface of $Si_{0.2}Ge_{0.8}$ channel characterized by average height Δ=1.3nm in the growth direction and the correlation length Λ=43nm in the plane. The average distance between $Si_{0.2}Ge_{0.8}$ channel and Si layer on the surface is 16.5nm.

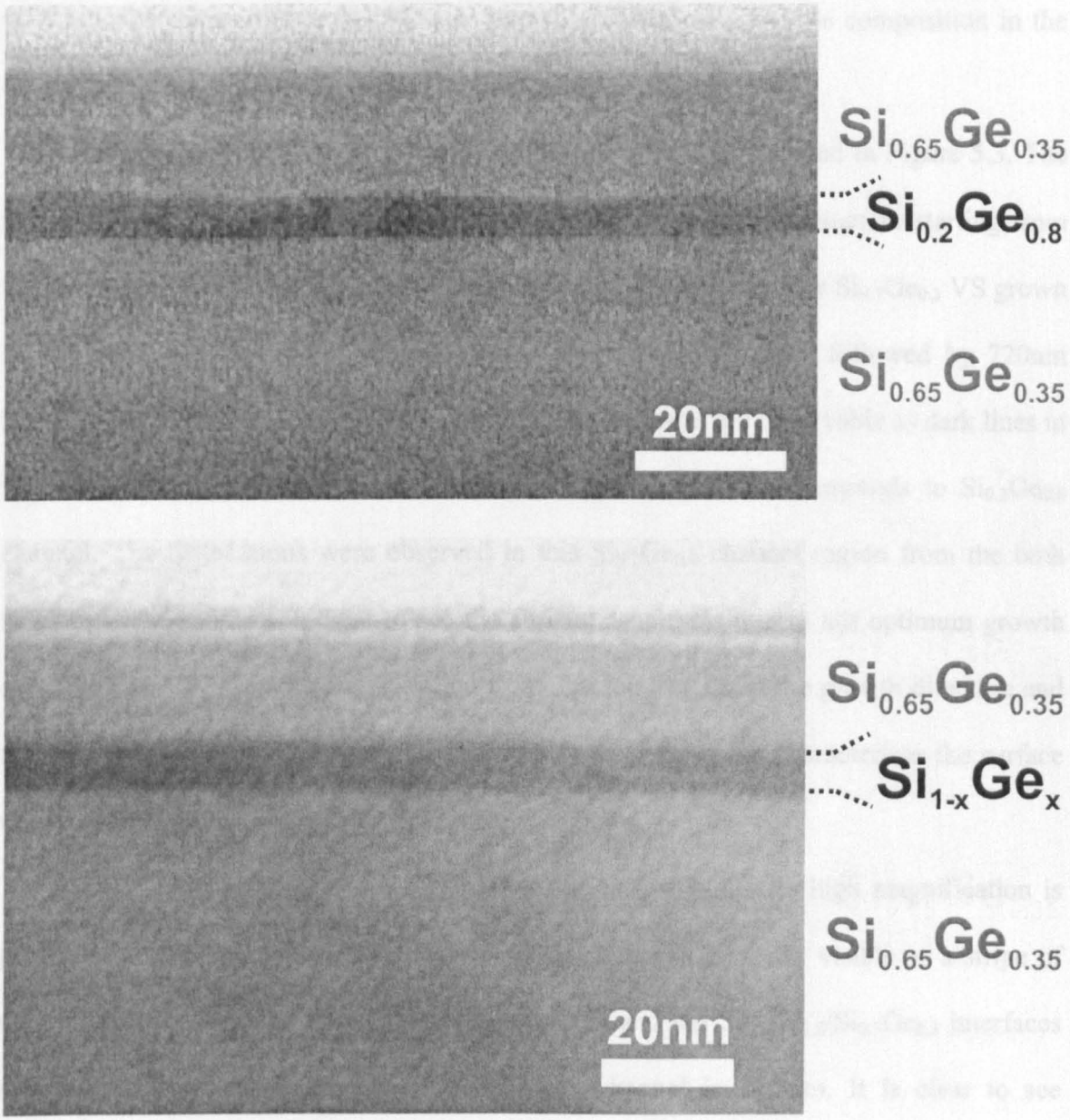

Figure 5.2 XTEM images of $Si_{0.2}Ge_{0.8}$ channel region in as-grown (top) and after FTA at 750C for 30min (bottom) samples #60.46.

After FTA at 750C for 30min performed on the sample #60.46 were observed significant changes in the $Si_{0.2}Ge_{0.8}$ channel region (bottom of Figure 5.2). The broadening of $Si_{0.2}Ge_{0.8}$ channel accompanied with smearing of bottom and top $Si_{0.2}Ge_{0.8}/Si_{0.65}Ge_{0.35}$

interfaces were observed. The average thickness of $Si_{0.2}Ge_{0.8}$ channel increased up to 7nm. The average distance between $Si_{0.2}Ge_{0.8}$ channel and Si layer on the surface decreased to 14.9nm. The broadening of $Si_{0.2}Ge_{0.8}$ channel was due to Ge diffusion during thermal annealing from the region with high Ge concentration ($Si_{0.2}Ge_{0.8}$ channel) to the region with low Ge concentration ($Si_{0.65}Ge_{0.35}$ layers). Consequently the Ge composition in the $Si_{0.2}Ge_{0.8}$ channel after FTA at 750C for 30min decreased.

XTEM images of sample #622.83 (see chapter 4.2) are presented in Figure 5.3. The bottom image in Figure 5.3 shows the cross-section of the grown structure starting from the Si(001) substrate and finishing with thin Si cap on the surface. The $Si_{0.7}Ge_{0.3}$ VS grown by SS-MBE consists of low temperature Si layer grown at 390C followed by 720nm $Si_{0.7}Ge_{0.3}$ layer of constant Ge composition. The dislocations are observable as dark lines in the VS and Si substrate. The dark band close to the surface corresponds to $Si_{0.2}Ge_{0.8}$ channel. The dislocations were observed in this $Si_{0.2}Ge_{0.8}$ channel region from the both sides of the channel. It is clear to see the surface roughness due to not optimum growth conditions of VS. Average height varied from 3nm up to 8nm in the growth direction and the correlation length varied from 230nm to 300nm in the plane characterizes the surface roughness.

The XTEM image of $Si_{0.2}Ge_{0.8}$ channel region obtained with high magnification is presented in the top of Figure 5.3. The $Si_{0.2}Ge_{0.8}$ channel is clearly visible as a stripe of dark contrast between $Si_{0.7}Ge_{0.3}$ layers. The bottom and top $Si_{0.2}Ge_{0.8}/Si_{0.7}Ge_{0.3}$ interfaces are abrupt. The average thickness of $Si_{0.2}Ge_{0.8}$ channel is 11.3nm. It is clear to see roughness of the top interface of $Si_{0.2}Ge_{0.8}$ channel characterized by average height $\Delta<1$nm in the growth direction and the correlation length $\Lambda=47$nm in the plane. The average distance between $Si_{0.2}Ge_{0.8}$ channel and Si layer on the surface is 60.5nm. The average thickness of Si cap layer is around 5nm

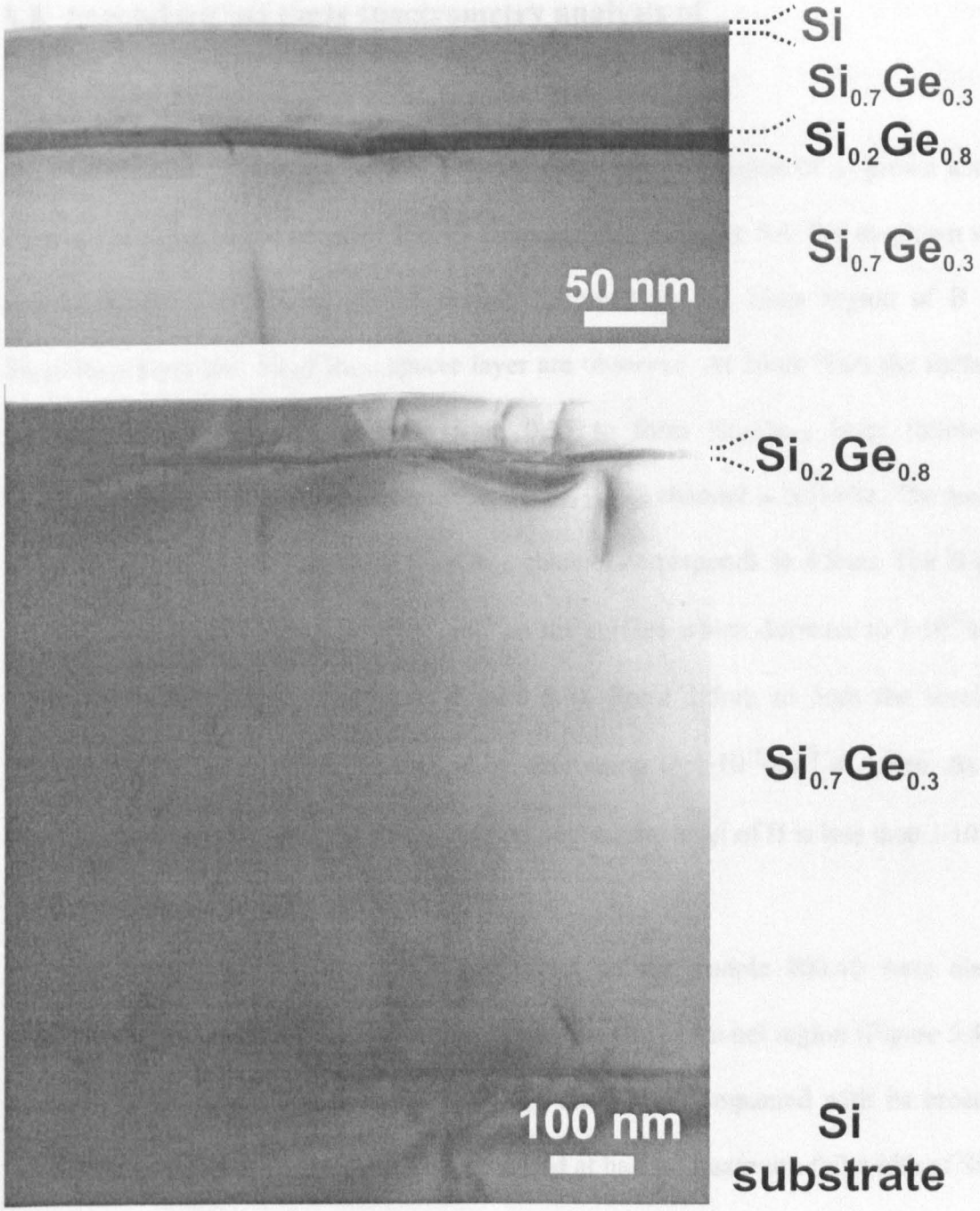

Figure 5.3 XTEM images of $Si_{0.2}Ge_{0.8}$ channel region (top) and all grown layers (bottom) of as-grown sample #622.83.

The results of XTEM analysis of p-type MOD $Si_{1-x}Ge_x/Si_{1-y}Ge_y$ heterostructures were presented at "Condensed Matter and Materials Physics '99 Conference"[1], "10th European Heterostructure Technology Workshop"[2]&[3], "International Conference on Solid State Crystals 2000: Materials Science and Applications"[4] and "SiGe (C) 2001 Workshop"[5].

5.3 Secondary ion mass spectrometry analysis of p-type MOD $Si_{1-x}Ge_x/Si_{1-y}Ge_y$ heterostructures

ULE-SIMS profiles of Ge and B in $Si_{0.2}Ge_{0.8}$ channel region of as-grown and after FTA at 750C for 30min samples #60.46 are presented in Figure 5.4. For as-grown sample (top of Figure 5.4) Si cap on the surface followed by the 15nm region of B doped $Si_{0.65}Ge_{0.35}$ layer and $Si_{0.65}Ge_{0.35}$ spacer layer are observed. At 20nm from the surface the Ge composition began to increase from 0.35 to form $Si_{0.2}Ge_{0.8}$ layer followed by $Si_{0.65}Ge_{0.35}$ buffer layers. The Ge profile in the $Si_{0.2}Ge_{0.8}$ channel is bell-like. The measured at half of maximum full width of $Si_{0.2}Ge_{0.8}$ channel corresponds to 4.9nm. The B profile for as-grown sample shows $B=2\cdot10^{19}cm^{-3}$ on the surface which decrease to $1\cdot10^{18}cm^{-3}$ at 1.5nm from the surface (bottom of Figure 5.4). From 1.5nm to 5nm the level of B increased up to $2.82\cdot10^{18}cm^{-3}$ followed by decreasing to $1\cdot10^{18}cm^{-3}$ at 14nm. At 20nm from the surface, where the $Si_{0.2}Ge_{0.8}$ channel begins, the level of B is less than $1\cdot10^{17}cm^{-3}$ that are the recognition limit of SIMS.

After FTA at 750C for 30min performed on the sample #60.46 were observed significant changes for Ge and B profiles in the $Si_{0.2}Ge_{0.8}$ channel region (Figure 5.4). The decrease of Ge concentration in the $Si_{0.2}Ge_{0.8}$ channel accompanied with its broadening were observed (top of Figure 5.4). The measured at half of maximum full width of $Si_{1-x}Ge_x$ channel is increased and corresponds to 9.3nm. The Ge composition in the $Si_{0.65}Ge_{0.35}$ layers has not changed. The B profile for annealed sample showed an increase of B concentration on the surface up to $\sim1\cdot10^{20}cm^{-3}$ on the surface which decreased to $2\cdot10^{18}cm^{-3}$ at 3nm from the surface (bottom of Figure 5.4). These values increased due to unintentional B doping during furnace thermal annealing. From 3nm to 6nm the level of B increased up to $2.76\cdot10^{18}cm^{-3}$ followed by decreasing to $1\cdot10^{18}cm^{-3}$ at 15nm. The increase of B level was observed in the $Si_{0.65}Ge_{0.35}$ spacer layer after FTA.

ULE-SIMS profiles of Ge and B in $Si_{0.2}Ge_{0.8}$ channel region of as-grown and after FTA at 750C for 30min samples #60.46 and sample #60.45 are presented in Figure 5.5. The designs of samples #60.45 and #60.46 are similar, exclusive in-situ annealing of sample #60.45. Sample #60.45 (see chapter 4.2) was annealed in-situ of SS-MBE chamber before the growth of B doped $Si_{0.65}Ge_{0.35}$ layer and Si cap layer. The annealing was performed at 800C for 30min in vacuum. Sample #60.46 after FTA at 750C was annealed for 30min after growth in nitrogen ambient. It is clear to see from Ge profile for sample #60.45 that the $Si_{0.2}Ge_{0.8}$ channel was smeared during in situ annealing at 800C for 30min (top of Figure 5.5). The B profiles in the $Si_{0.2}Ge_{0.8}$ channel region are the same for samples #60.45 and as-grown #60.46. It is clear because of B doped $Si_{0.65}Ge_{0.35}$ layer for sample #60.45 was grown after in-situ annealing at 800C, at the same conditions as for sample #60.46. Due to this no B diffusion was observed.

The results of ULE-SIMS analysis of p-type MOD $Si_{1-x}Ge_x/Si_{1-y}Ge_y$ heterostructures were presented at "10th European Heterostructure Technology Workshop"[3] and "SiGe (C) 2001 Workshop"[5].

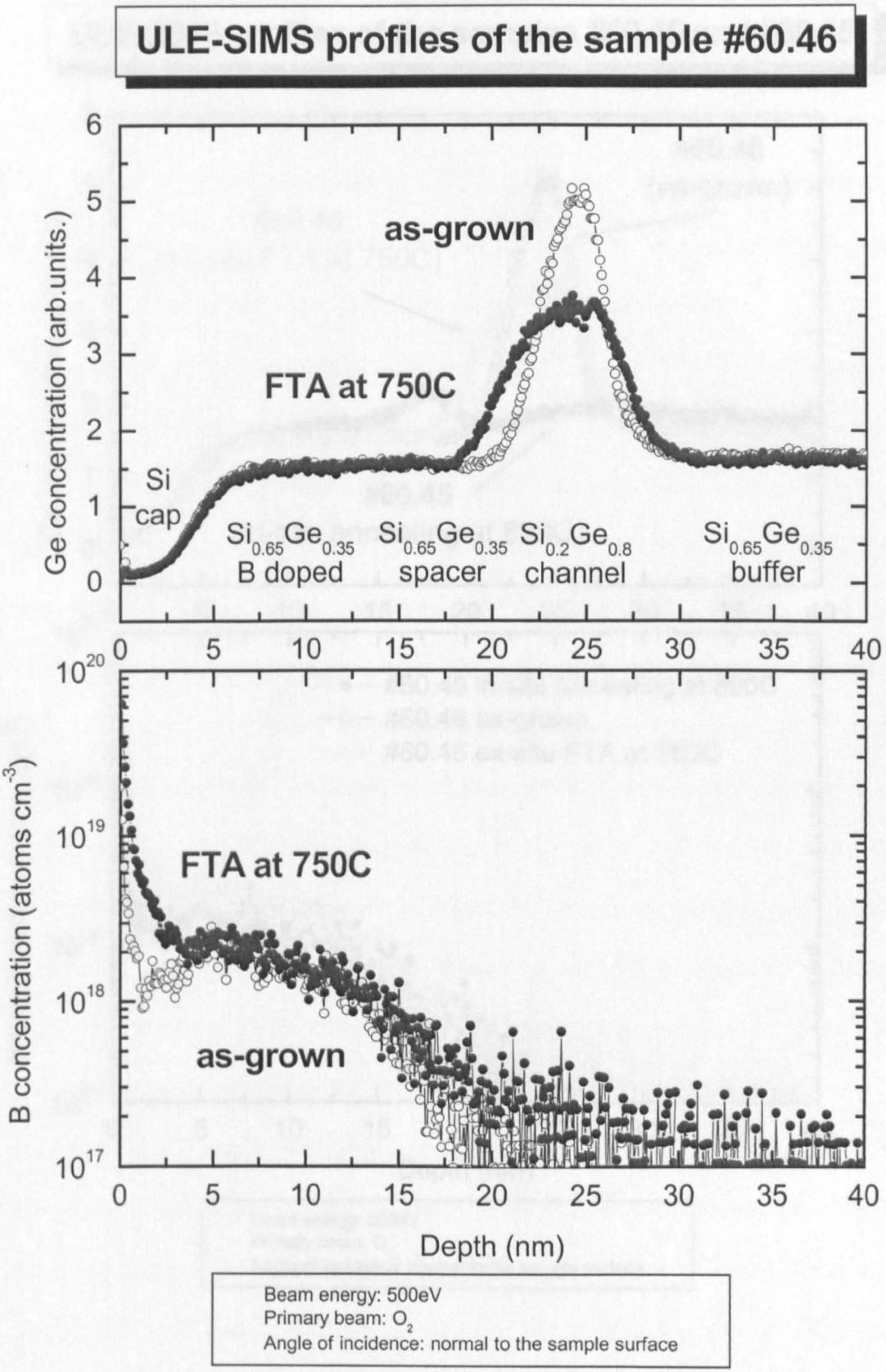

Figure 5.4 ULE-SIMS profiles of Ge (top) and B (bottom) in $Si_{1-x}Ge_x$ channel region of as-grown and after FTA at 750C for 30min samples #60.46.

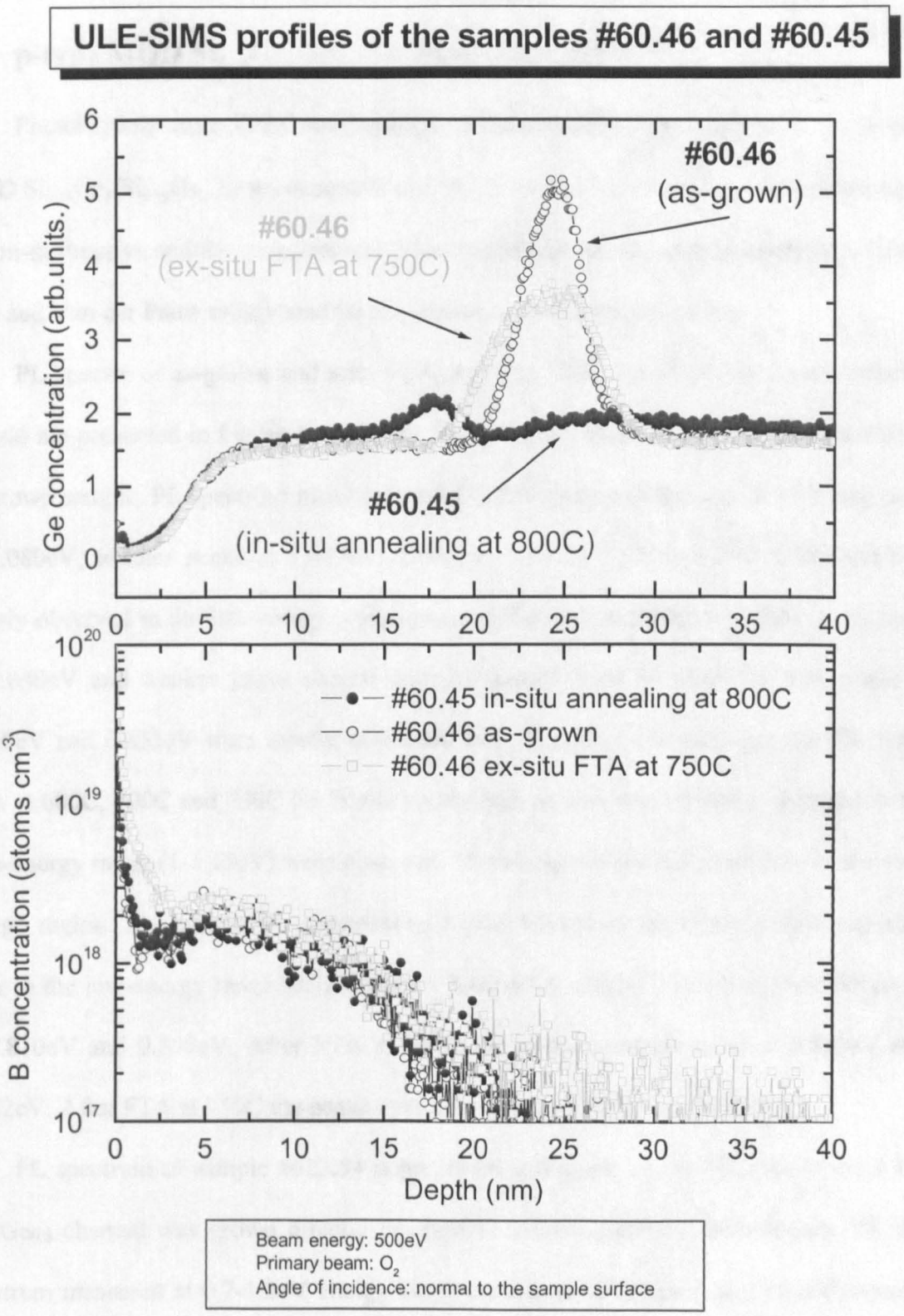

Figure 5.5 ULE-SIMS profiles of Ge (top) and B (bottom) in $Si_{1-x}Ge_x$ channel region of samples #60.45 and #60.46.

5.4 Photoluminescence spectroscopy analysis of p-type MOD $Si_{1-x}Ge_x/Si_{1-y}Ge_y$ heterostructures

Photoluminescence (PL) spectroscopy measurements were performed on p-type MOD $Si_{1-x}Ge_x/Si_{1-y}Ge_y$ heterostructures at 5.5K. It is necessary to point, that the technique is non-destructive and the measurements were performed on the very same samples (Hall-bars and Van der Pauw cross) used for magnetotransport characterization.

PL spectra of as-grown and after FTA at 600C, 700C and 750C for 30min samples #60.46 are presented in Figure 5.6. The top PL spectrum in Figure 5.6 was obtained from as-grown sample. PL spectrum measured at 0.7-1.2eV energy range consist of strong peak at 1.080eV, weaker peaks at 1.017eV, 1.091eV, 1.097eV, 1.119eV and 1.149 and two clearly observed in the low energy region peaks at 0.810eV and 0.855eV. The strong peak at 1.080eV and weaker peaks around were originated from Si substrate. The peaks at 0.810eV and 0.855eV were mostly originated from $Si_{0.65}Ge_{0.35}$ linearly graded VS. After FTA at 600C, 700C and 750C for 30min no changes in positions of peaks allocated in the high-energy range (1-1.15eV) were observed. The changes were observed only in the low-energy region. The bottom PL spectrum in Figure 5.6 shows the changes observed after FTA in the low-energy range (0.72-0.94eV). After FTA at 600C the peaks were observed at 0.810eV and 0.850eV. After FTA at 700C the peaks were observed at 0.813eV and 0.852eV. After FTA at 750C the peaks were observed at 0.813eV and 0.854eV.

PL spectrum of sample #622.54 is presented in Figure 5.7. In this sample the 2 nm $Si_{0.2}Ge_{0.8}$ channel was grown directly on Si(001) substrate without intermediate VS. PL spectrum measured at 0.7-1.2eV energy range consist of strong peak at 1.081eV, weaker peaks at 1.017eV, 1.092eV, 1.097eV, 1.121eV and 1.150. The strong peak at 1.081eV and weaker peaks around were mostly originated from Si substrate. There are no peaks were observed in the low-energy range (0.7-0.95eV).

PL spectra of as-grown and after FTA at 600C, 750C and 900C for 30min samples #622.83 are presented in Figure 5.8. The top PL spectrum in Figure 5.8 was obtained from as-grown sample. PL spectrum measured at 0.7-1.2eV energy range consist of strong peak at 1.080eV, weaker peaks at 1.017eV, 1.091eV, 1.096eV, 1.120eV and 1.149 and one clearly observed in the low energy region peak at 0.807eV. The strong peak at 1.080eV and weaker peaks around were originated from Si substrate. The peak at 0.807eV was mostly originated from $Si_{0.7}Ge_{0.3}$ VS with low temperature Si buffer. After FTA at 600C, 750C and 900C for 30min no changes in positions of peaks allocated in the high-energy range (1-1.15eV) were observed. The changes were observed only in the low-energy region. The bottom PL spectrum in Figure 5.8 shows the changes observed after FTA in the low-energy range (0.72-0.92eV). After FTA at 600C the peak were observed at 0.811eV. After FTA at 750C the peak were observed at 0.811eV. And after FTA at 900C the peak were observed at 0.813eV.

PL spectra of as-grown samples #C1957 and #C1987 are presented in Figure 5.9. PL spectrum of sample #C1957 measured at 0.7-1.2eV energy range (top of Figure 5.9) consist of clearly observed peaks at 1.096eV, 0.950eV, 0.864eV, 0.806eV and 0.766eV. The peaks at 0.950eV, 0.864eV, 0.806eV and 0.766eV were mostly originated from $Si_{0.37}Ge_{0.63}$ linearly graded VS. PL spectrum of sample #C1987 measured at 0.7-1.2eV energy range (top of Figure 5.9) consist of clearly observed peaks at 1.097eV, 1.082eV, 0.954eV, 0.867eV and 0.807eV. The peaks at 0.954eV, 0.867eV and 0.807eV were mostly originated from $Si_{0.65}Ge_{0.35}$ linearly graded VS.

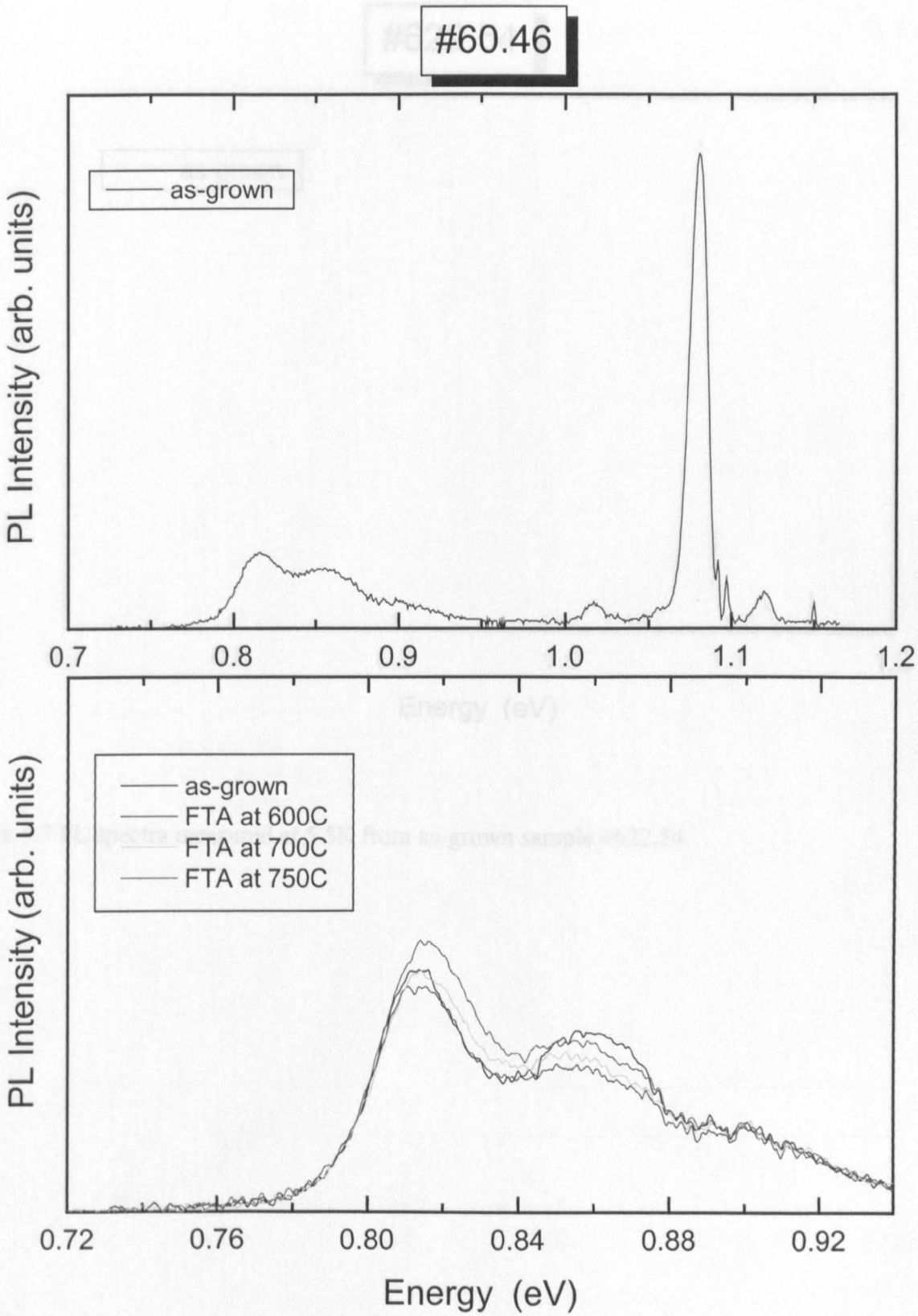

Figure 5.6 PL spectra measured at 5.5K from as-grown and after FTA at 600C, 700C and 750C for 30min samples #60.46.

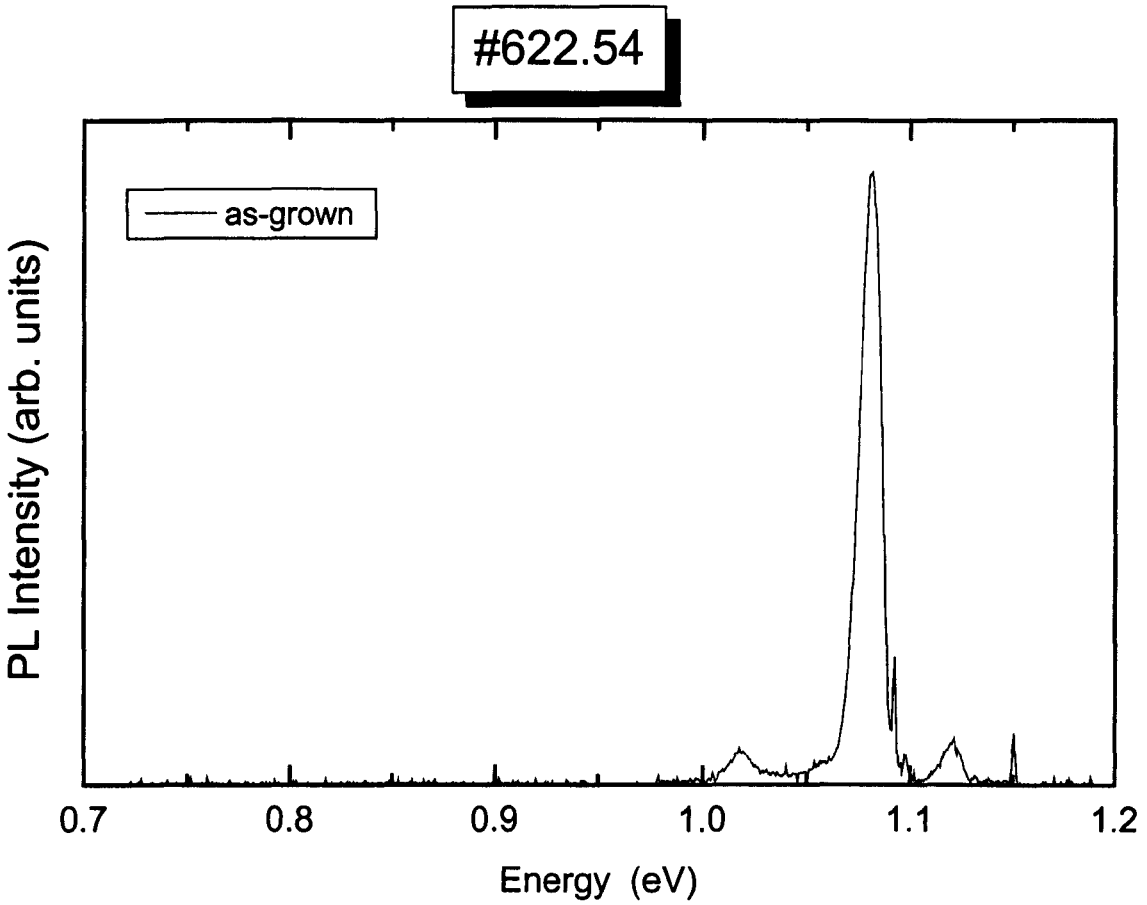

Figure 5.7 PL spectra measured at 5.5K from as-grown sample #622.54.

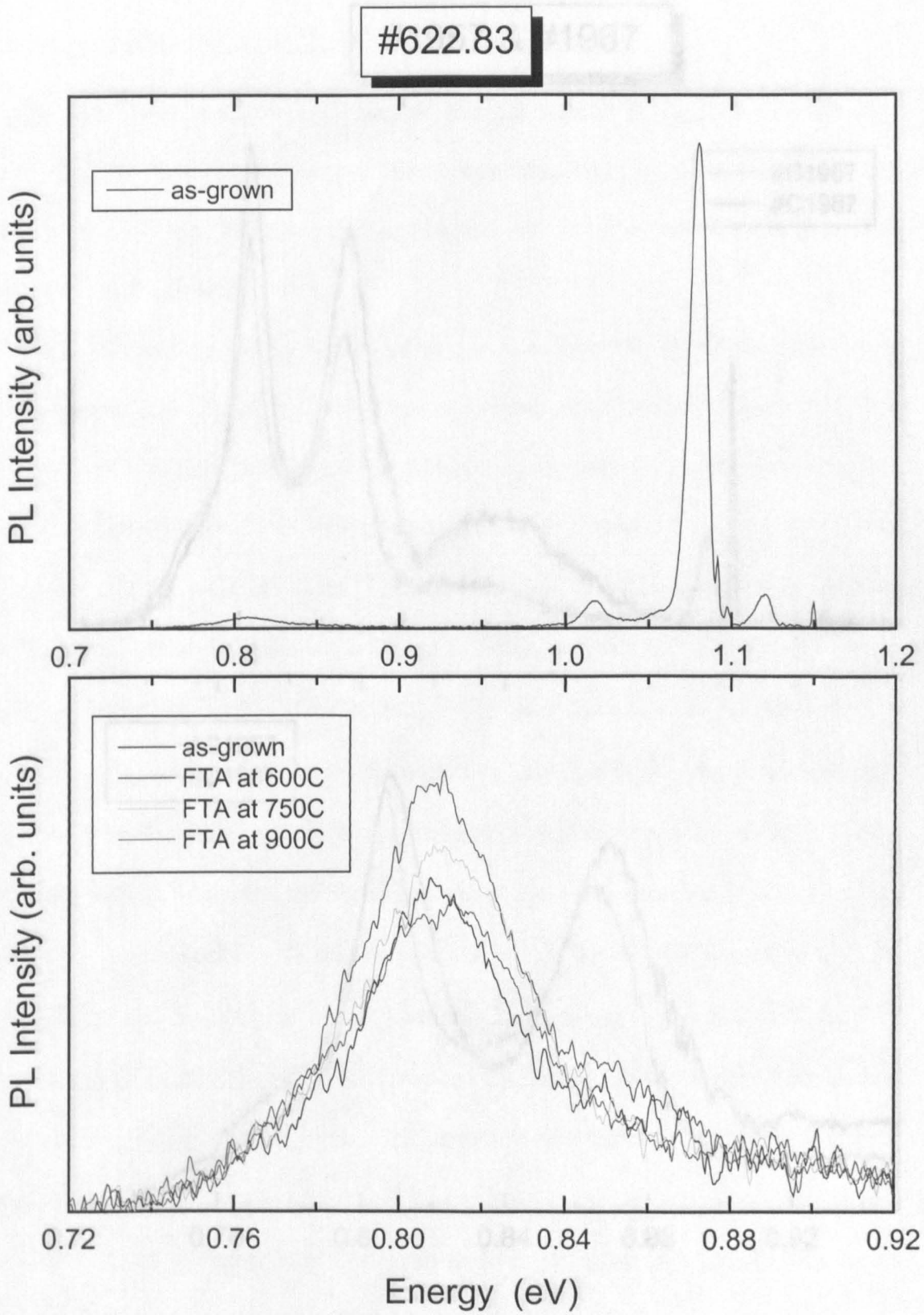

Figure 5.8 PL spectra measured at 5.5K from as-grown and after FTA at 600C, 750C and 900C for 30min samples #622.83.

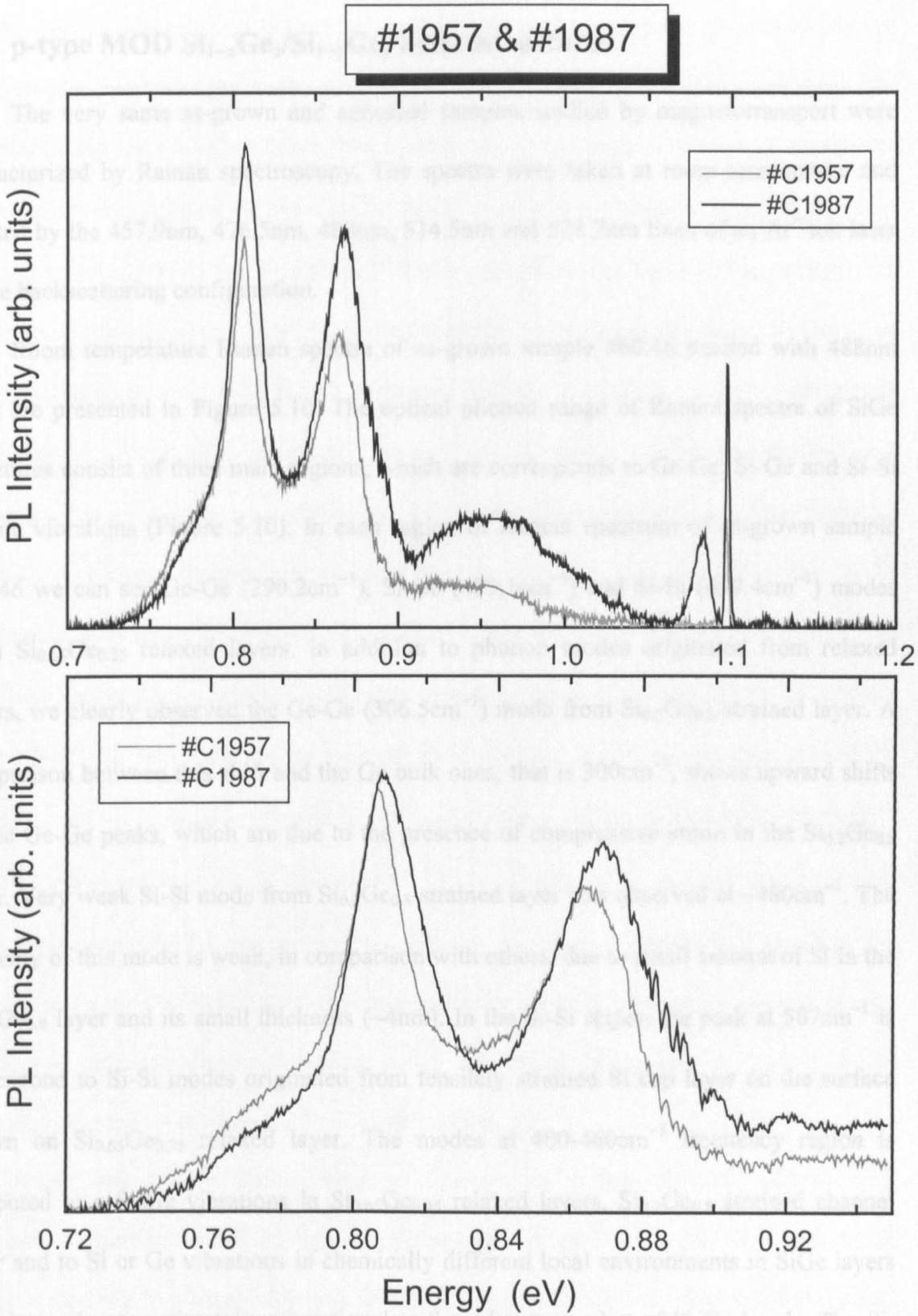

Figure 5.9 PL spectra measured at 5.5K from samples #1957 and #1987.

5.5 Raman spectroscopy analysis of p-type MOD $Si_{1-x}Ge_x/Si_{1-y}Ge_y$ heterostructures

The very same as-grown and annealed samples studied by magnetotransport were characterized by Raman spectroscopy. The spectra were taken at room temperature and excited by the 457.9nm, 476.5nm, 488nm, 514.5nm and 528.7nm lines of an Ar^+ ion laser in the backscattering configuration.

Room temperature Raman spectra of as-grown sample #60.46 excited with 488nm light are presented in Figure 5.10. The optical phonon range of Raman spectra of SiGe structures consist of three main regions, which are corresponds to Ge-Ge, Si-Ge and Si-Si atomic vibrations (Figure 5.10). In each region of Raman spectrum of as-grown sample #60.46 we can see Ge-Ge (290.2cm^{-1}), Si-Ge (409.1cm^{-1}) and Si-Si (499.4cm^{-1}) modes from $Si_{0.65}Ge_{0.35}$ relaxed layers. In addition to phonon modes originated from relaxed layers, we clearly observed the Ge-Ge (306.5cm^{-1}) mode from $Si_{0.2}Ge_{0.8}$ strained layer. A comparison between this shift and the Ge bulk ones, that is 300cm^{-1}, shows upward shifts of the Ge-Ge peaks, which are due to the presence of compressive strain in the $Si_{0.2}Ge_{0.8}$ layer. Very weak Si-Si mode from $Si_{0.2}Ge_{0.8}$ strained layer was observed at ~480cm^{-1}. The intensity of this mode is weak, in comparison with others, due to small amount of Si in the $Si_{0.2}Ge_{0.8}$ layer and its small thickness (~4nm). In the Si-Si region the peak at 507cm^{-1} is correspond to Si-Si modes originated from tensilely strained Si cap layer on the surface grown on $Si_{0.65}Ge_{0.35}$ relaxed layer. The modes at 400-460cm^{-1} frequency region is attributed to a Si-Ge vibrations in $Si_{0.65}Ge_{0.35}$ relaxed layers, $Si_{0.2}Ge_{0.8}$ strained channel layer and to Si or Ge vibrations in chemically different local environments in SiGe layers with intensity approximately proportional to the relative number of Si-Ge bonds. The Si-Ge phonon modes seem to have properties that are coming partly from the Ge and Si atoms. Another spectrum in Figure 5.10 ($Si_{0.65}Ge_{0.35}$ virtual substrate only) corresponds to the spectrum of as-grown sample #60.46 without first ~250nm from the surface removed

by wet chemical etching and consists of linearly graded $Si_{0.65}Ge_{0.35}$ VS grown by LP-CVD and $Si_{0.65}Ge_{0.35}$ buffer layers grown by SS-MBE. It was done with the purpose to remove from Raman spectrum the peaks originated from $Si_{0.2}Ge_{0.8}$ strained channel layer and strained Si cap layer on the surface. It is clear to see from Figure 5.10 that the spectra are different by the absence of the Ge-Ge mode at 306.5cm^{-1} originated from $Si_{0.2}Ge_{0.8}$ strained layer and Si-Si mode at 507cm^{-1} from strained Si cap layer on the surface. The value of Ge composition in the $Si_{1-y}Ge_y$ relaxed layers extracted from the ratio of intensities of Si-Si and Ge-Ge modes originated from these layers [6], [7], [8] corresponds to 0.33±0.02. After FTA significant changes in all regions of Raman spectra were observed. Raman spectra of as-grown and after FTA at 700C and 750C for 30min samples #60.46 excited with 488nm light are presented in Figure 5.11. In the Si-Si region the position of Si-Si mode from $Si_{0.65}Ge_{0.35}$ relaxed layers shifted downward to 499.0cm^{-1}. In the Si-Ge region the position of Si-Ge mode from $Si_{0.65}Ge_{0.35}$ relaxed layers shifted upward to 413.0cm^{-1}. In the Ge-Ge region were observed the most significant changes. After FTA at 700C the Ge-Ge mode originated from $Si_{0.2}Ge_{0.8}$ layer shifted downward to 301.3cm^{-1}. Further downward shift of Ge-Ge mode to 297.9cm^{-1} after FTA at 750C was observed. With increasing of FTA temperature we can see increases of intensity mode from the channel and their downward shift, that demonstrating the sensitivity of the phonon spectra to Ge out diffusion during annealing which results in decreasing Ge content in the $Si_{0.2}Ge_{0.8}$ strained layer or(and) its partial relaxation.

Room temperature Raman spectra of as-grown sample #622.83 excited with 457.9nm, 488nm and 514.5nm light are presented in Figure 5.12. The light penetration depth in the bulk Si strongly depends from the wavelength, and increases from 280nm (at 457.9nm), up to 490nm (at 488nm) and 680nm (at 514.5nm). In the bulk Ge the penetration depth almost does not depend from the used wavelength and at 457.9, 488 and 514.5nm is close to 16nm. Consequently, the penetration depth of the light at given

wavelength have to reduce with increasing the Ge composition in the alloys. Also it is necessary to take into account that the investigated structures consist of several SiGe layers of various Ge compositions and state of strain, which could take effect on propagation of the light. Using 457.9, 488 and 514.5nm wavelength information from various depths in the as-grown sample #622.83 was obtained (Figure 5.12). In the Raman spectrum excited with 457.9nm wavelength the intensity of Ge-Ge mode originated from the $Si_{0.2}Ge_{0.8}$ strained channel became just observable and much weaker than Ge-Ge mode from $Si_{0.7}Ge_{0.3}$ relaxed layers. At 488nm the intensities of Ge-Ge modes from $Si_{0.2}Ge_{0.8}$ strained channel and $Si_{0.7}Ge_{0.3}$ relaxed layers became comparable and increasing the wavelength up to 514.5nm results in pronounced increase of $Si_{0.2}Ge_{0.8}$ strained channel Ge-Ge mode. The positions of Ge-Ge modes from $Si_{0.7}Ge_{0.3}$ relaxed layers and $Si_{0.2}Ge_{0.8}$ strained layers were observed at 289.7cm^{-1} and 305.9cm^{-1} respectively. The Si-Ge and Si-Si modes from the $Si_{0.7}Ge_{0.3}$ relaxed layers are increase with increasing wavelength. Just in the Raman spectrum excited with 514.5nm wavelength we clearly observed peak at 521cm^{-1} corresponding to Si-Si mode originated from Si bulk layer. Therefore the light with 514.5nm wavelength penetrates through full structure to Si layer and Raman spectra contains information about all SiGe layers. The positions of Si-Ge and Si-Si modes originated from $Si_{0.7}Ge_{0.3}$ relaxed layers were observed at 410.3cm^{-1} and 500.2cm^{-1} respectively. The value of Ge composition in the $Si_{1-y}Ge_y$ relaxed layers extracted from the ratio of intensities of Si-Si and Ge-Ge modes originated from these layers corresponds to 0.32±0.02. After FTA significant changes in all regions of Raman spectra were observed. Raman spectra of as-grown and after FTA at 600C, 700C, 750C, 800C and 900C for 30min samples #622.83 excited with 514.5nm light are presented in Figure 5.13. In Raman spectra of as-grown and after FTA samples we see that the original Si-Si mode originated from $Si_{0.7}Ge_{0.3}$ relaxed layers decreases with increasing annealing temperature and almost not shifted after FTA. In Si-Ge region we see the pronounced rise of the Si-Ge modes from

$Si_{0.7}Ge_{0.3}$ relaxed layers and an increase of additional ones at 431cm^{-1}, 455cm^{-1}. The intensities of the various modes could change, as long as the intermixing of Si and Ge atoms can occur during FTA. In the Ge-Ge region were observed the most significant changes (Figure 5.14). With increasing of FTA temperature we can see increases of intensity of Ge-Ge mode originated from the $Si_{0.2}Ge_{0.8}$ strained layer and their downward shift. The Ge-Ge mode originated from $Si_{0.7}Ge_{0.3}$ relaxed layers is almost not shifted after FTA. The peak at 521cm^{-1} corresponding to Si-Si mode from Si bulk layer remained unchangeable after FTA.

Room temperature Raman spectra of as-grown and after RTA at 750C for 30sec samples #C2072 excited with 514.5nm light are presented in Figure 5.15. In each region of Raman spectrum of as-grown sample #C2072 we can see Ge-Ge (291.4cm^{-1}), Si-Ge (410.0cm^{-1}) and Si-Si (491.9cm^{-1}) modes from $Si_{0.47}Ge_{0.53}$ relaxed layers. In addition to phonon modes originated from relaxed layers, we clearly observed the Ge-Ge (302.0cm^{-1}) mode from $Si_{0.18}Ge_{0.82}$ strained layer. The peak at 504.3cm^{-1} corresponds to Si-Si mode originated from strained Si cap layer on the surface. The value of Ge composition in the $Si_{1-y}Ge_y$ relaxed layers extracted from the ratio of intensities of Si-Si and Ge-Ge modes originated from these layers corresponds to 0.49±0.02. After RTA at 750C for 30sec significant changes in all regions of Raman spectra were observed (Figure 5.15). The downward shift of Ge-Ge (291.0cm^{-1}), Si-Ge (409.3cm^{-1}) and Si-Si (490.4cm^{-1}) modes from $Si_{0.47}Ge_{0.53}$ relaxed layers were observed. The Ge-Ge mode originated from $Si_{0.18}Ge_{0.82}$ strained layer downward shifted to 300.8cm^{-1}. The increase of intensity of Ge-Ge mode from the channel and their downward shift is due to the Ge out diffusion during annealing which results in decreasing Ge content in the $Si_{0.18}Ge_{0.82}$ strained layer or(and) its partial relaxation.

The results of Raman spectroscopy analysis of p-type MOD $Si_{1-x}Ge_x/Si_{1-y}Ge_y$ heterostructures were presented at "Condensed Matter and Materials Physics '99

Conference"[1], "10th European Heterostructure Technology Workshop"[2] and "SiGe (C) 2001 Workshop"[5].

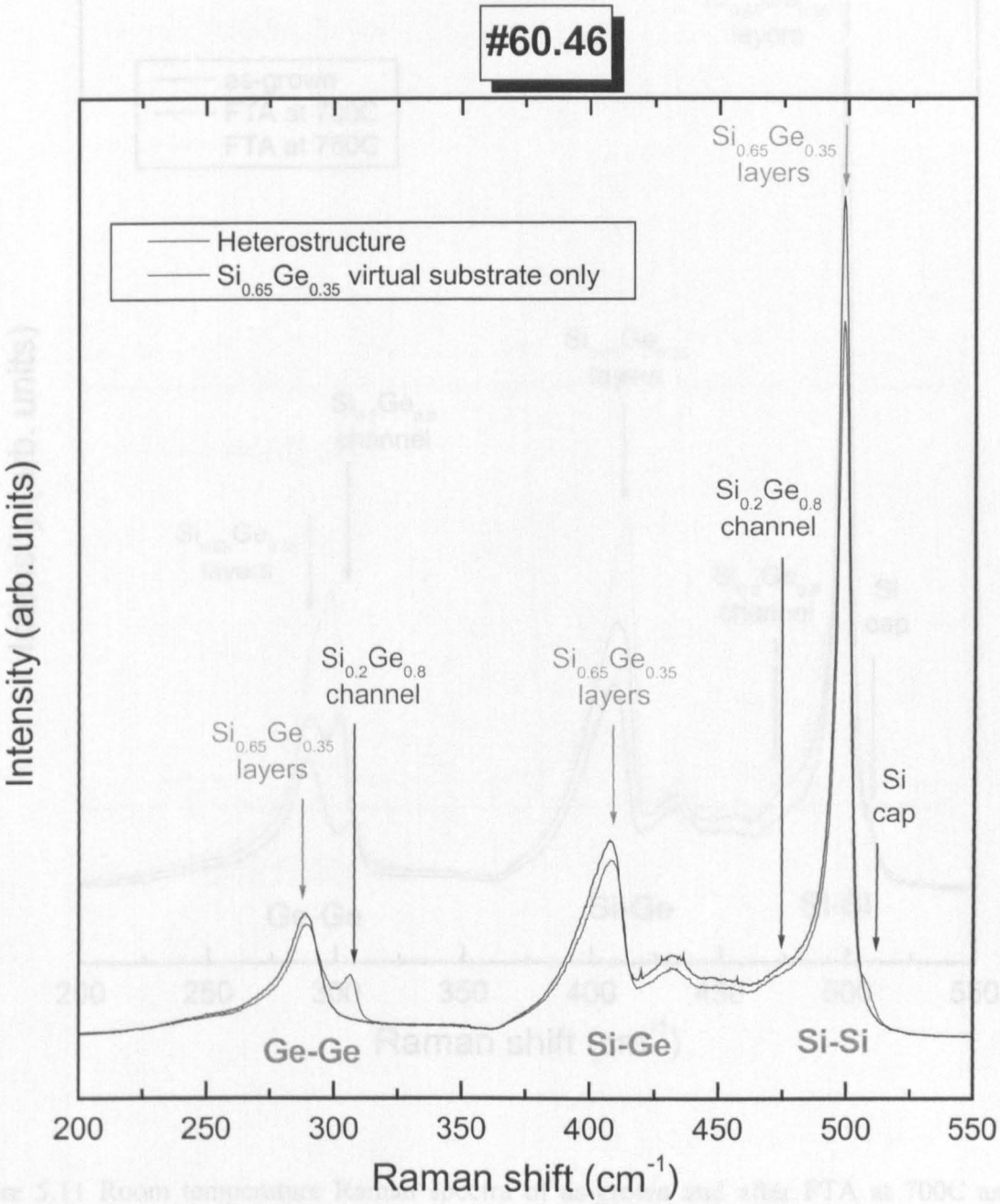

Figure 5.10 Room temperature Raman spectra of as-grown sample #60.46 excited with 488nm light.

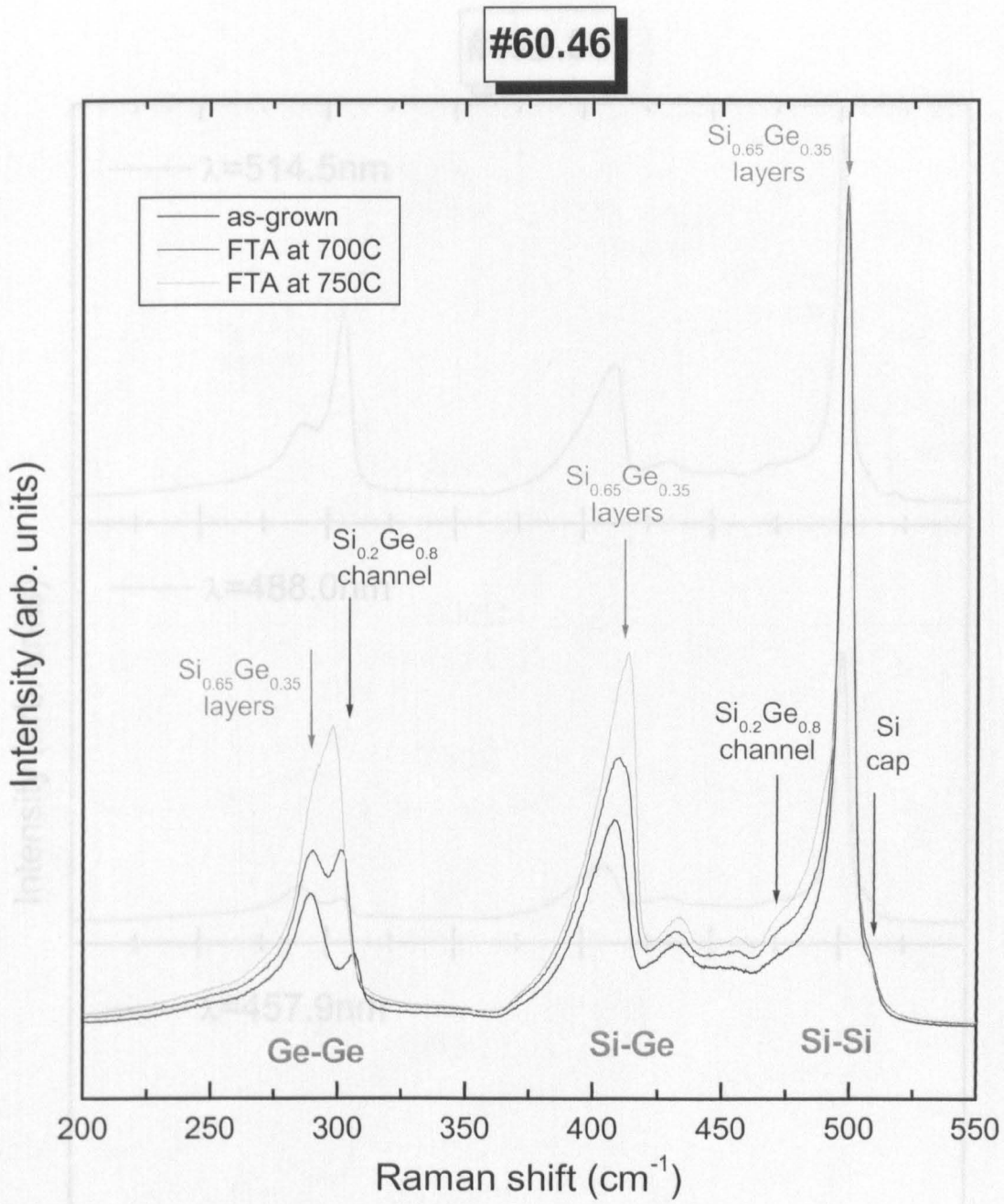

Figure 5.11 Room temperature Raman spectra of as-grown and after FTA at 700C and 750C for 30min samples #60.46 excited with 488nm light.

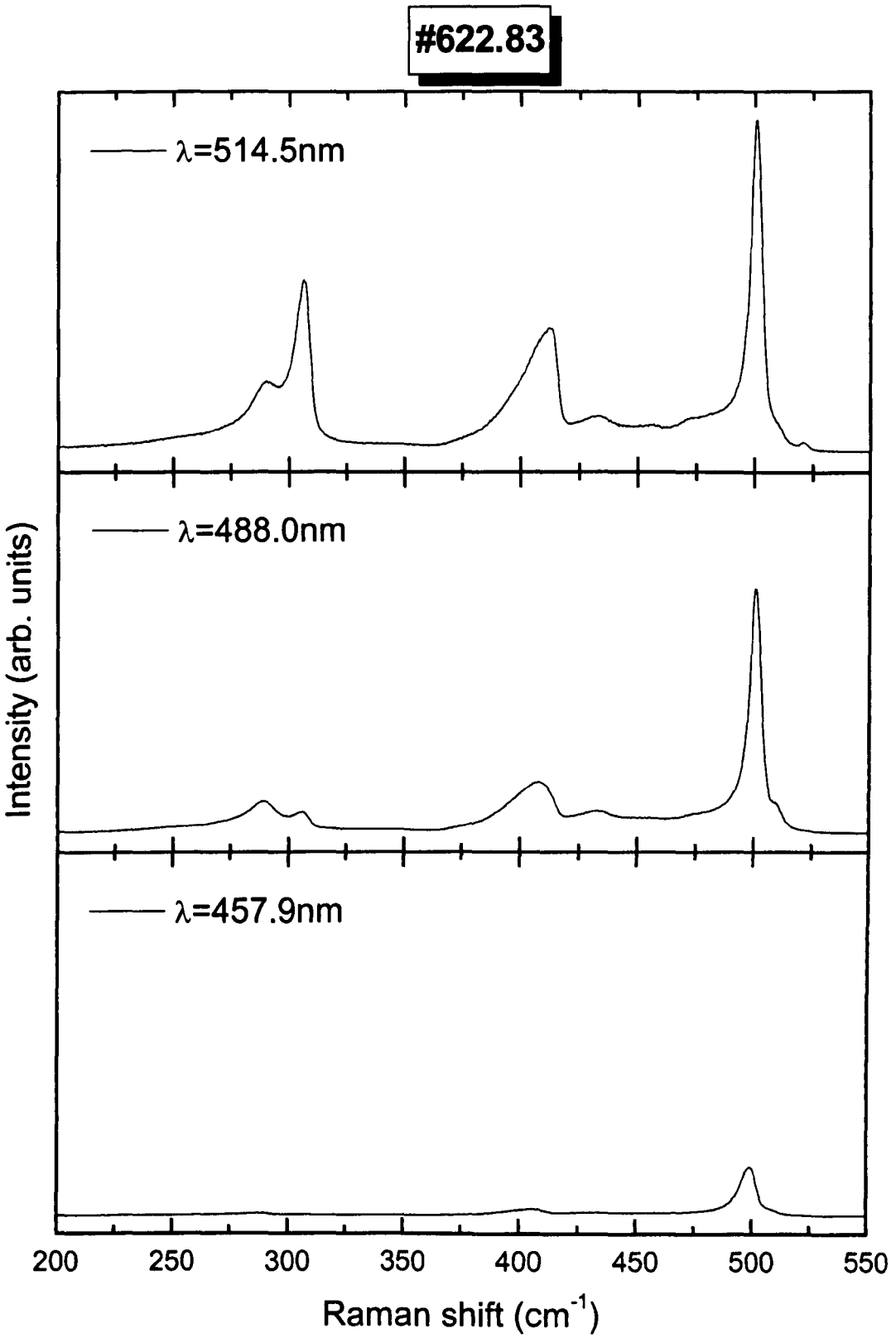

Figure 5.12 Room temperature Raman spectra of as-grown sample #622.83 excited with 457.9nm, 488nm and 514.5nm light.

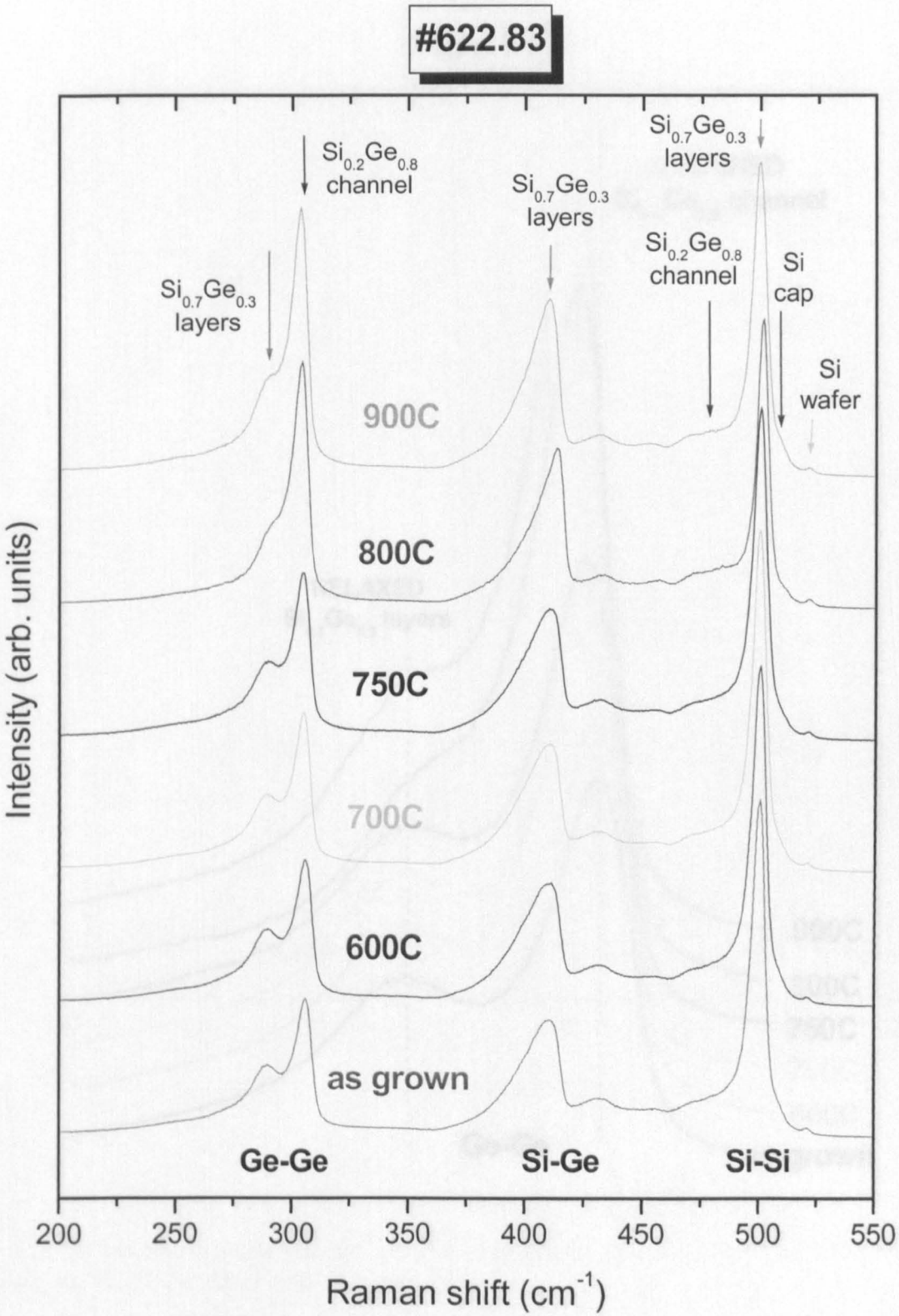

Figure 5.13 Room temperature Raman spectra of as-grown and after FTA at 600C, 700C, 750C, 800C and 900C for 30min samples #622.83 excited with 514.5nm light.

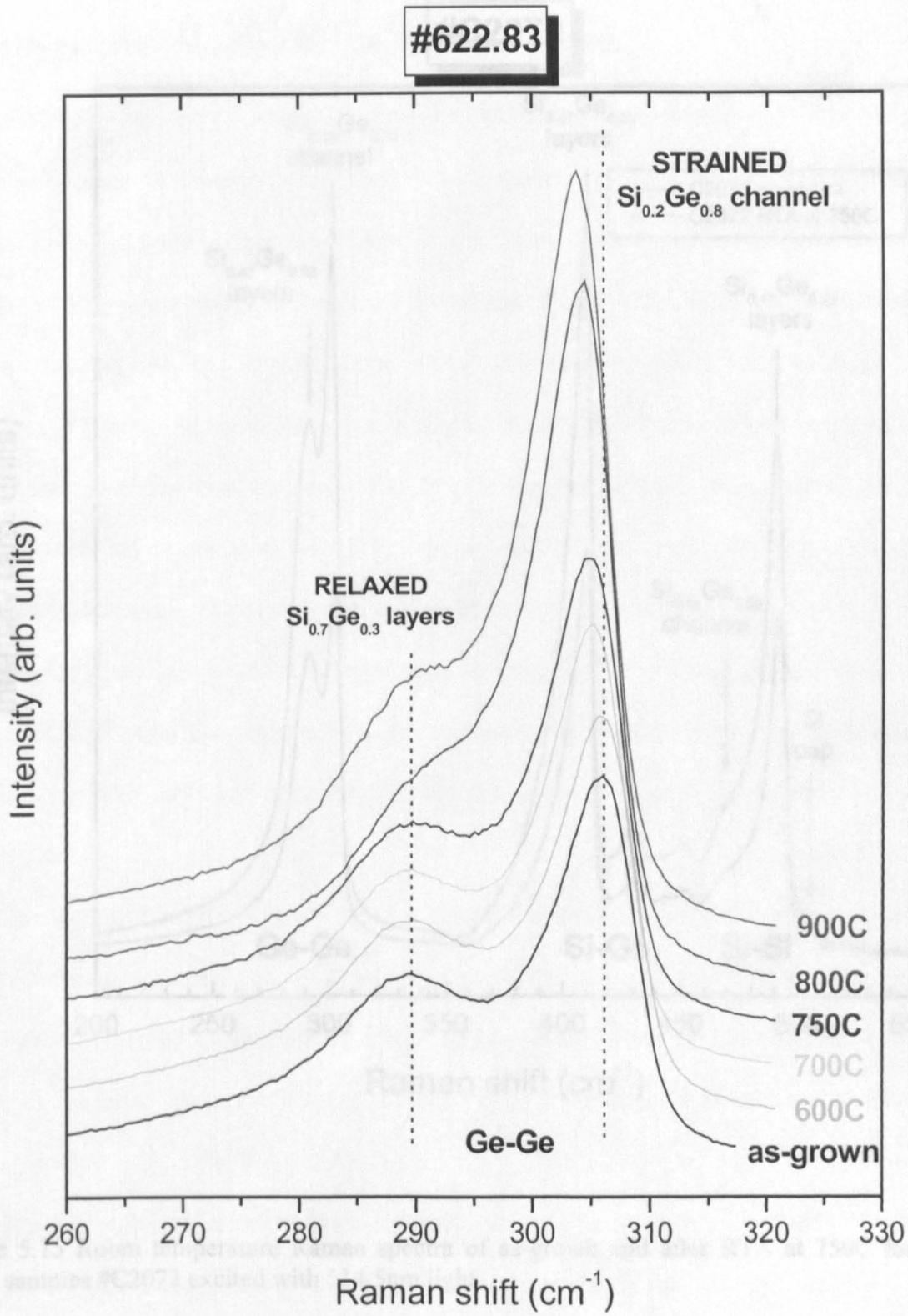

Figure 5.14 FTA effect on position and intensity of Ge-Ge modes in room temperature Raman spectra of sample #622.83 excited with 514.5nm light.

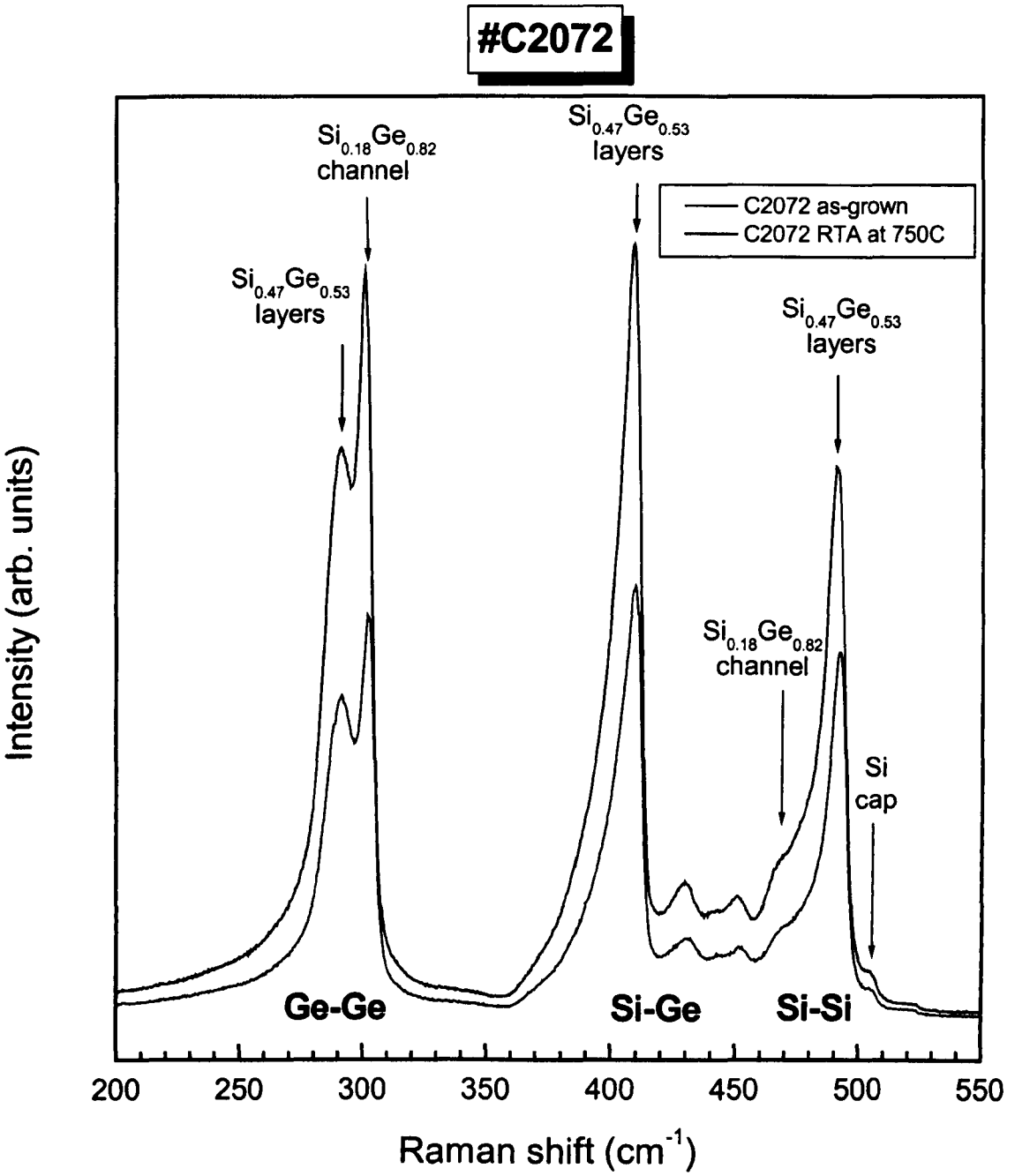

Figure 5.15 Room temperature Raman spectra of as-grown and after RTA at 750C for 30sec samples #C2072 excited with 514.5nm light.

5.6 Scanning white-light interferometry analysis of p-type MOD $Si_{1-x}Ge_x/Si_{1-y}Ge_y$ heterostructures

Scanning white-light interferometry used to analysis surface profiles of p-type MOD $Si_{1-x}Ge_x/Si_{1-y}Ge_y$ heterostructures. The data acquired by Zygo New View 5000 interferometer were analysed by Metro Pro 7.2.2 software. The samples were characterized in terms of surface roughness parameters: PV, and rms. PV (Peak-to-Valley) is the distance between the highest and lowest points within the sample. When used to quantify roughness, PV is the maximum roughness height. Root-Mean-Square or rms is the root-mean-square deviation from the center line. This is a method of calculating an average by squaring each value and then taking the square root of the mean. The rms result is calculated as the standard deviation of the height (or depth) of the test surface relative to the reference at all data points in the data set. The rms result is an area weighted statistic; when used for optical components, it more accurately depicts the optical performance of the surface being measured than the PV statistic because it uses all the data in the calculation.

The surface profile is strongly depends from the growth conditions. The investigated heterostructures are possible to divide into the groups depending on used type of VS due to their dominated effect on the quality of the surface. For all samples the used VS were grown by SS-MBE exclusive linearly graded VS used in samples #60.45 and #60.46, which were grown by LP-CVD.

The active layers of MOD heterostructure in samples #51.33, #52.16 and #54.08 were grown on $Si_{0.7}Ge_{0.3}$ step graded VS. The characteristic feature for this samples are crosshatches on the surface due to step graded VS (Figure 5.16). The measured PV for samples #51.33, #52.16 and #54.08 are 7.6nm, 5.8nm and 6.4nm respectively. The measured rms for samples #51.33, #52.16 and #54.08 are 1.0nm, 0.8nm and 0.9nm

respectively. It is clear to see that these values are the same order of magnitude and varied mostly due to the growth conditions of $Si_{0.7}Ge_{0.3}$ step graded VS.

The $Si_{0.65}Ge_{0.35}$ linearly graded VS used in the samples #6045 and #6046 were grown by LPCVD. The characteristic feature for this samples are crosshatches on the surface due to linearly graded VS (Figure 5.17). The measured PV and rms for these samples are 42-124nm and 5-15nm respectively.

In the samples #622.54, #622.55 and #622.56 the $Si_{0.2}Ge_{0.8}$ channel of thickness varied from 2 to 8nm was grown directly on Si(001) substrate without intermediate VS. No crosshatches were observed in these samples (Figure 5.18). The measured PV and rms for these samples are less than 2nm and 0.5nm respectively.

The active layers of MOD heterostructure in samples #622.83 and #622.84 were grown on $Si_{0.7}Ge_{0.3}$ VS with low temperature Si buffer. No crosshatches were observed in these samples (Figure 5.19). The measured PV for samples #622.83 and #622.84 are 4.5nm and 5.5nm respectively. The measured rms for samples #622.83 and #622.84 are 0.5nm and 0.7nm respectively.

Thick (>3μm) $Si_{1-y}Ge_y$ ($0.35 \leq y \leq 0.63$) linearly graded VS used in the samples #C1957, #C1987, #C2015f, #C2072, #C2475 and #C2476 were grown by SS-MBE. The characteristic feature for this samples are crosshatches on the surface due to linearly graded VS (Figure 5.20, Figure 5.21). The measured PV and rms for these samples are 20-30nm and 3-5nm respectively

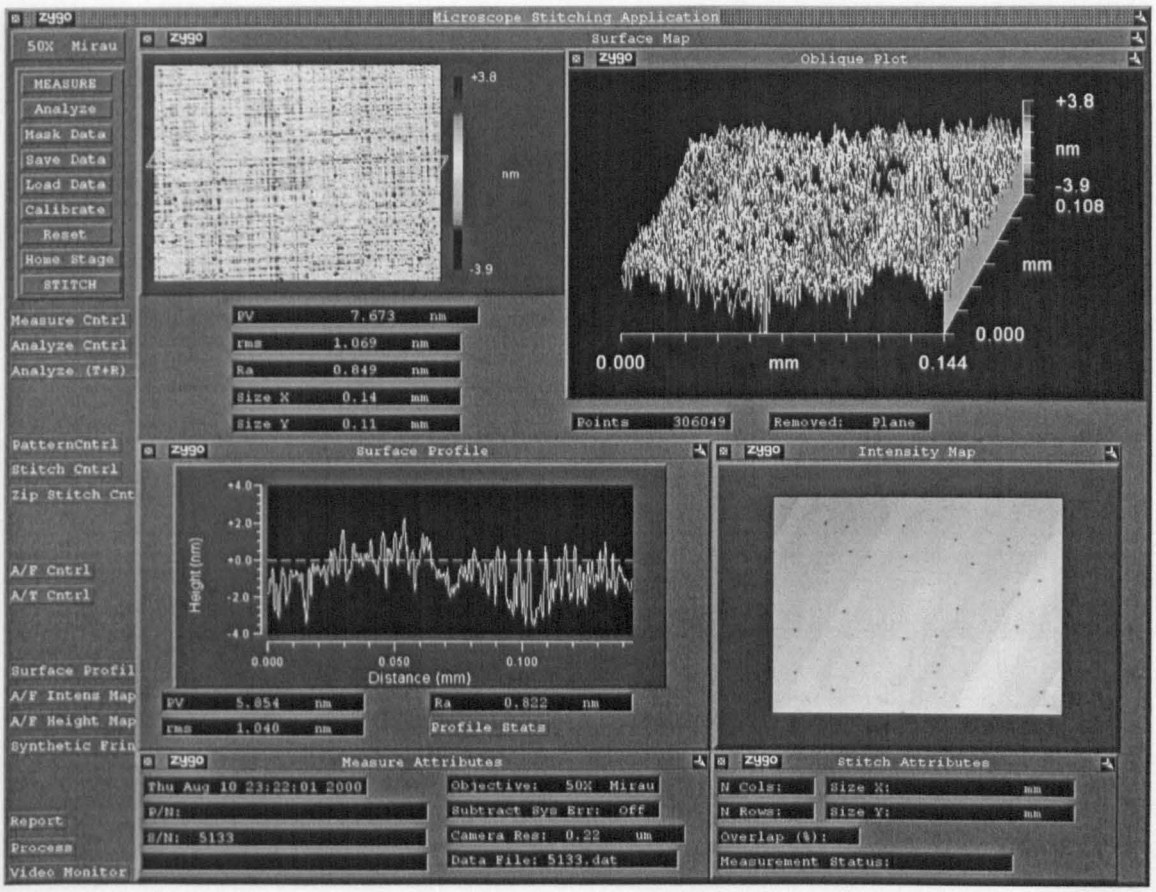

Figure 5.16 Scanning white-light interferometry surface profiles of sample #51.33 analysed by Metro Pro software.

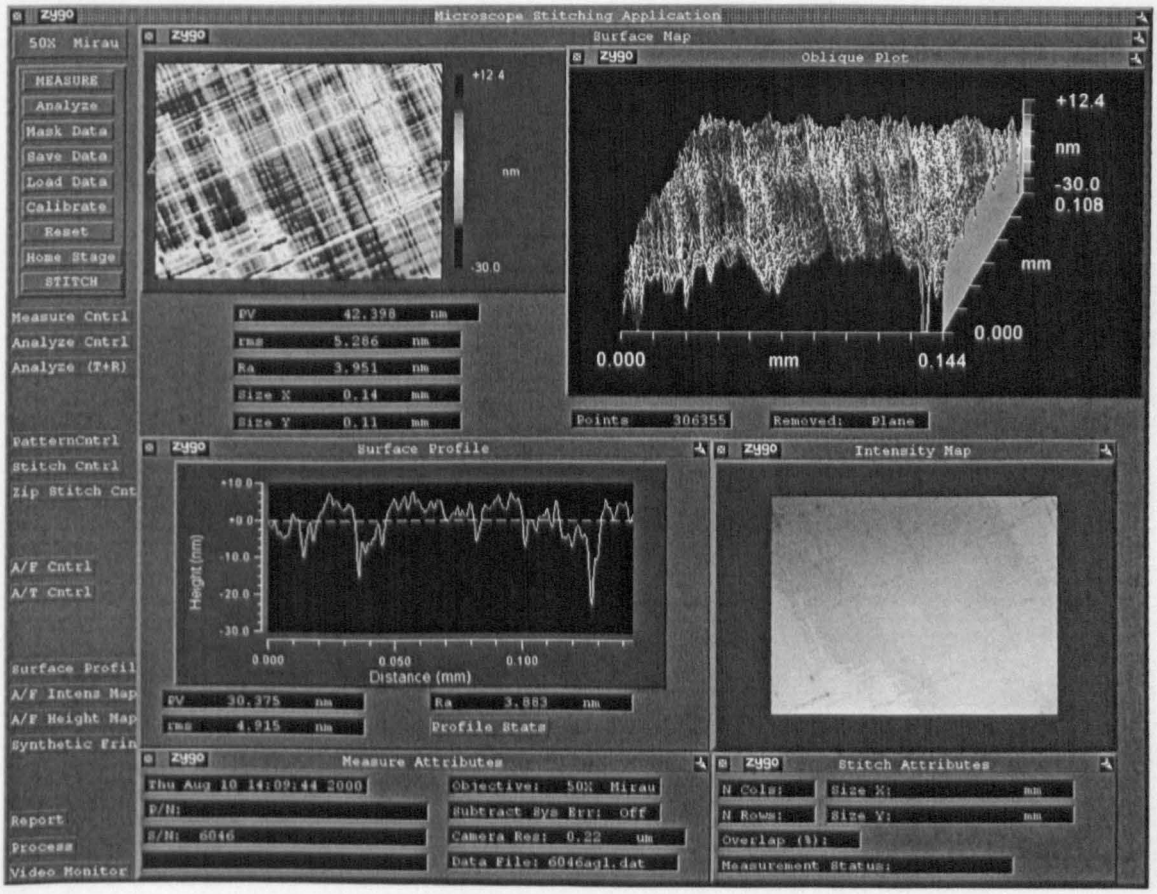

Figure 5.17 Scanning white-light interferometry surface profiles of sample #60.46 analysed by Metro Pro software.

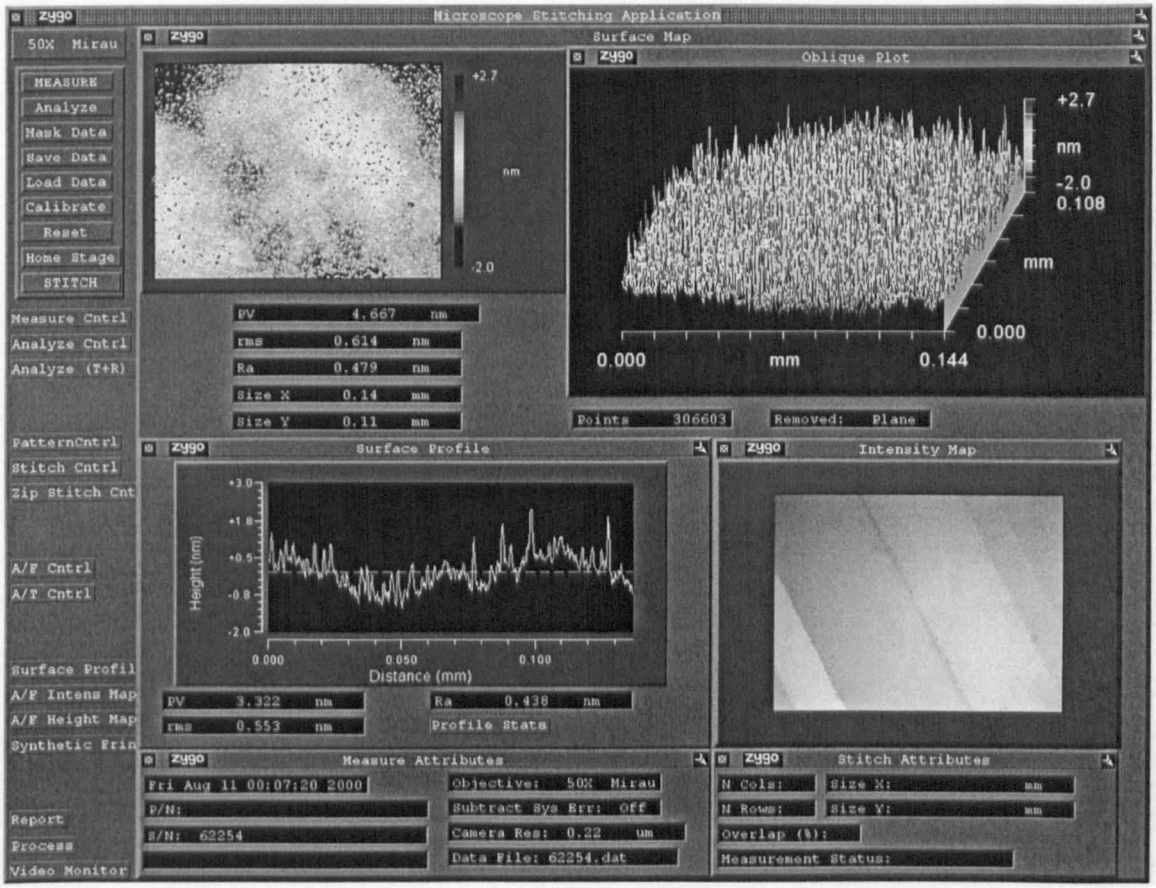

Figure 5.18 Scanning white-light interferometry surface profiles of sample #622.54 analysed by Metro Pro software.

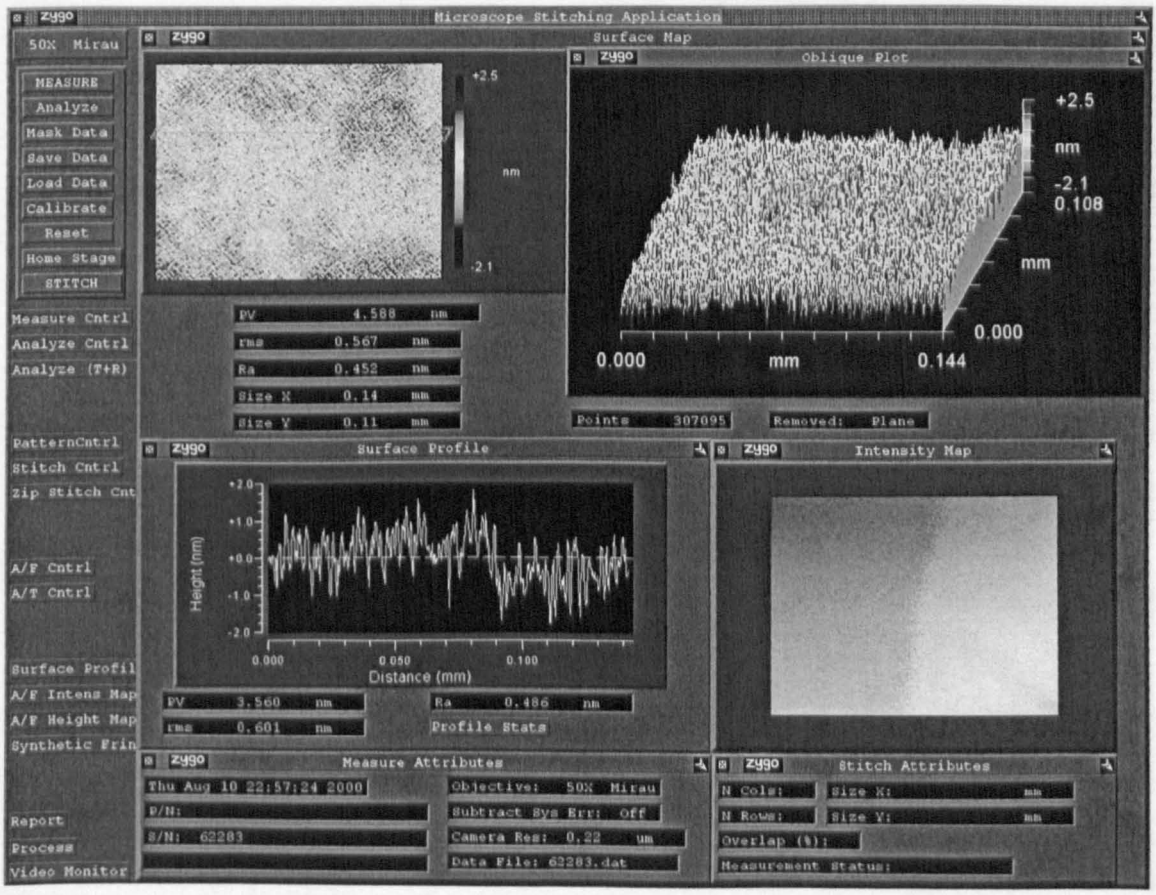

Figure 5.19 Scanning white-light interferometry surface profiles of sample #622.83 analysed by Metro Pro software.

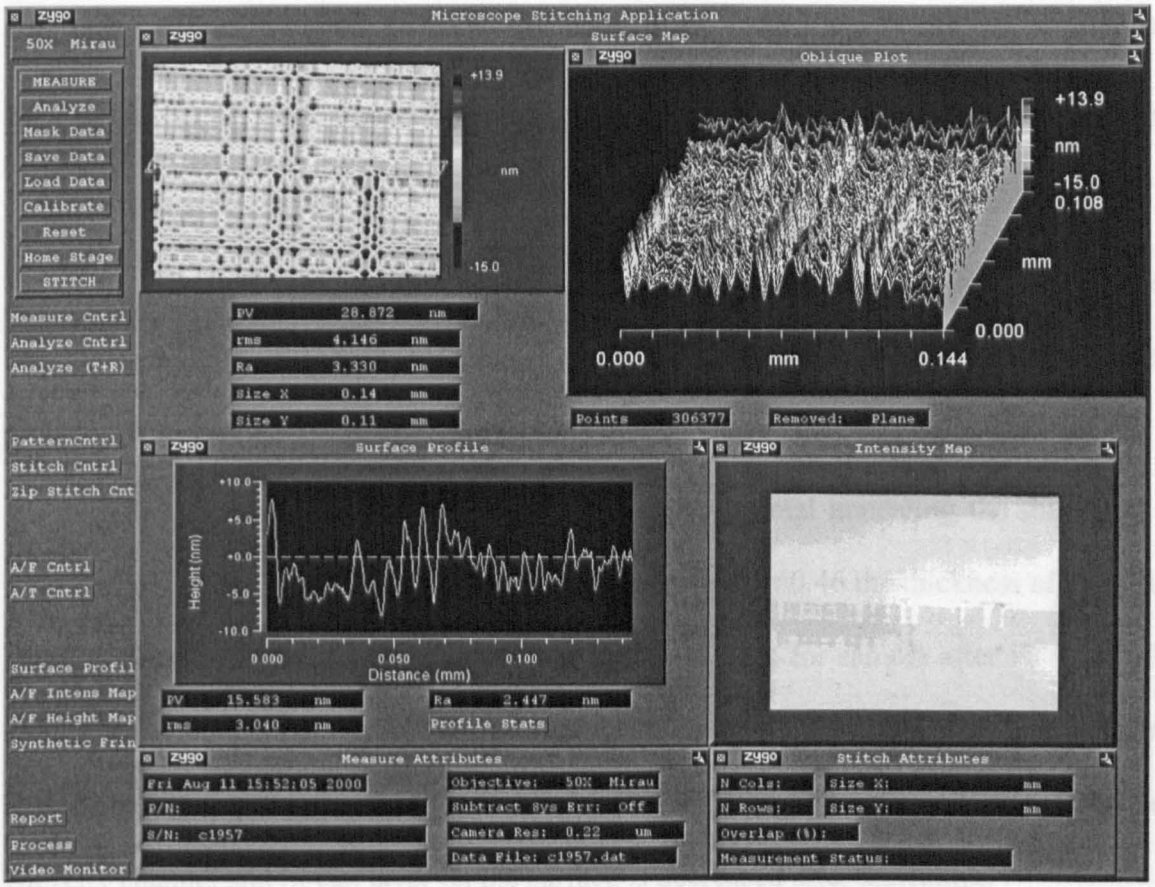

Figure 5.20 Scanning white-light interferometry surface profiles of sample #C1957 analysed by Metro Pro software.

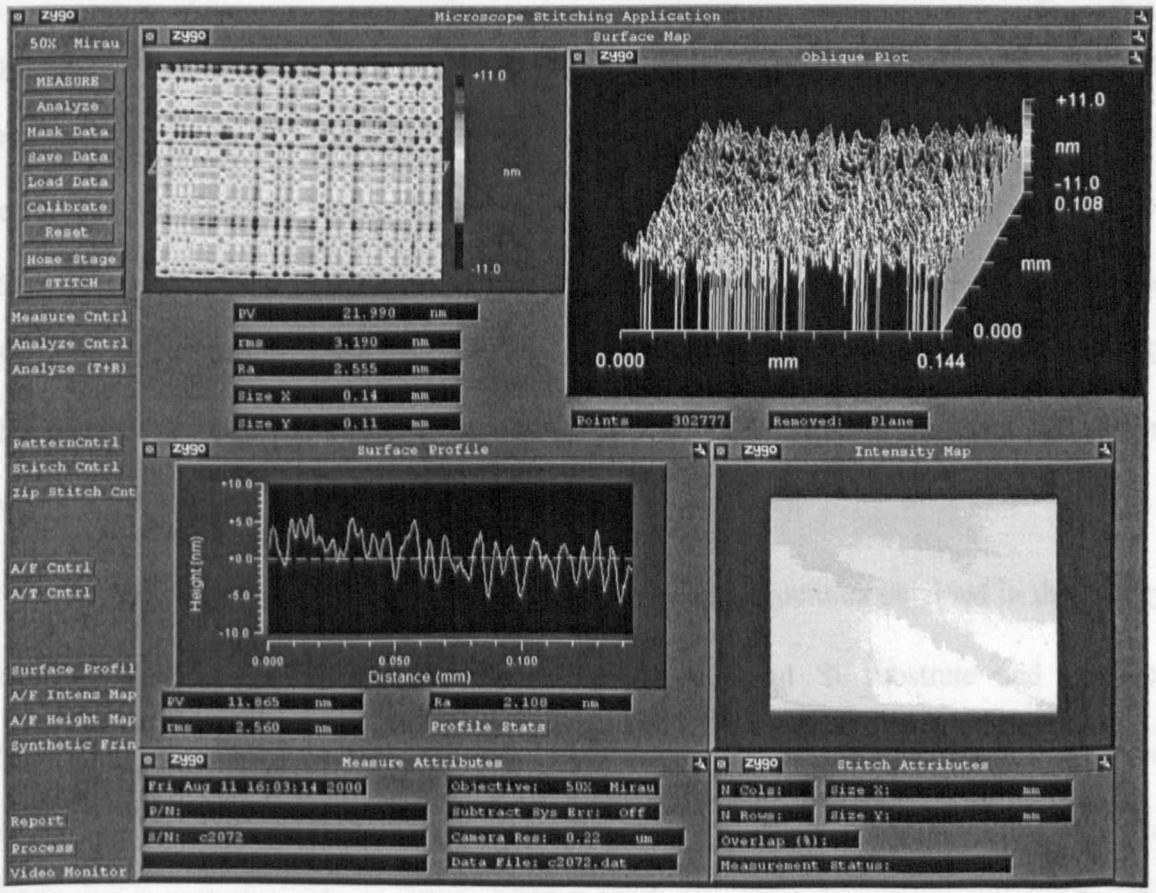

Figure 5.21 Scanning white-light interferometry surface profiles of sample #C2072 analysed by Metro Pro software.

5.7 The effect of post growth furnace and rapid thermal annealing on structural and optical properties of p-type MOD $Si_{1-x}Ge_x/Si_{1-y}Ge_y$ heterostructures

The effect of post growth furnace and rapid thermal annealing on structural and optical properties of p-type MOD $Si_{1-x}Ge_x/Si_{1-y}Ge_y$ heterostructures was studied by XTEM, ULE-SIMS, PL spectroscopy and micro-Raman spectroscopy.

XTEM analysis showed that after post growth thermal annealing the thickness of high Ge content $Si_{1-x}Ge_x$ channel is increased. For sample #60.46 the thickness of $Si_{0.2}Ge_{0.8}$ channel increased from 4.2nm for as-grown one up to 7nm for sample after FTA at 750C for 30min (Figure 5.2). The increasing of $Si_{1-x}Ge_x$ channel is accompanied with smearing of bottom and top $Si_{1-x}Ge_x/Si_{1-y}Ge_y$ interfaces (Figure 5.2). The average distance between $Si_{1-x}Ge_x$ channel and Si cap layer on the surface is decreased after annealing.

The analysis of ULE-SIMS profiles of Ge, Si and B showed that during the post growth thermal annealing the Ge and B diffusion is occurred. The Ge diffusion from the region with high Ge concentration ($Si_{1-x}Ge_x$ channel) to the region with low Ge concentration ($Si_{1-y}Ge_y$ layers) and B diffusion from doped $Si_{1-y}Ge_y$ layers to the undoped $Si_{1-y}Ge_y$ spacer layers were observed after annealing. For sample #60.46 the broadening of $Si_{0.2}Ge_{0.8}$ channel from 4.9nm for as-grown sample to 9.3nm for sample after FTA at 750C for 30min was observed (Figure 5.4). The broadening of $Si_{1-x}Ge_x$ channel is accompanied with decreasing of Ge composition in the channel (Figure 5.4).

PL spectra of p-type MOD $Si_{1-x}Ge_x/Si_{1-y}Ge_y$ heterostructures obtained in the energy range 0.7-1.2eV at 5.5K contain information only about Si substrate and $Si_{1-y}Ge_y$ (0.3–0.63) relaxed layers. The peak at 1.080eV originated from Si substrate was observed in PL spectra of all investigated samples. No changes of its position were observed even after post growth thermal annealing at 900C 30min. Small changes in positions of peaks

originated from $Si_{1-y}Ge_y$ relaxed layers were observed after annealing up to 900C (Figure 5.8).

After post growth thermal annealing significant changes in all regions of room temperature Raman spectra of p-type MOD $Si_{1-x}Ge_x/Si_{1-y}Ge_y$ heterostructures were observed (Figure 5.13). The intensities of the various modes change, as long as the intermixing of Si and Ge atoms occur during annealing. The most significant changes were observed in the Ge-Ge region (Figure 5.14). With increasing of annealing temperature the increase of intensity of Ge-Ge mode originated from the $Si_{1-x}Ge_x$ strained channel layers and their downward shift is observed. This is demonstrate the sensitivity of the Raman spectra to Ge out diffusion during annealing which results in decreasing Ge content in the $Si_{1-x}Ge_x$ strained channel or (and) its partial relaxation. The Ge-Ge mode originated from $Si_{1-y}Ge_y$ relaxed layers is almost not shifted after annealing. The peak at $521cm^{-1}$ corresponding to Si-Si mode originated from Si substrate remains unchangeable after annealing.

5.8 The effect of Ge composition in the $Si_{1-x}Ge_x$ channel and $Si_{1-y}Ge_y$ layers on structural and optical properties of p-type MOD $Si_{1-x}Ge_x/Si_{1-y}Ge_y$ heterostructures

The effect of Ge composition in the $Si_{1-x}Ge_x$ channel and $Si_{1-y}Ge_y$ layers on structural and optical properties of p-type MOD $Si_{1-x}Ge_x/Si_{1-y}Ge_y$ heterostructures was studied by XTEM, ULE-SIMS, PL spectroscopy, micro-Raman spectroscopy and scanning white-light interferometry.

XTEM was performed on as-grown and annealed samples to determine the structural integrity of the layers and also to determine the dislocations microstructure in relaxed VS. In particular, the thicknesses of high Ge content $Si_{1-x}Ge_x$ channel layer, the distance

between its top interface, Si cap layer on the surface and the thickness of the later were obtained (Figure 5.1). Also short-range roughness of $Si_{1-x}Ge_x$ channel layer interfaces caused by not optimum growth conditions was studied. The thicknesses of VS were obtained as well (Figure 5.1). The characteristic feature of $Si_{1-y}Ge_y$ linearly and step graded VS is massive dislocations network in the linearly or step graded part of VS (Figure 5.1). The relatively thin VS (850nm) used in samples #622.83 and #622.84 consists of $Si_{0.7}Ge_{0.3}$ layer grown on low-temperature Si buffer. Such type of VS does not contain massive dislocations network (Figure 5.3). Long-range roughness of samples surface cased by various types of VS was studied as well.

ULE-SIMS was performed on as-grown and annealed samples to determine Ge, Si and B profiles. In particular, the thicknesses of high Ge content $Si_{1-x}Ge_x$ channel layer, the distance between its top interface, Si cap layer on the surface and the thickness of the later were obtained from Ge and Si profiles. The Ge profile in the $Si_{1-x}Ge_x$ channel layer is bell-like (Figure 5.4). The level of B doping in active layers of MOD heterostructures was obtained from B profile.

PL spectra of p-type MOD $Si_{1-x}Ge_x/Si_{1-y}Ge_y$ heterostructures obtained in the energy range 0.7-1.2eV at 5.5K contain information only about Si substrate and $Si_{1-y}Ge_y$ (0.3-0.63) relaxed layers. The peak at 1.080eV originated from Si substrate was observed in PL spectra of all investigated samples (Figure 5.8). In the energy range 0.75-1eV the peaks originated from $Si_{1-y}Ge_y$ relaxed layers were observed (Figure 5.9).

Raman spectroscopy measurements were performed on as-grown and annealed samples to obtain information about state of strain in $Si_{1-x}Ge_x$, $Si_{1-y}Ge_y$ and Si layers. The Ge composition in $Si_{1-y}Ge_y$ relaxed layers was obtained as well. The optical phonon range of Raman spectra of SiGe structures consist of three main regions, which are corresponds to Ge-Ge, Si-Ge and Si-Si atomic vibrations (Figure 5.10). In each region of Raman spectrum we can see Ge-Ge (285-295cm^{-1}), Si-Ge (around 410cm^{-1}) and Si-Si (480-

505cm^{-1}) modes from $Si_{1-y}Ge_y$ relaxed layers. In addition to phonon modes originated from relaxed layers, were clearly observed the Ge-Ge modes (>300cm^{-1}) from $Si_{1-x}Ge_x$ strained channel layers. A comparison between these shifts and the Ge bulk ones, that is 300cm^{-1}, shows upward shifts of the Ge-Ge peaks, which are due to the presence of compressive strain in the $Si_{1-x}Ge_x$ layers. Very weak Si-Si modes (470-490cm^{-1}) from $Si_{1-x}Ge_x$ strained layers were observed. The intensities of these modes were weak, in comparison with others, due to small amount of Si in the $Si_{1-x}Ge_x$ layers and their small thicknesses (<14nm for most of samples). In the Si-Si region the peak at 495-515cm^{-1} are correspond to Si-Si modes originated from tensilely strained Si cap layers on the surface grown on $Si_{1-y}Ge_y$ relaxed layers. The modes at 400-460cm^{-1} frequency region are attributed to a Si-Ge vibrations in $Si_{1-y}Ge_y$ relaxed layers, $Si_{1-x}Ge_x$ strained channel layer and to Si or Ge vibrations in chemically different local environments in SiGe layers with intensity approximately proportional to the relative number of Si-Ge bonds. The Si-Ge phonon modes seem to have properties that are coming partly from the Ge and Si atoms. In particular for sample #622.83, the $Si_{0.2}Ge_{0.8}$ channel layer is fully strained and $Si_{0.7}Ge_{0.3}$ layers are almost fully relaxed. The value of Ge composition in the $Si_{1-y}Ge_y$ relaxed layers of sample #622.83 extracted from the ratio of intensities of Si-Si and Ge-Ge modes originated from these layers corresponds to 0.32±0.02. The $Si_{1-x}Ge_x$ channels grown on $Si_{1-y}Ge_y$ VS in the as-grown samples #51.33, #52.16, #54.08, #60.46, #622.83, #C1957, #C1987, #C2015f, #C2072, #C2475 and #C2476 were fully strained. In the as-grown sample #622.84 the 14nm $Si_{0.2}Ge_{0.8}$ channel (grown on $Si_{0.7}Ge_{0.3}$ VS) was partially relaxed due to exceeded critical thickness. The calculations of degree of relaxation from positions of Ge-Ge and Si-Si modes originated from $Si_{1-x}Ge_x$ and $Si_{1-y}Ge_y$ layers were done using anharmonic Keating model for SiGe [6].

Scanning white-light interferometry used to analysis surface profiles of p-type MOD $Si_{1-x}Ge_x/Si_{1-y}Ge_y$ heterostructures. The surface profile is strongly depends from the growth

conditions. The investigated heterostructures are possible to divide into the groups depending on used type of VS due to their dominated effect on the quality of the surface. For all samples the used VS were grown by SS-MBE exclusive linearly graded VS used in samples #60.45 and #60.46, which were grown by LP-CVD. The characteristic feature for samples contained linearly or step graded VS are crosshatches on the surface due to linearly or step graded changes of Ge composition and high density of dislocations in VS (Figure 5.20, Figure 5.16). The measured PV and rms (see chapter 5.8) for samples with step graded VS (#51.33, #52.16 and #54.08) are 6-8nm and 0.8-1nm respectively (Figure 5.16). For samples with linearly graded VS grown by LP-CVD (#60.45 and #60.46) the measured PV and rms are 42-124nm and 5-15nm respectively (Figure 5.17). For samples with thick (>3μm) linearly graded VS grown by SS-MBE (#C1957, #C1987, #C2015f, #C2072, #C2475 and #C2476) the measured PV and rms are 20-30nm and 3-5nm respectively (Figure 5.20). The active layers of MOD heterostructure in samples #622.83 and #622.84 were grown on $Si_{0.7}Ge_{0.3}$ VS with low temperature Si buffer. No crosshatches were observed in these samples (Figure 5.19). The measured PV and rms are 4.5-5.5nm and 0.5-0.7nm respectively.

5.9 Conclusions

The results and discussions of structural and optical analysis of p-type MOD $Si_{1-x}Ge_x/Si_{1-y}Ge_y$ heterostructures were presented in this chapter. The as-grown and after post growth thermal annealing samples were analyzed by XTEM, ULE-SIMS, PL spectroscopy, micro-Raman spectroscopy and scanning white-light interferometry.

The structural integrity of the layers and the dislocations microstructure in relaxed VS were determined by XTEM. In particular, the thicknesses of high Ge content $Si_{1-x}Ge_x$ channel layer were determined. Also short-range roughness of $Si_{1-x}Ge_x$ channel layer interfaces caused by not optimum growth conditions and long-range roughness cased by

various types of VS were studied by XTEM as well. The Ge, Si and B profiles were obtained by ULE-SIMS that allowed determine the structural integrity of the layers, $Si_{1-x}Ge_x$ channel layer thickness and level of B doping in the active layers of MOD heterostructures. PL spectra of p-type MOD $Si_{1-x}Ge_x/Si_{1-y}Ge_y$ heterostructures obtained in the energy range 0.7-1.2eV at 5.5K contain information only about Si substrate and $Si_{1-y}Ge_y$ (0.3-0.63) relaxed layers. State of strain in the $Si_{1-x}Ge_x$ strained and $Si_{1-y}Ge_y$ relaxed layers and the Ge composition in the later were obtained from room temperature Raman spectra. The $Si_{1-x}Ge_x$ channels grown on $Si_{1-y}Ge_y$ VS in the as-grown samples #51.33, #52.16, #54.08, #60.46, #622.83, #C1957, #C1987, #C2015f, #C2072, #C2475 and #C2476 (see chapter 4.2) were fully strained. In the as-grown sample #622.84 the 14nm $Si_{0.2}Ge_{0.8}$ channel (grown on $Si_{0.7}Ge_{0.3}$ VS) was partially relaxed due to exceeded critical thickness. The surface profiles of p-type MOD $Si_{1-x}Ge_x/Si_{1-y}Ge_y$ heterostructures were obtained by scanning white-light interferometry. The characteristic feature for samples contained linearly or step graded VS are crosshatches on the surface due to linearly or step graded changes of Ge composition and high density of dislocations in VS. No crosshatches were observed in the samples contained relatively thin (850nm) $Si_{0.7}Ge_{0.3}$ VS with low temperature Si buffer (#622.83 and #622.84). The lowest surface roughness was observed in these samples. The highest surface roughness was observed in the samples with $Si_{0.65}Ge_{0.35}$ linearly graded VS grown by LP-CVD (#60.45 and #60.46).

After post growth thermal annealing (FTA and RTA) the Ge diffusion from the region with high Ge concentration ($Si_{1-x}Ge_x$ channel) to the region with low Ge concentration ($Si_{1-y}Ge_y$ layers) and B diffusion from doped $Si_{1-y}Ge_y$ layers to the undoped $Si_{1-y}Ge_y$ spacer layers were observed. The broadening of $Si_{1-x}Ge_x$ channel caused by Ge diffusion was accompanied with smearing of bottom and top $Si_{1-x}Ge_x/Si_{1-y}Ge_y$ interfaces. After annealing significant changes in all regions of Raman spectra of p-type MOD $Si_{1-x}Ge_x/Si_{1-y}Ge_y$ heterostructures were observed. The intensities of the various modes

changed, as long as the intermixing of Si and Ge atoms occurred during annealing. The most significant changes were observed in the Ge-Ge region. With increasing of annealing temperature the increase of intensity of Ge-Ge mode originated from the $Si_{1-x}Ge_x$ strained channel layers and their downward shift were observed. This is demonstrate the sensitivity of Raman spectra to Ge diffusion during annealing which results in decreasing Ge content in the $Si_{1-x}Ge_x$ strained channel or (and) its partial relaxation. With increasing annealing temperature the $Si_{1-y}Ge_y$ relaxed layers became more relaxed just in the case if they were not fully relaxed in as-grown samples. The peak at 521cm^{-1} corresponding to Si-Si mode originated from Si substrate remained unchangeable after annealing up to 900C for 30min.

It is necessary to point, that micro-Raman spectroscopy, PL spectroscopy and ULE-SIMS measurements were performed on the very same samples (Hall-bars and Van der Pauw cross) used for magnetotransport characterization.

References:

1. Myronov, M., S.G. Lyapin, C. Parry, E.H.C. Parker, T.E. Whall, P.C. Klipstein, and J.M. Bonar. *Post-growth annealing effect on properties of p-type modulation doped Si0.2Ge0.8/Si0.65Ge0.35/Si(001) heterostructure studied by XTEM and Raman spectroscopy.* in *Condensed Matter and Materials Physics '99.* 1999. University of Leicester, Leicester, UK.
2. Myronov, M., E.H.C. Parker, T.E. Whall, S.G. Lyapin, and P.C. Klipstein. *Thermal annealing effect on properties of Si0.2Ge0.8/Si0.7Ge0.3/Si(001) p-type modulation doped heterostructures.* in *10th European Heterostructure Technology Workshop.* 2000. University of Ulm, International Institute Schloss Reisensburg, Gunzburg, Germany.
3. Myronov, M., C.P. Parry, O.A. Mironov, E.H.C. Parker, T.E. Whall, E. Hoeflinger, and G. Bauer. *Post-growth annealing effect on magnetotransport and structural properties of Si0.2Ge0.8/Si0.65Ge0.35/Si(001) modulation doped heterostructure.* in *10th European Heterostructure Technology Workshop.* 2000. University of Ulm, International Institute Schloss Reisensburg, Gunzburg, Germany.
4. Myronov, M., C.P. Parry, O.A. Mironov, E.H.C. Parker, O.A. Soltanovich, and E.B. Yakimov. *Growth and annealing induced defects analysis in Si1-xGex/Si1-yGey/Si(001) heterostructures with high Ge content.* in *International Conference on Solid State Crystals 2000: Materials Science and Applications.* 2000. Zakopane, Poland.

5. Mironov, O.A., M. Myronov, E.H.C. Parker, and T.E. Whall. *High Ge content SiGe MODFET heterostructures on virtual substrates for device applications: HOLE MOBILITIES higher than electrons in the room temperature range of operation.* in *SiGe (C) 2001 Workshop.* 2001. Hotel Jal City, Sendai, Japan.

6. Rucker, H. and M. Methfessel, *Anharmonic Keating Model for Group-Iv Semiconductors with Application to the Lattice-Dynamics in Alloys of Si, Ge, and C.* Physical Review B-Condensed Matter, 1995. **52**(15): p. 11059-11072.

7. Bhagavannarayana, G., B. Dietrich, P. Zaumseil, and K.F. Dombrowski, *Determination of germanium content and relaxation in Si1- xGex/Si layers by Raman spectroscopy and X-ray diffractometry.* Physica Status Solidi a-Applied Research, 1999. **172**(2): p. 425-432.

8. Rath, S., C. Grigorescu, M.L. Hsieh, E. Voudouris, and R.A. Stradling, *Polarization-dependent Raman spectroscopic protocols for calibration of the alloy composition and strain in bulk and thin-film Si1-xGex.* Semiconductor Science and Technology, 2000. **15**(2): p. L1-L5.

6. Results and discussions of magnetotransport characterization of p-type MOD $Si_{1-x}Ge_x/Si_{1-y}Ge_y$ heterostructures

The samples were firstly measured in the closed-cycle cryostat system by the combination of resistivity and Hall effect techniques at temperature range 9-300K. At low temperatures the measured Hall mobility at sheet carrier density is attributed to 2DHG formed in the $Si_{1-x}Ge_x$ channel of p-type MOD $Si_{1-x}Ge_x/Si_{1-y}Ge_y$ heterostructures. At high temperatures the measured Hall mobility at sheet carrier density is resulted at least from 2DHG formed in the $Si_{1-x}Ge_x$ channel and carriers in parallel conducted B doped $Si_{1-y}Ge_y$ layer.

To extract the room temperature drift mobility and sheet carrier density of 2DHG the magnetic field dependences of magnetoresistance and Hall resistance at the high temperatures were measured in cryomagnetic system as the magnetic field was swept continuously up to 11T, and the technique of MEMSA (see chapter 2.3.4.2) was applied.

Low temperature magnetotransport measurements down to 350mK and at magnetic fields up to 11T were carried out in cryomagnetic system. From the temperature dependence of the Shubnikov-de Haas oscillations were extracted followed parameters of 2DHG, — effective mass, sheet carrier density, transport and quantum scattering times, and related ones.

6.1 Magnetotransport properties of p-type MOD $Si_{1-x}Ge_x/Si_{1-y}Ge_y$ heterostructures measured at temperatures 9-300K

6.1.1 Introduction

Hall mobility and sheet carrier density of p-type MOD $Si_{1-x}Ge_x/Si_{1-y}Ge_y$ heterostructures were obtained from the combination of resistivity and Hall effect techniques at temperature range 9-300K. The measurements were performed in the closed-cycle cryostat

system (see chapter 3.8.1). The data were obtained in the dark beginning at low temperature. The measurements were performed on as-grown and after FTA and RTA samples.

6.1.2 Results and discussion

Temperature dependences of Hall mobility and sheet carrier density for as-grown and after FTA at 600C, 700C, 800C and 900C for 30min samples #51.33 are presented in Figure 6.1. The as-grown heterostructure consist of 5nm $Si_{0.22}Ge_{0.78}$ channel grown on 2200nm $Si_{0.7}Ge_{0.3}$ step graded VS and inverted $4 \cdot 10^{18} cm^{-3}$ B doped 10nm $Si_{0.8}Ge_{0.2}$ layer (see chapter 4.2). The Hall mobility of 2DHG (at sheet carrier density) formed in the $Si_{0.22}Ge_{0.78}$ channel of as-grown sample measured at 9K is $350 cm^2 \cdot V^{-1} \cdot s^{-1}$ ($7.45 \cdot 10^{12} cm^{-2}$). This value of carrier density is higher than expected from design due to unintentional increased B doping level during the growth. The sheet carrier density is almost constant at low temperatures and starts to rise slowly as the temperature is increased. At high temperatures it increases exponentially due to the ionization of the B doped $Si_{0.7}Ge_{0.3}$ layer. The Hall mobility is almost constant at 9-70K of temperature range followed by decreases with increasing temperatures. The Hall mobility (at sheet carrier density) for as-grown sample measured at 293K is $113 cm^2 \cdot V^{-1} \cdot s^{-1}$ ($9.82 \cdot 10^{12} cm^{-2}$). The annealing at 600C is seen to have a negligible effect on the Hall mobility as well as on carrier sheet density. Increasing the annealing temperature results in pronounced successive increases of Hall mobility. The highest Hall mobility at 9K and 293K was observed after annealing at 700C for 30min. The values are $670 cm^2 \cdot V^{-1} \cdot s^{-1}$ ($7 \cdot 10^{12} cm^{-2}$) and $180 cm^2 \cdot V^{-1} \cdot s^{-1}$ ($9.14 \cdot 10^{12} cm^{-2}$) at 9K and 293K respectively. Further increasing of annealing temperatures up to 800C and 900C results in decreases of Hall mobility. For sheet carrier density was observed opposite behaviour.

Temperature dependences of Hall mobility and sheet carrier density for as-grown and after FTA at 600C, 700C, 800C and 900C for 30min samples #52.16 are presented in Figure 6.2. The as-grown heterostructure consist of 5nm $Si_{0.24}Ge_{0.76}$ channel grown on 1150nm

$Si_{0.7}Ge_{0.3}$ step graded VS and normal $2.4 \cdot 10^{18} cm^{-3}$ B doped 50nm $Si_{0.7}Ge_{0.3}$ layer (see chapter 4.2). The Hall mobility of 2DHG (at sheet carrier density) formed in the $Si_{0.24}Ge_{0.76}$ channel of as-grown sample measured at 9K is $131 cm^2 \cdot V^{-1} \cdot s^{-1}$ ($2.08 \cdot 10^{13} cm^{-2}$). This value of carrier density is higher than expected from design due to unintentional increased B doping level during the growth. The Hall mobility (at sheet carrier density) for as-grown sample measured at 293K is $85 cm^2 \cdot V^{-1} \cdot s^{-1}$ ($3.23 \cdot 10^{13} cm^{-2}$). The annealing at 600C is seen to have a negligible effect on the Hall mobility as well as on carrier sheet density. Increasing the annealing temperature results in pronounced successive increases of Hall mobility. The highest Hall mobility at 9K and 293K was observed after annealing at 800C for 30min. The values are $841 cm^2 \cdot V^{-1} \cdot s^{-1}$ ($5.29 \cdot 10^{12} cm^{-2}$) and $134 cm^2 \cdot V^{-1} \cdot s^{-1}$ ($1.82 \cdot 10^{13} cm^{-2}$) at 9K and 293K respectively. Further increasing of annealing temperatures up to 900C results in decreases of Hall mobility. For sheet carrier density was observed opposite behaviour.

Temperature dependences of Hall mobility and sheet carrier density for as-grown and after FTA at 600C, 700C, 800C and 900C for 30min samples #54.08 are presented in Figure 6.3. The as-grown heterostructure consist of 6nm $Si_{0.4}Ge_{0.6}$ channel grown on 1350nm $Si_{0.7}Ge_{0.3}$ step graded VS and normal $2 \cdot 10^{18} cm^{-3}$ B doped 50nm $Si_{0.7}Ge_{0.3}$ layer (see chapter 4.2). The Hall mobility of 2DHG (at sheet carrier density) formed in the $Si_{0.4}Ge_{0.6}$ channel of as-grown sample measured at 9K is $173 cm^2 \cdot V^{-1} \cdot s^{-1}$ ($2.33 \cdot 10^{12} cm^{-2}$). The Hall mobility (at sheet carrier density) for as-grown sample measured at 293K is $88 cm^2 \cdot V^{-1} \cdot s^{-1}$ ($1.07 \cdot 10^{13} cm^{-2}$). The annealing at 600C is seen to have a negligible effect on the Hall mobility as well as on carrier sheet density. Increasing the annealing temperature results in pronounced successive increases of Hall mobility. The highest Hall mobility at 9K and 293K was observed after annealing at 900C for 30min. The values are $1477 cm^2 \cdot V^{-1} \cdot s^{-1}$ ($5.29 \cdot 10^{11} cm^{-2}$) and $145 cm^2 \cdot V^{-1} \cdot s^{-1}$ ($3.9 \cdot 10^{12} cm^{-2}$) at 9K and 293K respectively. For sheet carrier density was observed opposite behaviour.

Temperature dependences of Hall mobility and sheet carrier density for as-grown and after FTA at 600C, 700C, 750C and 800C for 30min samples #60.46 are presented in Figure 6.4. The as-grown heterostructure consist of 4nm $Si_{0.2}Ge_{0.8}$ channel grown on 300nm $Si_{0.65}Ge_{0.35}$ buffer on 1200nm $Si_{0.65}Ge_{0.35}$ linearly graded VS and normal $2 \cdot 10^{18} cm^{-3}$ B doped 10nm $Si_{0.7}Ge_{0.3}$ layer (see chapter 4.2). The Hall mobility of 2DHG (at sheet carrier density) formed in the $Si_{0.2}Ge_{0.8}$ channel of as-grown sample measured at 9K is $654 cm^2 \cdot V^{-1} \cdot s^{-1}$ ($1.43 \cdot 10^{12} cm^{-2}$). The Hall mobility (at sheet carrier density) for as-grown sample measured at 293K is $97 cm^2 \cdot V^{-1} \cdot s^{-1}$ ($1.92 \cdot 10^{14} cm^{-2}$). The annealing at 600C is seen to have a negligible effect on the Hall mobility as well as on carrier sheet density. Increasing the annealing temperature results in pronounced successive increases of Hall mobility. The highest Hall mobility of 2DHG measured at 9K was observed after FTA at 700C for 30min which correspond to $1955 cm^2 \cdot V^{-1} \cdot s^{-1}$ ($8.62 \cdot 10^{11} cm^{-2}$). The room temperature Hall mobility for the sample after annealing at 700C is $408 cm^2 \cdot V^{-1} \cdot s^{-1}$ ($6.65 \cdot 10^{12} cm^{-2}$). Further increasing of annealing temperature up to 750C results in increases of room temperature Hall mobility up to $1776 cm^2 \cdot V^{-1} \cdot s^{-1}$ ($2.37 \cdot 10^{13} cm^{-2}$) followed by decreasing down to $993 cm^2 \cdot V^{-1} \cdot s^{-1}$ ($2.78 \cdot 10^{13} cm^{-2}$).

The electronic properties of semiconductors depend strongly on the presence of deep electronic states within the energy bandgap of semiconductors. Deep levels are ubiquitous in that they are a consequence of unintentional impurities, intrinsic point defects, and variety of extended defects such as dislocations, grain boundaries, interfaces and general crystalline disorder [1]. Sample #60.46 has the highest density of threading dislocations in comparison with others ones, generated during the LP-CVD growth of $Si_{0.65}Ge_{0.35}$ linearly graded VS. It could be that during annealing the conductivity type of background has changed that caused compensation of Boron acceptor centres by deep defects levels. Previously P.N. Grillot *et al* [2] observed that strain-relaxed, compositionally graded $Si_{0.7}Ge_{0.3}$/Si VS grown by UHV-CVD were shown to display a consistent change from p-type to n-type conductivity as a

function of RTA temperature in the range 700–850C for 60sec. The self-consistent solution of the Poisson and Schrodinger equations (see chapter 4.1) performed for sample #60.46 after FTA at 750C in 200K temperature region showed that after introduction of n-type background doping at $N_D \sim 10^{17} cm^{-3}$ it is possible to get dramatic decreasing of 2DHG sheet density and to see results similar to those obtained experimentally (Figure 6.4). Pronounced decrease of Hall mobility and sheet carrier density with activation energy 20meV below 200K could be explained by appearing of deep hole and electron traps after annealing at 750C and 800C similar to [2]. The exist of these hole traps in SiGe graded layers containing dislocations with several activation energies $E_{A1}=E_v+240meV$, $E_{A2}=E_v+380meV$, $E_{A3}=E_v+420meV$, $E_{A4}=E_v+430meV$ and two types of electron traps with $E_{T1}=E_c-640meV$, $E_{T1}=E_c-570meV$ have been experimentally demonstrated with the help of DLTS and EBIC techniques by P.N. Grillot *et al* [3]. The possibility to capture free holes from valence band and also carriers from the shallow dislocations bands in the Si was experimentally shown with the help of DLTS and EBIC techniques and theoretically supported by M. Kittler *et al* [4]. Hole and electron traps energy levels are much deeper than estimated activation energy of the Boron (~20meV) in $Si_{0.65}Ge_{0.35}$ and could easily decrease its ability to supply free holes to valence band and essential for understanding of "freezing out" of 2DHG if one could suggest the concentration of donor-like centres with $N_D \sim 10^{17} cm^{-3}$. The proposed scenario is very similar to very well known phenomena of dramatic decreasing of free carriers concentration in heavily doped semiconductors with increasing degree of impurity compensation $K=N_A/N_D>0.9$ [5], [6].

Temperature dependences of Hall mobility and sheet carrier density for as-grown and after FTA at 600C, 700C, 750C, 800C and 900C for 30min samples #622.83 are presented in Figure 6.5. The as-grown heterostructure consist of 10nm $Si_{0.2}Ge_{0.8}$ channel grown on 850nm $Si_{0.7}Ge_{0.3}$ LT-Si VS and normal $2 \cdot 10^{18} cm^{-3}$ B doped 10nm $Si_{0.7}Ge_{0.3}$ layer (see chapter 4.2). The Hall mobility of 2DHG (at sheet carrier density) formed in the $Si_{0.2}Ge_{0.8}$ channel of as-grown sample measured at 9K is $624 cm^2 \cdot V^{-1} \cdot s^{-1}$ ($1.37 \cdot 10^{12} cm^{-2}$). The Hall mobility (at sheet

carrier density) for as-grown sample measured at 293K is $170cm^2 \cdot V^{-1} \cdot s^{-1}$ ($2.6 \cdot 10^{12} cm^{-2}$). The annealing at 600C is seen to have a negligible effect on the Hall mobility as well as on carrier sheet density. Increasing the annealing temperature results in pronounced successive increases of Hall mobility. The highest Hall mobility at 9K and 293K was observed after annealing at 750C for 30min. The values are $1680cm^2 \cdot V^{-1} \cdot s^{-1}$ ($1.27 \cdot 10^{12} cm^{-2}$) and $512cm^2 \cdot V^{-1} \cdot s^{-1}$ ($2.11 \cdot 10^{12} cm^{-2}$) at 9K and 293K respectively. Further increasing of annealing temperatures up to 900C results in decreases of Hall mobility. For sheet carrier density was observed opposite behaviour.

Temperature dependences of Hall mobility and sheet carrier density for as-grown and after FTA at 600C, 700C, 750C, 800C and 900C for 30min samples #622.84 are presented in Figure 6.6. The as-grown heterostructure consist of 14nm $Si_{0.2}Ge_{0.8}$ channel grown on 850nm $Si_{0.7}Ge_{0.3}$ LT-Si VS and normal $2 \cdot 10^{18} cm^{-3}$ B doped 10nm $Si_{0.7}Ge_{0.3}$ layer (see chapter 4.2). The Hall mobility of 2DHG (at sheet carrier density) formed in the $Si_{0.2}Ge_{0.8}$ channel of as-grown sample measured at 9K is $297cm^2 \cdot V^{-1} \cdot s^{-1}$ ($1.4 \cdot 10^{12} cm^{-2}$). The Hall mobility (at sheet carrier density) for as-grown sample measured at 293K is $98cm^2 \cdot V^{-1} \cdot s^{-1}$ ($3.28 \cdot 10^{12} cm^{-2}$). The annealing at 600C is seen to have a negligible effect on the Hall mobility as well as on carrier sheet density. Increasing the annealing temperature results in pronounced successive increases of Hall mobility. The highest Hall mobility at 9K and 293K was observed after annealing at 750C for 30min. The values are $938cm^2 \cdot V^{-1} \cdot s^{-1}$ ($9.86 \cdot 10^{11} cm^{-2}$) and $153cm^2 \cdot V^{-1} \cdot s^{-1}$ ($3.11 \cdot 10^{12} cm^{-2}$) at 9K and 293K respectively. Further increasing of annealing temperatures up to 900C results in decreases of Hall mobility. For sheet carrier density was observed opposite behaviour.

Temperature dependences of Hall mobility and sheet carrier density for as-grown and after RTA at 750C for 30sec samples #C1987 are presented in Figure 6.7. The as-grown heterostructure consist of 12.3nm $Si_{0.34}Ge_{0.66}$ channel grown on 3600nm $Si_{0.65}Ge_{0.35}$ linearly graded VS and normal $2.4 \cdot 10^{18} cm^{-3}$ B doped 10nm $Si_{0.7}Ge_{0.3}$ layer (see chapter 4.2). The Hall

mobility of 2DHG (at sheet carrier density) formed in the $Si_{0.34}Ge_{0.66}$ channel of as-grown sample measured at 9K is $3877cm^2 \cdot V^{-1} \cdot s^{-1}$ ($7.41 \cdot 10^{11}cm^{-2}$). The Hall mobility (at sheet carrier density) for as-grown sample measured at 293K is $346cm^2 \cdot V^{-1} \cdot s^{-1}$ ($1.6 \cdot 10^{12}cm^{-2}$). After RTA at 750C was observed an increase of Hall mobility as well as sheet carrier density at 9K and 293K. The values are $6574cm^2 \cdot V^{-1} \cdot s^{-1}$ ($1.1 \cdot 10^{12}cm^{-2}$) and $438cm^2 \cdot V^{-1} \cdot s^{-1}$ ($2.14 \cdot 10^{12}cm^{-2}$) at 9K and 293K respectively.

Temperature dependences of Hall mobility and sheet carrier density for as-grown and after RTA at 750C for 30sec samples #C2072 are presented in Figure 6.8. The as-grown heterostructure consist of 12nm $Si_{0.18}Ge_{0.82}$ channel grown on 3100nm $Si_{0.47}Ge_{0.53}$ linearly graded VS and normal $2.4 \cdot 10^{18}cm^{-3}$ B doped 10nm $Si_{0.47}Ge_{0.53}$ layer (see chapter 4.2). The Hall mobility of 2DHG (at sheet carrier density) formed in the $Si_{0.18}Ge_{0.82}$ channel of as-grown sample measured at 9K is $2102cm^2 \cdot V^{-1} \cdot s^{-1}$ ($1.28 \cdot 10^{12}cm^{-2}$). The Hall mobility (at sheet carrier density) for as-grown sample measured at 293K is $515cm^2 \cdot V^{-1} \cdot s^{-1}$ ($1.87 \cdot 10^{12}cm^{-2}$). After RTA at 750C was observed an increase of Hall mobility accompanied with decreases of sheet carrier density at 9K and 293K. The values are $5567cm^2 \cdot V^{-1} \cdot s^{-1}$ ($1.13 \cdot 10^{12}cm^{-2}$) and $564cm^2 \cdot V^{-1} \cdot s^{-1}$ ($1.77 \cdot 10^{12}cm^{-2}$) at 9K and 293K respectively.

Temperature dependences of Hall mobility and sheet carrier density for as-grown sample #C1957 are presented in Figure 6.9. The heterostructure consist of 11nm $Si_{0.05}Ge_{0.95}$ channel grown on 5250nm $Si_{0.37}Ge_{0.63}$ linearly graded VS and normal $2 \cdot 10^{18}cm^{-3}$ B doped 10nm $Si_{0.37}Ge_{0.63}$ layer (see chapter 4.2). The Hall mobility of 2DHG (at sheet carrier density) formed in the $Si_{0.05}Ge_{0.95}$ channel at 9K is $9301cm^2 \cdot V^{-1} \cdot s^{-1}$ ($1.58 \cdot 10^{12}cm^{-2}$). The Hall mobility (at sheet carrier density) measured at 293K is $1161cm^2 \cdot V^{-1} \cdot s^{-1}$ ($2.1 \cdot 10^{12}cm^{-2}$).

Temperature dependences of Hall mobility and sheet carrier density for as-grown sample #C2475 are presented in Figure 6.9. The heterostructure consist of 10nm $Si_{0.02}Ge_{0.98}$ channel grown on 3950nm $Si_{0.41}Ge_{0.59}$ linearly graded VS and symmetrical $8 \cdot 10^{18}cm^{-3}$ (top) and $2 \cdot 10^{18}cm^{-3}$ (bottom) B doped 5nm and 5nm $Si_{0.41}Ge_{0.59}$ layers, respectively (see chapter

4.2). The Hall mobility of 2DHG (at sheet carrier density) formed in the $Si_{0.02}Ge_{0.98}$ channel at 9K is 9309$cm^2 \cdot V^{-1} \cdot s^{-1}$ ($2.76 \cdot 10^{12} cm^{-2}$). The Hall mobility (at sheet carrier density) measured at 293K is 711$cm^2 \cdot V^{-1} \cdot s^{-1}$ ($4.83 \cdot 10^{12} cm^{-2}$).

Temperature dependences of Hall mobility and sheet carrier density for as-grown sample #C2476 are presented in Figure 6.9. The heterostructure consist of 9nm Ge channel grown on 3950nm $Si_{0.4}Ge_{0.6}$ linearly graded VS and inverted $1 \cdot 10^{19} cm^{-3}$ B doped 4nm $Si_{0.4}Ge_{0.6}$ layer (see chapter 4.2). The Hall mobility of 2DHG (at sheet carrier density) formed in the Ge channel at 9K is 14855$cm^2 \cdot V^{-1} \cdot s^{-1}$ ($2.87 \cdot 10^{12} cm^{-2}$). The Hall mobility (at sheet carrier density) measured at 293K is 1380$cm^2 \cdot V^{-1} \cdot s^{-1}$ ($3.82 \cdot 10^{12} cm^{-2}$).

The results of magnetotransport characterization at temperatures 9-300K of p-type MOD $Si_{1-x}Ge_x/Si_{1-y}Ge_y$ heterostructures were presented at "10th European Heterostructure Technology Workshop"[7], [8], [9] and "SiGe (C) 2001 Workshop"[10].

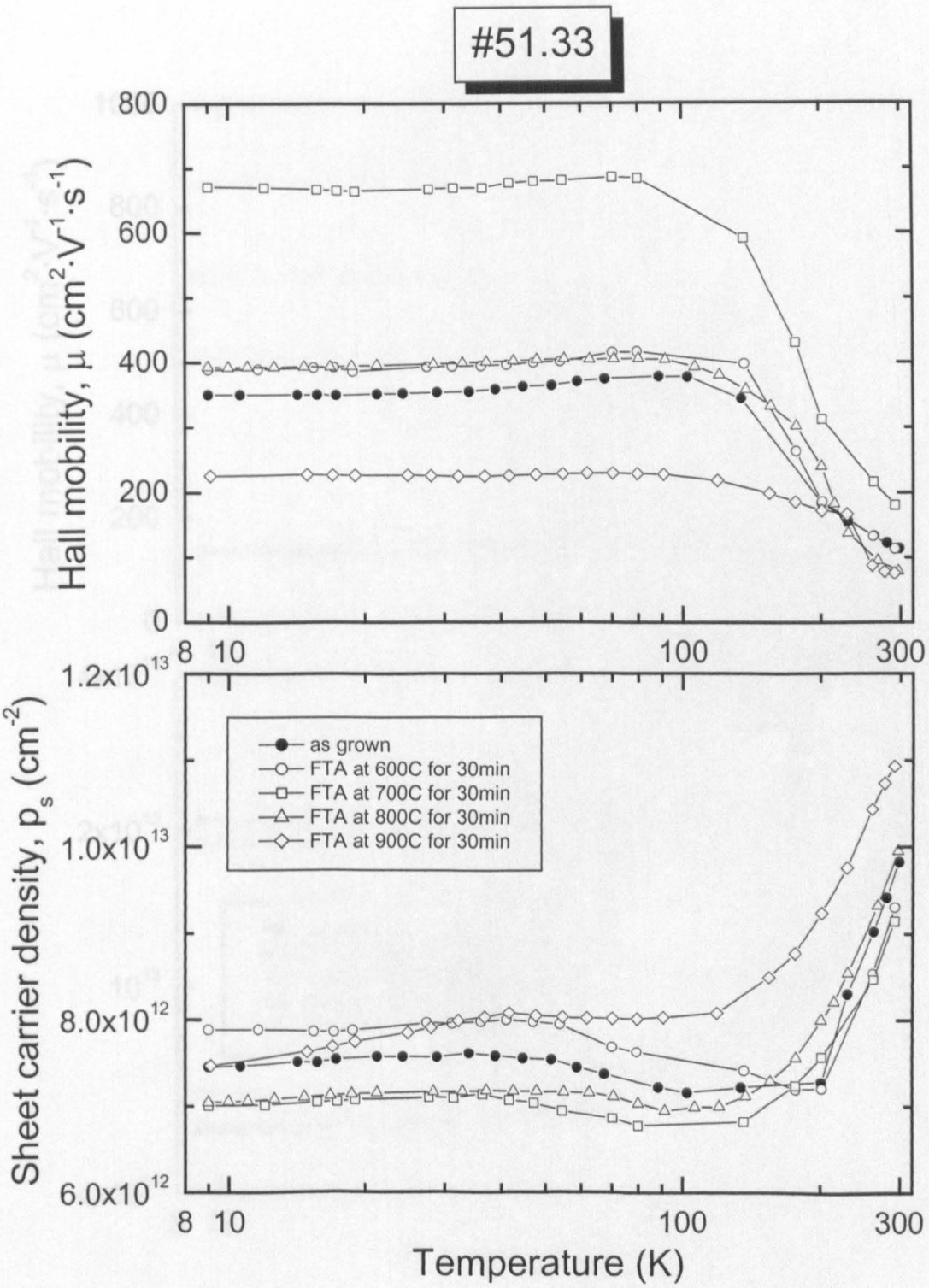

Figure 6.1 Temperature dependences of Hall mobility and sheet carrier density for as-grown sample #51.33 and after FTA at 600C, 700C, 800C and 900C for 30min.

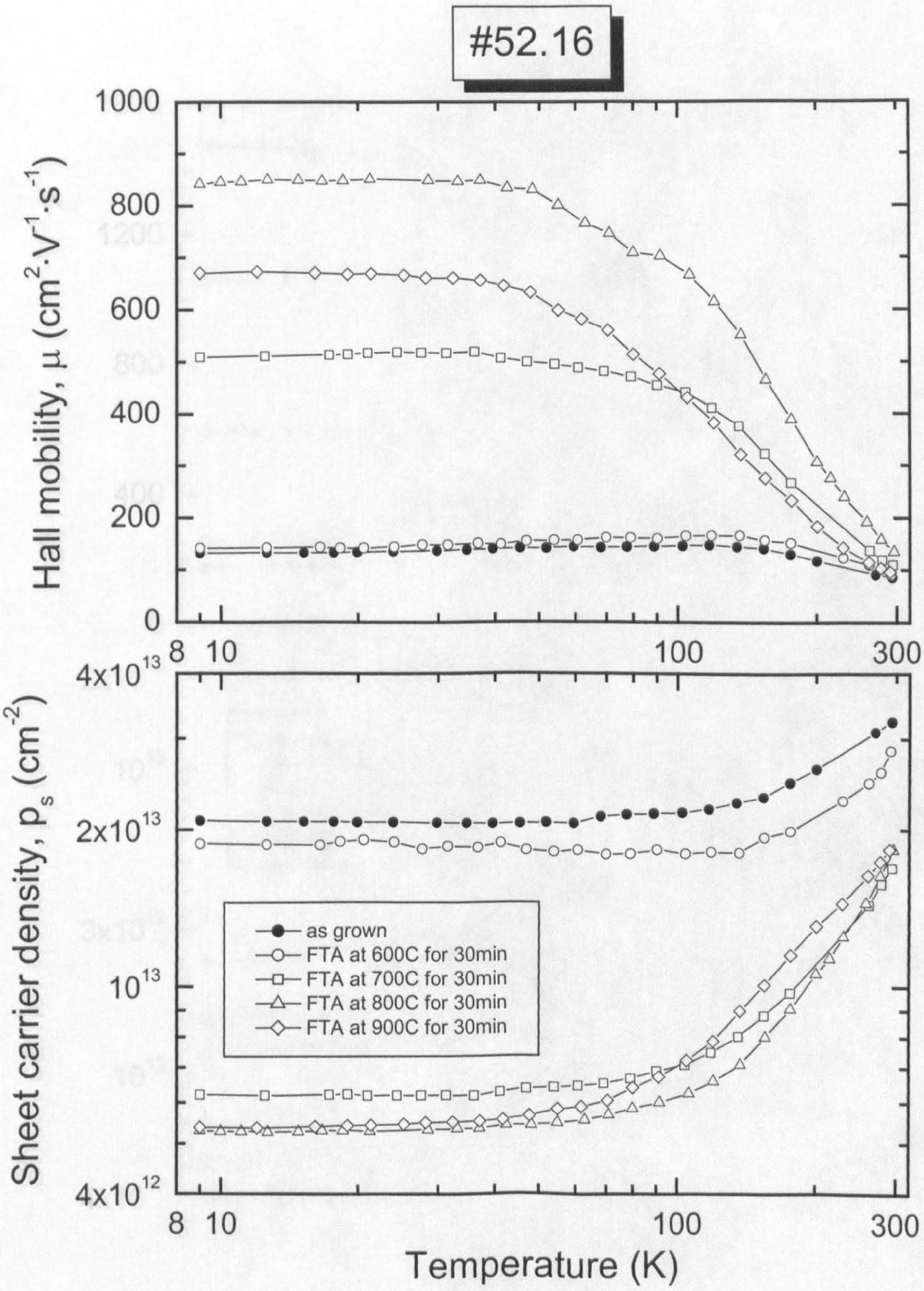

Figure 6.2 Temperature dependences of Hall mobility and sheet carrier density for as-grown sample #52.16 and after FTA at 600C, 700C, 800C and 900C for 30min.

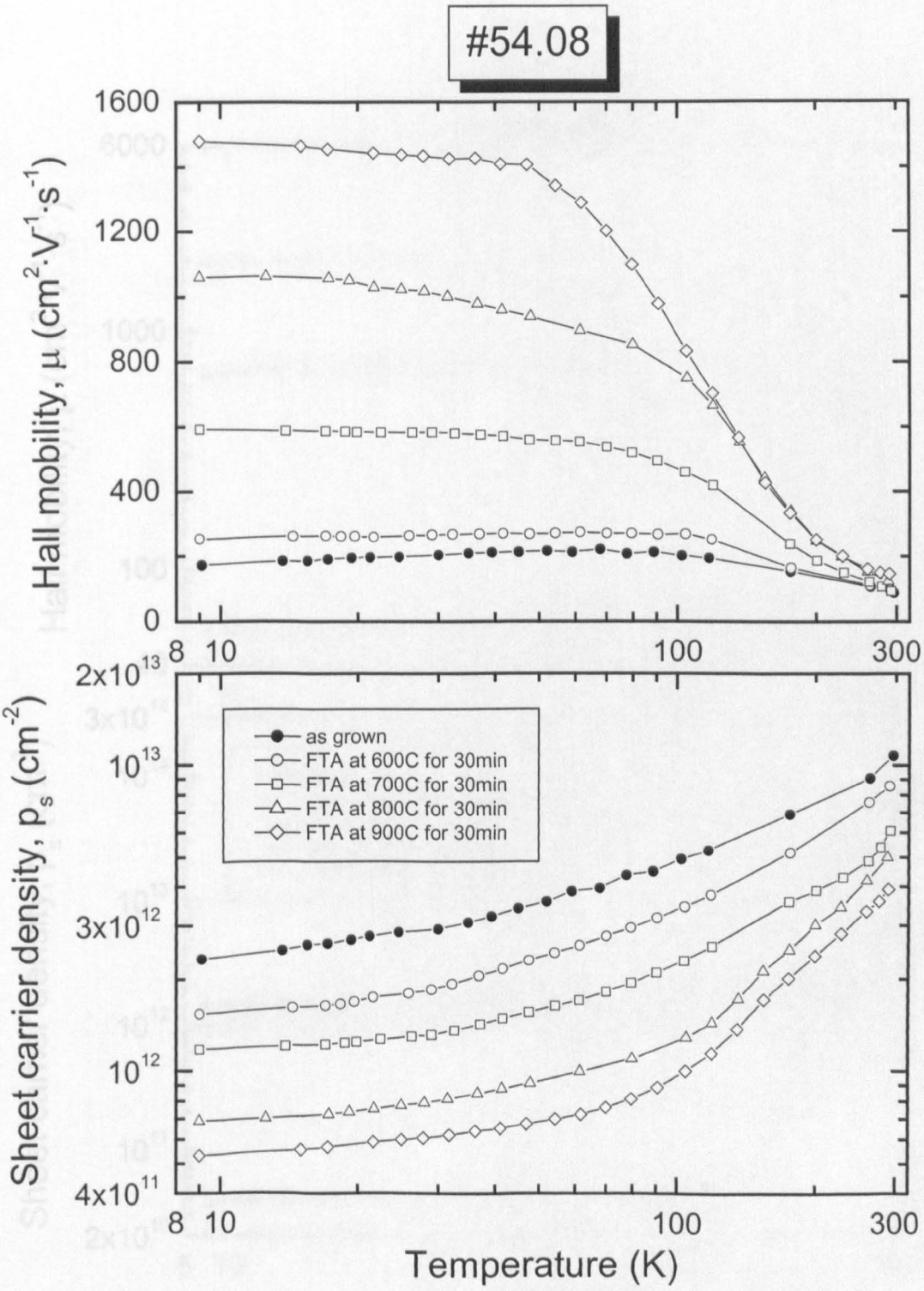

Figure 6.3 Temperature dependences of Hall mobility and sheet carrier density for as-grown sample #54.08 and after FTA at 600C, 700C, 800C and 900C for 30min.

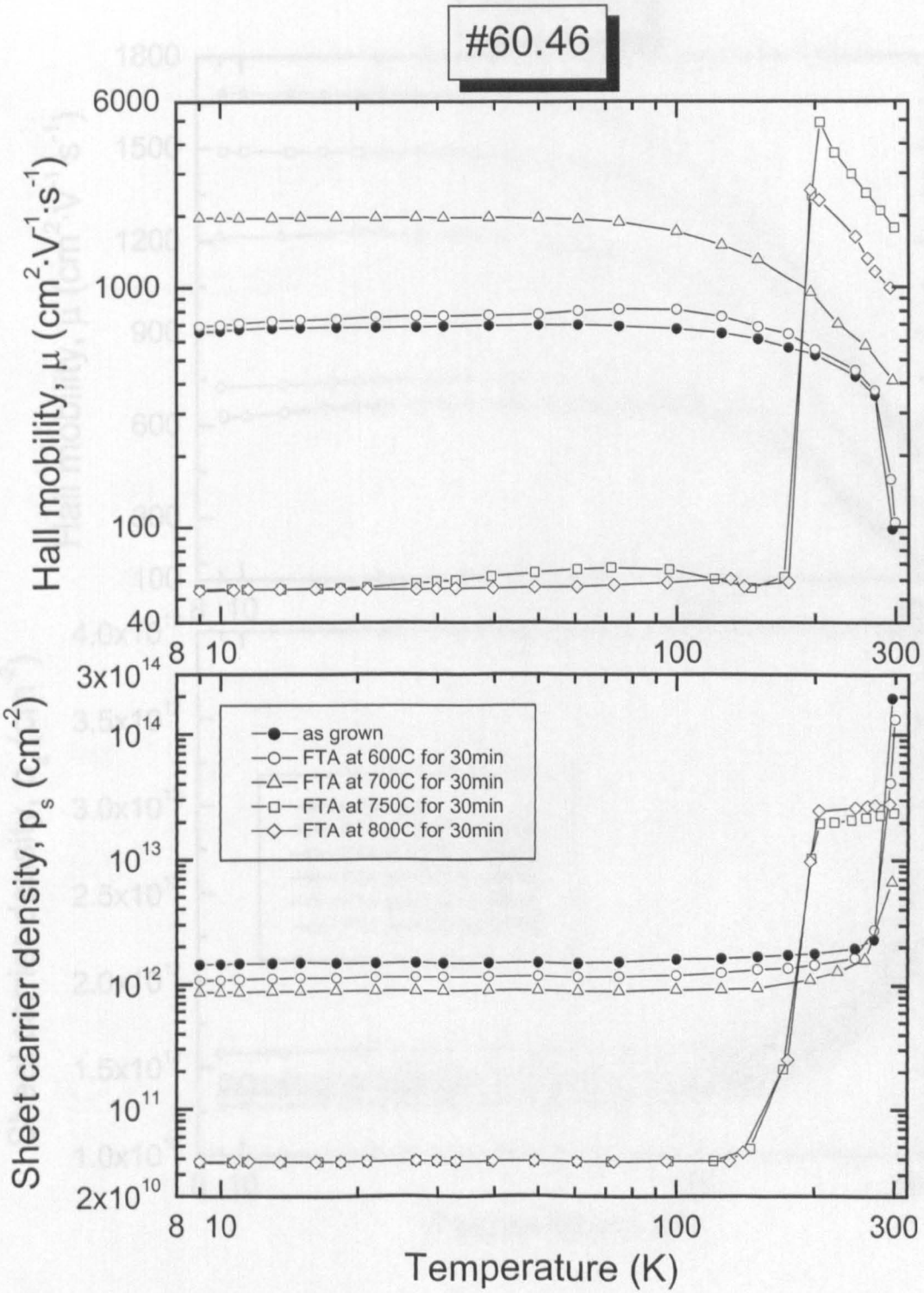

Figure 6.4 Temperature dependences of Hall mobility and sheet carrier density for as-grown sample #60.46 and after FTA at 600C, 700C, 750C and 800C for 30min.

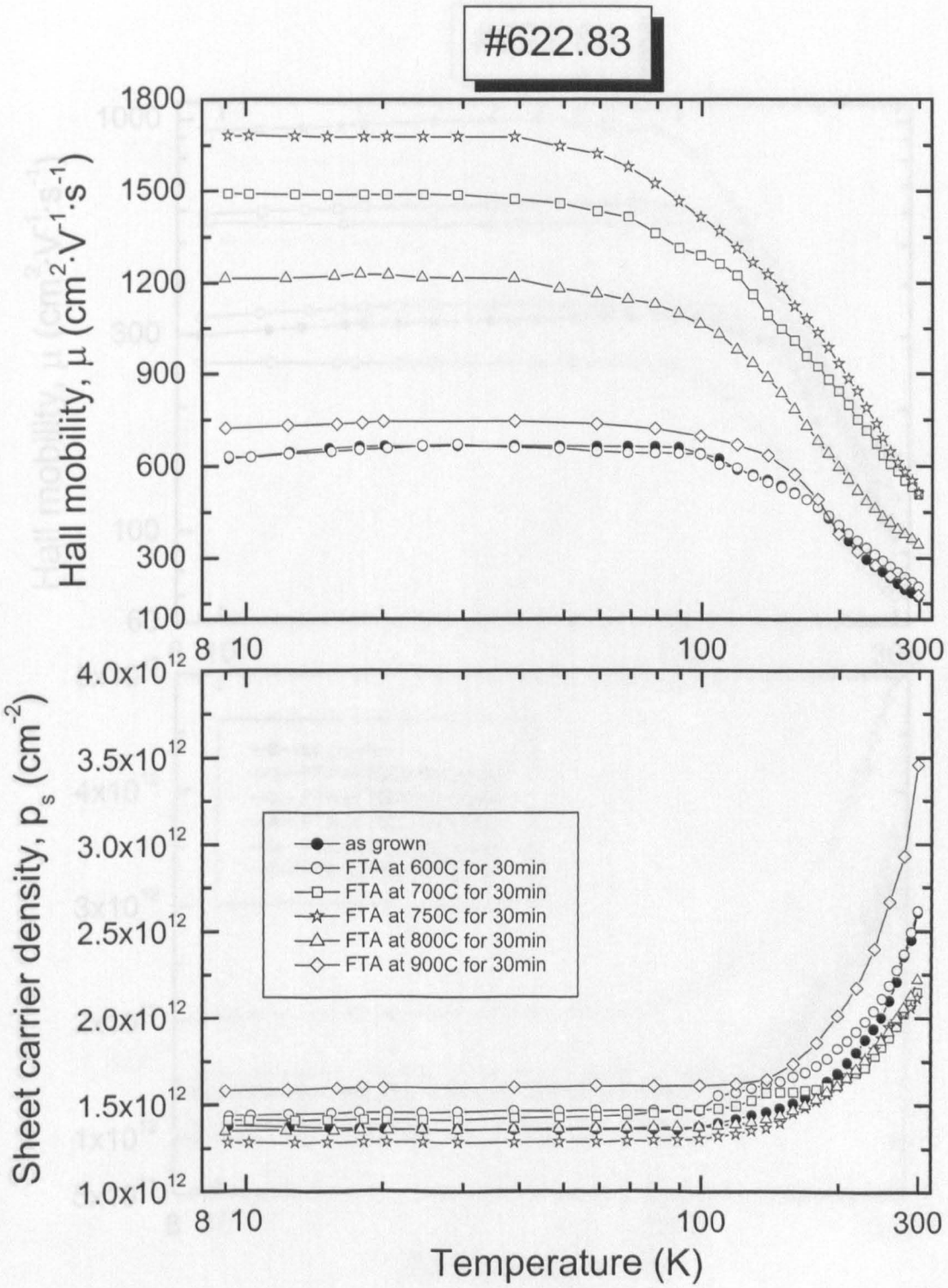

Figure 6.5 Temperature dependences of Hall mobility and sheet carrier density for as-grown sample #622.83 and after FTA at 600C, 700C, 750C, 800C and 900C for 30min.

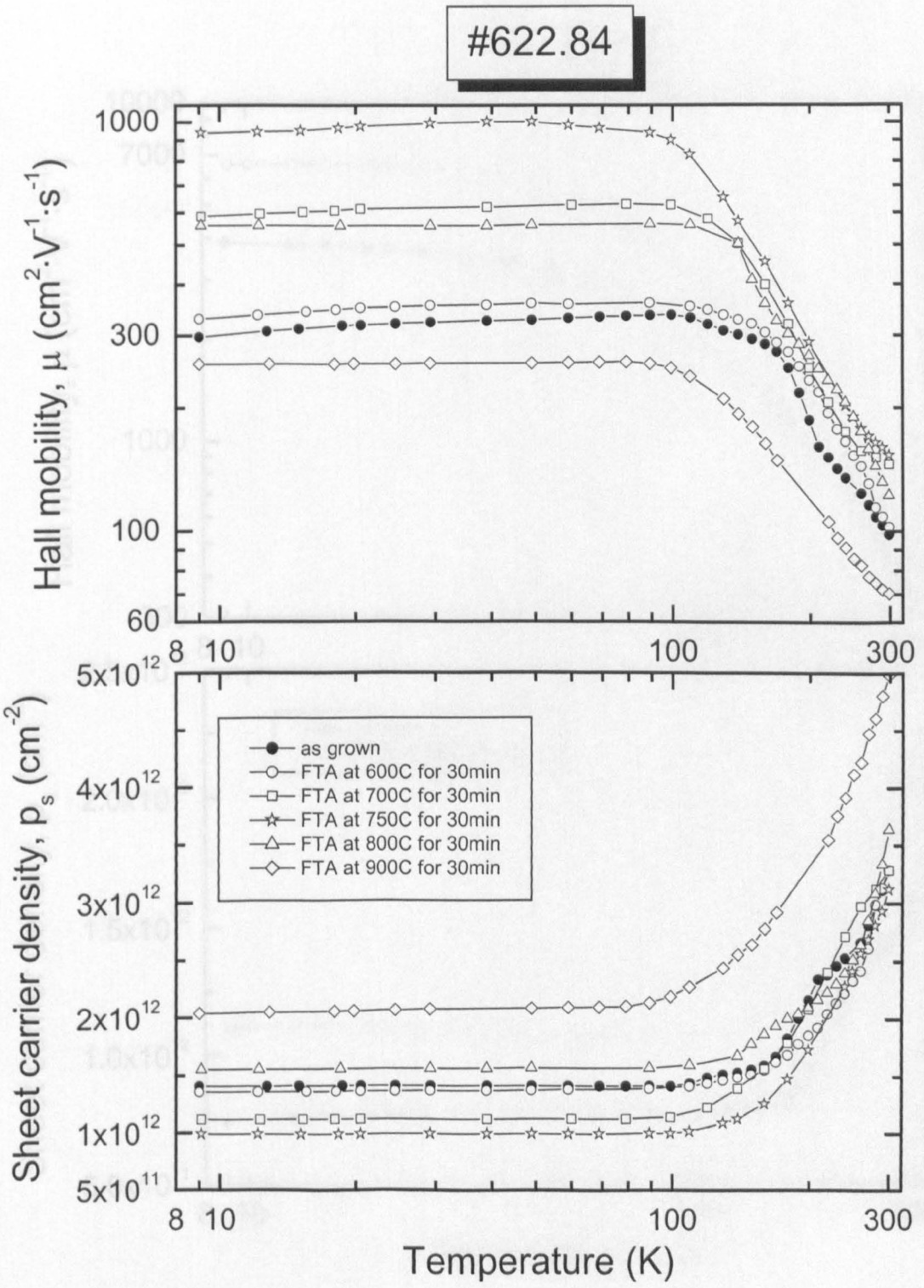

Figure 6.6 Temperature dependences of Hall mobility and sheet carrier density for as-grown sample #622.84 and after FTA at 600C, 700C, 750C, 800C and 900C for 30min.

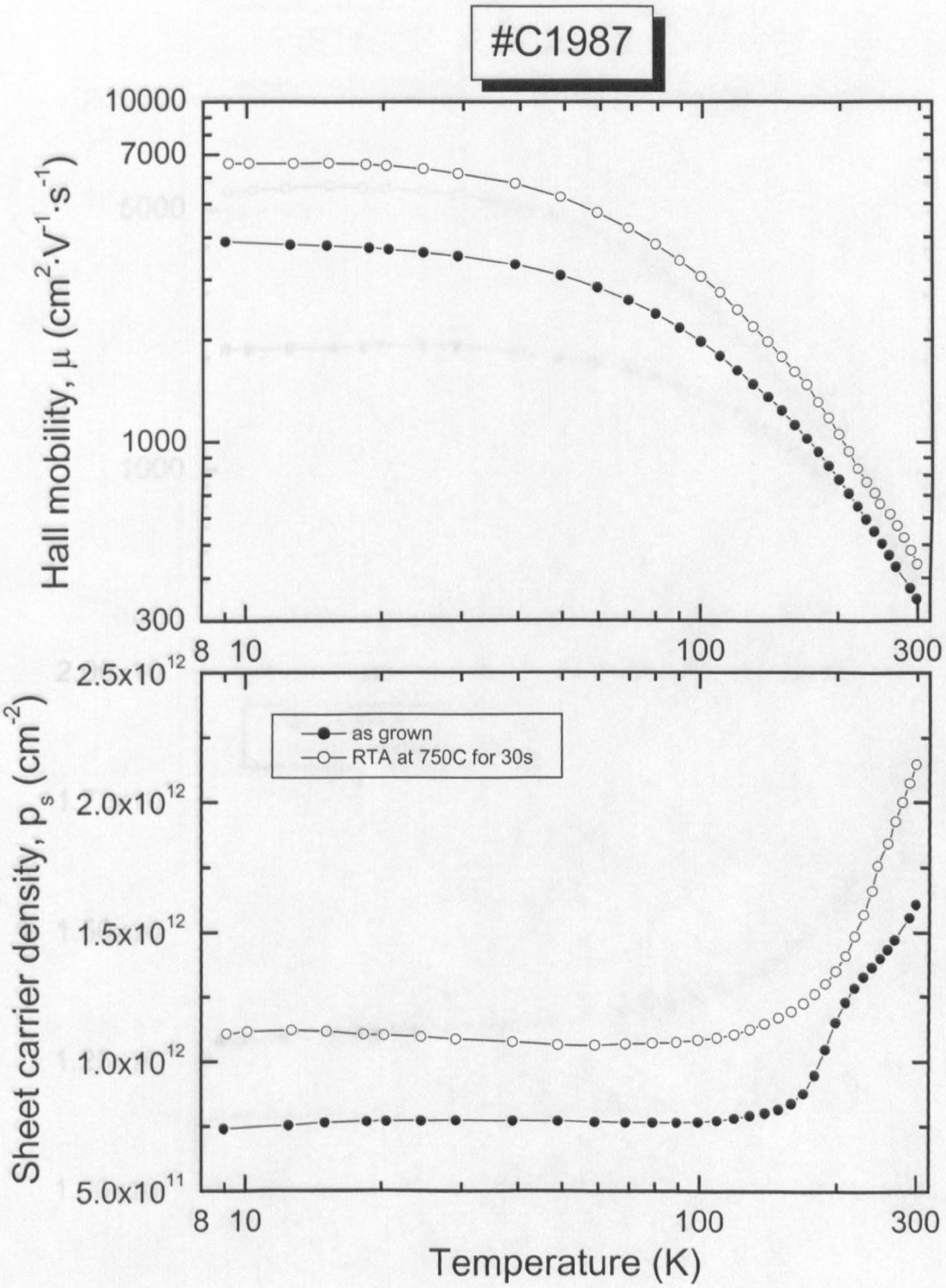

Figure 6.7 Temperature dependences of Hall mobility and sheet carrier density for as-grown sample #C1987 and after RTA at 750C for 30min.

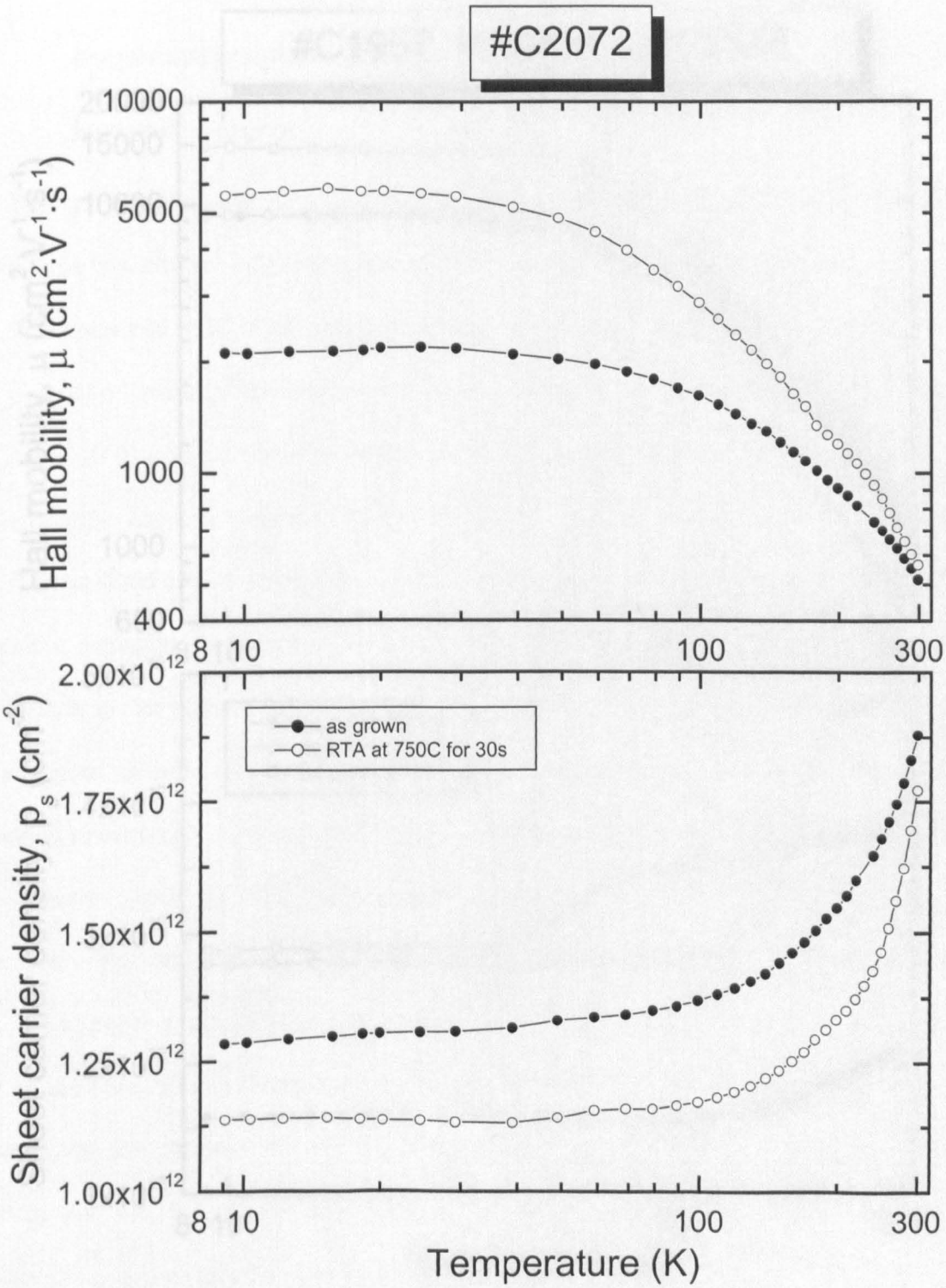

Figure 6.8 Temperature dependences of Hall mobility and sheet carrier density for as-grown sample #C2072 and after RTA at 750C for 30min.

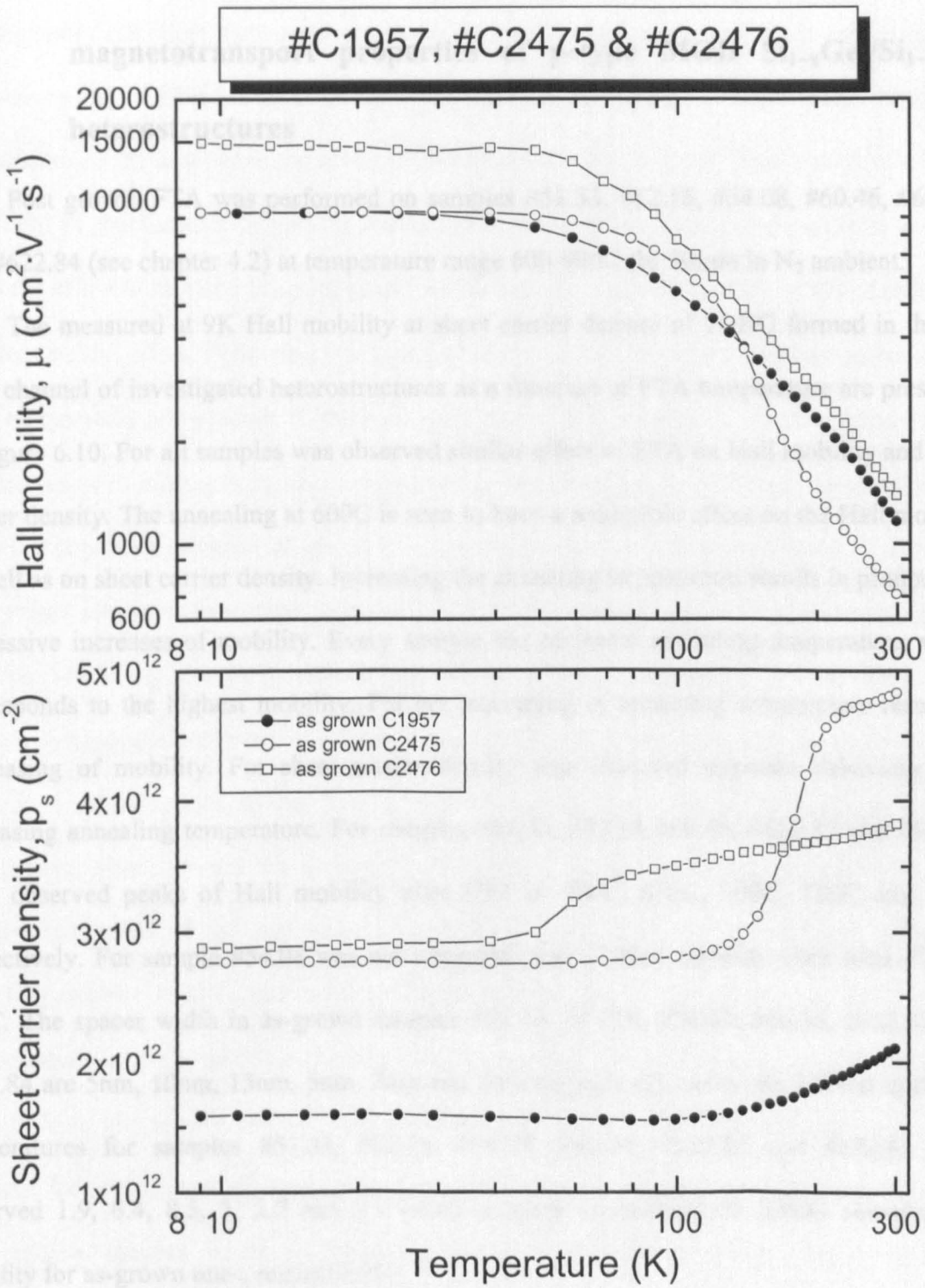

Figure 6.9 Temperature dependences of Hall mobility and sheet carrier density for as-grown samples #C1957, #C2475 and #C2476.

6.1.2.1 The effect of post growth furnace thermal annealing on magnetotransport properties of p-type MOD $Si_{1-x}Ge_x/Si_{1-y}Ge_y$ heterostructures

Post growth FTA was performed on samples #51.33, #52.16, #54.08, #60.46, #622.83 and #622.84 (see chapter 4.2) at temperature range 600-900C for 30min in N_2 ambient.

The measured at 9K Hall mobility at sheet carrier density of 2DHG formed in the $Si_{1-x}Ge_x$ channel of investigated heterostructures as a function of FTA temperature are presented in Figure 6.10. For all samples was observed similar effect of FTA on Hall mobility and sheet carrier density. The annealing at 600C is seen to have a negligible effect on the Hall mobility as well as on sheet carrier density. Increasing the annealing temperature results in pronounced successive increases of mobility. Every sample has optimum annealing temperature, which corresponds to the highest mobility. Further increasing of annealing temperature results in decreasing of mobility. For sheet carrier density was observed opposite behaviour with increasing annealing temperature. For samples #51.33, #52.16 #60.46, #622.83 and #622.84 were observed peaks of Hall mobility after FTA at 700C, 800C, 700C, 750C and 750C respectively. For sample #54.08 was not observed peak of Hall mobility even after FTA at 900C. The spacer width in as-grown samples #51.33, #52.16, #54.08, #60.46, #622.83 and #622.84 are 5nm, 10nm, 15nm, 5nm, 7nm and 7nm respectively. After the FTA at optimum temperatures for samples #51.33, #52.16, #54.08, #60.46, #622.83 and #622.84 were observed 1.9, 6.4, 8.5, 3, 2.7 and 3.1 times increase in mobility of 2DHG compared to mobility for as-grown ones, respectively.

The decrease of sheet carrier density was found to be consistent with the decreased hole transfer from B doped region to the $Si_{1-x}Ge_x$ channel due to Ge diffusion in the buffer\channel\spacer region during FTA, resulted in decreased Ge concentration in the channel and as consequence the valence band offset is decreased. As soon as the $Si_{1-y}Ge_y$ spacer width is decreased due to B diffusion from doped $Si_{1-y}Ge_y$ layer and Ge diffusion from

the $Si_{1-x}Ge_x$ channel (x>y) the carriers transfer from B doped region is increased. Consequently the sheet carrier density is increased. The decreasing of sheet carrier density with increasing of FTA temperature observed for investigated heterostructures (Figure 6.10) corresponds to the case when the effect of reduction of valence band offset is dominated. The minimum in sheet carrier density as a function of FTA temperature corresponds to the case when the effect of reduced $Si_{1-y}Ge_y$ spacer width becomes balanced by the effect of reduction of valence band offset. Following increasing of sheet carrier density with further increasing of FTA temperature corresponds to the case when the effect of reduced $Si_{1-y}Ge_y$ spacer width becomes more dominant in comparison with the effect of reduction of valence band offset.

The low Hall mobility observed in as-grown samples could be explained by effect of short-range interface roughness scattering due to not optimum growth conditions, remote impurity scattering and point defects that appear at low temperature growth because of reduced surface adatom mobility. When growing high Ge content $Si_{1-x}Ge_x$ channels by SS-MBE it is advantageous to use low growth temperatures to kinetically suppress surface segregation, which smears the Ge profile, and also to suppress surface diffusion that can produce roughness of the surface to relieve strain energy. As was mentioned before the annealing causes Ge diffusion in the buffer\channel\spacer region resulted in decreased Ge concentration in the channel and consequently increased $Si_{1-x}Ge_x$ channel width. Also the point defects are annihilated during annealing. The increase of Hall mobility after FTA observed for investigated heterostructures (Figure 6.10) can be associated with the reduction of interface roughness scattering due to smearing of channel/spacer interface and broadening of $Si_{1-x}Ge_x$ channel width L due to Ge diffusion because of $\mu_{IR} \propto L^6$ (see chapter 2.3.2.3). The mobility will increase until the effects of remote impurity scattering and alloy scattering begin to dominate. Mobility will be reducing due to the decreasing of spacer thickness L_s ($\mu_{RI} \propto L_s^3$,

see chapter 2.3.2.2) and decreasing of Ge composition x in the $Si_{1-x}Ge_x$ channel ($\mu_{AL} \propto \frac{L}{x \cdot (1-x)}$, see chapter 2.3.2.4).

The measured at 293K Hall mobility at sheet carrier density for investigated heterostructures as a function of FTA temperature are presented in Figure 6.11. For all samples was observed similar effect of FTA on Hall mobility and sheet carrier density as was observed at 9K. The annealing at 600C is seen to have a negligible effect on the Hall mobility as well as on sheet carrier density. Increasing the annealing temperature results in pronounced successive increases of mobility. Every sample has optimum annealing temperature, which corresponds to the highest mobility. Further increasing of annealing temperature results in decreasing of mobility. For samples #51.33, #52.16 #60.46, #622.83 and #622.84 were observed peaks of Hall mobility after FTA at 700C, 800C, 750C, 750C and 750C respectively. For sample #54.08 was not observed peak of Hall mobility even after FTA at 900C. After the FTA at optimum temperatures for samples #51.33, #52.16, #54.08, #60.46, #622.83 and #622.84 were observed 1.5, 1.5, 1.6, 18, 3 and 1.5 times increase in Hall mobility measured at 293K compared to mobility for as-grown ones, respectively.

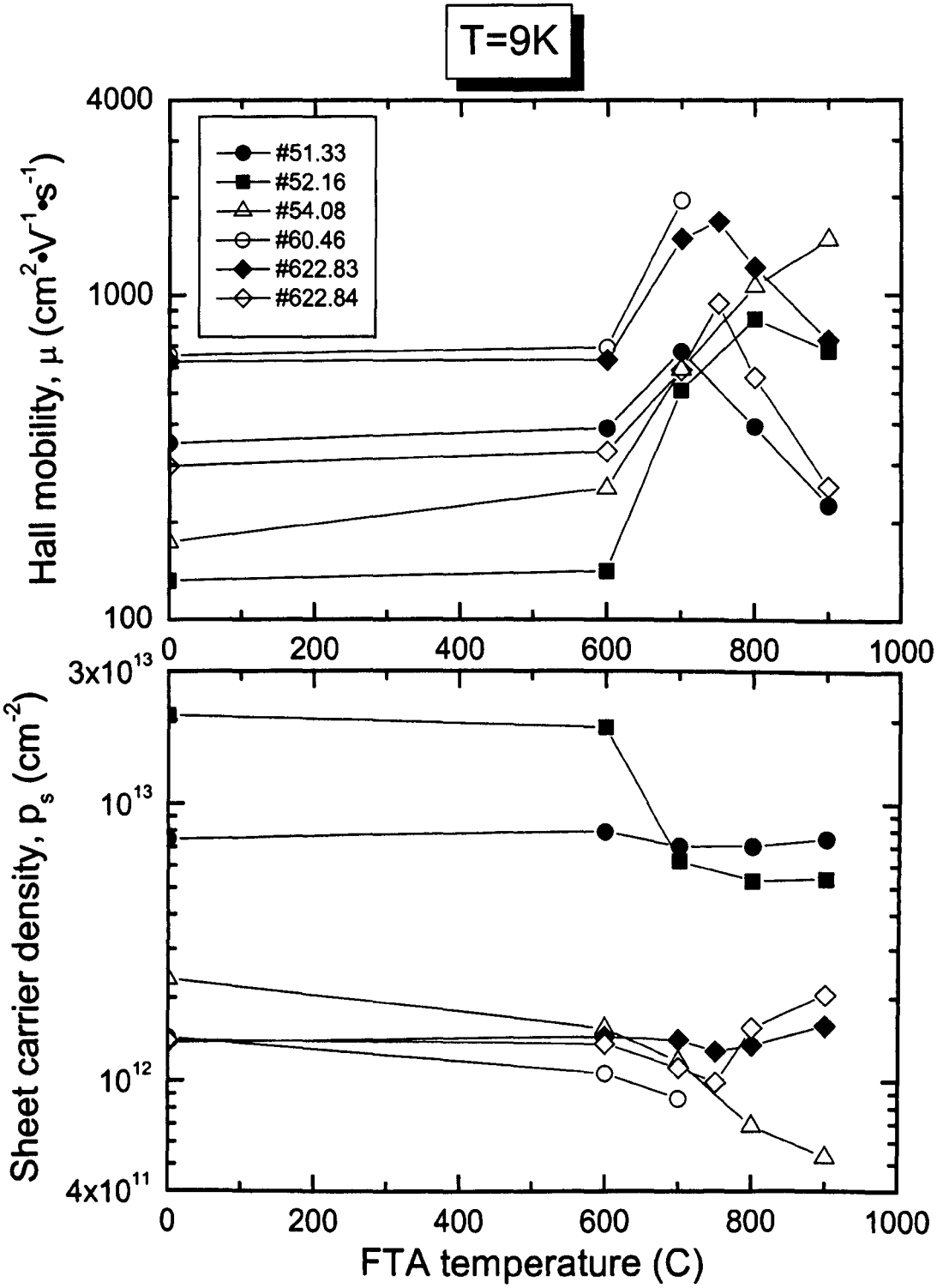

Figure 6.10 FTA effect on Hall mobility and sheet carrier density of 2DHG formed in the channel of samples #51.33, #52.16, #54.08, 60.46, #622.83 and #622.84 measured at 9K.

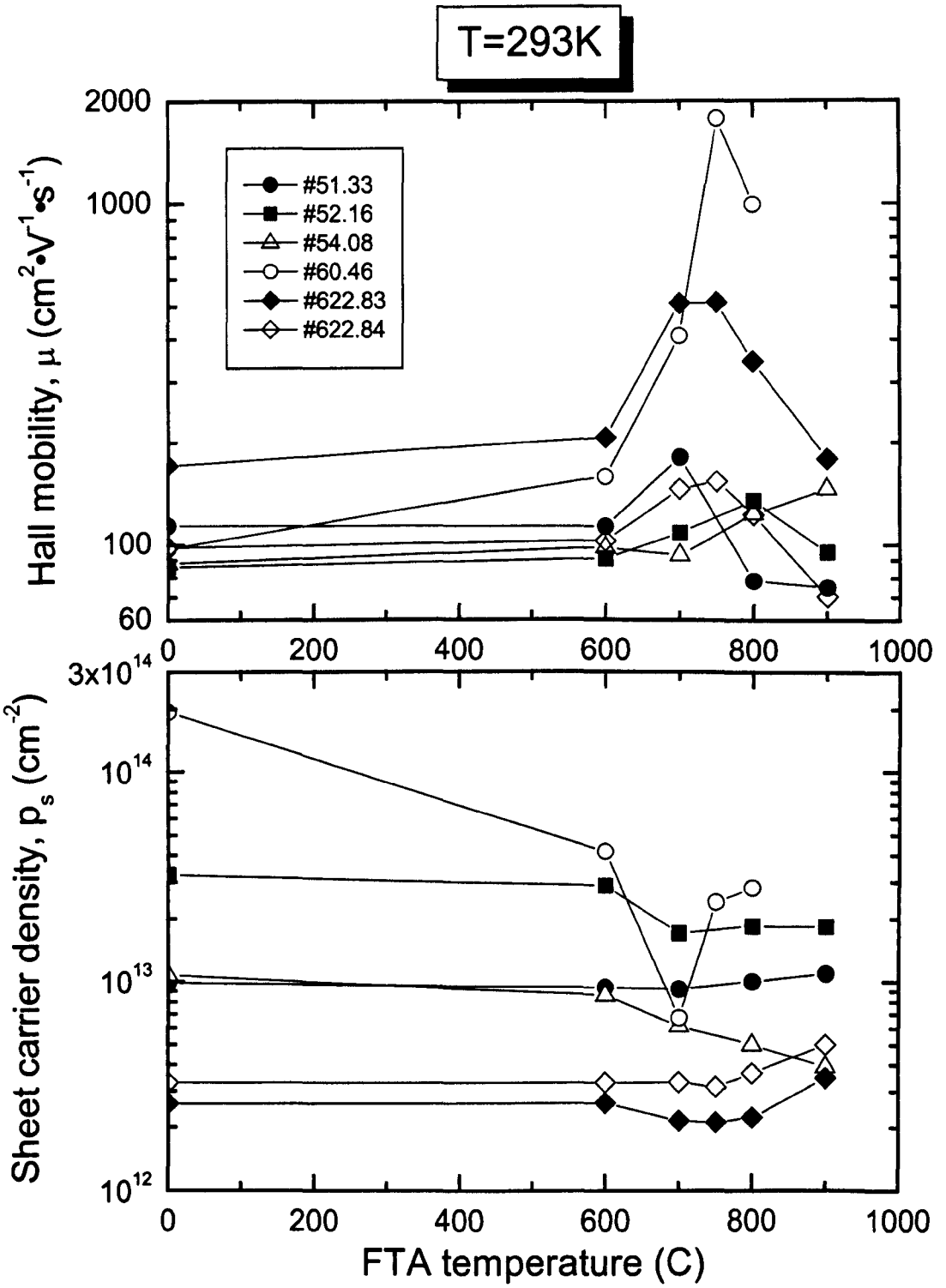

Figure 6.11 FTA effect on Hall mobility and sheet carrier density of samples #51.33, #52.16, #54.08, 60.46, #622.83 and #622.84 measured at 293K.

6.1.2.2 The effect of post growth rapid thermal annealing on magnetotransport properties of p-type MOD $Si_{1-x}Ge_x/Si_{1-y}Ge_y$ heterostructures

Post growth RTA was performed on samples #C1987, #C2015f and #C2072 (see chapter 4.2) at temperature 750C for 30sec in N_2 ambient.

The measured at 9K Hall mobility at sheet carrier density of 2DHG formed in the $Si_{1-x}Ge_x$ channel of investigated as-grown and after RTA heterostructures are presented in Table 6.1. For all samples was observed similar effect of RTA on Hall mobility. After the RTA at 750C for 30sec for samples #C1987, #C2015f and #C2072 were observed 1.7, 3, and 2.6 times increase in mobility of 2DHG compared to mobility for as-grown ones, respectively. For sample #C1987 after RTA was observed an increase in carrier sheet density but in samples #C2015f and #C2072 the carrier sheet density was decreased.

Table 6.1 Hall mobility and sheet carrier density of 2DHG formed in the $Si_{1-x}Ge_x$ channel of as-grown and after RTA at 750C for 30sec samples #C1987, #C2015f, #C2072 measured at 9K.

Sample ID		Channel/buffer (as-grown)	μ_{Hall} ($cm^2 \cdot V^{-1} \cdot s^{-1}$)	p_{Hall} (cm^{-2})
#C1987	As-grown	$Si_{0.34}Ge_{0.66}$/ $Si_{0.65}Ge_{0.35}$	3877	$7.41 \cdot 10^{11}$
	RTA at 750C for 30sec		6574	$1.10 \cdot 10^{12}$
#C2015f	As-grown	$Si_{0.18}Ge_{0.82}$/ $Si_{0.5}Ge_{0.5}$	2525	$1.10 \cdot 10^{12}$
	RTA at 750C for 30sec		7657	$1.00 \cdot 10^{12}$
#C2072	As-grown	$Si_{0.18}Ge_{0.82}$/ $Si_{0.47}Ge_{0.53}$	2102	$1.28 \cdot 10^{12}$
	RTA at 750C for 30 sec		5567	$1.13 \cdot 10^{12}$

The decrease of sheet carrier density observed after RTA in samples #C2015f and C2072 could be because of decreased hole transfer from B doped region to the $Si_{1-x}Ge_x$ channel due to Ge diffusion in the buffer\channel\spacer region during RTA, resulted in decreased Ge concentration in the channel and as consequence the valence band offset is decreased. The increase of sheet carrier density observed after RTA in sample #C1987 could

be because of the $Si_{1-y}Ge_y$ spacer width is decreased due to B diffusion from doped $Si_{1-y}Ge_y$ layer and Ge diffusion from the $Si_{1-x}Ge_x$ channel (x>y) and consequently the carriers transfer from B doped region is increased.

As was mentioned before the annealing causes Ge diffusion in the buffer\channel\spacer region resulted in decreased Ge concentration in the channel and consequently increased $Si_{1-x}Ge_x$ channel width. The increase of Hall mobility after RTA observed for investigated heterostructures (Table 6.1) can be associated with annihilation of point defects caused by low temperature growth and the reduction of interface roughness scattering due to smearing of channel/spacer interface and broadening of $Si_{1-x}Ge_x$ channel width L due to Ge diffusion because of $\mu_{IR} \propto L^6$ (see chapter 2.3.2.3).

The measured at 293K Hall mobility at sheet carrier density for investigated as-grown and after RTA heterostructures are presented in Table 6.2. For all samples was observed similar effect of RTA on Hall mobility and sheet carrier density as was observed at 9K. After the RTA at 750C for 30sec for samples #C1987, #C2015f and #C2072 were observed 1.2, 1.3, and 1.1 times increase in Hall mobility compared to mobility for as-grown ones, respectively. For sample #C1987 after RTA was observed an increase in carrier sheet density but in samples #C2015f and #C2072 the carrier sheet density was decreased.

Table 6.2 Hall mobility and sheet carrier density of as-grown and after RTA at 750C for 30sec samples #C1987, #C2015f, #C2072 measured at 293K.

Sample ID		Channel/buffer (as-grown)	μ_{Hall} ($cm^2 \cdot V^{-1} \cdot s^{-1}$)	p_{Hall} (cm^{-2})
#C1987	As-grown	$Si_{0.34}Ge_{0.66}$/ $Si_{0.65}Ge_{0.35}$	346	$1.60 \cdot 10^{12}$
	RTA at 750C for 30 sec		438	$2.14 \cdot 10^{12}$
#C2015f	As-grown	$Si_{0.18}Ge_{0.82}$/ $Si_{0.5}Ge_{0.5}$	498	$2.42 \cdot 10^{12}$
	RTA at 750C for 30sec		671	$1.72 \cdot 10^{12}$
#C2072	As-grown	$Si_{0.18}Ge_{0.82}$/ $Si_{0.47}Ge_{0.53}$	515	$1.87 \cdot 10^{12}$
	RTA at 750C for 30sec		564	$1.77 \cdot 10^{12}$

6.1.2.3 The effect of Ge composition in the $Si_{1-x}Ge_x$ channel and $Si_{1-y}Ge_y$ layers on magnetotransport properties of p-type MOD $Si_{1-x}Ge_x/Si_{1-y}Ge_y$ heterostructures

All investigated samples could be divided into three groups regarding to Ge composition in the $Si_{1-x}Ge_x$ channel. The first group consists of samples #54.08 and #1987 containing $Si_{0.4}Ge_{0.6}$ and $Si_{0.34}Ge_{0.66}$ channels respectively. For the as-grown samples from the first group the Ge composition in the $Si_{1-x}Ge_x$ channel is close to x=0.6. The second group consists of samples #52.16, #51.33, #60.46, #622.54, #622.83, #622.84, #C2015f and #C2072 containing $Si_{0.24}Ge_{0.76}$, $Si_{0.22}Ge_{0.78}$, $Si_{0.2}Ge_{0.8}$, $Si_{0.2}Ge_{0.8}$, $Si_{0.2}Ge_{0.8}$, $Si_{0.2}Ge_{0.8}$, $Si_{0.18}Ge_{0.82}$, and $Si_{0.18}Ge_{0.82}$ channels respectively. For the as-grown samples from the second group the Ge composition in the $Si_{1-x}Ge_x$ channel is around x=0.8. And the third group consists of samples #C1957, #C2475 and #C2476 containing $Si_{0.05}Ge_{0.95}$, $Si_{0.02}Ge_{0.98}$ and Ge channels respectively. For the samples from the third group the Ge composition in the $Si_{1-x}Ge_x$ channel is close to x=1.

Hall mobility and sheet carrier density of 2DHG formed in the $Si_{1-x}Ge_x$ channel of as-grown and after optimum thermal annealing samples #51.33, #52.16, #54.08, #60.46, #622.54, #622.83, #622.84, #C1957, #C1987, C2015f, #C2072, #C2475, #C2476 measured at 9K are presented in Table 6.3.

For the sample #54.08 containing $Si_{0.4}Ge_{0.6}$ channel grown on $Si_{0.7}Ge_{0.3}$ step graded VS the highest mobility (at sheet carrier density) of 2DHG was obtained after FTA at 900C for 30min and corresponds to $1477 cm^2 \cdot V^{-1} \cdot s^{-1}$ ($5.29 \cdot 10^{11} cm^{-2}$). For the sample #1987 containing $Si_{0.34}Ge_{0.66}$ channel grown on $Si_{0.65}Ge_{0.35}$ linearly graded VS the highest mobility (at sheet carrier density) of 2DHG was obtained after RTA at 750C for 30sec and corresponds to $6574 cm^2 \cdot V^{-1} \cdot s^{-1}$ ($1.10 \cdot 10^{12} cm^{-2}$). It is clear to see that the sample #C1987 has higher mobility of 2DHG measured at 9K.

Table 6.3 Hall mobility and sheet carrier density of 2DHG formed in the $Si_{1-x}Ge_x$ channel of as-grown and after optimum thermal annealing samples #51.33, #52.16, #54.08, #60.46, #622.54, #622.83, #622.84, #C1957, #C1987, C2015f, #C2072, #C2475, #C2476 measured at 9K.

Sample ID		Channel/buffer (as-grown)	μ_{Hall} ($cm^2 \cdot V^{-1} \cdot s^{-1}$)	p_{Hall} (cm^{-2})
#5408	As-grown	$Si_{0.4}Ge_{0.6}$/ $Si_{0.7}Ge_{0.3}$	173	$2.33 \cdot 10^{12}$
	FTA at 900C for 30min		1477	$5.29 \cdot 10^{11}$
#C1987	As-grown	$Si_{0.34}Ge_{0.66}$/ $Si_{0.65}Ge_{0.35}$	3877	$7.41 \cdot 10^{11}$
	RTA at 750C for 30sec		6574	$1.10 \cdot 10^{12}$
#5216	As-grown	$Si_{0.24}Ge_{0.76}$/ $Si_{0.7}Ge_{0.3}$	131	$2.08 \cdot 10^{13}$
	FTA at 800C for 30min		841	$5.29 \cdot 10^{12}$
#5133	As-grown	$Si_{0.22}Ge_{0.78}$/ $Si_{0.7}Ge_{0.3}$	350	$7.45 \cdot 10^{12}$
	FTA at 700C for 30min		670	$7.00 \cdot 10^{12}$
#6046	As-grown	$Si_{0.2}Ge_{0.8}$/ $Si_{0.7}Ge_{0.3}$	654	$1.43 \cdot 10^{12}$
	FTA at 700C for 30min		1955	$8.62 \cdot 10^{11}$
#62254	As-grown	$Si_{0.2}Ge_{0.8}$/ Si	154	$6.73 \cdot 10^{11}$
#62283	As-grown	$Si_{0.2}Ge_{0.8}$/ $Si_{0.7}Ge_{0.3}$	624	$1.37 \cdot 10^{12}$
	FTA at 750C for 30min		1680	$1.27 \cdot 10^{12}$
#62284	As-grown	$Si_{0.2}Ge_{0.8}$/ $Si_{0.7}Ge_{0.3}$	297	$1.40 \cdot 10^{12}$
	FTA at 750C for 30min		938	$9.86 \cdot 10^{11}$
#C2015f	As-grown	$Si_{0.18}Ge_{0.82}$/ $Si_{0.5}Ge_{0.5}$	2525	$1.10 \cdot 10^{12}$
	RTA at 750C for 30sec		7657	$1.00 \cdot 10^{12}$
#C2072	As-grown	$Si_{0.18}Ge_{0.82}$/ $Si_{0.47}Ge_{0.53}$	2102	$1.28 \cdot 10^{12}$
	RTA at 750C for 30sec		5567	$1.13 \cdot 10^{12}$
#C1957	As-grown	$Si_{0.05}Ge_{0.95}$/ $Si_{0.37}Ge_{0.63}$	9301	$1.58 \cdot 10^{12}$
#C2475	As-grown	$Si_{0.02}Ge_{0.98}$/ $Si_{0.41}Ge_{0.59}$	9309	$2.76 \cdot 10^{12}$
#C2476	As-grown	Ge/ $Si_{0.40}Ge_{0.60}$	14855	$2.87 \cdot 10^{12}$

The second group could be divided into series regarding to the type of used VS. Samples #51.33 and #52.16 contain $Si_{0.7}Ge_{0.3}$ step graded VS. Sample #60.46 contains relatively thin $Si_{0.65}Ge_{0.35}$ linearly graded VS. The thin $Si_{0.2}Ge_{0.8}$ channel in sample #622.54 was grown directly on Si, without intermediate VS. Samples #622.83 and #622.84 contain $Si_{0.7}Ge_{0.3}$ VS with LT-Si buffer. And samples #C2015f and #C2072 contain thick $Si_{0.5}Ge_{0.5}$ and $Si_{0.47}Ge_{0.53}$ linearly graded VS respectively. From the samples with $Si_{1-x}Ge_x$ channel grown on $Si_{0.7}Ge_{0.3}$ step graded VS the highest mobility (at sheet carrier density) of 2DHG

was obtained for the sample #52.16 after FTA at 800C for 30min and corresponds to $841cm^2 \cdot V^{-1} \cdot s^{-1}$ ($5.29 \cdot 10^{12} cm^{-2}$). For the sample #60.46 the highest mobility (at sheet carrier density) of 2DHG was obtained after FTA at 700C for 30min and corresponds to $1955cm^2 \cdot V^{-1} \cdot s^{-1}$ ($8.62 \cdot 10^{11} cm^{-2}$). For the sample #622.54 the mobility (at sheet carrier density) of 2DHG measured at 9K is $154cm^2 \cdot V^{-1} \cdot s^{-1}$ ($6.73 \cdot 10^{11} cm^{-2}$). From the samples with $Si_{0.2}Ge_{0.8}$ channel grown on $Si_{0.7}Ge_{0.3}$ VS with LT-Si buffer the highest mobility (at sheet carrier density) of 2DHG was obtained for the sample #622.83 after FTA at 750C for 30min and corresponds to $1680cm^2 \cdot V^{-1} \cdot s^{-1}$ ($1.27 \cdot 10^{12} cm^{-2}$). From the samples with $Si_{0.18}Ge_{0.82}$ channel grown on thick $Si_{0.5}Ge_{0.5}$ linearly graded VS the highest mobility (at sheet carrier density) of 2DHG was obtained for the sample #C2015f after RTA at 750C for 30sec and corresponds to $7657cm^2 \cdot V^{-1} \cdot s^{-1}$ ($1.00 \cdot 10^{12} cm^{-2}$). It is clear to see that for samples from second group the highest mobility of 2DHG measured at 9K was observed in the sample #C2015f containing $Si_{0.18}Ge_{0.82}$ channel grown on thick $Si_{0.5}Ge_{0.5}$ linearly graded VS.

For the samples from the third group with Ge composition in the $Si_{1-x}Ge_x$ channel closed to 1 and grown on thick $Si_{0.4}Ge_{0.6}$ linearly graded VS the highest mobility (at sheet carrier density) of 2DHG measured at 9K was observed for sample #C2476 and corresponds to $14855cm^2 \cdot V^{-1} \cdot s^{-1}$ ($2.87 \cdot 10^{12} cm^{-2}$).

Hall mobility and sheet carrier density of as-grown and after optimum thermal annealing samples #51.33, #52.16, #54.08, #60.46, #622.54, #622.83, #622.84, #C1957, #C1987, C2015f, #C2072, #C2475, #C2476 measured at 293K are presented in Table 6.4.

From the first group of samples the highest mobility (at sheet carrier density) measured at 293K was observed for sample #C1987 after RTA at 750C for 30sec and corresponds to $438cm^2 \cdot V^{-1} \cdot s^{-1}$ ($2.14 \cdot 10^{12} cm^{-2}$).

From the second group of samples the highest mobility (at sheet carrier density) measured at 293K was observed for sample #C60.46 after FTA at 750C for 30min and corresponds to $1776cm^2 \cdot V^{-1} \cdot s^{-1}$ ($2.37 \cdot 10^{13} cm^{-2}$).

And from the third group of samples the highest mobility (at sheet carrier density) measured at 293K was observed for sample #C2476 and corresponds to $1380cm^2 \cdot V^{-1} \cdot s^{-1}$ ($3.82 \cdot 10^{12} cm^{-2}$).

Table 6.4 Hall mobility and sheet carrier density of as-grown and after optimum thermal annealing samples #51.33, #52.16, #54.08, #60.46, #622.54, #622.83, #622.84, #C1957, #C1987, C2015f, #C2072, #C2475, #C2476 measured at 293K.

Sample ID		Channel/buffer (as-grown)	μ_{Hall} ($cm^2 \cdot V^{-1} \cdot s^{-1}$)	p_{Hall} (cm^{-2})
#5408	As-grown	$Si_{0.4}Ge_{0.6}$/ $Si_{0.7}Ge_{0.3}$	88	$1.07 \cdot 10^{13}$
	FTA at 900C for 30min		145	$3.90 \cdot 10^{12}$
#C1987	As-grown	$Si_{0.34}Ge_{0.66}$/ $Si_{0.65}Ge_{0.35}$	346	$1.60 \cdot 10^{12}$
	RTA at 750C for 30sec		438	$2.14 \cdot 10^{12}$
#5216	As-grown	$Si_{0.24}Ge_{0.76}$/ $Si_{0.7}Ge_{0.3}$	85	$3.23 \cdot 10^{13}$
	FTA at 800C for 30min		134	$1.82 \cdot 10^{13}$
#5133	As-grown	$Si_{0.22}Ge_{0.78}$/ $Si_{0.7}Ge_{0.3}$	113	$9.82 \cdot 10^{12}$
	FTA at 700C for 30min		180	$9.14 \cdot 10^{12}$
#6046	As-grown	$Si_{0.2}Ge_{0.8}$/ $Si_{0.7}Ge_{0.3}$	97	$1.92 \cdot 10^{14}$
	FTA at 750C for 30min		1776	$2.37 \cdot 10^{13}$
#62254	As-grown	$Si_{0.2}Ge_{0.8}$/ Si	128	$5.73 \cdot 10^{12}$
#62283	As-grown	$Si_{0.2}Ge_{0.8}$/ $Si_{0.7}Ge_{0.3}$	170	$2.60 \cdot 10^{12}$
	FTA at 750C for 30min		512	$2.11 \cdot 10^{12}$
#62284	As-grown	$Si_{0.2}Ge_{0.8}$/ $Si_{0.7}Ge_{0.3}$	98	$3.28 \cdot 10^{12}$
	FTA at 750C for 30min		153	$3.11 \cdot 10^{12}$
#C2015f	As-grown	$Si_{0.18}Ge_{0.82}$/ $Si_{0.5}Ge_{0.5}$	498	$2.42 \cdot 10^{12}$
	RTA at 750C for 30sec		671	$1.72 \cdot 10^{12}$
#C2072	As-grown	$Si_{0.18}Ge_{0.82}$/ $Si_{0.47}Ge_{0.53}$	515	$1.87 \cdot 10^{12}$
	RTA at 750C for 30sec		564	$1.77 \cdot 10^{12}$
#C1957	As-grown	$Si_{0.05}Ge_{0.95}$/ $Si_{0.37}Ge_{0.63}$	1161	$2.10 \cdot 10^{12}$
#C2475	As-grown	$Si_{0.02}Ge_{0.98}$/ $Si_{0.41}Ge_{0.59}$	711	$4.83 \cdot 10^{12}$
#C2476	As-grown	Ge/ $Si_{0.40}Ge_{0.60}$	1380	$3.82 \cdot 10^{12}$

6.1.3 Conclusions

In this research were investigated p-type MOD $Si_{1-x}Ge_x/Si_{1-y}Ge_y$ heterostructures with Ge composition in the $Si_{1-x}Ge_x$ channel varied from 0.6 up to 1 and grown on linearly graded, step graded or with LT-Si buffer $Si_{1-y}Ge_y$ VS with $0.3 \leq y \leq 0.63$. Hall mobility and sheet carrier

density of p-type MOD $Si_{1-x}Ge_x/Si_{1-y}Ge_y$ heterostructures were obtained from the combination of resistivity and Hall effect techniques at temperature range 9-300K. The measurements were performed on as-grown and after FTA and RTA samples. Post growth FTA was performed on samples #51.33, #52.16, #54.08, #60.46, #622.83 and #622.84 (see chapter 4.2) at temperature range 600-900C for 30min in N_2 ambient. Post growth RTA was performed on samples #C1987, #C2015f and #C2072 (see chapter 4.2) at temperature 750C for 30sec in N_2 ambient.

For all investigated samples was observed similar effect of FTA on Hall mobility and sheet carrier density measured at 9 and 293K. The annealing at 600C is seen to have a negligible effect on the Hall mobility as well as on sheet carrier density. Increasing the annealing temperature results in pronounced successive increases of mobility. Every sample has optimum annealing temperature, which corresponds to the highest mobility. Further increasing of annealing temperature results in decreasing of mobility. For sheet carrier density was observed opposite behaviour with increasing annealing temperature. The maximum increase of Hall mobility measured at 9K was observed in sample #54.08 after FTA at 900C and corresponds to 8.5 times. But the maximum increase of Hall mobility measured at 293K was observed in sample #60.46 after FTA at 750C and corresponds to 18 times.

For all investigated samples was observed similar effect of RTA on Hall mobility measured at 9 and 293K. After the RTA at 750C for 30sec was observed an increase in mobility compared to as-grown ones. The maximum increase of Hall mobility after RTA measured at 9 and 293K were observed in sample #C2015f and corresponds to 3.8 and 1.3 times respectively.

The highest mobility (at sheet carrier density) of 2DHG measured at 9K was observed for sample #C2476 containing Ge channel grown on thick $Si_{0.4}Ge_{0.6}$ linearly graded VS and corresponds to $14855 cm^2 \cdot V^{-1} \cdot s^{-1}$ ($2.87 \cdot 10^{12} cm^{-2}$).

The highest Hall mobility (at sheet carrier density) measured at 293K was observed for sample #60.46 after FTA at 750C for 30min and corresponds to $1776cm^2 \cdot V^{-1} \cdot s^{-1}$ ($2.37 \cdot 10^{13} cm^{-2}$). The as-grown sample #60.46 consists of $Si_{0.2}Ge_{0.8}$ channel grown on $Si_{0.65}Ge_{0.35}$ linearly graded VS. This value of Hall mobility (at sheet carrier density) measured at room temperature is the highest ever reported for p-type MOD $Si_{1-x}Ge_x/Si_{1-y}Ge_y$ heterostructures.

6.2 Room temperatures magnetotransport properties of 2DHG formed in the $Si_{1-x}Ge_x$ channel of p-type MOD $Si_{1-x}Ge_x/Si_{1-y}Ge_y$ heterostructures: Maximum-entropy mobility spectrum analysis

6.2.1 Introduction

To extract the room temperature drift mobility and sheet carrier density of 2DHG the magnetic field dependences of magnetoresistance and Hall resistance were measured in cryomagnetic system as the magnetic field was swept continuously up to 11T. The measured data were analysed with the help of MEMSA and the values of drift mobility and sheet carrier density of 2DHG formed in the $Si_{1-x}Ge_x$ channel of investigated p-type MOD $Si_{1-x}Ge_x/Si_{1-y}Ge_y$ heterostructures were obtained. These measurements followed by MEMSA were done on samples #60.46 after FTA at 750C for 30min, #C2072 after RTA at 750C for 30sec and #C1957.

6.2.2 Results and discussion

The MEMSA were performed without making the assumption about the number of carrier groups. The benefit of MEMSA over other techniques of mobility spectrum analysis (see 2.3.4.1) is that MEMSA can use all available data points while, for example, BAMSA only uses between 2-6 data points. The number of mobility points used in MEMSA was typically around 300 while the number of magnetic field points varies between 50 and 300 in order to optimise the calculation time. The trend is that one needs to use more magnetic field points as the temperature increases because of the mobility of the sample decreases and hence B_{max} increases. The calculation time increases proportionally to the square of the product of the number of mobility and magnetic field points. The iteration process converges rapidly at the beginning. As soon as all the peaks emerge, the convergence continues at slower speed with the peaks only getting sharper. The calculations were usually continued until the error

does not decrease significantly over a certain number of iterations and all peaks completely separated. The typical iterations of 10^6-10^9 were tested to yield the correct MEMSA within the experimental error. The number of iterations strongly depends from the mobility of 2DHG and other carries presented in the heterostructure, and decrease with decrease of temperature. At low temperatures the 2DHG peak was dominated. As the temperature increases, the 2DHG peak moves toward the B:SiGe peak. At sufficiently high temperatures, these two peaks merge and only one peak can be observed that causes to perform more iterations until all peaks are observed and completely separated. The σ_{xx}(total) and σ_{xy}(total) correspond to measured σ_{xx} and σ_{xy} while σ_{xx}(2DHG) and σ_{xy}(2DHG) correspond to ones calculated using extracted from MEMSA values of drift mobility and sheet carrier density by:

$$\sigma_{xx}(B) = \frac{e \cdot p_s \cdot \mu}{1 + (\mu \cdot B)^2} \tag{6.1}$$

$$\sigma_{xy}(B) = \frac{e \cdot p_s \cdot \mu^2 \cdot B}{1 + (\mu \cdot B)^2} \tag{6.2}$$

MEMS (top) as the result of σ_{xx} and σ_{xy} fit (bottom) measured at 221K for sample #60.46 after FTA at 750C for 30min are presented in Figure 6.12. The number of performed iterations is $50 \cdot 10^6$. Fitted magnetic field dependences of σ_{xx} and σ_{xy} are in very good agreement with measured ones (Figure 6.12). MEMS consist of peaks corresponded to 2DHG formed in the $Si_{1-x}Ge_x$ channel, carriers in B doped $Si_{0.65}Ge_{0.35}$ layer, and electron-like carriers. The drift mobility (at sheet carrier density) of 2DHG at 221K extracted from MEMS is $7669 cm^2 \cdot V^{-1} \cdot s^{-1}$ ($3.57 \cdot 10^{12} cm^{-2}$).

At 290K were performed $300 \cdot 10^6$ iterations to completely resolve all peaks in MEMS for sample #60.46 after FTA at 750C for 30min (top of Figure 6.13). Fitted magnetic field dependences of σ_{xx} and σ_{xy} are in very good agreement with measured ones (bottom of Figure 6.13). The drift mobility (at sheet carrier density) of 2DHG at 290K extracted from MEMS is $3607 cm^2 \cdot V^{-1} \cdot s^{-1}$ ($4.94 \cdot 10^{12} cm^{-2}$).

Temperature dependences of drift mobility and sheet carrier density of 2DHG formed in the $Si_{1-x}Ge_x$ channel obtained with the help of MEMSA, and measured by combination of resistivity and Hall effect techniques Hall mobility and sheet carrier density at 290K for sample #60.46 after FTA at 750C for 30min are presented in Figure 6.14. At temperature range 220-290K the drift mobility of 2DHG increases with the decrease of temperature and sheet carrier density decreases with the decrease of temperature.

MEMS (top) as the result of σ_{xx} and σ_{xy} fit (bottom) measured at 293K for sample #C1957 are presented in Figure 6.15. The number of performed iterations is $300 \cdot 10^6$. Fitted magnetic field dependences of σ_{xx} and σ_{xy} are in very good agreement with measured ones (Figure 6.15). MEMS consist of peaks corresponded to 2DHG formed in the $Si_{0.05}Ge_{0.95}$ channel, carriers in B doped $Si_{0.37}Ge_{0.63}$ layer, and electron-like carriers. The drift mobility (at sheet carrier density) of 2DHG at 293K extracted from MEMS is $1906 cm^2 \cdot V^{-1} \cdot s^{-1}$ ($3.99 \cdot 10^{11} cm^{-2}$).

Room temperature drift mobility and sheet carrier density of 2DHG formed in the $Si_{1-x}Ge_x$ channel obtained by MEMSA and measured by combination of resistivity and Hall effect techniques Hall mobility and sheet carrier density for samples #60.46 after FTA at 750C for 30min, #C2072 after RTA at 750C for 30sec and #C1957 are presented in Table 6.5.

Table 6.5 Room temperature drift mobility and sheet carrier density of 2DHG formed in the $Si_{1-x}Ge_x$ channel obtained by MEMSA and measured by combination of resistivity and Hall effect techniques Hall mobility and sheet carrier density for samples #60.46 after FTA at 750C for 30min, #C2072 after RTA at 750C for 30sec and #C1957.

Sample ID	Channel/buffer (as-grown)	μ_d(2DHG) ($cm^2 \cdot V^{-1} \cdot s^{-1}$)	p_s(2DHG) (cm^{-2})	μ_{Hall} ($cm^2 \cdot V^{-1} \cdot s^{-1}$)	p_{Hall} (cm^{-2})
#60.46 (FTA at 750C for 30min)	$Si_{0.2}Ge_{0.8}$/ $Si_{0.65}Ge_{0.35}$	3607	$4.94 \cdot 10^{12}$	1776	$2.37 \cdot 10^{13}$
#C2072 (RTA at 750C for 30sec)	$Si_{0.18}Ge_{0.82}$/ $Si_{0.47}Ge_{0.53}$	1534	$1.86 \cdot 10^{11}$	564	$1.77 \cdot 10^{12}$
#C1957	$Si_{0.05}Ge_{0.95}$/ $Si_{0.37}Ge_{0.63}$	1906	$3.99 \cdot 10^{11}$	1161	$2.10 \cdot 10^{12}$

For all investigated samples the drift mobility of 2DHG formed in the $Si_{1-x}Ge_x$ channel is higher than the measured Hall mobility of heterostructure. The opposite situation is observed with sheet carrier density. For sample #C2072 after RTA at 750C for 30sec the drift mobility (at sheet carrier density) of 2DHG corresponds to $1534cm^2 \cdot V^{-1} \cdot s^{-1}$ ($1.86 \cdot 10^{11} cm^{-2}$). The as-grown sample #C2072 consists of $Si_{0.18}Ge_{0.82}$ channel grown on $Si_{0.47}Ge_{0.53}$ linearly graded VS. For sample #C1957 the drift mobility (at sheet carrier density) of 2DHG formed in the $Si_{0.05}Ge_{0.95}$ channel grown on $Si_{0.37}Ge_{0.63}$ linearly graded VS corresponds to $1906cm^2 \cdot V^{-1} \cdot s^{-1}$ ($3.99 \cdot 10^{11} cm^{-2}$). The highest mobility (at sheet carrier density) of 2DHG was obtained for sample #60.46 after FTA at 750C for 30min and corresponds to $3607cm^2 \cdot V^{-1} \cdot s^{-1}$ ($4.94 \cdot 10^{12} cm^{-2}$). The as-grown sample #60.46 consists of $Si_{0.2}Ge_{0.8}$ channel grown on $Si_{0.65}Ge_{0.35}$ linearly graded VS.

The results of MEMSA of p-type MOD $Si_{1-x}Ge_x/Si_{1-y}Ge_y$ heterostructures were presented at "11^{th} General Conference of the European Physical Society (EPS-11): Trends in Physics"[11], "10^{th} European Heterostructure Technology Workshop"[12], "International Conference on Solid State Crystals 2000: Materials Science and Applications"[13] and "SiGe (C) 2001 Workshop"[10].

6.2.3 Conclusions

The room temperature magnetotransport properties of 2DHG formed in the $Si_{1-x}Ge_x$ channel of p-type MOD $Si_{1-x}Ge_x/Si_{1-y}Ge_y$ heterostructures were studied by measuring magnetic field dependences of magnetoresistance and Hall resistance followed by applying the technique of MEMSA. The investigated samples consist of $Si_{1-x}Ge_x$ channel with $0.8<x<0.95$ and $Si_{1-y}Ge_y$ linearly graded with VS $0.35<y<0.63$. The highest drift mobility (at sheet carrier density) of 2DHG was obtained for sample #60.46 after FTA at 750C for 30min and corresponds to $3607cm^2 \cdot V^{-1} \cdot s^{-1}$ ($4.94 \cdot 10^{12} cm^{-2}$). The as-grown sample #60.46 consists of

$Si_{0.2}Ge_{0.8}$ channel grown on $Si_{0.65}Ge_{0.35}$ linearly graded VS. This value of 2DHG mobility (at sheet carrier density) measured at room temperature is the highest ever reported for p-type MOD $Si_{1-x}Ge_x/Si_{1-y}Ge_y$ heterostructures. For this sample was obtained the temperature dependence of mobility and sheet carrier density of 2DHG without parallel conduction in the temperature range 221-290K. It was found that the drift mobility of 2DHG increases with the decrease of temperature and sheet carrier density decreases with the decrease of temperature.

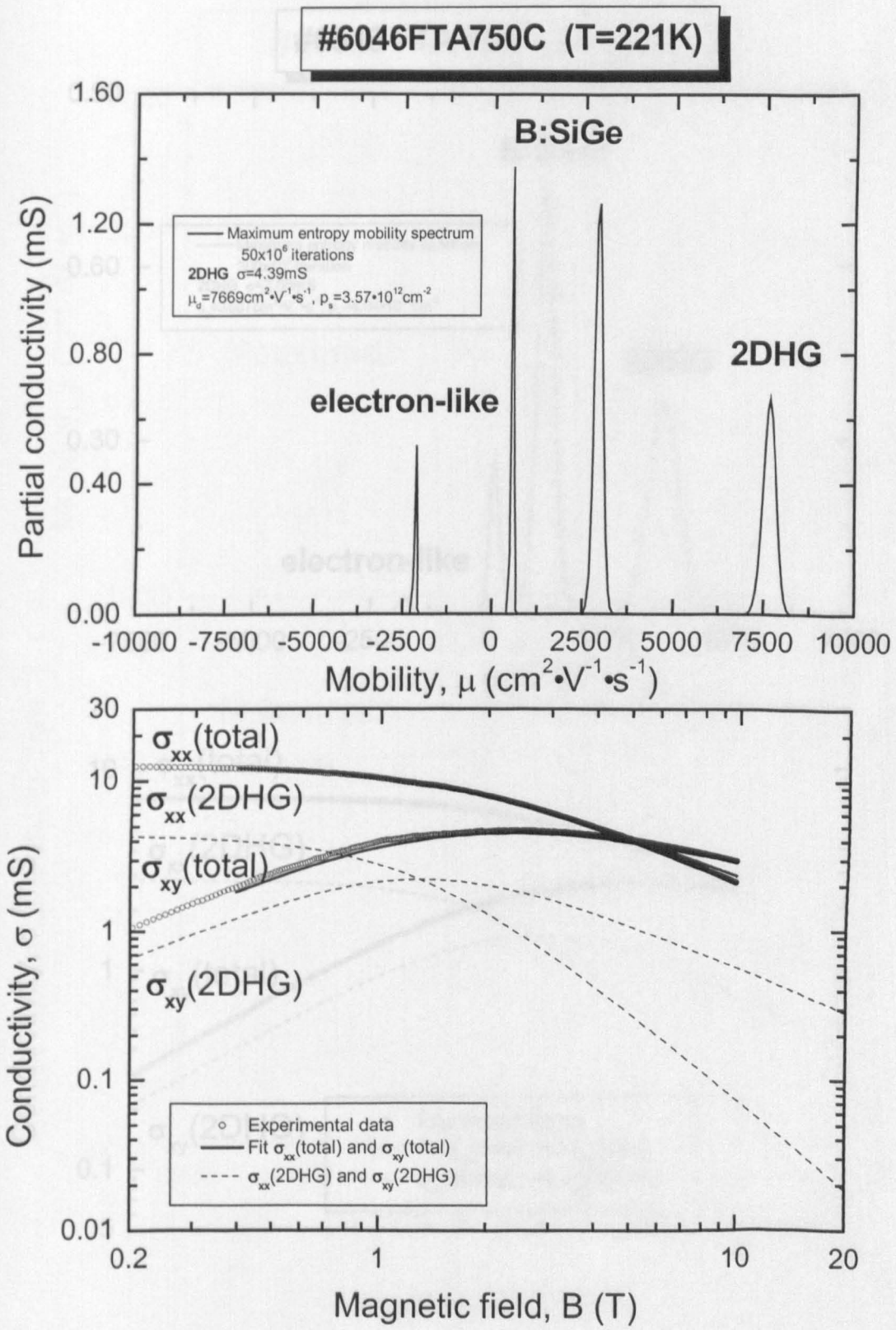

Figure 6.12 MEMS (top) as the result of σ_{xx} and σ_{xy} fit (bottom) measured at 221K for sample #60.46 after FTA at 750C for 30min.

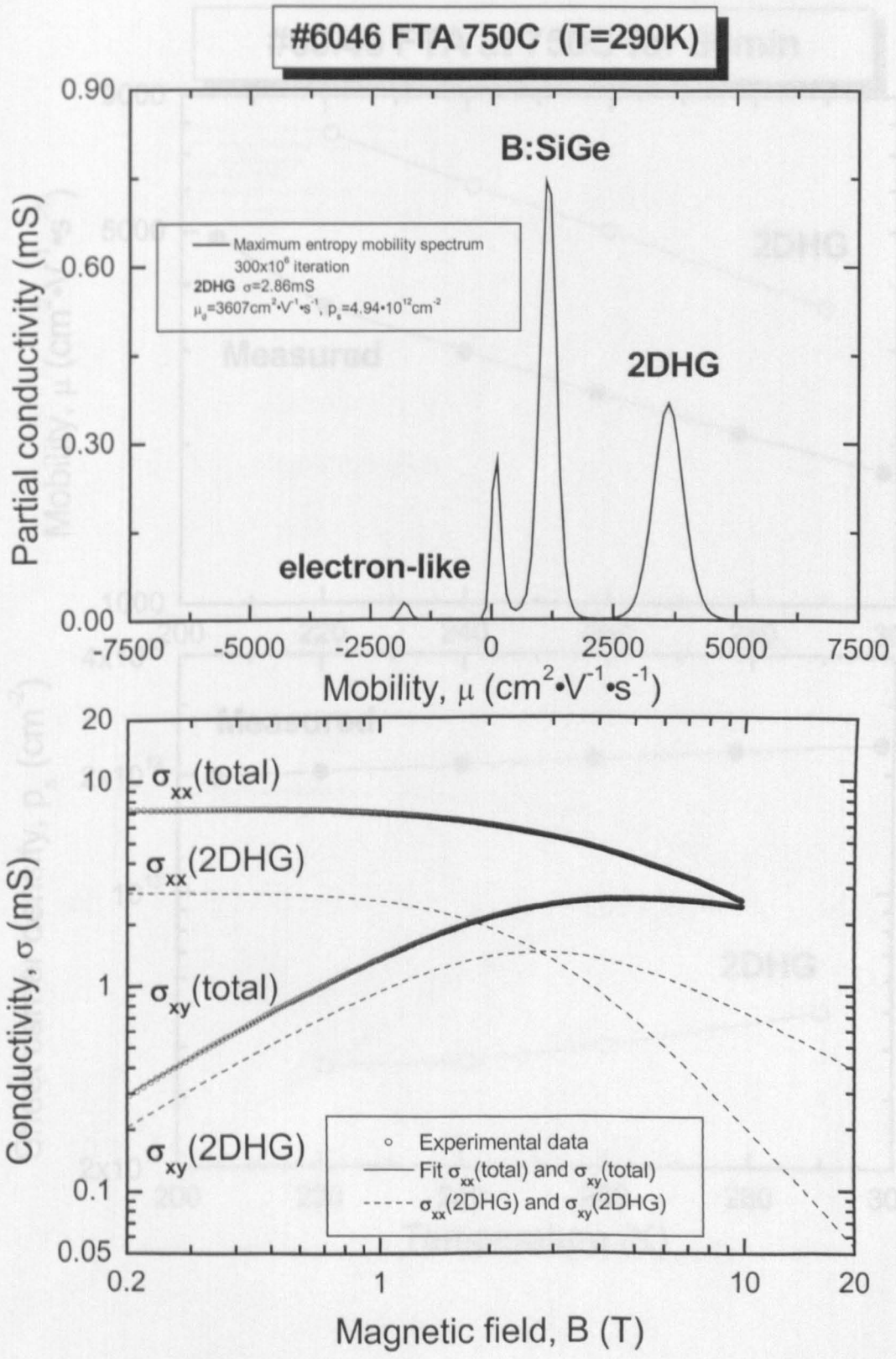

Figure 6.13 MEMS (top) as the result of σ_{xx} and σ_{xy} fit (bottom) measured at 290K for sample #60.46 after FTA at 750C for 30min.

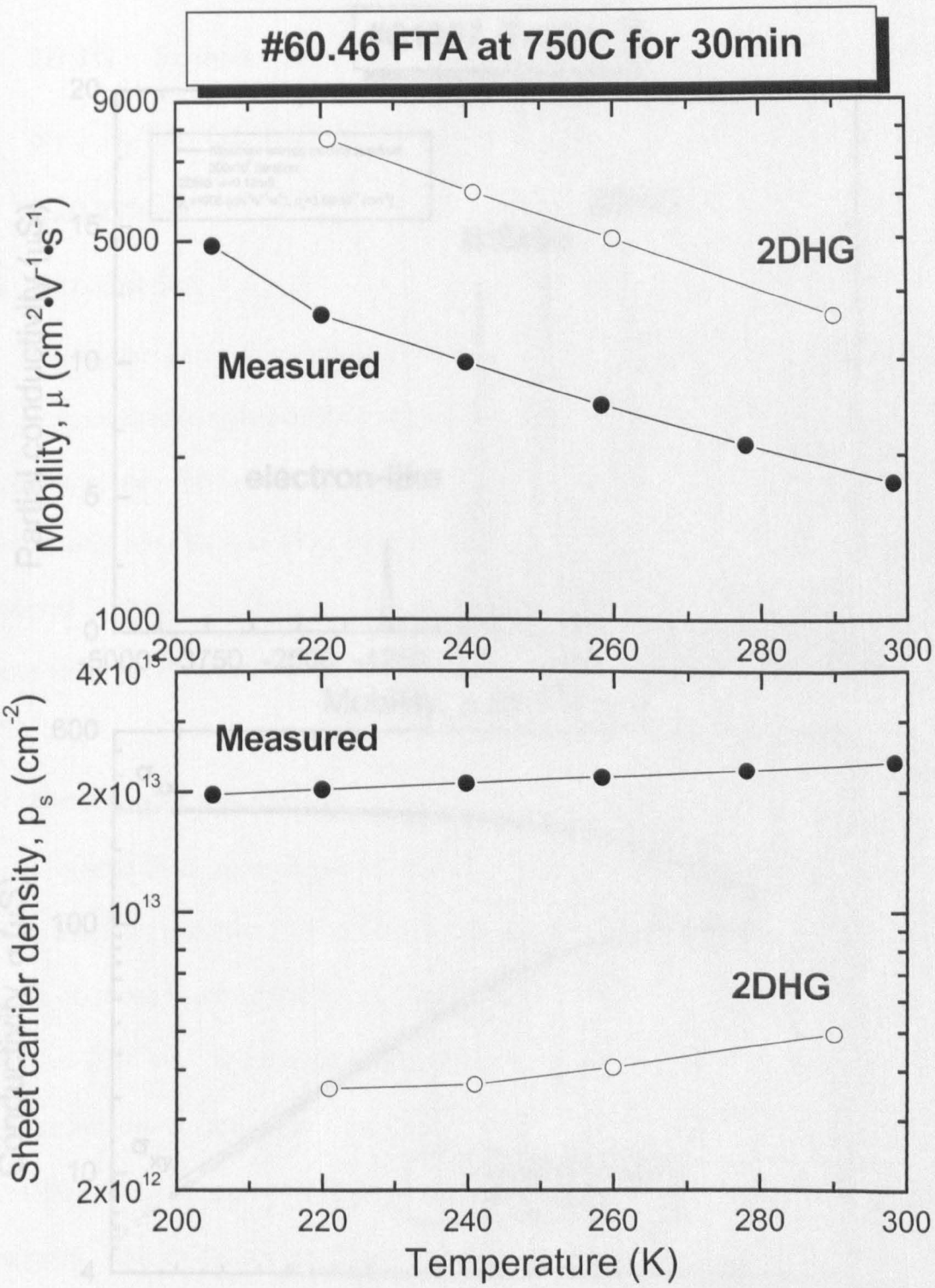

Figure 6.14 Temperature dependences of drift mobility and sheet carrier density (o) of 2DHG formed in the $Si_{1-x}Ge_x$ channel obtained with the help of MEMSA, and measured by combination of resistivity and Hall effect techniques Hall mobility and sheet carrier density (•) at 290K for sample #60.46 after FTA at 750C for 30min.

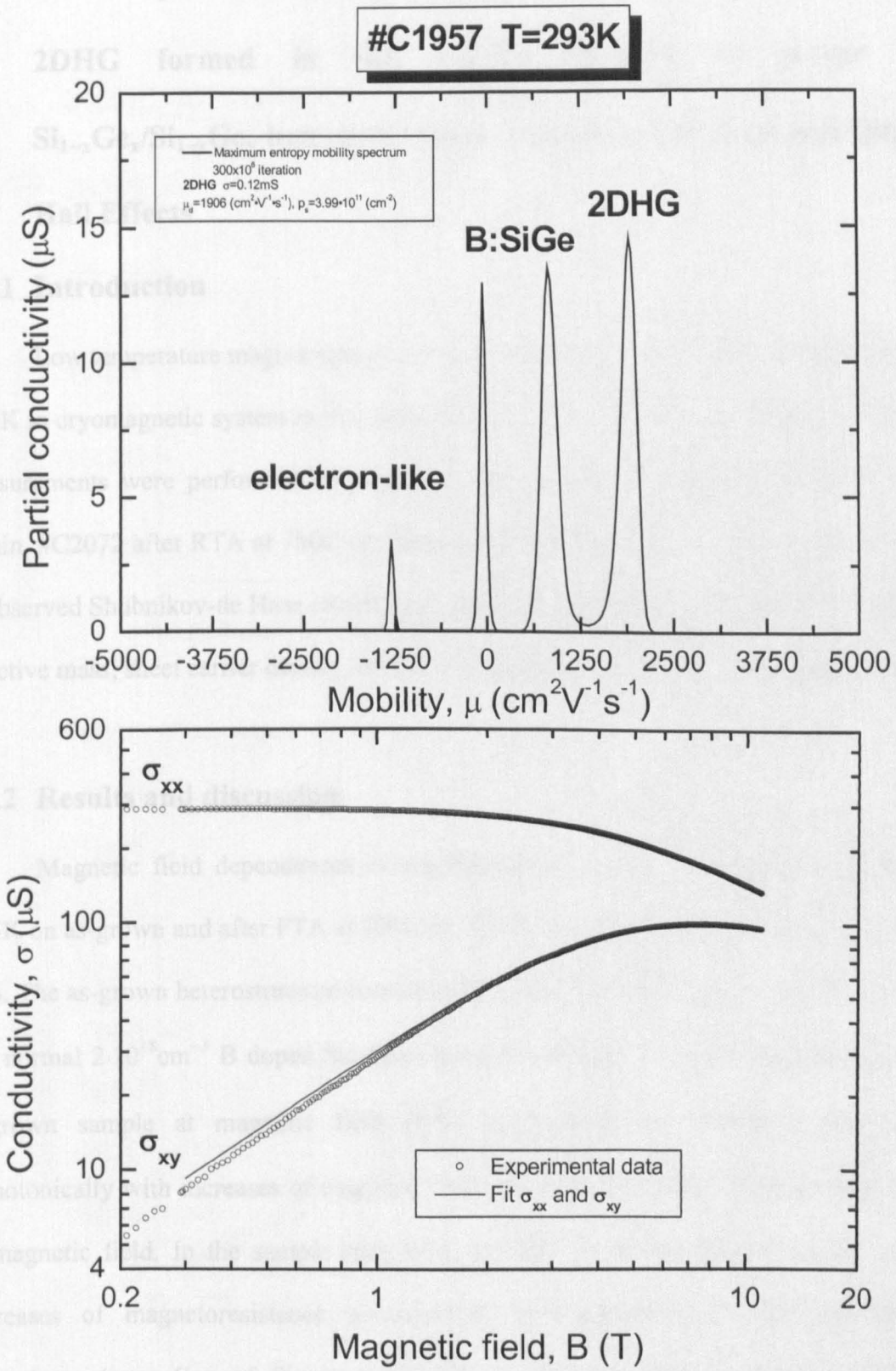

Figure 6.15 MEMS (top) as the result of σ_{xx} and σ_{xy} fit (bottom) measured at 293K for sample #C1957.

6.3 Low temperatures (down to 0.35K) magnetotransport properties of 2DHG formed in the $Si_{1-x}Ge_x$ channel of p-type MOD $Si_{1-x}Ge_x/Si_{1-y}Ge_y$ heterostructures: Shubnikov-de Haas and Quantum Hall Effects

6.3.1 Introduction

Low temperature magnetotransport measurements were carried out at temperatures 25-0.35K in cryomagnetic system as the magnetic field was swept continuously up to 11T. These measurements were performed on samples #622.83 as-grown and after FTA at 700C for 30min, #C2072 after RTA at 750C for 30sec and #C1957. From the temperature dependence of observed Shubnikov-de Haas oscillations were extracted followed parameters of 2DHG, — effective mass, sheet carrier density, transport and quantum life times, and related ones.

6.3.2 Results and discussion

Magnetic field dependences of magnetoresistance and Hall resistance measured at 0.35K on as-grown and after FTA at 700C for 30min samples #622.83 are presented in Figure 6.16. The as-grown heterostructure consist of $Si_{0.2}Ge_{0.8}$ channel grown on $Si_{0.7}Ge_{0.3}$ LT-Si VS and normal $2 \cdot 10^{18} cm^{-3}$ B doped $Si_{0.7}Ge_{0.3}$ layer (see chapter 4.2). The magnetoresistance of as-grown sample at magnetic field B=0T corresponds to 29166Ω/sq and decreases monotonically with increases of magnetic field. The Hall resistance increases with increases of magnetic field. In the sample after FTA at 700C for 30min were observed significant decreases of magnetoresistance accompanied with appearing of SdH oscillations of magnetoresistance (top of Figure 6.16). The magnetoresistance at magnetic field B=0T decreased from 29166Ω/sq for as-grown sample down to 3155Ω/sq for annealed one. Also, the annealing caused the increase of the slope of Hall resistance (bottom of Figure 6.16).

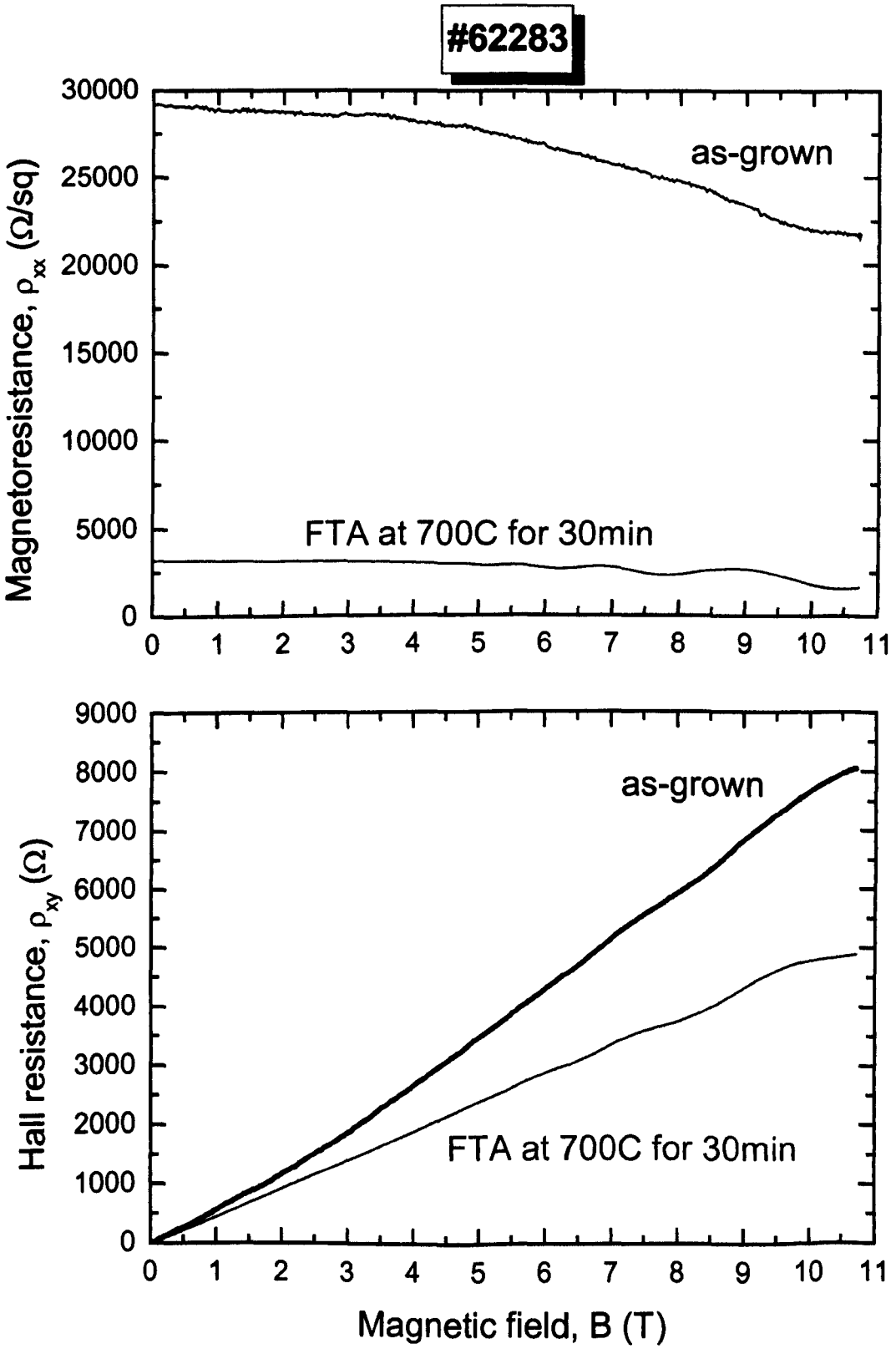

Figure 6.16 Magnetic field dependences of magnetoresistance (top) and Hall resistance (bottom) measured at 0.35K on as-grown and after FTA at 700C for 30min samples #622.83.

Magnetic field dependences of magnetoresistance and Hall resistance measured at 0.346-24.5K temperatures on the sample #622.83 after FTA at 700C for 30min are presented in Figure 6.17. The SdH oscillations of magnetoresistance are clearly observed. At 0.346K the oscillations appearing from magnetic field $B \approx 3.5$T and their amplitude increases with increases of magnetic field. As soon as the temperature increases the amplitude of SdH oscillations decreases accompanied with disappearing of oscillations at low magnetic fields. But even at 24.5K were observed the SdH oscillations at high magnetic fields. The plateaus observed on Hall resistance at low temperatures disappearing with temperature increasing.

Magnetic field dependences of magnetoresistance and Hall resistance measured at 0.348-8.47K temperatures on the sample #C2072 after RTA at 750C for 30min are presented in Figure 6.18. The SdH oscillations of magnetoresistance are clearly observed as well as plateaus on Hall resistance. At temperature 0.348K the oscillations appearing from magnetic field $B \approx 1.5$T and their amplitude increases with increases of magnetic field. As soon as the temperature increases the amplitude of SdH oscillations decreases accompanied with disappearing of oscillations at low magnetic fields. Also at temperature 8.47K were observed the SdH oscillations. The plateaus observed on Hall resistance at low temperatures disappearing with temperature increasing.

Magnetic field dependences of magnetoresistance and Hall resistance measured at 0.356-20.71K temperatures on the sample #C1957 are presented in Figure 6.18. The SdH oscillations of magnetoresistance are clearly observed. At temperature 0.356K the oscillations appearing from magnetic field $B \approx 1.3$T and their amplitude increases with increases of magnetic field. As soon as the temperature increases the amplitude of SdH oscillations decreases accompanied with disappearing of oscillations at low magnetic fields. But even at temperature 20.71K were observed the SdH oscillations. The plateaus observed on Hall resistance at low temperatures disappearing with temperature increasing.

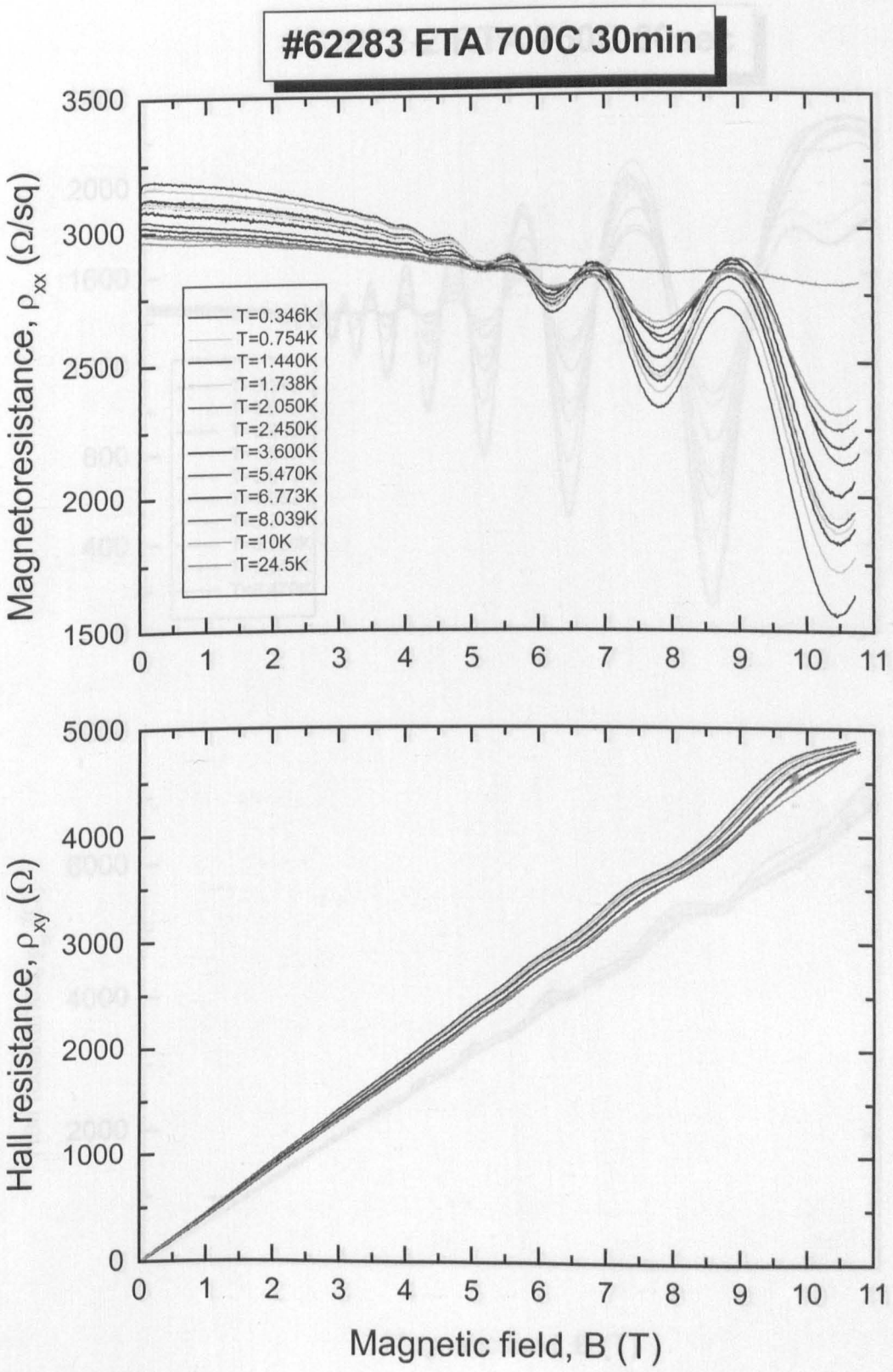

Figure 6.17 Magnetic field dependences of magnetoresistance (top) and Hall resistance (bottom) measured at 0.346-24.5K temperatures on the sample #622.83 after FTA at 700C for 30min.

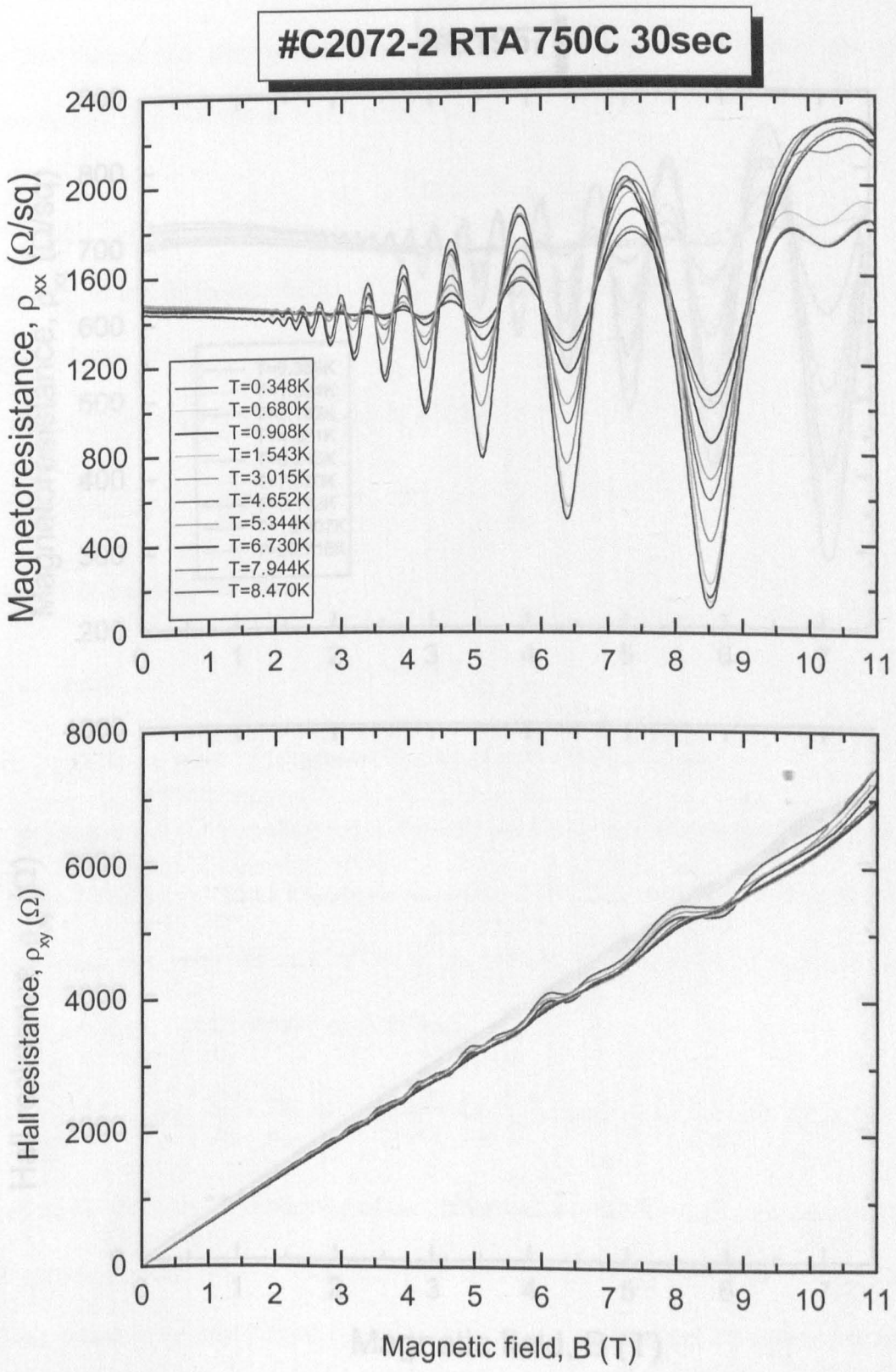

Figure 6.18 Magnetic field dependences of magnetoresistance (top) and Hall resistance (bottom) measured at 0.348-8.47K temperatures on the sample #C2072 after RTA at 750C for 30sec.

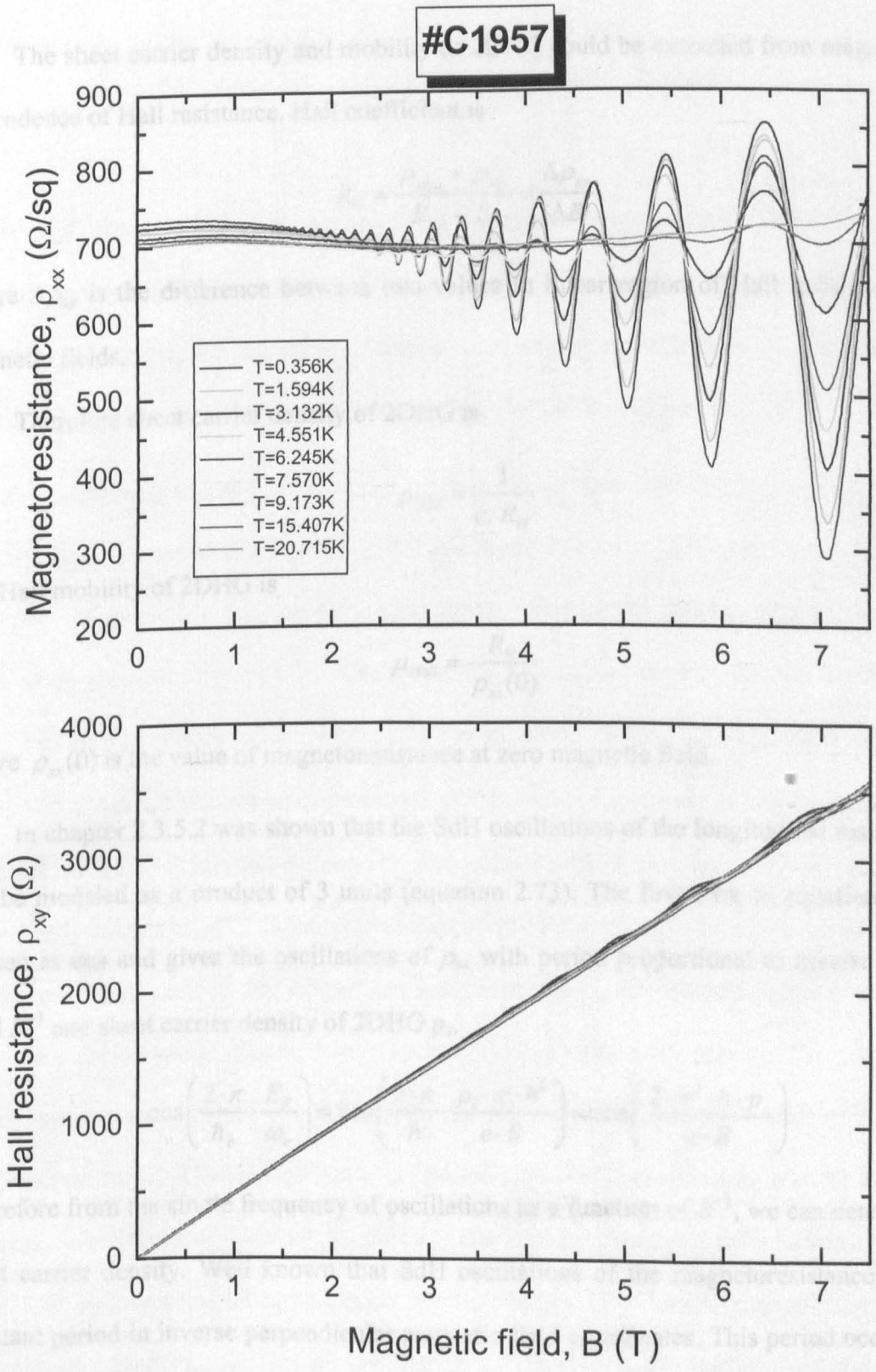

Figure 6.19 Magnetic field dependences of magnetoresistance (top) and Hall resistance (bottom) measured at 0.356-20.715K temperatures on the sample #C1957.

6.3.3 Extraction of sheet carrier density and mobility of 2DHG

The sheet carrier density and mobility of 2DHG could be extracted from magnetic field dependence of Hall resistance. Hall coefficient is

$$R_H = \frac{\rho_{xy_{i+1}} - \rho_{xy_i}}{B_{i+1} - B_i} = \frac{\Delta\rho_{xy}}{\Delta B} \tag{6.3}$$

where $\Delta\rho_{xy}$ is the difference between two values in linear region of Hall resistance at low magnetic fields.

Therefore sheet carrier density of 2DHG is

$$p_{Hall} = \frac{1}{e \cdot R_H} \tag{6.4}$$

and Hall mobility of 2DHG is

$$\mu_{Hall} = \frac{R_H}{\rho_{xx}(0)} \tag{6.5}$$

where $\rho_{xx}(0)$ is the value of magnetoresistance at zero magnetic field.

In chapter 2.3.5.2 was shown that the SdH oscillations of the longitudinal resistance ρ_{xx} can be modeled as a product of 3 units (equation 2.73). The first term in equation (2.69) is written as cos and gives the oscillations of ρ_{xx} with period proportional to inverse magnetic field B^{-1} and sheet carrier density of 2DHG p_s.

$$\cos\left(\frac{2\cdot\pi}{\hbar_c}\cdot\frac{E_F}{\omega_c}\right) = \cos\left(\frac{2\cdot\pi}{\hbar}\cdot\frac{p_s\cdot\pi\cdot\hbar^2}{e\cdot B}\right) = \cos\left(\frac{2\cdot\pi^2\cdot\hbar\cdot p_s}{e\cdot B}\right) \tag{6.6}$$

Therefore from the single frequency of oscillations as a function of B^{-1}, we can determine the sheet carrier density. Well known that SdH oscillations of the magnetoresistance have the constant period in inverse perpendicular magnetic field coordinates. This period occurs when the argument of the cos term increases up to $2\cdot\pi$. So, for two adjacent minimum or maxim we have:

$$2\cdot\pi = \left(\frac{2\cdot\pi^2\cdot\hbar\cdot p_s}{e}\cdot\frac{1}{B_{i+1}}\right) - \left(\frac{2\cdot\pi^2\cdot\hbar\cdot p_s}{e}\cdot\frac{1}{B_i}\right) = \left(\frac{2\cdot\pi^2\cdot\hbar\cdot p_s}{e}\right)\cdot\left(\frac{1}{B_{i+1}} - \frac{1}{B_i}\right) \tag{6.7}$$

consequently, the sheet carrier density extracted from the SdH oscillations at given temperature is

$$p_{SdH} = \frac{e}{\pi \cdot \hbar \cdot \Delta(B^{-1})} \tag{6.8}$$

where $\Delta(B^{-1})$ is a period of SdH oscillations in inverse magnetic field. The accuracy of this method is very high. It increases with the increasing of the number of SdH oscillations to be plotted. As example, the extraction of carrier sheet density from SdH oscillations measured at T=0.356K for sample #C1957 is presented in Figure 6.20 and Figure 6.21.

Another way to determine carrier concentration from SdH oscillations is to use Fast Fourier Transformation (FFT). FFT is the fast algorithm for Fourier spectrum calculation. If SdH oscillations have a constant period (frequency) they can be presented by one harmonic of the Fourier spectrum Figure 6.21. The frequency found from the Fourier plot can be directly used for carrier concentration determined by equation (6.8). The full width of the peak measured at half of maximum corresponds to the value of quantum scattering time (τ_q). The accuracy of the FFT method depends on the number of SdH oscillations in the investigating region of magnetic fields. The simplest methods of FFT spectrum clarifying are: removing of the monotonous part of the magnetoresistance, removing exponential growth of the SdH amplitude in magnetic fields, using special FFT windows to smooth the edges of the investigated region, use of the differential (or the second order deferential) of the original magnetoresistance. All these methods can improve the experimental data in order to make the original curve be closer to sinus-like function (the best for Fourier transformation).

The accuracy of these methods is very high. It is much higher then e.g. Hall measurements where p_{Hall} can be different from the real concentration. For multi-subband case p_{Hall}, in the best case, can give the sum of subbands concentrations. SdH oscillations always show the right concentration. For multi-subband case the result magnetoresistance field dependence is the sum of SdH oscillations from different subband. Each type of

oscillations has its own period and amplitude, which corresponds to the subband carrier concentration and effective mass.

The Hall mobility and sheet carrier density of 2DHG at 0.35K for samples #622.83 after FTA at 700C for 30min, #C2072 after RTA at 750C for 30sec and #C1957 were extracted from magnetic field dependences of magnetoresistance and Hall resistance by described techniques and presented in Table 6.6.

Table 6.6 Resistivity, Hall mobility and sheet carrier density of 2DHG at 0.35K extracted from magnetic field dependences of magnetoresistance and Hall resistance for samples 622.83 after FTA at 700C for 30min, #C2072 after RTA at 750C for 30sec and #C1957.

Sample ID	Channel/buffer	$\rho_{xx}(0)$ (Ω/sq)	p_{SdH} (cm^{-2})	p_{Hall} (cm^{-2})	μ_{Hall} ($cm^2 \cdot V^{-1} \cdot s^{-1}$)
#622.83 (as-grown)	$Si_{0.2}Ge_{0.8}$/ $Si_{0.7}Ge_{0.3}$	29166	-	$1.09 \cdot 10^{12}$	195
#622.83 (FTA at 700C for 30min)		3155	$1.45 \cdot 10^{12}$	$1.35 \cdot 10^{12}$	1460
#C2072 (RTA at 750C for 30sec)	$Si_{0.18}Ge_{0.82}$/ $Si_{0.47}Ge_{0.53}$	1479	$1.13 \cdot 10^{12}$	$9.54 \cdot 10^{11}$	4427
#C1957	$Si_{0.05}Ge_{0.95}$/ $Si_{0.37}Ge_{0.63}$	728	$1.68 \cdot 10^{12}$	$1.30 \cdot 10^{12}$	6581

For the sample #622.83 after FTA at 700C for 30min in comparison with as-grown one were observed an improvements of magnetotransport characteristic of 2DHG at temperature 0.35K. The 9.2 times decrease of magnetoresistance at zero magnetic field accompanied with an increase of carrier sheet density and 7.4 times an increase of Hall mobility were observed after annealing. For sample #C2072 after RTA at 750C for 30sec the magnetoresistance at zero magnetic field, sheet carrier density extracted from SdH oscillations of magnetoresistance, sheet carrier density and Hall mobility extracted from magnetic field dependence of Hall resistance are 1479Ω/sq, $1.13 \cdot 10^{12}$ cm^{-2}, $9.54 \cdot 10^{11}$ cm^{-2} and 4427$cm^2 \cdot V^{-1} \cdot s^{-1}$ respectively. For sample #C1957 the magnetoresistance at zero magnetic field, sheet carrier density extracted from SdH oscillations of magnetoresistance, sheet carrier density and Hall mobility extracted from magnetic field dependence of Hall resistance are 728Ω/sq, $1.68 \cdot 10^{12}$ cm^{-2}, $1.30 \cdot 10^{12}$ cm^{-2} and 6581$cm^2 \cdot V^{-1} \cdot s^{-1}$ respectively.

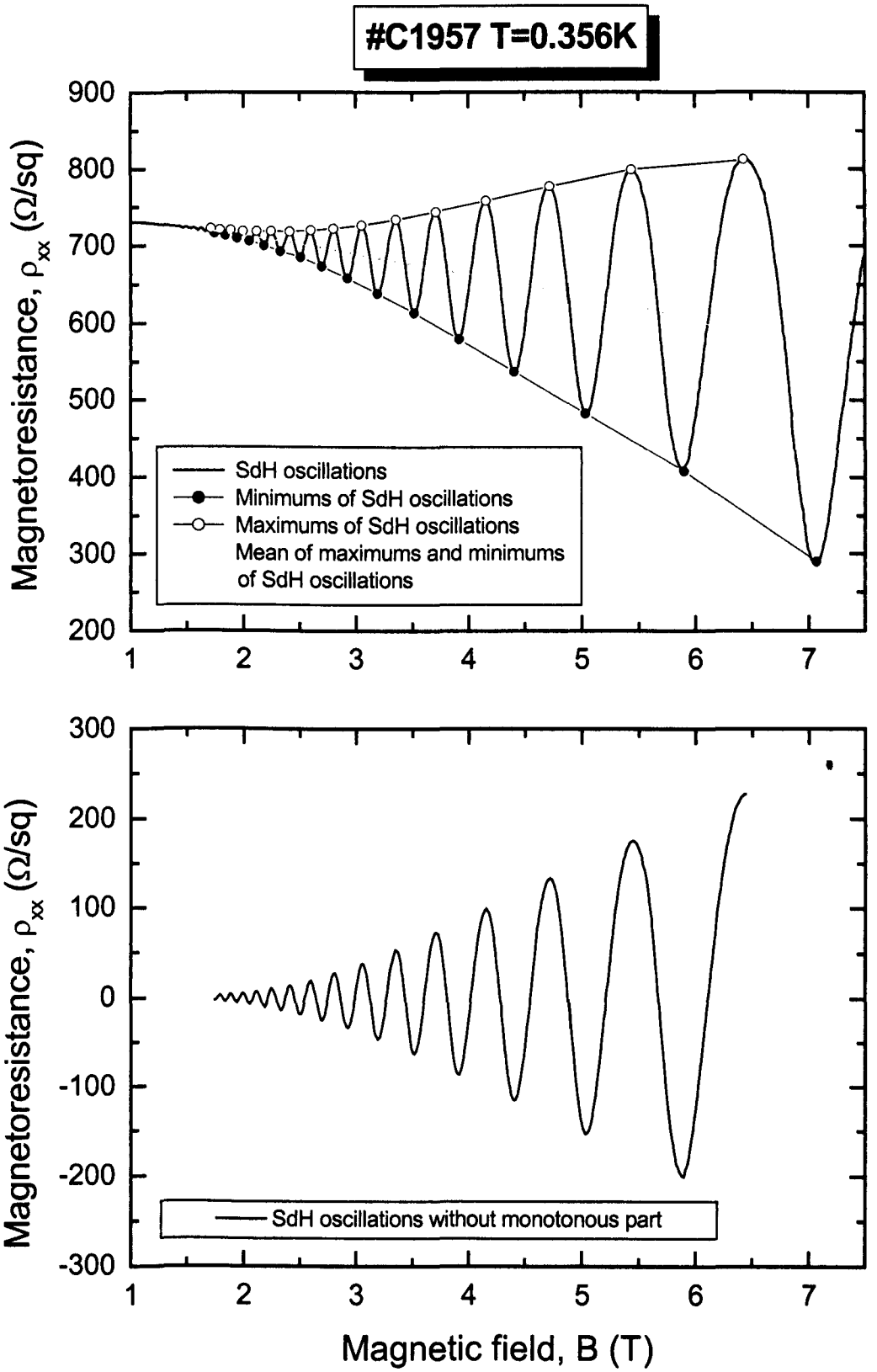

Figure 6.20 Measured SdH oscillations (top) and SdH oscillations without monotonic part (bottom) for sample #C1957 at T=0.356K.

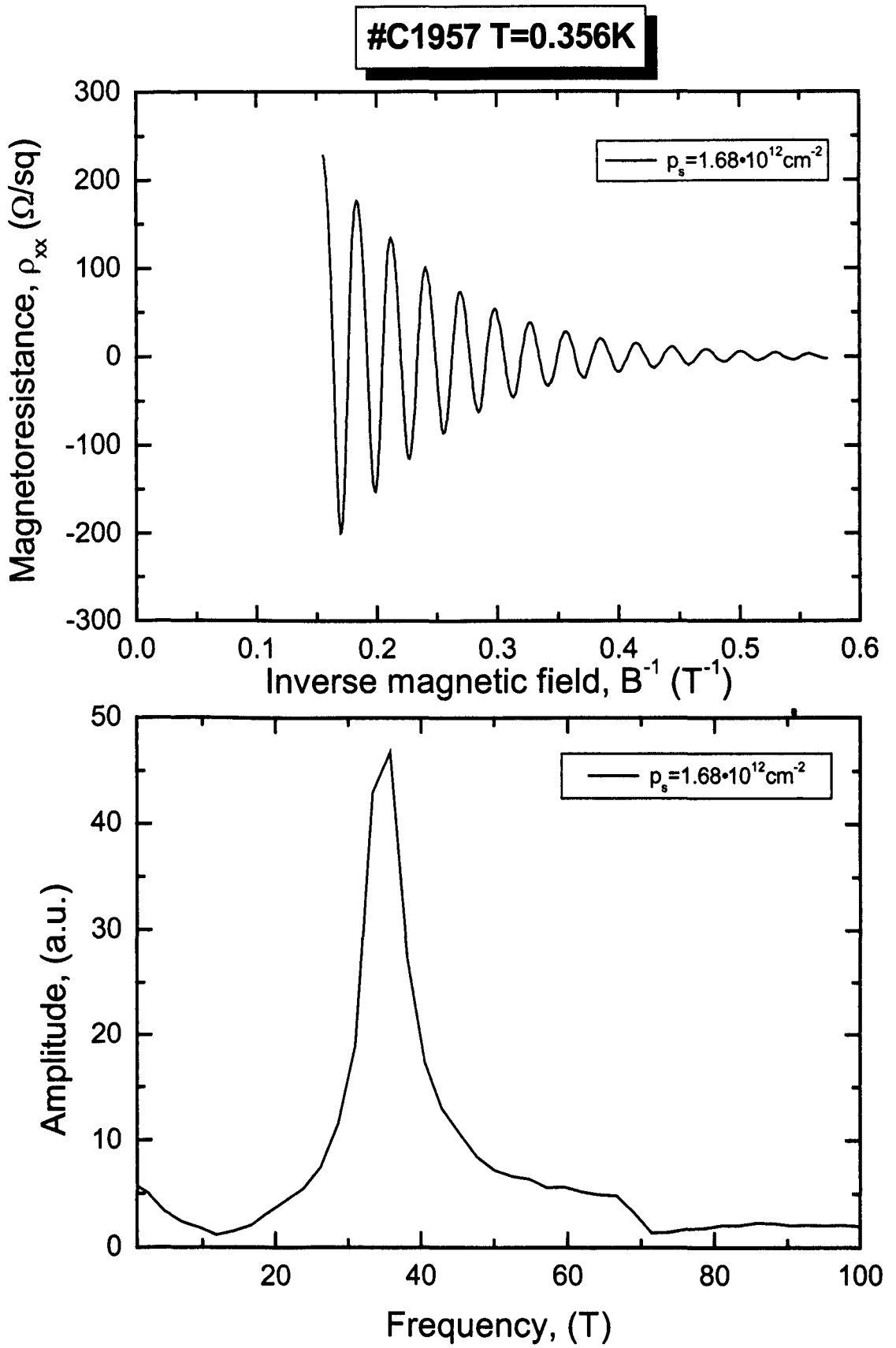

Figure 6.21 SdH oscillations in inverse magnetic field (top) and their FFT spectrum (bottom) for sample #C1957 at T=0.356K.

6.3.4 Extraction of effective mass and related parameters of 2DHG

In chapter 2.3.5.2 was shown that the SdH oscillations of the longitudinal resistance ρ_{xx} can be modeled as a product of 3 units (equation 2.73). Replacing $\tau_q = \frac{\tau_t}{\alpha}$, $\omega_c = \frac{e \cdot B}{m^*}$ and $\frac{2 \cdot \pi^2 \cdot k_B \cdot T}{\hbar \cdot \omega_c} = \frac{2 \cdot \pi^2 \cdot k_B \cdot T \cdot m^*}{\hbar \cdot e \cdot B} = \psi$ in equation (2.73) we can write the equation that describes SdH oscillations for the case when one subband is occupied

$$\frac{\Delta\rho_{xx}(B)}{\rho_{xx}(0)} = 4 \cdot \cos\left(\frac{2 \cdot \pi \cdot E_F \cdot m^*}{\hbar \cdot e \cdot B}\right) \cdot \exp\left(-\frac{\pi \cdot m^* \cdot \alpha}{e \cdot B \cdot \tau_t}\right) \cdot \frac{\psi}{\sinh(\psi)} \tag{6.9}$$

where τ_t is the transport (or classical) scattering time, τ_q is the quantum (or single particle) scattering time, $\rho_{xx}(0)$ is magnetoresistance at zero magnetic field for given temperature, $\Delta\rho_{xx}(B)$ is the amplitude of SdH oscillations for given temperature. For a 2DCG Fermi energy is

$$E_F = \frac{\pi \cdot \hbar^2 \cdot p_s}{m^*} \tag{6.10}$$

The unknown parameters in equation (6.9) are the effective mass (m^*) and (α). The desired value of m^* can be found by methods which are well known in the literature.

The third term in equation (6.9) depends on three parameters: effective mass, magnetic field and temperature. The temperature dependence allows to change the value of the third term (the amplitude of SdH oscillations) vary temperature only. Varying the temperature one does not change anything else (e.g. position of peaks). This phenomenon can be used to find the effective mass using SdH measurements.

The technique used to find the m^* and α is as follows [14]. First determine a value for α. Assume some value for m^*. Take a set of $\Delta\rho_{xx}(T)$ as a function of magnetic field at given temperatures (top Figure 6.22). A plot of

$$\ln\left(\frac{\Delta\rho_{xx}(T)}{\rho_{xx}(0)} \cdot \frac{\sinh(\psi(T))}{\psi(T)}\right) \tag{6.11}$$

versus

$$\frac{1}{\mu \cdot B} \tag{6.12}$$

have to be a straight line with a gradient of $-\pi \cdot \alpha$ (top Figure 6.23).

For obtained α determine m^*. Take a set of $\Delta\rho_{xx}(B)$ as a function of temperature at given magnetic fields (bottom Figure 6.22). A plot of

$$\ln\left(\frac{\Delta\rho_{xx}(B)}{\rho_{xx}(0)}\right) \tag{6.13}$$

versus

$$\ln\left(\frac{\psi(B)}{\sinh(\psi(B))}\right) - \left(\frac{\pi \cdot \alpha}{\mu \cdot B}\right) \tag{6.14}$$

have to be a straight line with a gradient of unity (bottom Figure 6.23). The only unknown (with fixed α) is the effective mass.

If the gradient is not unity, then the α have to be recalculated using the obtained value of m^*. A new value of m^* have to be calculated with the new value of α. This loop have to be repeated until a self-consist pair of values for m^* and α is found.

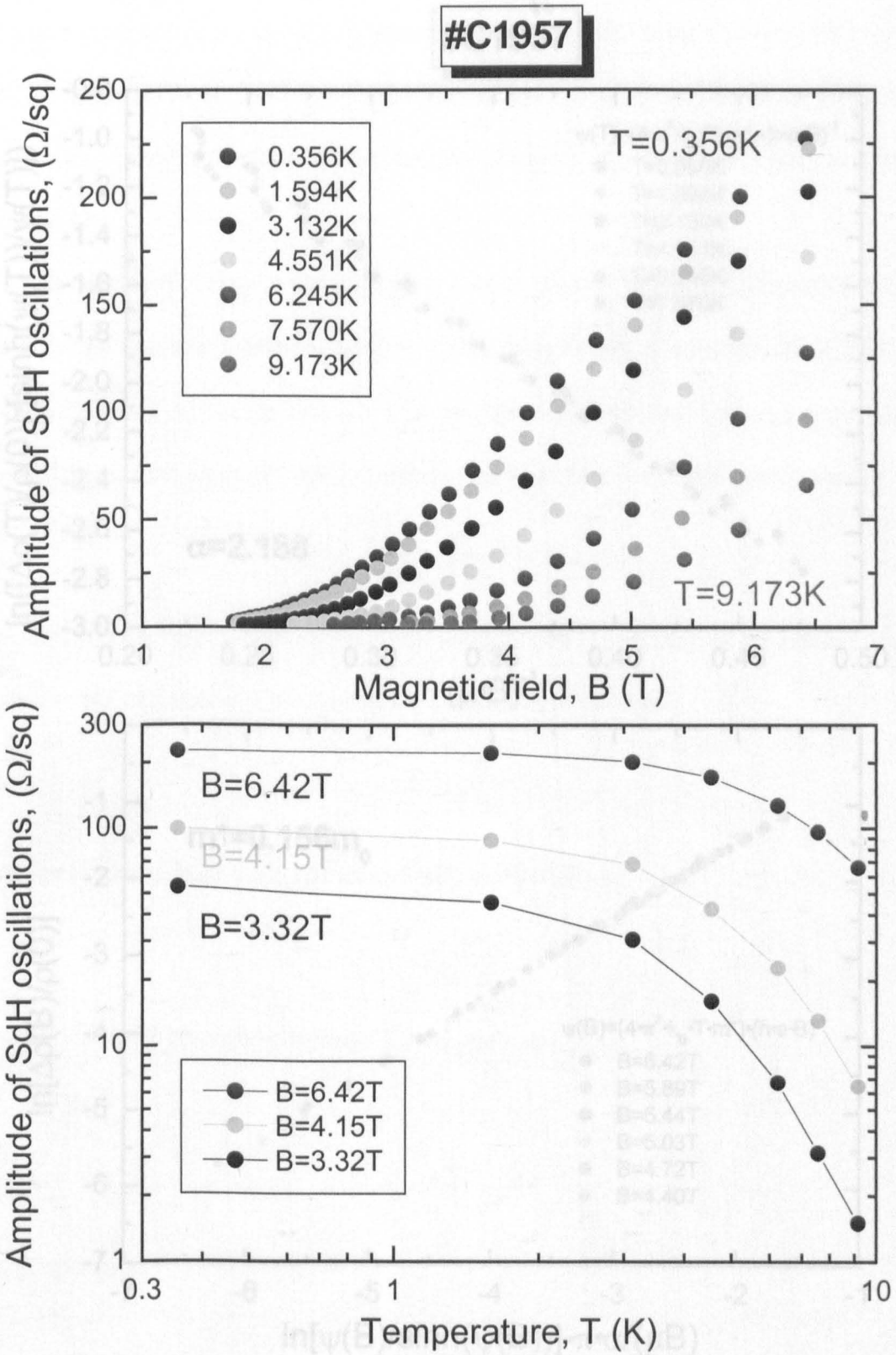

Figure 6.22 Amplitudes of SdH oscillations ($\Delta\rho_{xx}(T)$) as a function of magnetic field at given temperatures (top) and amplitudes of SdH oscillations ($\Delta\rho_{xx}(B)$) as a function of temperature at given magnetic fields (bottom) for sample #C1957.

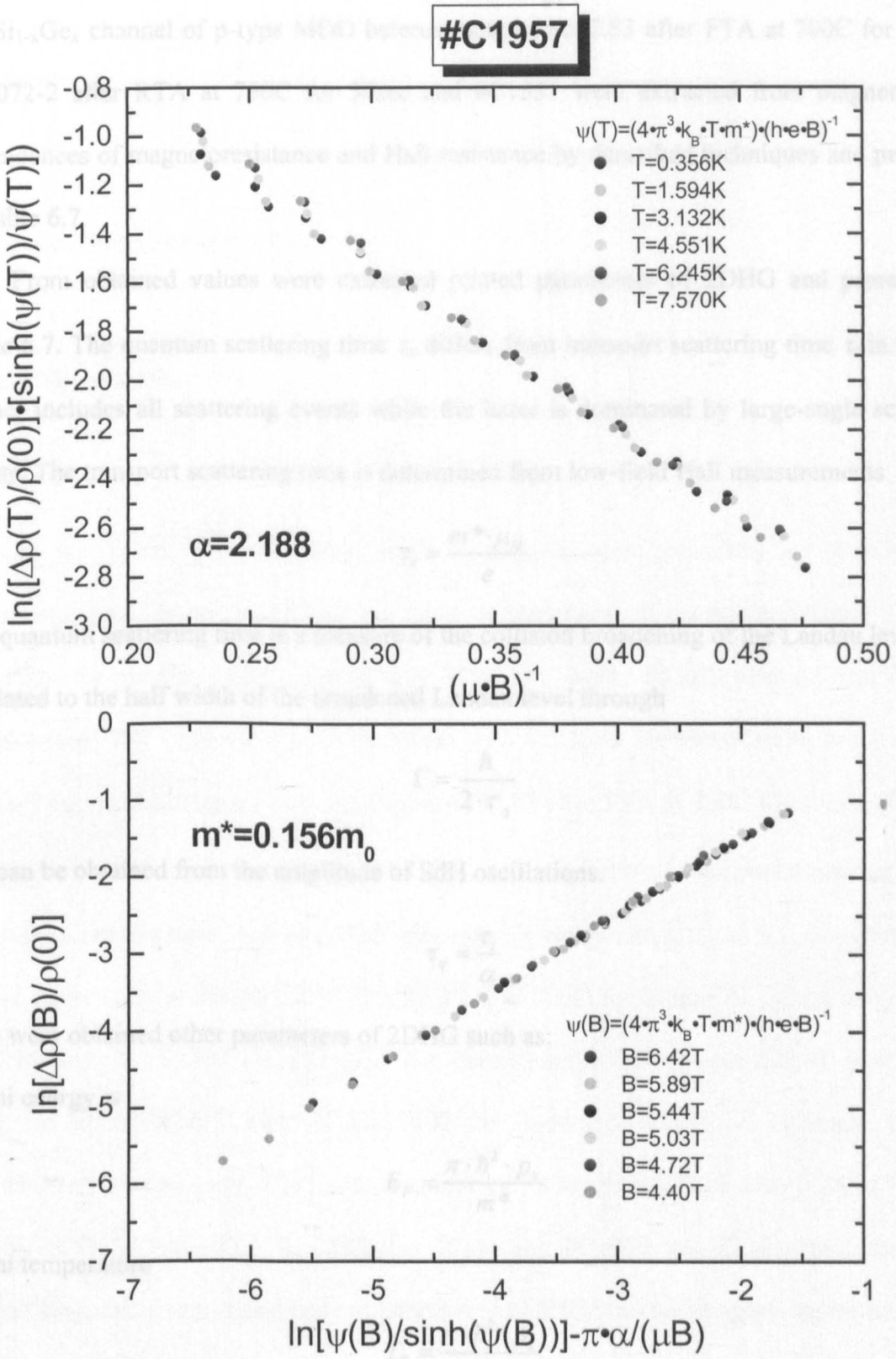

Figure 6.23 Plots for self-consistent extraction of transport to quantum scattering times ratio α (top) and effective mass m^* (bottom) of 2DHG formed in the $Si_{0.05}Ge_{0.95}$ channel of p-type MOD heterostructures #C1957.

The effective mass and transport to quantum scattering times ratio of 2DHG formed in the $Si_{1-x}Ge_x$ channel of p-type MOD heterostructures #622.83 after FTA at 700C for 30min, #C2072-2 after RTA at 750C for 30sec and #C1957 were extracted from magnetic field dependences of magnetoresistance and Hall resistance by described techniques and presented in Table 6.7.

From obtained values were extracted related parameters of 2DHG and presented in Table 6.7. The quantum scattering time τ_q differs from transport scattering time τ_t in that the former includes all scattering events while the latter is dominated by large-angle scattering events. The transport scattering time is determined from low-field Hall measurements

$$\tau_t = \frac{m^* \cdot \mu_H}{e} \tag{6.15}$$

The quantum scattering time is a measure of the collision broadening of the Landau levels and is related to the half width of the broadened Landau level through

$$\Gamma = \frac{\hbar}{2 \cdot \tau_q} \tag{6.16}$$

and can be obtained from the amplitude of SdH oscillations.

$$\tau_q = \frac{\tau_t}{\alpha} \tag{6.17}$$

Also were obtained other parameters of 2DHG such as:

Fermi energy is

$$E_F = \frac{\pi \cdot \hbar^2 \cdot p_s}{m^*} \tag{6.18}$$

Fermi temperature

$$T_F = \frac{\pi \cdot \hbar^2 \cdot p_s}{m^* \cdot k_B} \tag{6.19}$$

Fermi wavevector

$$k_F = \sqrt{2 \cdot \pi \cdot p_s} \tag{6.20}$$

Fermi wavelength

$$\lambda_F = \frac{2 \cdot \pi}{k_F} \tag{6.21}$$

Fermi velocity

$$\upsilon_F = \frac{\hbar \cdot k_F}{m^*} \tag{6.22}$$

Low temperature mean free path

$$l = \upsilon_F \cdot \tau_t \tag{6.23}$$

Dingle temperature

$$T_D = \frac{\hbar}{2 \cdot \pi \cdot \tau_q \cdot k_B} \tag{6.24}$$

In the Table 6.7 were summarized magnetotransport properties of 2DHG at low temperatures extracted from magnetic field dependences of magnetoresistance and Hall resistance for samples 622.83 after FTA at 700C for 30min, #C2072 after RTA at 750C for 30sec and #C1957. Effective mass decreases with increases Ge composition in the $Si_{1-x}Ge_x$ channel and varied from $0.17 \cdot m_0$ for sample #622.83 after FTA at 700C for 30min ($Si_{0.2}Ge_{0.8}$ as-grown) to $0.15 \cdot m_0$ for sample #C1957 ($Si_{0.05}Ge_{0.95}$). Ratio of transport scattering time to quantum scattering time increases with increases Ge composition in the $Si_{1-x}Ge_x$ channel and varied from 1.29 for sample #622.83 after FTA at 700C for 30min ($Si_{0.2}Ge_{0.8}$ as-grown) to 2.18 for sample #C1957 ($Si_{0.05}Ge_{0.95}$). The Fermi energy for samples 622.83 after FTA at 700C for 30min, #C2072 after RTA at 750C for 30sec and #C1957 are 19.5meV, 16.1meV and 25.7meV respectively. The Fermi temperature for samples 622.83 after FTA at 700C for 30min, #C2072 after RTA at 750C for 30sec and #C1957 are 226K, 186K and 299K respectively. Others magnetotransport parameters of 2DHG obtained at low temperature from magnetic field dependences of magnetoresistance and Hall resistance for investigated p-type MOD $Si_{1-x}Ge_x/Si_{1-y}Ge_y$ heterostructures are listed in Table 6.7.

Table 6.7 Magnetotransport properties of 2DHG at low temperatures extracted from magnetic field dependences of magnetoresistance and Hall resistance for samples 622.83 after FTA at 700C for 30min, #C2072 after RTA at 750C for 30sec and #C1957.

Sample ID	#622.83 (FTA at 700C for 30min)	#C2072 (RTA at 750C for 30sec)	#C1957
Channel/ buffer	$Si_{0.2}Ge_{0.8}$/ $Si_{0.7}Ge_{0.3}$	$Si_{0.18}Ge_{0.82}$/ $Si_{0.47}Ge_{0.53}$	$Si_{0.05}Ge_{0.95}$/ $Si_{0.37}Ge_{0.63}$
m^* (m_0)	0.17	0.16	0.15
α (τ_t/τ_q)	1.29	1.44	2.18
τ_t (ps)	0.14	0.42	0.58
τ_q (ps)	0.11	0.29	0.26
E_F (meV)	19.5	16.1	25.7
T_F (K)	226	186	299
k_F (nm^{-1})	0.30	0.26	0.32
λ_F (nm)	20.81	23.58	19.33
υ_F ($\cdot 10^7$ $cm \cdot s^{-1}$)	1.96	1.83	2.41
l (nm)	29	77	140
T_D (K)	10.66	4.14	4.55
Γ (meV)	2.88	1.12	1.23

The results of low temperatures magnetotransport characterization of p-type MOD $Si_{1-x}Ge_x/Si_{1-y}Ge_y$ heterostructures were presented at "10th European Heterostructure Technology Workshop"[9], "Condensed Matter and Materials Physics 2000 [15] and "SiGe (C) 2001 Workshop"[10].

6.3.5 Conclusions

The low temperature magnetotransport properties of 2DHG formed in the $Si_{1-x}Ge_x$ channel of p-type MOD $Si_{1-x}Ge_x/Si_{1-y}Ge_y$ heterostructures were studied by measuring magnetic field dependences of magnetoresistance and Hall resistance at temperatures 25-0.34K and in magnetic fields up to 11T. The investigated samples consist of $Si_{1-x}Ge_x$ channel with $0.8<x<0.95$ and $Si_{1-y}Ge_y$ VS $0.3<y<0.63$. For the sample #622.83 after FTA at 700C for

30min in comparison with as-grown one ($Si_{0.2}Ge_{0.8}/Si_{0.7}Ge_{0.3}$) were observed an improvements of magnetotransport characteristic of 2DHG at temperature 0.35K. The 9.2 times decrease of magnetoresistance at zero magnetic field accompanied with appearing of SdH oscillations of magnetoresistance and an increase of carrier sheet density and 7.4 times an increase of Hall mobility were observed after annealing. The magnetoresistance at zero magnetic measured at temperature 0.35K decreased with increase of Ge composition in the $Si_{1-x}Ge_x$ channel and varied from 3155Ω/sq for sample #622.83 after FTA at 700C for 30min ($Si_{0.2}Ge_{0.8}$ as-grown) to 3155Ω/sq for sample #C1957 ($Si_{0.05}Ge_{0.95}$). The Hall mobility of 2DHG extracted from magnetic field dependence of Hall resistance at temperature 0.35K increased with increase of Ge composition in the $Si_{1-x}Ge_x$ channel and varied from $1460cm^2 \cdot V^{-1} \cdot s^{-1}$ for sample #622.83 after FTA at 700C for 30min ($Si_{0.2}Ge_{0.8}$ as-grown) to $6581cm^2 \cdot V^{-1} \cdot s^{-1}$ for sample #C1957 ($Si_{0.05}Ge_{0.95}$). The sheet carrier density of 2DHG was obtained by two ways, — from SdH oscillations of magnetoresistance and magnetic field dependence of Hall resistance. For all samples the sheet carrier density obtained from SdH oscillations of magnetoresistance is higher than from magnetic field dependence of Hall resistance. Effective mass decreases with increases Ge composition in the $Si_{1-x}Ge_x$ channel and varied from $0.17 \cdot m_0$ for sample #622.83 after FTA at 700C for 30min ($Si_{0.2}Ge_{0.8}$ as-grown) to $0.15 \cdot m_0$ for sample #C1957 ($Si_{0.05}Ge_{0.95}$). Ratio of transport scattering time to quantum scattering time increases with increases Ge composition in the $Si_{1-x}Ge_x$ channel and varied from 1.29 for sample #622.83 after FTA at 700C for 30min ($Si_{0.2}Ge_{0.8}$ as-grown) to 2.18 for sample #C1957 ($Si_{0.05}Ge_{0.95}$). The values of effective mass $0.15 \cdot m_0$ and ratio of transport scattering time to quantum scattering time 2.18 obtained for p-type MOD $Si_{0.05}Ge_{0.95}/Si_{0.37}Ge_{0.63}$ heterostructure are the lowest and the highest respectively ever published for p-type MOD heterostructures with $Si_{1-x}Ge_x$ channel grown by SS-MBE on $Si_{1-y}Ge_y$ VS on Si(001) substrate.

References:

1. Hull, R. and J.C. Bean, *Germanium Silicon: Physics and Materials*. 1999: Academic Press.
2. Grillot, P.N., S.A. Ringel, J. Michel, and E.A. Fitzgerald, *Structural, electronic, and luminescence investigation of strain-relaxation induced electrical conductivity type conversion in GeSi/Si heterostructures.* Journal of Applied Physics, 1996. **80**(5): p. 2823-2832.
3. Grillot, P.N., S.A. Ringel, E.A. Fitzgerald, G.P. Watson, and Y.H. Xie, *Minority- and Majority-Carrier Trapping in Strain-Relaxed Ge0.3si0.7/Si Heterostructure Diodes Grown by Rapid Thermal Chemical-Vapor-Deposition.* Journal of Applied Physics, 1995. 77(2): p. 676-685.
4. Kittler, M., V.V. Kveder, and W. Schroter, *Temperature dependence of the recombination activity at contaminated dislocations in Si: A model describing the different EBIC contrast behaviour.* Solid State Phenomena, 1999. **70**: p. 417-422.
5. Shklovskii, B.I., *Electronic properties of doped semiconductors*. 1984, Berlin, New York: Springer-Verlag.
6. Mott, N.F. and E.A. Davis, *Electronic processes in non-crystalline materials*. 1979, Oxford: Clarendon Press.
7. Myronov, M., E.H.C. Parker, T.E. Whall, S.G. Lyapin, and P.C. Klipstein. *Thermal annealing effect on properties of Si0.2Ge0.8/Si0.7Ge0.3/Si(001) p-type modulation doped heterostructures.* in *10th European Heterostructure Technology Workshop.* 2000. University of Ulm, International Institute Schloss Reisensburg, Gunzburg, Germany.
8. Myronov, M., C.P. Parry, O.A. Mironov, E.H.C. Parker, T.E. Whall, E. Hoeflinger, and G. Bauer. *Post-growth annealing effect on magnetotransport and structural properties of Si0.2Ge0.8/Si0.65Ge0.35/Si(001) modulation doped heterostructure.* in *10th European Heterostructure Technology Workshop.* 2000. University of Ulm, International Institute Schloss Reisensburg, Gunzburg, Germany.
9. Hoeck, G., T. Hackbarth, M. Myronov, O.A. Mironov, E.H.C. Parker, and E. Kohn. *Magnetotransport properties of Si1-xGex/Si1-yGey/Si(001) p-type modulation doped heterostructures with high Ge content channel.* in *10th European Heterostructure Technology Workshop.* 2000. University of Ulm, International Institute Schloss Reisensburg, Gunzburg, Germany.
10. Mironov, O.A., M. Myronov, E.H.C. Parker, and T.E. Whall. *High Ge content SiGe MODFET heterostructures on virtual substrates for device applications: HOLE MOBILITIES higher than electrons in the room temperature range of operation.* in *SiGe (C) 2001 Workshop.* 2001. Hotel Jal City, Sendai, Japan.
11. Kiatgamolchai, S., M. Myronov, E.H.C. Parker, T.E. Whall, J.C. Yeoh, T.K. Fobelets, and T.J. Thornton. *Mobility Spectrum of 2DHG and 2DEG in SiGe-Si Heterostructures.* in *11th General Conference of the European Physical Society (EPS-11): Trends in Physics.* 1999. Church House Conference Centre, London, UK.
12. Kiatgamolchai, S., M. Myronov, O.A. Mironov, E.H.C. Parker, and T.E. Whall. *A Novel Mobility Spectrum Maximum Entropy Approach for Magnetotransport Analysis of SiGe/Si heterostructures.* in *10th European Heterostructure Technology Workshop.* 2000. University of Ulm, International Institute Schloss Reisensburg, Gunzburg, Germany.
13. Myronov, M., S. Kiatgamolchai, O.A. Mironov, T.E. Whall, E.M. Sheregii, G. Tomaka, T. Kakol, and J. Klamut. *Mobility spectrum analysis of high Ge content SiGe/Si heterostructures.* in *International Conference on Solid State Crystals 2000: Materials Science and Applications.* 2000. Zakopane, Poland.

14. Komnik, Y.F., V.V. Andrievskii, I.B. Berkutov, S.S. Kryachko, M. Myronov, and T.E. Whall, *Quantum effects in hole-type Si/SiGe heterojunctions.* Low Temperature Physics, 2000. **26**(8): p. 609-614.
15. Myronov, M., O.A. Mironov, E.H.C. Parker, T.E. Whall, V.V. Andrievskii, Y.F. Komnik, and I.B. Berkutov. *Transport properties of charge carriers in p-type modulation doped heterostructures with Si1-xGex channel.* in *Condensed Matter and Materials Physics 2000.* 2000. University of Bristol, Bristol, UK.

7. Conclusions and further work

Magnetotransport, structural and optical properties of p-type MOD heterostructures with high Ge content ($0.6<x<1$) $Si_{1-x}Ge_x$ channel grown on $Si_{1-y}Ge_y$/Si(001) virtual substrate have been studied experimentally. The active layers of MOD heterostructures were grown by SS-MBE and the virtual substrates were grown either by SS-MBE or LP-CVD.

The influence of thermal annealing on magnetotransport, structural and optical properties of $Si_{1-x}Ge_x/Si_{1-y}Ge_y$ heterostructures was studied by performing the post growth furnace thermal annealing treatments in the temperature range of 600-900C for 30min and rapid thermal annealing treatments at temperature 750C for 30sec.

Structural and optical analysis of p-type MOD $Si_{1-x}Ge_x/Si_{1-y}Ge_y$ heterostructures were done by XTEM, ULE-SIMS, PL spectroscopy, Raman spectroscopy and Scanning White-Light Interferometry. From the combinations of experimental results obtained by these techniques the Ge composition in the SiGe heteroepilayers, their thicknesses, state of strain in the heteroepilayers and dislocations microstructure in VS were obtained. The structural integrity of the layers and the dislocations microstructure in relaxed VS were determined by XTEM. In particular, the thicknesses of high Ge content $Si_{1-x}Ge_x$ channel layers were determined. Also short-range roughness of $Si_{1-x}Ge_x$ channel layer interfaces caused by not optimum growth conditions and long-range roughness cased by various types of VS were studied by XTEM as well. The Ge, Si and B profiles were obtained by ULE-SIMS that allowed determine the structural integrity of the layers, $Si_{1-x}Ge_x$ channel layer thickness and level of B doping in the active layers of MOD heterostructures. PL spectra of p-type MOD $Si_{1-x}Ge_x/Si_{1-y}Ge_y$ heterostructures obtained in the energy range 0.7-1.2eV at 5.5K contain information only about Si substrate and $Si_{1-y}Ge_y$ (0.3-0.63) relaxed layers. State of strain in the $Si_{1-x}Ge_x$ strained and $Si_{1-y}Ge_y$ relaxed layers and the Ge composition in the later were obtained from room temperature Raman spectra. The $Si_{1-x}Ge_x$ channels grown on $Si_{1-y}Ge_y$ VS in the as-grown samples #51.33, #52.16, #54.08, #60.46, #622.83, #C1957, #C1987, #C2015f, #C2072, #C2475 and #C2476 were

fully strained. In the as-grown sample #622.84 the 14nm $Si_{0.2}Ge_{0.8}$ channel grown on $Si_{0.7}Ge_{0.3}$ VS was partially relaxed due to exceeded critical thickness. The surface profiles of p-type MOD $Si_{1-x}Ge_x/Si_{1-y}Ge_y$ heterostructures were obtained by scanning white-light interferometry. The characteristic feature for samples contained linearly or step graded VS are crosshatches on the surface due to linearly or step graded changes of Ge composition and high density of dislocations in VS. No crosshatches were observed in the samples contained relatively thin (850nm) $Si_{0.7}Ge_{0.3}$ VS with low temperature Si buffer (#622.83 and #622.84). The lowest surface roughness was observed in these samples. The highest surface roughness was observed in the samples with $Si_{0.65}Ge_{0.35}$ linearly graded VS grown by LP-CVD (#60.45 and #60.46).

After post growth thermal annealing (FTA and RTA) the Ge diffusion from the region with high Ge concentration ($Si_{1-x}Ge_x$ channel) to the region with low Ge concentration ($Si_{1-y}Ge_y$ layers) and B diffusion from doped $Si_{1-y}Ge_y$ layers to the undoped $Si_{1-y}Ge_y$ spacer layers were observed by ULE-SIMS. The broadening of $Si_{1-x}Ge_x$ channel caused by Ge diffusion was accompanied with smearing of bottom and top $Si_{1-x}Ge_x/Si_{1-y}Ge_y$ interfaces (XTEM). After annealing significant changes in all regions of Raman spectra of p-type MOD $Si_{1-x}Ge_x/Si_{1-y}Ge_y$ heterostructures were observed. The intensities of the various modes changed, as long as the intermixing of Si and Ge atoms occurred during annealing. The most significant changes were observed in the Ge-Ge region. With increasing of annealing temperature the increase of intensity of Ge-Ge mode originated from the $Si_{1-x}Ge_x$ strained channel layers and their downward shift were observed. These changes demonstrated the sensitivity of Raman spectra to Ge diffusion during annealing which results in decreasing Ge content in the $Si_{1-x}Ge_x$ strained channel or (and) its partial relaxation. With increasing annealing temperature the $Si_{1-y}Ge_y$ relaxed layers became more relaxed just in the case if they were not fully relaxed in as-grown samples. The peak at 521cm^{-1} corresponding to Si-Si mode originated from Si substrate remained unchangeable after annealing up to 900C for 30min.

It is necessary to point, that micro-Raman spectroscopy, PL spectroscopy and ULE-SIMS measurements were performed on the very same samples (Hall-bars and Van der Pauw cross) used for magnetotransport characterization.

In this research were investigated p-type MOD $Si_{1-x}Ge_x/Si_{1-y}Ge_y$ heterostructures with Ge composition in the $Si_{1-x}Ge_x$ channel varied from 0.6 up to 1 and grown on linearly graded, step graded or with LT-Si buffer $Si_{1-y}Ge_y$ VS with $0.3 \leq y \leq 0.63$. Hall mobility and sheet carrier density of p-type MOD $Si_{1-x}Ge_x/Si_{1-y}Ge_y$ heterostructures were obtained from the combination of resistivity and Hall effect techniques at temperature range 9-300K. The measurements were performed on as-grown and after FTA and RTA samples. Post growth FTA was performed on samples #51.33, #52.16, #54.08, #60.46, #622.83 and #622.84 at temperature range 600-900C for 30min in N_2 ambient. Post growth RTA was performed on samples #C1987, #C2015f and #C2072 at temperature 750C for 30sec in N_2 ambient.

For all investigated samples was observed similar effect of FTA on Hall mobility and sheet carrier density measured at 9 and 293K. The annealing at 600C was seen to have a negligible effect on the Hall mobility as well as on sheet carrier density. Increasing the annealing temperature resulted in pronounced successive increased of mobility. Every sample had optimum annealing temperature, which corresponded to the highest mobility. Further increasing of annealing temperature resulted in decreasing of mobility. For sheet carrier density was observed opposite behaviour with increasing annealing temperature. The maximum increase of Hall mobility measured at 9K was observed in sample #54.08 after FTA at 900C and corresponds to 8.5 times. But the maximum increase of Hall mobility measured at 293K was observed in sample #60.46 after FTA at 750C and corresponds to 18 times.

For all investigated samples was observed similar effect of RTA on Hall mobility measured at 9 and 293K. After RTA at 750C for 30sec was observed an increase in mobility compared to as-grown ones. The maximum increase of Hall mobility after RTA measured at 9 and 293K was observed in sample #C2015f and corresponds to 3.8 and 1.3 times respectively.

The highest mobility (at sheet carrier density) of 2DHG measured at 9K was observed for sample #C2476 containing Ge channel grown on thick $Si_{0.4}Ge_{0.6}$ linearly graded VS and corresponds to $14855cm^2 \cdot V^{-1} \cdot s^{-1}$ ($2.87 \cdot 10^{12} cm^{-2}$).

The highest Hall mobility (at sheet carrier density) measured at 293K was observed for sample #60.46 after FTA at 750C for 30min and corresponds to $1776cm^2 \cdot V^{-1} \cdot s^{-1}$ ($2.37 \cdot 10^{13} cm^{-2}$). The as-grown sample #60.46 consists of $Si_{0.2}Ge_{0.8}$ channel grown on $Si_{0.65}Ge_{0.35}$ linearly graded VS. This value of Hall mobility (at sheet carrier density) measured at room temperature is the highest ever reported for p-type MOD $Si_{1-x}Ge_x/Si_{1-y}Ge_y$ heterostructures.

The room temperature magnetotransport properties of 2DHG formed in the $Si_{1-x}Ge_x$ channel of p-type MOD $Si_{1-x}Ge_x/Si_{1-y}Ge_y$ heterostructures were studied by measuring magnetic field dependences of magnetoresistance and Hall resistance followed by applying the technique of MEMSA. The investigated samples consist of $Si_{1-x}Ge_x$ channel with $0.8<x<0.95$ and $Si_{1-y}Ge_y$ linearly graded VS with $0.35<y<0.63$. The highest drift mobility (at sheet carrier density) of 2DHG was obtained for sample #60.46 after FTA at 750C for 30min and corresponds to $3607cm^2 \cdot V^{-1} \cdot s^{-1}$ ($4.94 \cdot 10^{12} cm^{-2}$) at 290K. The as-grown sample #60.46 consists of $Si_{0.2}Ge_{0.8}$ channel grown on $Si_{0.65}Ge_{0.35}$ linearly graded VS. This value of 2DHG mobility (at sheet carrier density) measured at room temperature is the highest ever reported for p-type MOD $Si_{1-x}Ge_x/Si_{1-y}Ge_y$ heterostructures. For this sample was obtained the temperature dependence of mobility and sheet carrier density of 2DHG without parallel conduction in the temperature range 221-290K. It was found that the drift mobility of 2DHG increases with the decrease of temperature and sheet carrier density decreases with the decrease of temperature.

The low temperature magnetotransport properties of 2DHG formed in the $Si_{1-x}Ge_x$ channel of p-type MOD $Si_{1-x}Ge_x/Si_{1-y}Ge_y$ heterostructures were studied by measuring magnetic field dependences of magnetoresistance and Hall resistance at temperatures 25-0.34K and in magnetic fields up to 11T. The investigated samples consist of $Si_{1-x}Ge_x$ channel with $0.8<x<0.95$ and $Si_{1-y}Ge_y$ VS $0.3<y<0.63$. For the sample #622.83 after FTA at 700C for 30min in comparison

with as-grown one ($Si_{0.2}Ge_{0.8}/Si_{0.7}Ge_{0.3}$) were observed an improvements of magnetotransport characteristic of 2DHG at temperature 0.35K. The 9.2 times decrease of resistivity accompanied with appearing of SdH oscillations of magnetoresistance, an increase of carrier sheet density and 7.4 times an increase of Hall mobility were observed after annealing. The resistivity measured at temperature 0.35K decreased with increase of Ge composition in the $Si_{1-x}Ge_x$ channel and varied from 3155Ω/sq for sample #622.83 after FTA at 700C for 30min ($Si_{0.2}Ge_{0.8}$ as-grown) to 3155Ω/sq for sample #C1957 ($Si_{0.05}Ge_{0.95}$). The Hall mobility of 2DHG extracted from magnetic field dependence of Hall resistance at temperature 0.35K increased with increase of Ge composition in the $Si_{1-x}Ge_x$ channel and varied from $1460cm^2 \cdot V^{-1} \cdot s^{-1}$ for sample #622.83 after FTA at 700C for 30min ($Si_{0.2}Ge_{0.8}$ as-grown) to $6581cm^2 \cdot V^{-1} \cdot s^{-1}$ for sample #C1957 ($Si_{0.05}Ge_{0.95}$). The sheet carrier density of 2DHG was obtained by two ways, — from SdH oscillations of magnetoresistance and magnetic field dependence of Hall resistance. For all samples the sheet carrier density obtained from SdH oscillations of magnetoresistance is higher than from magnetic field dependence of Hall resistance. Effective mass decreases with increases Ge composition in the $Si_{1-x}Ge_x$ channel and varied from $0.17 \cdot m_0$ for sample #622.83 after FTA at 700C for 30min ($Si_{0.2}Ge_{0.8}$ as-grown) to $0.15 \cdot m_0$ for sample #C1957 ($Si_{0.05}Ge_{0.95}$). Ratio of transport scattering time to quantum scattering time increases with increases Ge composition in the $Si_{1-x}Ge_x$ channel and varied from 1.29 for sample #622.83 after FTA at 700C for 30min ($Si_{0.2}Ge_{0.8}$ as-grown) to 2.18 for sample #C1957 ($Si_{0.05}Ge_{0.95}$). The values of effective mass $0.15 \cdot m_0$ and ratio of transport scattering time to quantum scattering time 2.18 obtained for p-type MOD $Si_{0.05}Ge_{0.95}/Si_{0.37}Ge_{0.63}$ heterostructure are the lowest and the highest respectively ever published for p-type MOD heterostructures with $Si_{1-x}Ge_x$ channel grown by SS-MBE on $Si_{1-y}Ge_y$ VS on Si(001) substrate.

The investigation of p-type MOD heterostructures with high Ge content ($0.6<x<1$) $Si_{1-x}Ge_x$ channel grown on $Si_{1-y}Ge_y$/Si(001) virtual substrate have been studied by the author for first time in Advanced Semiconductors Research group at Warwick University. Due to this there are many

ways for further research. One of these ways has to be further optimisation of growth conditions and designs of active layers of MOD $Si_{1-x}Ge_x/Si_{1-y}Ge_y/Si(001)$ heterostructures with respect to higher mobility and sheet carrier density of 2DHG at room temperature range. It is also proposed to use gated Hall bar structures in order to measure sheet carrier density dependence of mobility of 2DHG. This will allow to test the relaxation time approximation theory of carriers transport and to define carriers scattering mechanisms, which limit the mobility of 2DHG. Another field of research is virtual substrates. The work on reduction the thickness of VS and improvement its surface quality has to be continued. Further work on optimisation of growth conditions and design of $Si_{1-y}Ge_y$ on low temperature Si buffer VS has to be continued as well.